

# Experiments in Neutrino Mass and Mixing:

Part I - New Limits on Heavy Neutrino Emission in  
Nuclear Beta Decay

Part II - Fast Neutron Backgrounds for the San Onofre  
Neutrino Detector

Thesis by  
Mark C. Chen

In Partial Fulfillment of the Requirements  
for the Degree of  
Doctor of Philosophy



California Institute of Technology  
Pasadena, California

1994  
(Submitted May 13, 1994)

©1994

Mark C. Chen

All rights reserved

## Acknowledgements

I am most grateful for the support given to me by Professor Felix Boehm. I benefited greatly from his guidance and experience. Much of what I've learned as a student at Caltech, I owe to him.

I've enjoyed the stimulating discussions I've had with Petr Vogel and I appreciate that he endured my many speculative questions, all the while offering clear thought and rational answers.

I cheerfully acknowledge all my collaborators, each of whom have taught me much about experimental physics, in addition to helping me stack a ton of lead bricks. They are Ralf Hertzenberger, Nicholas Mascarenhas, Vladimir Novikov, Brian Cook, Brian Dougherty and David Imel. In particular, special thanks go to Tom Radcliffe for showing me, amongst other things, the scientific virtue of skepticism. Luckily, I didn't believe everything he said. I also would like to thank Albert Young who, through our many enlightening conversations, always reminded me what the scientific pursuit was all about.

Special thanks go to Elsa Villate and to Herb Henrikson for all their assistance. They have made working with this group a true delight.

I hold, with greatest respect, my parents and I am incapable of expressing my gratitude for everything they have done for me. They instilled in me the desire to learn and their encouragement and support were always present. I dedicate this thesis to them.

Finally, I wish to express my deepest gratitude to my wife, Martha Shaw, for her love and especially for her patience and understanding through the strange and wonderful times that graduate studies have brought.

## Abstract

In Part I of this thesis, a new magnetic spectrometer experiment which measured the  $\beta$  spectrum of  $^{35}\text{S}$  is described. New limits on heavy neutrino emission in nuclear  $\beta$  decay were set, for a heavy neutrino mass range between 12 and 22 keV. In particular, this measurement rejects the hypothesis that a 17 keV neutrino is emitted, with  $\sin^2\theta = 0.0085$ , at the  $6\sigma$  statistical level. In addition, an auxiliary experiment was performed, in which an artificial kink was induced in the  $\beta$  spectrum by means of an absorber foil which masked a fraction of the source area. In this measurement, the sensitivity of the magnetic spectrometer to the spectral features of heavy neutrino emission was demonstrated.

In Part II, a measurement of the neutron spallation yield and multiplicity by the Cosmic-ray Underground Background Experiment is described. The production of fast neutrons by muons was investigated at an underground depth of 20 meters water equivalent, with a 200 liter detector filled with 0.09% Gd-loaded liquid scintillator. We measured a neutron production yield of  $(3.4 \pm 0.7) \times 10^{-5}$  neutrons per muon-g/cm<sup>2</sup>, in agreement with other experiments. A single-to-double neutron multiplicity ratio of 4:1 was observed. In addition, stopped  $\pi^+$  decays to  $\mu^+$  and then  $e^+$  were observed as was the associated production of pions and neutrons, by the muon spallation interaction. It was seen that practically all of the  $\pi^+$  produced by muons were also accompanied by at least one neutron. These measurements serve as the basis for neutron background estimates for the San Onofre neutrino detector.

# Contents

<b>I</b>	<b>New Limits on Heavy Neutrino Emission in Nuclear Beta Decay</b>	<b>1</b>
<b>1</b>	<b>Neutrinos in Beta Decay</b>	<b>2</b>
1.1	Signature of Massive Neutrino Emission in Beta Spectra . . . . .	3
1.2	Neutrino Mixing . . . . .	6
1.3	Signature of Admixed Heavy Neutrino Emission in Beta Spectra	7
<b>2</b>	<b>History of the 17 keV Neutrino</b>	<b>10</b>
2.1	The Early Experiments . . . . .	10
2.2	The Flames Rekindled . . . . .	16
2.3	The Shape Factor Issue . . . . .	28
<b>3</b>	<b>Details of the New Experiment</b>	<b>36</b>
3.1	The Magnetic Spectrometer . . . . .	36
3.2	Sources . . . . .	39
3.3	Detector and Data Acquisition . . . . .	44
3.4	Current Supply and Magnetic Field Instrumentation . . . . .	46
3.5	Environmental Monitoring . . . . .	50
<b>4</b>	<b>Data and Analysis</b>	<b>52</b>
4.1	Calibration . . . . .	52
4.2	Analysis of the Silicon Detector Spectra . . . . .	56
4.3	Magnetic Field Stability . . . . .	60

4.4	Other Analytical Issues . . . . .	64
4.5	Wide Scan Data . . . . .	66
4.6	Narrow Scan Data . . . . .	74
4.7	Strong Source Data . . . . .	81
4.8	Unified Discussion . . . . .	90
<b>5</b>	<b>Demonstration of Sensitivity</b>	<b>93</b>
5.1	Calibration Lines with the Foil . . . . .	94
5.2	Observing an Artificial Spectral Kink . . . . .	96
5.3	Analysis of the Spectral Distortion . . . . .	98
<b>6</b>	<b>The End of the 17 keV Neutrino</b>	<b>103</b>
6.1	Magnetic Spectrometers Retaliate . . . . .	103
6.2	Results from Other New Experiments . . . . .	109
6.3	Retraction of Positive Claims . . . . .	114
6.4	Conclusions . . . . .	117
 <b>II Fast Neutron Backgrounds for the San Onofre Neutrino Detector</b>		 <b>120</b>
<b>7</b>	<b>A Detector for Neutrino Oscillations</b>	<b>121</b>
7.1	Physics of Neutrino Oscillations . . . . .	121
7.2	Experimental Motivation . . . . .	123
7.3	Detector Description . . . . .	128
7.4	Signal and Background in the Detector . . . . .	131
<b>8</b>	<b>Fast Neutron Production by Muons</b>	<b>135</b>
8.1	Muon Spallation . . . . .	135

8.2	Neutron production processes . . . . .	137
<b>9</b>	<b>Measuring Neutrons from Muon Spallation</b>	<b>140</b>
9.1	Experimental Apparatus . . . . .	141
9.2	The Liquid Scintillator . . . . .	144
9.3	Electronics and Data Acquisition . . . . .	145
9.4	Energy and Time Calibrations . . . . .	149
<b>10</b>	<b>Stanford Data and Analysis</b>	<b>152</b>
10.1	Phase I - Preliminary Run . . . . .	152
10.2	Phase II - Single and Double Neutrons . . . . .	164
10.3	Phase III - Pion Production by Muons . . . . .	175
10.4	Associated Pion-Neutron Production . . . . .	185
<b>11</b>	<b>Discussion of Neutrons and Pions</b>	<b>193</b>
11.1	Modeling Neutrons in the Detector . . . . .	193
11.2	Neutron Multiplicity . . . . .	199
11.3	Relating Neutrons and Pions . . . . .	202
11.4	Comparison to Other Experiments . . . . .	206
11.5	Conclusions . . . . .	209

## List of Tables

1.1	Upper limits on $m_\nu$ from recent ${}^3\text{H}$ endpoint measurements. . .	5
2.1	Results of experiments on the 17 keV neutrino. . . . .	27
4.1	Gaussian fitted parameters for the ${}^{57}\text{Co}$ calibration lines. . . .	52
4.2	Results from fits to the wide scan data. . . . .	72
4.3	Results from fits to the narrow scan data. . . . .	79
4.4	Results from fits to the strong source data. . . . .	89
6.1	Results from new experiments that reject the 17 keV neutrino hypothesis. . . . .	114
10.1	Effect of analysis cuts on the Phase II second neutron data. .	171
10.2	Accidental contributions to various classes of double neutron counting events. . . . .	173
10.3	Double neutron analysis for the Phase III data. . . . .	177
10.4	Real over fake ratios in the veto counters. . . . .	184
10.5	Pion-neutron double count analysis for the Phase III data. . .	188
11.1	Single neutron production yield. . . . .	198
11.2	Double neutron production and multiplicity. . . . .	202

## List of Figures

1.1	Kurie plot of $\beta$ spectra with and without neutrino mass. . . .	4
1.2	Kurie plot of a two-component $\beta$ spectrum with admixed heavy neutrino emission, exhibiting a kink. . . . .	8
2.1	Data from Simpson's $^3\text{H}$ experiment showing the original evidence for a 17 keV neutrino. . . . .	11
2.2	Data from the Princeton magnetic spectrometer measurement of the $^{35}\text{S}$ $\beta$ spectrum. . . . .	14
2.3	Data from the Caltech 1985 $^{35}\text{S}$ experiment. . . . .	14
2.4	Data from the Chalk River $^{63}\text{Ni}$ experiment. . . . .	15
2.5	Raw data from the Simpson and Hime $^{35}\text{S}$ experiment. . . . .	19
2.6	Data from the Simpson and Hime $^{35}\text{S}$ experiment. . . . .	20
2.7	Apparatus of Hime and Jelley. . . . .	23
2.8	Data from the Hime and Jelley $^{35}\text{S}$ experiment. . . . .	24
2.9	Data from the Sur et al. $^{14}\text{C}$ experiment. . . . .	26
3.1	Sketch of the Caltech iron-free double-focusing $\beta$ spectrometer. . . . .	37
3.2	Photograph of the $\beta$ spectrometer. . . . .	37
3.3	Visualization of double-focusing. . . . .	38
3.4	Design drawing of the source positioning assembly. . . . .	40
3.5	Aluminum rings for mounting the source foils. . . . .	41
3.6	Crude sulfate solution deposition apparatus. . . . .	43
3.7	Diagram of the spectroscopy portion of the data acquisition system. . . . .	45

3.8	Sample detector spectrum with the spectrometer field set to transmit 150 keV electrons. . . . .	46
3.9	Power supply and control for the spectrometer coils. . . . .	48
3.10	$^{57}\text{Co}$ calibration spectrum. . . . .	49
4.1	Fitted Gaussian peaks to the $^{57}\text{Co}$ K-conversion lines. . . . .	53
4.2	Momentum calibration of the spectrometer. . . . .	55
4.3	Energy dependence of the fraction of excluded counts. . . . .	58
4.4	Magnetic field measurements swept during a wide scan data run. . . . .	60
4.5	Magnetic field stability during a 15 minute spectrum measurement. . . . .	61
4.6	Background spectrum measured above the $^{35}\text{S}$ endpoint. . . . .	65
4.7	Decaying intensity of the $^{35}\text{S}$ source. . . . .	66
4.8	Wide scan data. . . . .	68
4.9	Fitted wide scan data. . . . .	71
4.10	Minimum $\chi^2$ parabola, from the wide scan results. . . . .	73
4.11	Wide scan data with linear shape correction. . . . .	75
4.12	Narrow scan data without any shape correction. . . . .	77
4.13	Fitted narrow scan data. . . . .	80
4.14	Effects of field fluctuations on the count rate. . . . .	84
4.15	Field versus field scatter plot for many sweeps. . . . .	86
4.16	Fitted strong source data. . . . .	88
4.17	Mixing probability versus heavy neutrino mass. . . . .	92
5.1	Internal conversion lines from $^{57}\text{Co}$ , with the energy loss foil. . . . .	95
5.2	Kurie plot of the artificial kink data. . . . .	96
5.3	Artificial kink induced in the $^{35}\text{S}$ $\beta$ spectrum. . . . .	97

5.4	Sample Monte Carlo calculations of the aluminum foil strip. . . . .	100
5.5	Artificial kink with Monte Carlo simulation of the distortion. . . . .	101
6.1	Data from the Tokyo INS $^{63}\text{Ni}$ experiment. . . . .	106
6.2	Re-analyzed data from the Princeton 1985 $^{35}\text{S}$ measurement. . . . .	108
6.3	Apparatus of Mortara et al. . . . .	110
6.4	Data from Mortara et al. . . . .	111
6.5	Artificial kink from $^{35}\text{S}$ and $^{14}\text{C}$ . . . . .	111
6.6	Proportional counter $^3\text{H}$ data. . . . .	113
7.1	Oscillation parameter space for $\nu_e$ , allowed and excluded. . . . .	126
7.2	The San Onofre detector. . . . .	129
7.3	Neutrino detection scheme in the segmented detector. . . . .	130
7.4	Excluded regions of parameter space anticipated for this experiment. . . . .	132
9.1	Adapters for the 8-inch PMT's. . . . .	142
9.2	Experiment for measuring neutron production by muons. . . . .	143
9.3	Light attenuation length measurements for the Gd-loaded scintillator. . . . .	145
9.4	Schematic of the CUBE electronics. . . . .	146
9.5	Th and AmBe calibration spectra in the CUBE. . . . .	149
9.6	Neutron capture time calibration for TAC1 and TAC2. . . . .	151
10.1	ADC1 and TAC1 data, before analysis cuts. . . . .	154
10.2	ADC1 data, with an 11 $\mu\text{s}$ time cut. . . . .	156
10.3	Spectra from the muon veto counters. . . . .	158
10.4	ADC1 data, including time and veto cuts. . . . .	159
10.5	TAC1 data, with veto or energy cut. . . . .	161

10.6	Fitted capture time data, with all neutron selection cuts. . . .	163
10.7	ADC1 and TAC1 histograms from the Phase II data. . . . .	165
10.8	Raw ADC2 data from the Phase II runs. . . . .	167
10.9	Scatter-plot of ADC2 versus ADC1, before cuts. . . . .	168
10.10	Scatter-plot of the fake data, with cuts to remove $\mu$ decay. . .	170
10.11	Double neutron scatter-plot, after veto and time cuts. . . . .	172
10.12	Single neutron excess in the Phase III data. . . . .	178
10.13	Double neutron scatter-plots, for the Phase III data. . . . .	179
10.14	Short time constant histograms, for the Phase III data. . . . .	181
10.15	ADC readout of the muon vetos, for the $\pi^+$ candidate events. . .	183
10.16	Associated pion-neutron scatter-plots, from Phase III data. . .	187
10.17	TAC2 histogram of the real pion-neutron events. . . . .	189
10.18	ADC2 histogram of the real pion-neutron events. . . . .	191
10.19	VEB1 values for the real pion-neutron events. . . . .	192
11.1	Monte Carlo calculated neutron capture time, in Gd-loaded liquid scintillator. . . . .	196
11.2	Monte Carlo calculation of the neutron capture probability in the CUBE detector. . . . .	197
11.3	TAC1 histogram for double neutron events. . . . .	201
11.4	World plot of underground neutron yield measurements. . . .	208

## Part I

# New Limits on Heavy Neutrino Emission in Nuclear Beta Decay

# Chapter 1

## Neutrinos in Beta Decay

Throughout the history of nuclear physics, the study of  $\beta$  decay has been the source of much controversy, discovery and intrigue. The earliest puzzle was the observation of a continuous spectrum of energies of the emitted electrons in the decay. At that time, physicists pondered whether this was evidence that energy conservation was violated in  $\beta$  decay. In 1931, Pauli proposed [1] that an undetected particle was emitted along with the electrons in  $\beta$  decay, which carried away the “missing” energy. This particle, dubbed *neutrino* by Fermi soon after, is now known to accompany the electron in the  $\beta$  decay process and the physics of neutrinos and  $\beta$  decay have maintained this close association up to the present day.

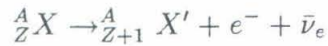
In 1957, Madame Wu and colleagues demonstrated that parity was violated in nuclear  $\beta$  decay [2]. This wondrous discovery spurred a large effort into the unraveling of the mysteries of the weak interaction, the only force known to violate this discrete symmetry. As a result, the observation of parity non-conservation led to an understanding of the  $V - A$  nature of the weak interaction and ultimately to the unification of the weak nuclear force with electromagnetism in the “electroweak” theory [3, 4, 5], now a cornerstone of the Standard Model.

This whirlwind tour of the history of  $\beta$  decay brings us to 1985. In a simple experiment which measured the  $\beta$  spectrum of  ${}^3\text{H}$  [6], Simpson ob-

served an excess of counts at low energies in the spectrum, below a threshold of 1.6 keV. He interpreted this as the signature of the emission of a heavy neutrino with a mass of about 17 keV. This “17 keV neutrino” was mixed with the ordinary electron neutrino and was emitted in a small fraction of the decays, while the remainder of the  $\beta$  decays involved just the light electron neutrino. Thus, another controversy and potential discovery was born out of the study of  $\beta$  decay. Would this claim of neutrino mass and of mixing between neutrino flavors persist, having the same impact as the discovery of parity violation? Or would this claim be rejected just as the earliest thoughts of energy non-conservation in  $\beta$  decay were ruled out?

## 1.1 Signature of Massive Neutrino Emission in Beta Spectra

In  $\beta$  decay:



the energy released in the process,  $Q$ , is given by

$$Q = [m({}^A_Z X) - m({}^A_{Z+1} X') - m_e - m_{\bar{\nu}_e}]c^2 \quad (1.1)$$

where  $m(X)$  is the mass of nucleus  $X$ . For this type of transition between two nuclei, the total energy released is shared by the final three bodies of the decay. Thus, the maximum amount of energy that the electron could carry away in the process is the total amount of  $Q$ , which is commonly referred to as the endpoint of the decay. From (1.1), it is evident that the presence or absence of a neutrino mass term can affect the electron spectrum by changing the endpoint behavior.

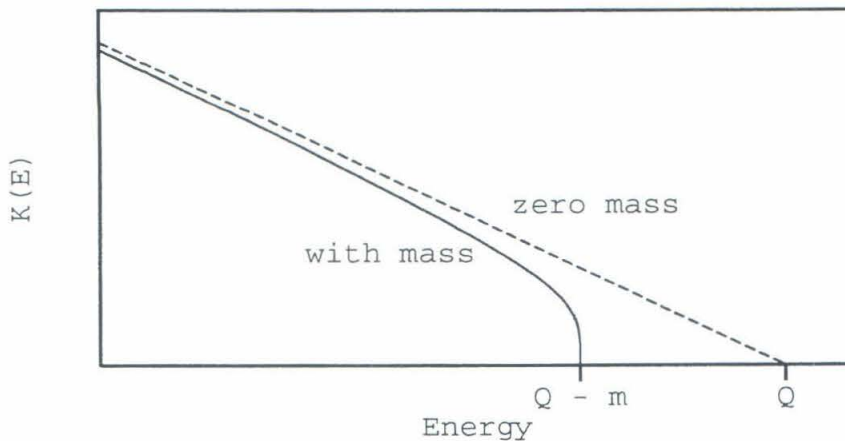


Figure 1.1: Kurie plot of  $\beta$  spectra with and without neutrino mass.

It is common to plot a  $\beta$  decay spectrum in the form of a Kurie plot [7]. For an allowed decay [8], this can be written as:

$$K(E) \equiv \left[ \frac{dN/dE}{pEF(Z, E)} \right]^{\frac{1}{2}} \propto [(Q - E)[(Q - E)^2 - m_\nu^2]^{\frac{1}{2}}]^{\frac{1}{2}} \quad (1.2)$$

where  $K(E)$  is the spectral strength as a function of energy,  $p$  and  $E$  are the electron momentum and energy,  $F(Z, E)$  is the Fermi function that corrects for effects of the nuclear Coulomb field,  $Q$  is the decay endpoint, and  $m_\nu$  is the neutrino mass. As illustrated in Fig. 1.1, the shape of the spectrum near the endpoint is dependent on whether neutrinos have a finite mass or not. The Kurie plot is a straight line for the case of perfectly massless neutrinos, intersecting zero at the endpoint  $Q$ . The spectrum with a massive neutrino exhibits a sharp rise with infinite slope just below a threshold energy equal to  $Q - m_\nu$ .

Many experiments have searched for evidence of neutrino mass by exam-

Experiment	Upper Limit on $m_\nu$ [eV]
LANL [12]	$< 9.3$
Zürich [13]	$< 11$
Tokyo INS [14]	$< 13$
Mainz [15]	$< 7.2$

Table 1.1: Upper limits on  $m_\nu$  from recent  ${}^3\text{H}$  endpoint measurements.

ining the shape of the electron spectrum near the  ${}^3\text{H}$   $\beta$  decay endpoint. As a  $\beta$  source,  ${}^3\text{H}$  has been the traditional choice for this type of measurement because the calculations of the final state effects for the relatively simple  ${}^3\text{H}$  decay give rise to the least uncertainty. Furthermore, when probing small values of  $m_\nu$ , in order to accumulate sufficient counts in the spectral region near  $Q - m_\nu$  where the shape is being measured, it is desirable to have a low  $Q$ -value. Thus, an additional reason to choose  ${}^3\text{H}$  decay for this type of measurement is its low endpoint value of 18.6 keV. Amongst experiments of this sort, only one has reported positive evidence for neutrino mass. Originally in 1980 [9] and in subsequent re-analyses [10, 11], Lubimov et al. reported observing an endpoint spectrum for  ${}^3\text{H}$  decay consistent with a finite neutrino mass of about 35 eV. The nature of the source used in this experiment, a thin foil of tritiated valine ( $\text{C}_5\text{H}_{11}\text{NO}_2$ ), introduced many problems in the analysis of the data and the understanding of the experimental response function. A number of recent experiments, which used  ${}^3\text{H}$  sources that were well understood, amongst other improvements, have disproved this claim. Table 1.1 lists the 95% CL upper limits on  $m_\nu$  set by these experiments. These results currently set the most stringent mass limits on the electron antineutrino.

## 1.2 Neutrino Mixing

The issue of neutrino mixing arises whenever neutrino mass is being considered. If neutrinos have non-zero mass, it is possible that the eigenstates for mass do not correspond to the flavor eigenstates of the weak interaction (see [16]). This behavior is seen in the quark sector where it is observed that the  $d, s, b$  quarks, which are the mass eigenstates, are mixed via the Kobayashi-Maskawa mixing matrix [17] when they participate in charged-current weak processes. If we allow analogous behavior in the lepton sector, we can write the weak eigenstates in terms of the mass eigenstates as follows:

$$\nu_l = \sum_{i=1}^3 U_{li} \nu_i \quad (1.3)$$

where  $\nu_l$  ( $l = e, \mu, \tau$ ) are identified as the familiar flavor eigenstates of the weak interaction,  $\nu_i$  ( $i = 1, 2, 3$ ) are the mass eigenstates, and  $U_{li}$  are the components of a unitary mixing matrix.

The following discussion is based again on analogy with the quark sector — the understanding of mass and of the Kobayashi-Maskawa mixing is imperfect in the Standard Model to begin with and this is, after all, physics beyond the Standard Model. From analogy to the quarks, it is thought that the neutrino mixing matrix between mass and weak eigenstates, if it exists, is constructed in such a way that the weak eigenstate of the electron neutrino, a mixture of the three mass eigenstates, consists predominantly of the lightest mass eigenstate. Similarly, it is believed that the muon neutrino is mostly  $\nu_2$  and that the tau neutrino is mostly  $\nu_3$ , where  $\nu_3$  is the heaviest. This would be similar to the mass hierarchy in the quark generations, where it is observed that the matrix elements between the up-like and down-like

quarks are nearly equal to one, for charged-current transitions within the same generation. If we take this assumption and if we make a further simplification that only one of the two heavier mass eigenstates participates in the mixing with an observable strength, we can write the flavor eigenstate for the electron neutrino as

$$\nu_e = \cos \theta \nu_1 + \sin \theta \nu_H \quad (1.4)$$

where  $\theta$  is a small mixing angle, similar in nature to the Cabibbo angle [18]. The notation  $\nu_H$  used in this two-component simplification represents some heavier mass eigenstate, be it  $\nu_2$ ,  $\nu_3$  or whatever, that has an observable mixing strength in the electron neutrino. The other mass eigenstate will be ignored for simplicity.

### 1.3 Signature of Admixed Heavy Neutrino Emission in Beta Spectra

Once we allow that neutrinos have mass and that mixing between different flavors of neutrinos can occur, it becomes possible that the heavier admixed neutrino mass can be observed in a  $\beta$  spectrum. This idea was first proposed by Nakagawa [19] and the consequences of such an admixture on the shape of a  $\beta$  spectrum are easily understood.

If it is energetically feasible to emit both the light neutrino  $\nu_1$  and the heavy neutrino  $\nu_H$  in the  $\beta$  decay process (two-component simplification used in this and all subsequent discussion), the electron energy spectrum will consist of two components having two different “endpoints.” When the ordinary light neutrino (mass  $< 7$  eV) is emitted, in  $\cos^2 \theta$  fraction of the decays, the energy spectrum will have a shape, as given in (1.2), dependent on

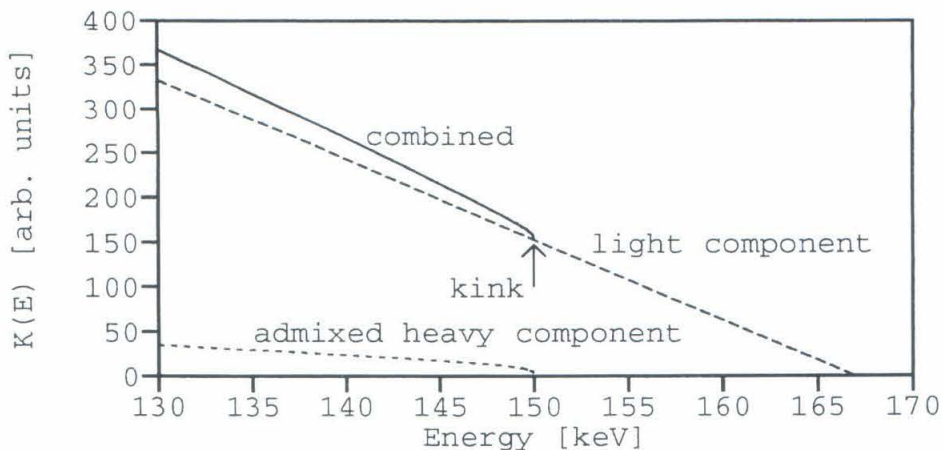


Figure 1.2: Kurie plot of a two-component  $\beta$  spectrum with admixed heavy neutrino emission, exhibiting a kink at  $Q - m_H = 150$  keV.

$m_1$ , the mass of  $\nu_1$ . In the other  $\sin^2 \theta$  fraction of the decays, this component of the spectrum will have a shape dependent on the large value  $m_H$ , the mass of the heavy neutrino. Combining both components gives a resultant spectrum which has an endpoint-like “kink” structure at  $Q - m_H$ , and which has a real endpoint at  $Q_0 = Q - m_1 \approx Q$  (as  $m_1$  is too small to observe). Such a two-component spectrum with a kink is illustrated in Fig. 1.2.

Thus, the signature of an admixed heavy neutrino being emitted in nuclear  $\beta$  decay is the observation of a two-component spectrum with a threshold-like kink. From the position of the kink, one gets the mass of the heavy neutrino. The size of the kink gives the magnitude of the effect (the emission probability of the heavy neutrino) and is equal to the squared mixing amplitude,  $\sin^2 \theta$ . Such an observation would be indicative of neutrino mass and of mixing between neutrino flavors, suggesting also that lepton flavor number is not a conserved quantity. In his 1985 experiment, Simpson

observed just such a kink in the  ${}^3\text{H}$   $\beta$  spectrum at 1.6 keV. He attributed this to the emission of a heavy neutrino with mass 17 keV and with mixing probability,  $\sin^2 \theta = 0.03$ . This was the origin of the 17 keV neutrino saga.

## Chapter 2

# History of the 17 keV Neutrino

### 2.1 The Early Experiments

Simpson's original experiment measured the  ${}^3\text{H}$   $\beta$  spectrum with a Si(Li) detector in which tritium was implanted. By implanting the  $\beta$  source in the detector itself, the apparatus was to behave as a total absorption calorimeter for measuring the electron energies. Originally designed to measure the endpoint of the  ${}^3\text{H}$  spectrum in order to examine Lubimov's claim of a 35 eV electron neutrino mass, Simpson turned his attention to the lower energy portion of the spectrum. Here he observed a sudden excess of counts below 1.6 keV. His data is displayed in Fig. 2.1. His claim was that the data supported the hypothesis that a 17 keV neutrino was emitted with a mixing probability of 3%.

At this point, it should be considered important to identify some experimental concerns with regards to this first piece of evidence for the 17 keV neutrino. The low energy region of the  $\beta$  spectrum observed to be in excess is quite difficult to measure reliably. At energies  $< 1.6$  keV, one is quite close to the noise level. Another challenge is the difficulty in calibrating these Si detectors at such low energies. Furthermore, radiation damage caused by the ion-implantation process has been observed to result in pulse-height defects in Si and Ge detectors [20, 26].

Aside from the experimental difficulties, it was pointed out by a number

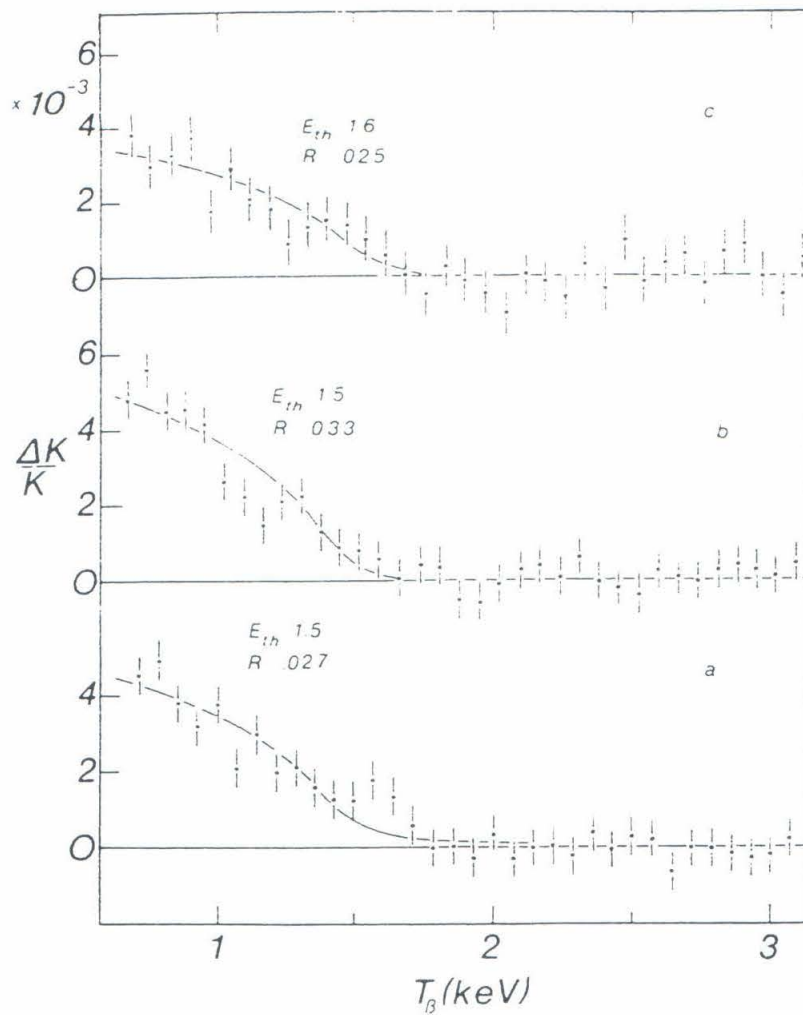


Figure 2.1: Data from Simpson's  $^3\text{H}$  experiment showing the original evidence for a 17 keV neutrino. Here the data is plotted as the fractional deviation from a straight-line Kurie plot, normalized above the threshold for heavy neutrino emission. The curves represent the theoretical expectation, assuming a 3% heavy neutrino admixture.

of authors [21, 22, 23, 24] that in the original analysis, an incorrect choice of screening potential and exchange effects might explain the excess of counts at low energy in the  ${}^3\text{H}$   $\beta$  spectrum. To further complicate matters, as the tritium was bound within a crystal lattice in this experiment, additional corrections are required [26, 27] that were not originally performed. Though all of these required corrections allow for the introduction of additional counts at low energy, re-analysis of the original data, performed by Simpson and Hime with all these effects properly treated, still could not account for all of the observed excess below 1.6 keV [25, 26, 27]. They quote a best fit mixing probability of  $\sin^2 \theta = 0.011 \pm 0.003$  after performing the re-analysis, down from the original 3% admixture, but not zero.

Immediately after this reported observation of heavy neutrino emission, and continuing in parallel with the analytical issues discussed prior, a number of experiments were performed by other groups who set out in search of the 17 keV neutrino. The experimental assault began with measurements of the  $\beta$  spectrum of  ${}^{35}\text{S}$ . Two of these experiments [28, 29] measured the  ${}^{35}\text{S}$   $\beta$  spectrum with Si(Li) detectors. The other three experiments were performed with magnetic spectrometers [30, 31, 32]. None of them were able to confirm Simpson's result.

I choose to comment on two of these magnetic spectrometer experiments. The Altitzoglou measurement at Princeton [30] used an iron-free intermediate-image magnetic spectrometer, which belonged to none other than Madame C.S. Wu. A surface-barrier detector was employed at the focus. Transmitted electrons that strike the detector may backscatter or lose energy in the contact layer at the entrance of the detector in front of the active layer. Consequently, the measured pulse-height spectrum for electrons transmitted at any given magnetic field setting consists of a full-energy peak

and a backscatter tail that extends all the way down to zero. Unfortunately, the backscatter spectrum runs into the detector noise at low energies. Thus, an extrapolation must be made to find the backscatter contribution below the noise and this must be added to the measured, transmitted electron intensity. This is an important point that will be discussed again later as it relates to the shape corrections required in fitting the data taken by magnetic spectrometer experiments. The procedure employed in the analysis of this data was to extrapolate the backscatter tail with a linear function determined just above the noise. In fitting the measured  $\beta$  spectrum taken by this spectrometer, a shape correcting function which included linear and quadratic terms was required. No kink was observed in the data and the limit on the admixture of a 17 keV neutrino reported by this experiment was  $\sin^2 \theta < 0.004$ , at the 99% confidence level. Their data are shown in Fig. 2.2.

The Markey and Boehm measurement employed the Caltech iron-free double-focusing beta spectrometer. Of course, more details about this spectrometer will follow as this was the same instrument employed in the new experiment. A 2 mCi “drop-source” of  $^{35}\text{S}$  was deposited onto a Mylar foil of thickness  $230 \mu\text{g}/\text{cm}^2$ . A liquid-nitrogen cooled Si(Li) detector recorded the transmitted electrons at each spectrometer field setting. Counts below the noise were extrapolated to zero energy — the procedure was not described so it is presumed that the extrapolation employed some linear function, possibly even a constant. The data are shown in Fig. 2.3. No shape correction was required to fit the measured  $\beta$  spectrum. The quoted upper limit on the mixing strength of a 17 keV neutrino was 0.3% at the 90% confidence level.

Among the early experiments were also two measurements of the  $^{63}\text{Ni}$   $\beta$  spectrum: one employed the Chalk River double-focusing magnetic spectrometer [33] and the other was at Caltech [34]. In the Chalk River exper-

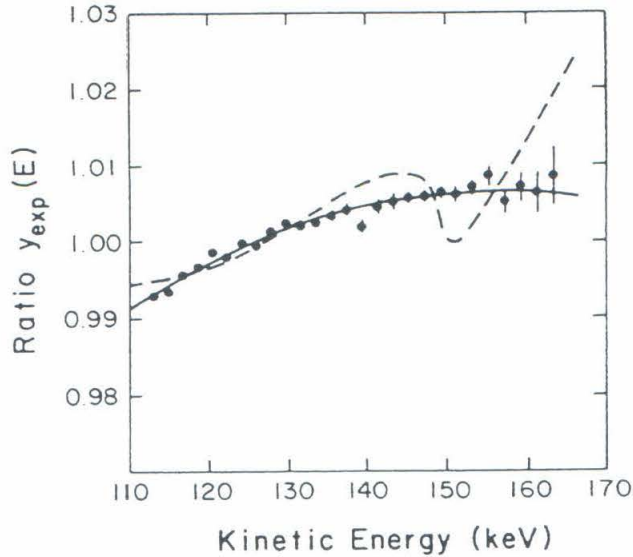


Figure 2.2: Data from the Princeton magnetic spectrometer measurement of the  $^{35}\text{S}$   $\beta$  spectrum. The solid line is the fit without heavy neutrino. The quadratic shape correction is easily seen. The dashed line is the fit for a 17 keV neutrino with 3% admixture.

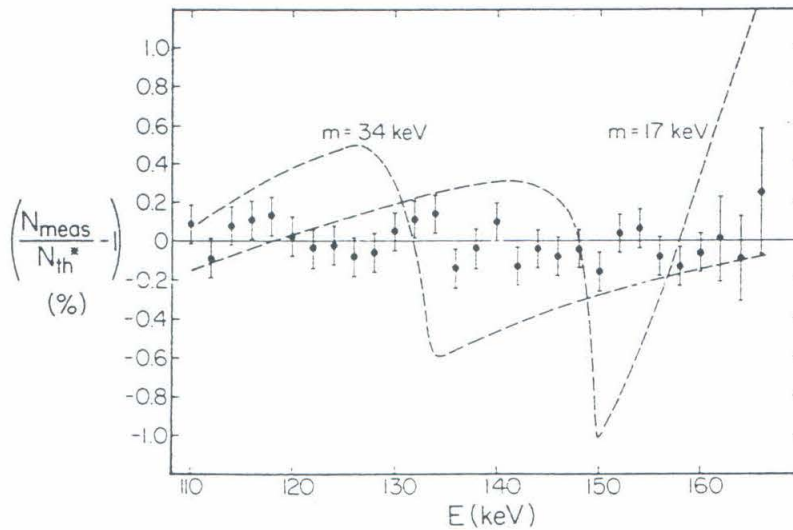


Figure 2.3: Data from the Caltech 1985  $^{35}\text{S}$  experiment. The data points are plotted as the deviation from the theoretical  $\beta$  spectrum without heavy neutrino. The dashed line is the expected result for a 17 keV neutrino with 3% admixture.

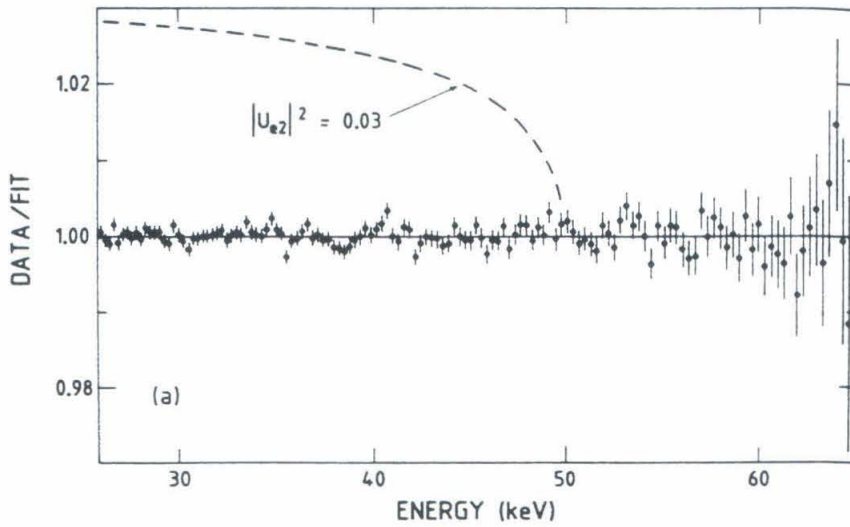


Figure 2.4: Data from the Chalk River  $^{63}\text{Ni}$  experiment. The data points are plotted as the deviation from the theoretical  $\beta$  spectrum with  $\sin^2\theta = 0$ . The dashed line is the expected spectral shape for a 17 keV neutrino with 3% admixture, normalized above the threshold for heavy neutrino emission.

iment, Hetherington employed a 19-strip source, inclined slightly off-radius, with electrostatic biasing potentials. This highly advanced source achieved its goal of enhanced count rate without sacrificing energy resolution; however, one drawback of this experiment was that the very thick source backing used necessitated sizeable source backscattering corrections in the data. The detector employed was an array of 22 thin-window proportional counters, also angled to the spectrometer radius. Despite the complexities of multiple source and detector elements in this experiment, the understanding of electron transport in the spectrometer was superb. Consequently, they were able to achieve fairly uniform resolution and acceptance across their detector plane and they were able to consolidate their data into one spectrum, using a common calibration. The data from this experiment are shown in Fig. 2.4. No evidence for heavy neutrino emission was observed and the limit set by this measurement was  $\sin^2 \theta < 0.3\%$  at the 90% confidence level. In this measurement of the  $^{63}\text{Ni}$   $\beta$  spectrum, a linear shape factor correction was required in the fitting. This careful and well-described experiment, able to benefit from the lower endpoint of  $^{63}\text{Ni}$  decay and consequently from the higher statistics this entails, was believed to be, at that time, among the most convincing refutations of the 17 keV neutrino.

## 2.2 The Flames Rekindled

Faced with this collection of negative results and with numerous experimental and analytical issues to resolve in the tritium experiment, Simpson, with the help of Hime, attempted to address these concerns. At this point, the experimental approach needed to resolve the situation was clear. As there was criticism of the original measurement which employed tritium implanted in

Si(Li), they chose to repeat the experiment with an alternative configuration, this time by implanting tritium in hyperpure germanium, seeking to overcome and address the problems that might have occurred earlier. As a second path to explore, they decided to measure their own  $^{35}\text{S}$   $\beta$  spectrum. With the higher endpoint of 167 keV, the effect of emission of a 17 keV neutrino would be visible at 150 keV in the  $^{35}\text{S}$  spectrum, far enough away from the low-energy  $^3\text{H}$  regime in which atomic effects could be important. (This was, of course, the same reasoning that motivated the early negative experiments to select  $^{35}\text{S}$  as their  $\beta$  sources.)

Their new  $^3\text{H}$  experiment [26] utilized high-purity germanium as the detector and as the medium in which the tritons were implanted. The advantage over Si(Li) was that the pure germanium crystal could be annealed at high temperatures after the ion-implantation process, with the hope that this would heal the radiation damage that was induced by the ion beam (and shown to result in pulse-height defects [20]). In this new experiment, care was taken in implanting the tritium away from the edges of the detector. Additionally, a careful and clever low-energy calibration was performed using x-ray fluorescence and escape of germanium K x-rays, producing calibration lines down to 1.33 keV. With these experimental modifications, they took data which showed the same deviation from a straight line Kurie plot at low energies and apparently were consistent with the spectral kink of heavy neutrino emission. For this data, they achieved a best fit with the emission of a  $16.9 \pm 0.1$  keV neutrino with  $(1.1 \pm 0.1)\%$  mixing probability. A study of the corrections for the effective screening potential for lattice-bound tritium was also made and they found that the uncertainty in the value of the screening potential introduces a systematic uncertainty in the mixing probability of  $\pm 0.5\%$ , thus allowing for a heavy neutrino admixture from 0.6 to 1.6%.

The Simpson and Hime  $^{35}\text{S}$  experiment [35] employed a Si(Li) detector, cooled to liquid-nitrogen temperature, to measure the energies of the  $^{35}\text{S}$  decay electrons. Two  $^{35}\text{S}$  sources were prepared using the technique of chemical adsorption [36]. The sources of 0.5  $\mu\text{Ci}$  and 5  $\mu\text{Ci}$  activity were deposited on aluminum and gold-coated Mylar. The Mylar backing used in this measurement was of thickness 10  $\mu\text{m}$ , certainly not negligible. This was estimated to introduce a 2–3% magnitude continuum distribution of backscattered electrons (with energies below the full-energy peak for a monoenergetic electron). Surprisingly, this was not thought of as a concern — perhaps because in this configuration of source and detector, with electrons travelling from the source and striking the detector diffusely, the backscattered fraction of electrons off the detector is about 30% [37]. Thus, present in this measurement of the  $^{35}\text{S}$   $\beta$  spectrum were backscatter contributions from both the detector and source backing, resulting in response functions that included a large fraction of electrons which deposited less than their full energy in the detector, on account of scattering out of the detector and on account of energy loss for electrons backscattered through the Mylar foil.

In their experiment, data were accumulated, first with the weak source close to the detector and with the stronger source at about four times the distance, with both configurations yielding the same count rate. A portion of their raw data is shown in Fig. 2.5. In this type of measurement which collects the entire  $\beta$  spectrum simultaneously, background is subtracted, a correction for pile-up is performed, and the resulting data is analyzed convolving the  $\beta$  spectrum with a detector response function that must be determined by a calibration source. A  $^{57}\text{Co}$  source was used in this experiment to calibrate the detector energies and to determine the response function. The fitted data from this measurement indicated evidence for a heavy neutrino and are

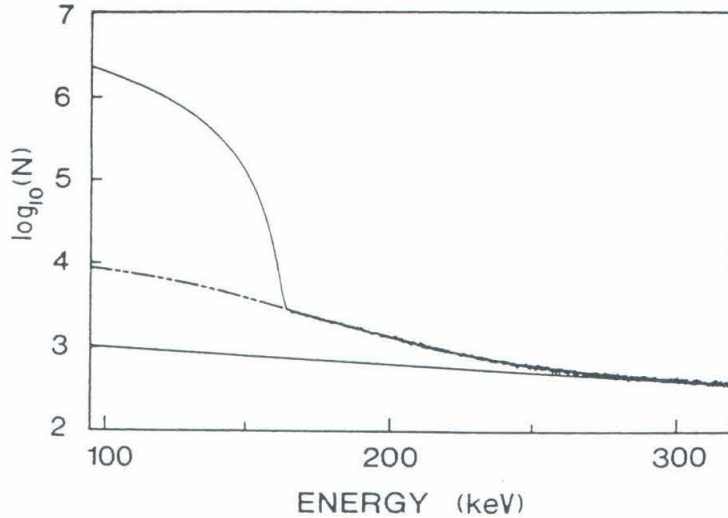


Figure 2.5: Raw data from the Simpson and Hime  $^{35}\text{S}$  experiment, showing background and pile-up that must be corrected.

shown in Fig. 2.6. They quote a best fit of  $16.9 \pm 0.4$  keV for the heavy neutrino mass, with an admixture of  $(0.73 \pm 0.09 \pm 0.06)\%$ .

With this apparent confirmation of the  $^3\text{H}$  experiment and with their own  $^{35}\text{S}$  data showing evidence for the 17 keV neutrino, Simpson was left with the task of explaining why it was that the host of negative experiments saw nothing. He noted that while the original effect was reported at the 3% level, it had since been corrected and found to exist, in the original and new data, at the 1% level. So a general point that he made was that the experiments which searched for a 3% admixture weren't capable of making a statement at the 1% level. Simpson also attacked each of the negative experiments individually [35], criticizing what he perceived as shortcomings in each experiment (from insufficient energy resolution of the Princeton measurement, anomalous scattering in the spectrometer of the Markey and Boehm experiment and excessive thickness of the source backing in the Chalk River experiment). He

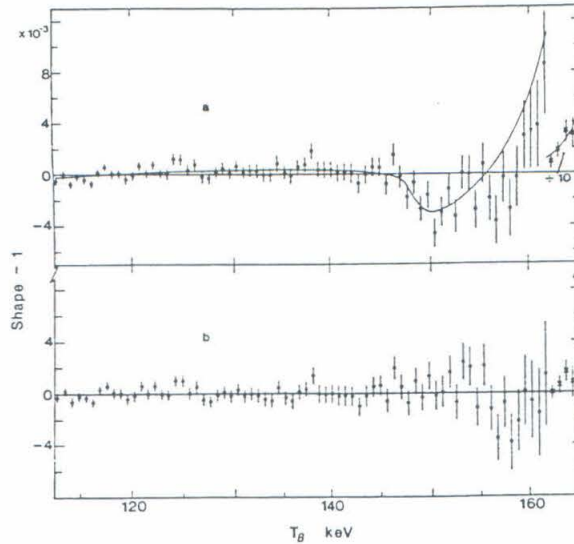


Figure 2.6: Data from the Simpson and Hime  $^{35}\text{S}$  experiment. Above, the data points are the deviation from the theoretical spectrum with  $\sin^2\theta = 0$ . The curve is the fit for a 17 keV neutrino with 0.8% admixture. Below is the residual of the data divided by the theoretical fit with heavy neutrino admixture.

even claimed [25] that a re-analysis of the data of Ohi et al. [29], taken with a semiconductor detector, showed evidence of some sort of kink close to where the 17 keV neutrino should appear. This re-analysis took extreme liberties in the fitting of what Simpson perceived as the kink in the Ohi data — so much so that it really invalidates the claim that the Ohi data supports the 17 keV neutrino hypothesis.

Aside from these individual attacks, one common issue was brought to attention by Simpson. In the fitting of the data taken by the magnetic spectrometer experiments, arbitrary shape-correcting functions are required to achieve a good fit to the  $\beta$  spectra. Simpson’s criticism, which will be discussed in some detail later, was that the small deviation in the spectral shape caused by heavy neutrino emission could be obscured by these shape factors. The kink would be “washed out” by the inclusion of these free

parameters. This shape factor issue was used as a universal dismissal of all magnetic spectrometer results. While the shape factor is an important point to consider, the significance of his argument was simply overstated.

These new results began to stimulate the experimental scene, but they weren't entirely convincing. The  $^3\text{H}$  experiments still had to contend with the pesky screening potential. The observed effect in the  $^{35}\text{S}$  experiment was suggestive. Additional experiments would attempt to sort it all out.

A new measurement of the  $^{35}\text{S}$   $\beta$  spectrum using the Caltech double-focusing, iron-free magnetic spectrometer was initiated to address some of the criticisms previously identified. Shutters were added to minimize the internal scattering, though it was never demonstrated that there was any real problem to begin with. The detector, electronics, and vacuum systems were improved. A 2 mCi source was prepared by vacuum evaporation of ammonium sulfate onto 0.9  $\mu\text{m}$  Mylar foil.

In comparison to the 1985 experiment, this is a preferable method of source preparation than the "drop" technique. However, it is indeed rather surprising that significant activity could be deposited by evaporation of ammonium sulfate. When heated, ammonium sulfate will dissociate into ammonia and  $\text{H}_2\text{SO}_4$ . The sulfuric acid, carrying the  $^{35}\text{S}$  activity, could react with the exposed, aluminized Mylar foil, leaving some form of aluminum sulfate on the foil. It seems more likely that, upon heating, the sulfate would react with the molybdenum boat. There were many difficulties observed by the participants in this experiments with the source preparation. The effective yield of their tests were very low. Much residual activity would be found in the molybdenum boat after attempts at vacuum evaporation. Ultimately they produced a reasonable source; however, it should be suspected that possibly some of the activity deposited on the foil might have been "splashed"

there rather than chemically adsorbed, during the bubbling of the material upon heating.

In this 1989 experiment [39], they did find some problems with their source. They observed that their  $^{35}\text{S}$  source intensity decreased with a half-life of 85 days rather than the 87.4 day tabulated value. This might have been due to desorption of source material into the vacuum. In this measurement, the spectrometer coil current would be fixed for a long duration and data would be accumulated at many different field settings to reproduce a  $\beta$  spectrum. Upon compilation of the many measurements into a single spectrum, the scatter distribution of the data points was observed to be non-statistical. The problem of source desorption could have potentially been a component of this extra fluctuation. More likely, it was magnetic field disturbances, local and global, that introduced additional variability in the count rates of each data point at each current setting. By adding an external error term to their data, they were able to fit the  $^{35}\text{S}$   $\beta$  spectrum. Linear and quadratic free parameters were required in the shape correction in order to achieve a good fit. The result of their analysis would exclude the emission of a 17 keV neutrino, but only with a 90% CL upper limit on the heavy neutrino admixture of 0.6%.

Hime, with an understanding of the potential shortcomings of the Guelph  $^{35}\text{S}$  experiment, continued by constructing a new spectrometer for a new measurement. With Jelley at Oxford, they measured the  $^{35}\text{S}$   $\beta$  spectrum, again with a Si(Li) semiconductor detector [41]. The aim of the new spectrometer was to perform a high statistics measurement using a source and detector geometry which would only select electrons that were incident approximately normal to the detector, with the use of collimators and apertures. With electrons striking the detector normally incident and away from the detector

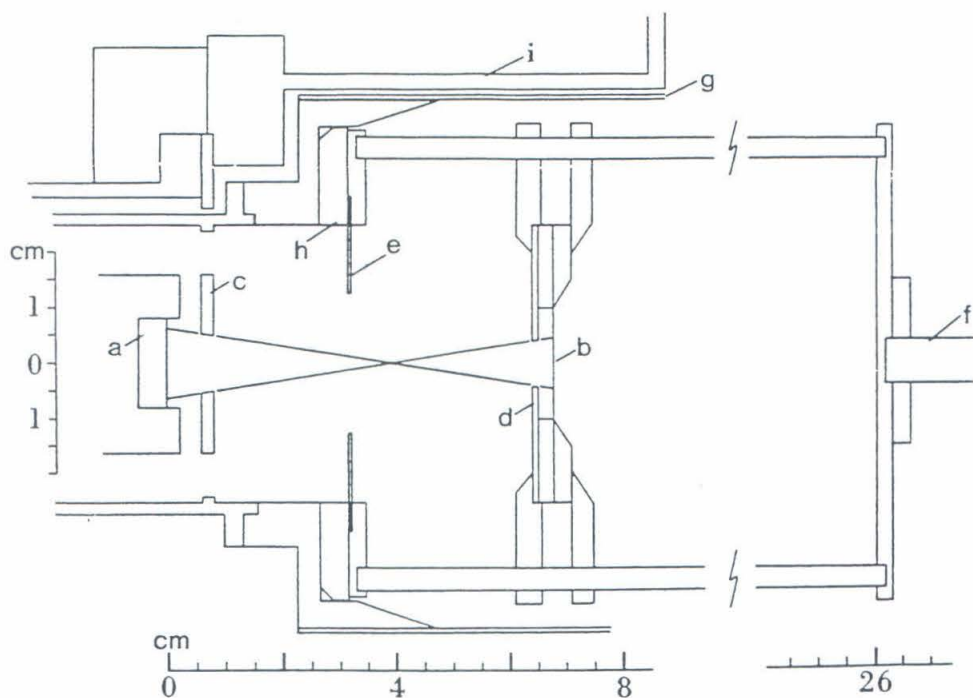


Figure 2.7: Apparatus of Hime and Jelley.

edges, the fraction of electrons which deposit less than their full energy, due to backscattering, is substantially reduced. Consequently, the uncertainty introduced by the understanding of the detector response would be much less significant. The Oxford  $\beta$  spectrometer is shown in Fig. 2.7.

Indeed, the measurement of the detector response function using monoenergetic, internal conversion electron lines, showed that the total backscattered fraction of electrons was about 13%, in agreement with other experimental data [37, 38] which had also measured the backscatter fraction for electrons on silicon at these energies. This was a big improvement over the Guelph configuration which had a backscatter fraction of about 30%. With a carefully determined response function and high statistics data taken with a 40  $\mu\text{Ci}$  source, Hime and Jelley presented the astonishing data shown in Fig. 2.8.

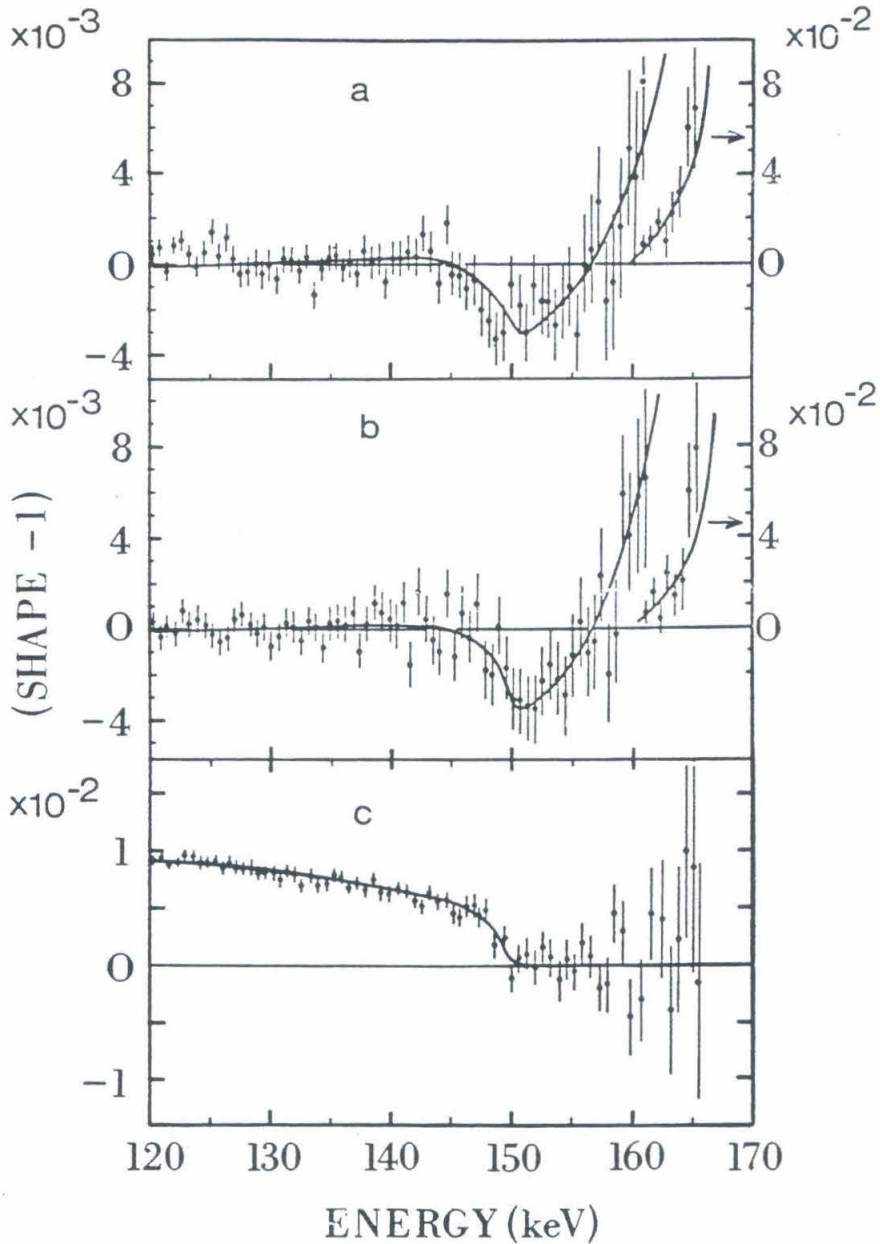


Figure 2.8: Data from the Hime and Jelley  $^{35}\text{S}$  experiment. The top two plots correspond to data taken in two separate runs. Data are plotted as deviation from a straight-line Kurie plot. The solid curves are the expected deviations from a 17 keV neutrino with  $\sin^2 \theta = 0.009$ . The bottom plot is a combined data set with the data and curves normalized above the threshold for 17 keV neutrino emission.

What a remarkably convincing result! The data shows strong evidence for emission of a massive neutrino, with mass of  $16.95 \pm 0.35$  keV and with  $\sin^2 \theta = 0.0078 \pm 0.0008$ .

Hime and Jelley proceeded to measure the  $\beta$  spectrum of  $^{63}\text{Ni}$  with the same apparatus [27]. In this data, they also found evidence for emission of a 17 keV neutrino, albeit with much less statistical significance and with much more uncertainty in the detector response (due to the lower energies of the  $^{63}\text{Ni}$   $\beta$  electrons). They found a best fit with a  $16.75 \pm 0.38$  keV neutrino mass and an admixture of  $(1.01 \pm 0.21)\%$ .

An even more provocative result was the observation by Sur et al. [42] of evidence for the 17 keV neutrino in the  $^{14}\text{C}$   $\beta$  spectrum. In this nifty experiment performed at LBL,  $^{14}\text{C}$  was dissolved into a germanium melt and a germanium crystal was grown with  $^{14}\text{C}$  activity distributed throughout. This crystal was instrumented as a Ge detector and they measured the  $\beta$  spectrum displayed in Fig. 2.9. They observed a best fit to a  $\beta$  spectrum which included emission of a  $17 \pm 2$  keV neutrino with a mixing probability of  $(1.40 \pm 0.45 \pm 0.14)\%$ . The statistical significance of this result was not overwhelming though, as it was in the Hime and Jelley measurement. Nevertheless, yet another measurement with a semiconductor detector revealed evidence for heavy neutrino emission. Important from the sociological point of view, this was the first positive observation of the 17 keV neutrino which did not originate from Simpson's Guelph group or its offshoot.

There was, in addition, a report of evidence for emission of the 17 keV neutrino in a measurement of the IBEC (internal bremsstrahlung electron capture)  $\gamma$  spectrum of  $^{71}\text{Ge}$  [43]. The observed distortion of the IBEC spectrum, measured with a Ge detector, was reported to be consistent with emission of a 17.2 keV neutrino with mixing probability of 1.6%. The statistical

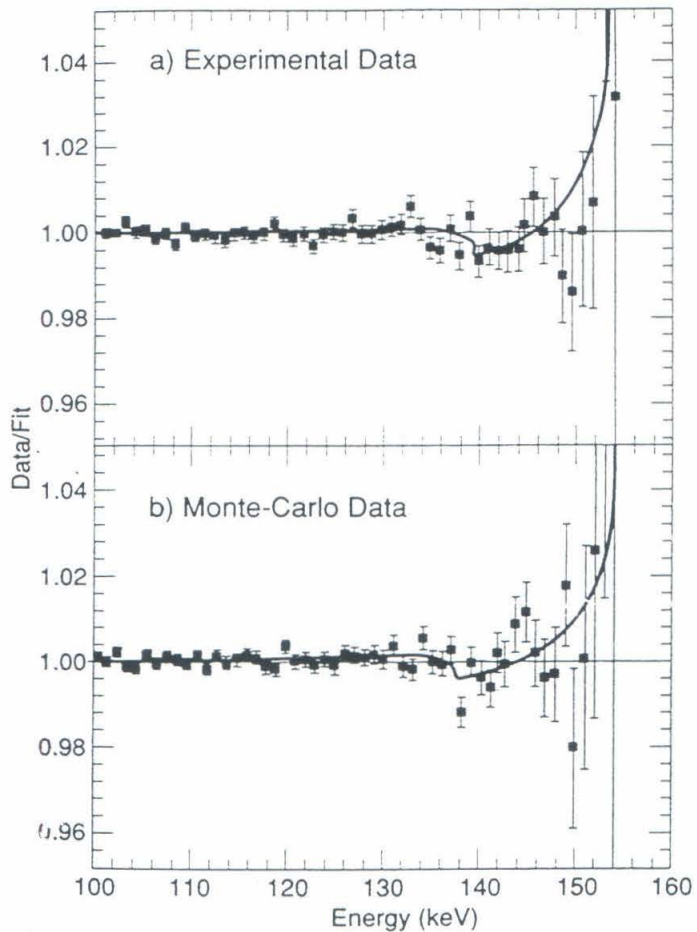


Figure 2.9: Data from the Sur et al.  $^{14}\text{C}$  experiment. Data divided by the fit with zero mixing are plotted. The solid curve is the expected shape from a 17 keV neutrino with 1% admixture. The bottom plot is of Monte Carlo generated data.

Experiment	Source	Technique	$\sin^2 \theta$ , $m_H = 17$ keV
Simpson (revised)	$^3\text{H}$ in Si(Li)	semiconductor	0.011(3)
Altitzoglou et al.	$^{35}\text{S}$	magnetic	$< 0.004$ 99% CL
Ohi et al.	$^{35}\text{S}$	semiconductor	$< 0.0015$ 90% CL
Apalikov et al.	$^{35}\text{S}$	magnetic	$< 0.0017$ 90% CL
Datar et al.	$^{35}\text{S}$	semiconductor	$< 0.006$ 90% CL
Markey and Boehm	$^{35}\text{S}$	magnetic	$< 0.003$ 90% CL
Hetherington et al.	$^{63}\text{Ni}$	magnetic	$< 0.003$ 90% CL
Hime and Simpson	$^3\text{H}$ in Ge	semiconductor	0.011(5)
Simpson and Hime	$^{35}\text{S}$	semiconductor	0.0073(9,6)
Hime and Jelley	$^{35}\text{S}$	semiconductor	0.0078(6,6)
Becker et al.	$^{35}\text{S}$	magnetic	$< 0.006$ 90% CL
Sur et al.	$^{14}\text{C}$ in Ge	semiconductor	0.0140(45,14)
Zlimen et al.	$^{71}\text{Ge}$	IBEC	0.016(8)
Hime and Jelley	$^{63}\text{Ni}$	semiconductor	0.0101(12,18)

Table 2.1: Results of experiments on the 17 keV neutrino. Positive experiments list their errors in parentheses (in the last digits, statistical and systematic given if meaningful). This chronology lists results which had been reported up to this point in the history of the 17 keV neutrino. Several experiments, including this one, had commenced prior to the actual publication dates of some of these results and will be included in a later summary.

significance of this curious result was at less than the  $2\sigma$  level, however.

A summary of the results of the various experiments leading up to this point is given in Table 2.1. What did this all suggest? The signature of heavy neutrino emission was observed in the  $\beta$  spectra of four different nuclei, in configurations including both internal and external sources to the semiconductor detectors. All the results, old and new, were consistent with an admixture of about 1% and they all reported masses of the heavy neutrino of around 17 keV. Was the 17 keV neutrino real? Could it be that the previous measurements with magnetic spectrometers weren't capable of observing the kink? Round three in the experimental activity was about to begin.

### 2.3 The Shape Factor Issue

It soon became apparent that all the experiments which reported evidence for the 17 keV neutrino employed semiconductor detectors to measure the energies of the emitted  $\beta$  electrons. Was there some heretofore unknown effect in the solid state that could account for this? This was inconceivable as the energies involved in the  $\beta$  decays of the various nuclei in which the kink was observed span such an enormous range: from 1–150 keV. Additionally, the positive evidence with both implanted and external sources seemingly eliminated any common effect that could be plaguing these experiments.

If indeed the 17 keV neutrino did exist, it was necessary to explain why the magnetic spectrometer experiments did not observe it. There was one common criticism which was used to derail the magnetic spectrometer experiments and that was the shape factor.

When one attempts to measure a  $\beta$  spectrum, it is not enough to simply place a source in an apparatus, record data, and interpret the raw data as a replica of a  $\beta$  spectrum. As the response of an instrument to electrons of various energies will not be identical, it is necessary to account for this when producing a spectrum, which is a measure of intensity as a function of energy. An experimental task which is necessary is to determine and understand the response function.

In experiments which employ semiconductor detectors and external sources, the measurement of the experimental response function is not so easy (in contrast, the situation for a total absorption calorimeter, such as in the  $^3\text{H}$  and  $^{14}\text{C}$  experiments, is much simpler). In those external source experiments which reported a positive 17 keV neutrino signature, one or maybe a few internal conversion electron lines were used to calibrate the response.

A semiconductor detector response has many components, including a full-energy Gaussian peak (the easy part to understand), and a low-energy tail due to energy loss, bremsstrahlung, and backscattering, each with varying contributions and shapes as a function of energy. In the Simpson and Hime  $^{35}\text{S}$  experiment, this low-energy tail contained about 43% of the intensity of the full-energy peak, implying that a sizable fraction of the measured electrons deposited energy in a quantity from which it is not trivial to extract a spectrum. A complete understanding of the shape of the response function is essential in these experiments and a careful determination of the detector response was indeed a feature of the Hime and Jelley  $^{35}\text{S}$  experiment. However, it should be emphasized that their detector response was only determined with one IC line and that it was assumed that this response did not vary significantly with electron energy. This is not necessarily a valid assumption and it was never demonstrated satisfactorily that this was the case. Nevertheless, by performing the proper deconvolutions in their raw data, these external source experiments were able to extract  $\beta$  spectra that agreed with predictions (and which included heavy neutrino emission). Strictly speaking however, achieving a fitted  $\chi^2/\nu \approx 1$ , over the range of interest, doesn't necessarily mean that the response function utilized and the assumptions made are complete.

In magnetic  $\beta$  spectrometers, the detection and dispersion of the electrons are separate processes. There are advantages and disadvantages in such a situation. One advantage is that, compared to the prior case in which a non-ideal response in a semiconductor detector simultaneously distorts both the intensity and energy information in the spectrum, in a magnetic spectrometer, the response solely affects the intensity, with only a minute effect on the energy. The disadvantage of a magnetic spectrometer, with regards to re-

sponse function determination, is that because the detection and dispersion are distinct, there are consequently two components of the apparatus which impact the response.

The resolution of a magnetic spectrometer arises from the selection of electrons in a narrow momentum range at a given magnetic field setting. Resolving slits at the spectrometer focus perform the selection. In an ideal magnetic spectrometer of the double-focusing design, the selected momentum slice,  $\Delta p$ , increases linearly with the electron momentum,  $p$ , such that the resolution of the instrument,  $\Delta p/p$ , is a constant. When the magnetic field environment in the spectrometer deviates from the ideal, it is possible that this response deviates slightly from this easily implemented functional form. Thus it can be understood qualitatively how the ambient magnetic field permeating the spectrometer can have an impact on the response function of the instrument. For example, if one were to perform measurements at various current settings and from the current setting infer the magnetic field and momentum setting of the spectrometer, one could easily account for the variation of the spectrometer acceptance using the  $\Delta p/p$  constant relation. However, if one forgets to include the vertical component of the Earth's magnetic field, which may not be negligible compared to the spectrometer field, then it can be seen that the linear  $\Delta p$  relationship will have an offset and will necessitate a small correction in this part of the response function to be utilized in the analysis.

In addition, the use of physical apertures always introduces the possibility of scattering. Electrons of the "wrong" momentum, whose image at the focus should be excluded by the resolving slits, could be scattered through the aperture, contaminating the measurement of the intensity at the "correct" momentum, thus altering the response. With properly designed slits,

this is only a miniscule effect (beyond the Gaussian of the aperture acceptance) compared to the 13–30% backscattered, “wrong” energy component in semiconductor detectors.

In the detection of the selected, transmitted electrons, one performs only a simple counting in order to determine the transmitted electron intensity at any particular momentum setting. The transmitted electrons should be monoenergetic and they should all be recorded. There exists the problem that the electrons may not deposit all of their energy into the detector performing the counting. This is a problem only to the extent that the number of electrons which deposit energy below the noise level of the detector cannot be determined. While this may seem to be a much less serious problem to overcome compared to the extraction of spectral information from backscattering in a semiconductor detector (and in many ways this is less difficult), nevertheless it is still a challenge. The fraction of counts which are below the noise limit is clearly a function of the transmitted electron energy. It is in this way that the detection process can distort the measured intensity as a function of energy — it is this effect that gives rise to the response function and shape factor in magnetic spectrometer experiments.

Armed with the knowledge of the origin of the non-ideal response function in a magnetic spectrometer, the next step in the procedure is to determine this response function for the measuring instrument, as a function of energy, and to utilize it to deconvolute the raw data and extract a  $\beta$  spectrum. The early magnetic spectrometer experiments attempted to measure and/or model their response functions. The extracted data, utilizing the response functions that were determined in their analyses, were fit to theoretical  $\beta$  spectra. These experiments were not able to perform their fits without the use of smooth shape correcting factors (with the exception of [32]).

The criticism of this shape factor correction, voiced by Simpson and Hime, is well summarized by this quote from Hime’s doctoral thesis [27].

*The difficulty with magnetic spectrometers is that, even after all the myriad corrections are invoked to a set of data, one seldom obtains a  $\beta$  spectrum shape which agrees with theoretical expectations. Moreover, there does not seem to be any physical explanation for the origin of the spectral distortions obtained. . . . The point is that, by arbitrarily invoking smooth corrections to the data, information about a heavy neutrino above and below the kink can be completely lost thus leaving only a very narrow region about the threshold for a reliable analysis.*

These issues will be examined below.

The analysis of magnetic spectrometer data generally does not require “myriad corrections.” In fact, it is rather simple. It may be perceived to be an involved process because one must account for both the magnetic dispersion response and the detector response compared to just the detector response in a semiconductor based experiment. Typically, the measured dispersion, using IC lines, can be given by a Gaussian whose momentum width,  $\Delta p$ , increases linearly with momentum,  $p$ . In the early magnetic spectrometer experiments, the detector response below the noise level was extrapolated linearly back to zero energy. What could be easier or more close to ideal than that? With just these simple corrections utilized as the response function of the instrument, magnetic spectrometer experiments are capable of extracting  $\beta$  spectra typically requiring only the inclusion of a smooth shape correction of magnitude  $\sim 10^{-4}$  keV $^{-1}$ . This should be compared to all the “corrections” that must be invoked for a semiconductor detector response (and by

corrections I mean all the various components contributing to the low-energy tail in the response) which amount to 13–30% intensity distributed over say 150 keV (the threshold energy for emission of a 17 keV neutrino in  $^{35}\text{S}$  decay), giving a correction of magnitude  $\sim 10^{-3} \text{ keV}^{-1}$  (and much larger for the case of  $^{63}\text{Ni}$ ).

It is true that it seems somewhat unsatisfying that magnetic spectrometer experiments do not have a complete understanding of their response and require shape corrections. But there are physical effects that are difficult to account for in magnetic spectrometer experiments, that can affect the response function, whose origins are known, contrary to what is stated by Simpson and Hime. These effects include the residual components of the Earth's field (if not fully compensated) and others that have been discussed above. The point to be made is that it is never possible to completely account for all the residual small effects that might impact the response. The inclusion of a smooth polynomial correction is justified to accommodate this incomplete knowledge. Perhaps smooth corrections should have been included in the analyses of those experiments which saw positive evidence for the 17 keV neutrino also, in order to account for any missing components that were not included in their analyses? It is not sufficient for those experiments to just tweak their detector response function enough until they achieve  $\chi^2/\nu \approx 1$  and then claim that everything has been understood. This would be tantamount to the inclusion of shape corrections that have been free to vary *prior* to the fitting procedure. (Actually, this point is somewhat exaggerated here. Suffice it to say that in the measurement of a semiconductor detector response, at just one energy, with one IC line possessing a complex shape due to atomic shake-off and shake-up effects, it is very difficult to accurately extract all the components, and their shapes, that contribute to the low-

energy tail. The energy dependence of the low-energy tail certainly cannot be determined from one line.)

The last issue with the shape factor, discussed by Hime, is really the central one. There is merit to the point that the inclusion of freely-floating shape parameters in the fit can suppress the sensitivity in one's data set to the signature for heavy neutrino emission. But it never eliminates it completely. The kink is a sharp feature and any measurement of sufficiently high resolution and statistics will always be able to identify such a feature, even allowing for a smooth shape correction. But it is possible that some of the spectral deviation far above and below the threshold could be absorbed by the freely-varying shape factors, reducing the statistical strength of one's conclusions. This is a statistical penalty that one must pay — it should be stated unequivocally that the inclusion of free shape parameters serves only to reduce the statistical confidence level derived from any given data set. As such, it is incorrect to use the shape factor issue to automatically dismiss all magnetic spectrometer experiments.

From this discussion of the shape factor issue it is clear how the experimental situation should be approached. If a magnetic spectrometer experiment were to take enormous quantities of data such that the statistical errors could be so restricting that the shape factor really didn't matter, that would be informative and decisive. If a study of the yet unaccounted for effects in the response of a magnetic spectrometer experiment could be done sufficiently well, it would be valuable and satisfying for such an experiment to demonstrate the origin of the shape correction and to do away with it via superior understanding of the instrument. Finally, if a magnetic spectrometer experiment could be performed which would be able to demonstrate sensitivity to the signature of heavy neutrino emission, regardless of the shape factor,

the controversy would be settled. The stage was set for the next round of experiments.

## Chapter 3

# Details of the New Experiment

### 3.1 The Magnetic Spectrometer

The same spectrometer at Caltech that was used in the previous measurements of the  $^{35}\text{S}$  and  $^{63}\text{Ni}$  spectra was employed in this new measurement. It is a 35 cm radius  $\pi\sqrt{2}$  iron-free double-focusing magnetic spectrometer. A design drawing is illustrated in Fig. 3.1 and a photograph of the apparatus is shown in Fig. 3.2. In the drawing, the three sets of coils and their positions can be seen. Such an arrangement, based on the Lee-Whiting and Taylor calculations [44], has also been utilized in the construction of the magnetic spectrometers at Chalk River [33] and at the Tokyo INS [14]. The field shape produced by these coils falls off with radius roughly as

$$B_z = \frac{B_0}{\sqrt{r}}, \quad (3.1)$$

and in the second-order approximation,

$$B_z = B_0 \left[ 1 - \frac{1}{2} \frac{r_0}{r} + \frac{3}{8} \left( \frac{r_0}{r} \right)^2 \right], \quad (3.2)$$

it has been shown that double-focusing, in both the  $z$  and  $r$  direction, is achieved for an extended radial region about the central orbit of the spectrometer [44]. Modeling of electron orbits in a second-order double-focusing spectrometer was performed with *Mathematica* [45], and the double-focusing

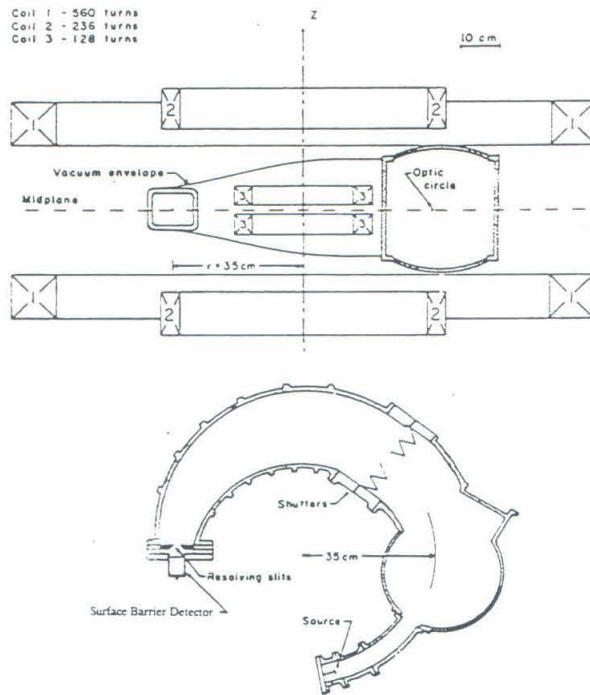


Figure 3.1: Sketch of the Caltech iron-free double-focusing  $\beta$  spectrometer.

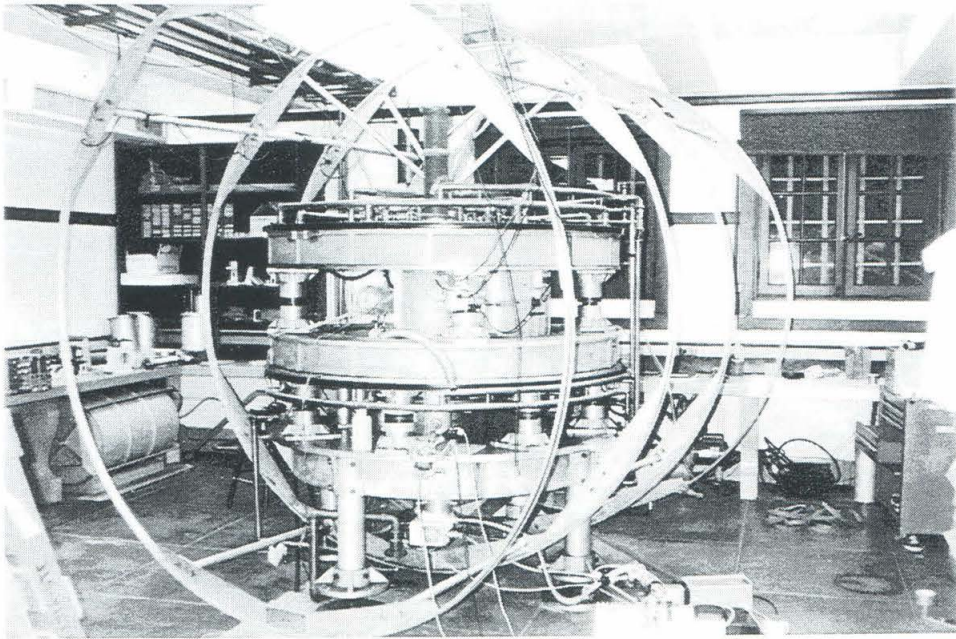


Figure 3.2: Photograph of the  $\beta$  spectrometer.

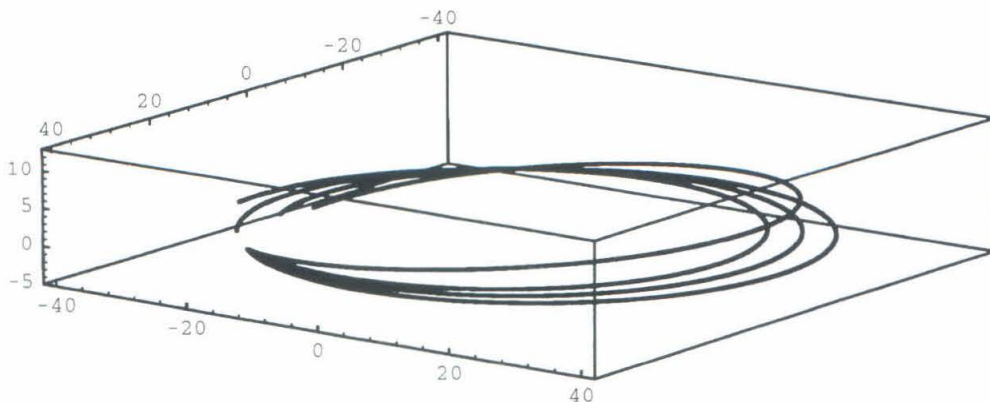


Figure 3.3: Visualization of double-focusing showing electron trajectories being focused at an azimuth  $\pi\sqrt{2}$  radians from their origin.

properties of this magnetic field configuration are illustrated in Fig. 3.3, with radial-focusing of electron orbits about the optic circle displayed as well as focusing of orbital trajectories which project out of that plane.

The source position and the location of the surface barrier detector within the spectrometer are fixed. The shutters and the resolving slits, shown in Fig. 3.1, can be adjusted to optimize the momentum resolution and transmission of the spectrometer, as well as to eliminate scattering. There are five adjustments that can be made: the horizontal and vertical opening of the shutter, the radial position of the resolving slits, and the horizontal and vertical opening of the slits. These settings were determined in the previous  $^{35}\text{S}$  experiment of Becker and Imel [39] and were not changed for this new measurement. A description of the tuning and optimization of these adjustments can be found in the doctoral thesis of Imel [40]. It is worthy to note here that in setting the openings for the resolving slits, there exists the constraint that the acceptance slit be narrower than the active area of the surface barrier detector, thus ensuring that the focused electrons, in passing

through the resolving slits, would strike the detector suitably away from the edges.

Helmholtz coils surrounding the spectrometer can be seen in the photograph. These can be used to cancel the horizontal component of the earth's magnetic field. The decision was made, however, not to employ them in this experiment as any fluctuations in the compensating field would introduce additional and unnecessary uncertainty in the measurement. The earlier studies of Becker and Imel found that the use of the compensating coils did not improve the spectrometer resolution. Studies in this new series of measurements were made with and without the compensating field. It was found that cancelling the horizontal component of the earth's field did affect the fitted shape factor that the spectrometer would measure; however, the compensation was not able to obviate the need of the shape correction. Thus, if a shape term would still be needed to fit the data, it was felt that running without the compensating field would be preferable, from the standpoint of minimizing experimental uncertainty.

## 3.2 Sources

Two  $^{35}\text{S}$  sources and one  $^{57}\text{Co}$  calibration source were prepared for this experiment. The preparation technique, up to the introduction of the activity, was identical for all three.

Aluminum rings were used to hold the source foils. Once prepared, a source ring can be mounted on the source positioning assembly of the spectrometer, with reasonable accuracy. A design drawing of the source holder assembly is presented in Fig. 3.4 and the dimensions of the aluminum rings are given in Fig. 3.5. In the preparation of the source foils, onto one side of

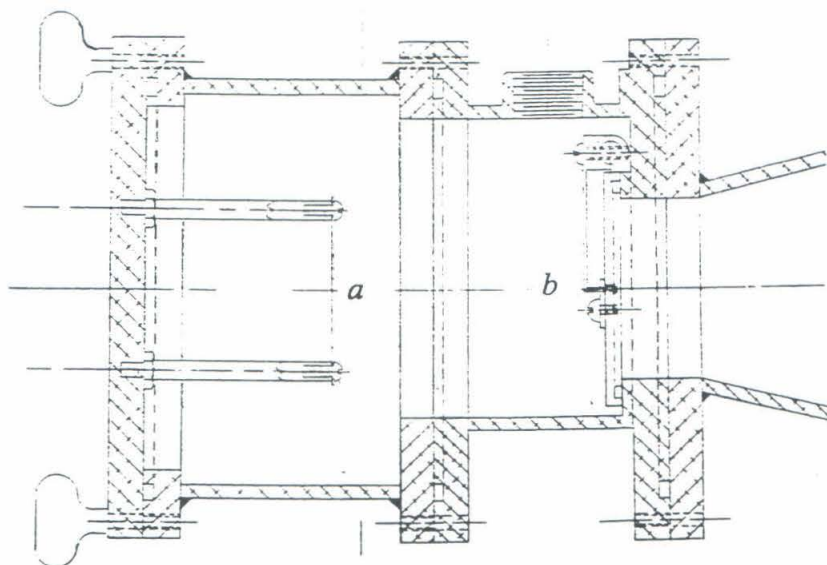


Figure 3.4: Design drawing of the source positioning assembly used in the spectrometer. The source foil is placed at A and vacuum shutters are at B.

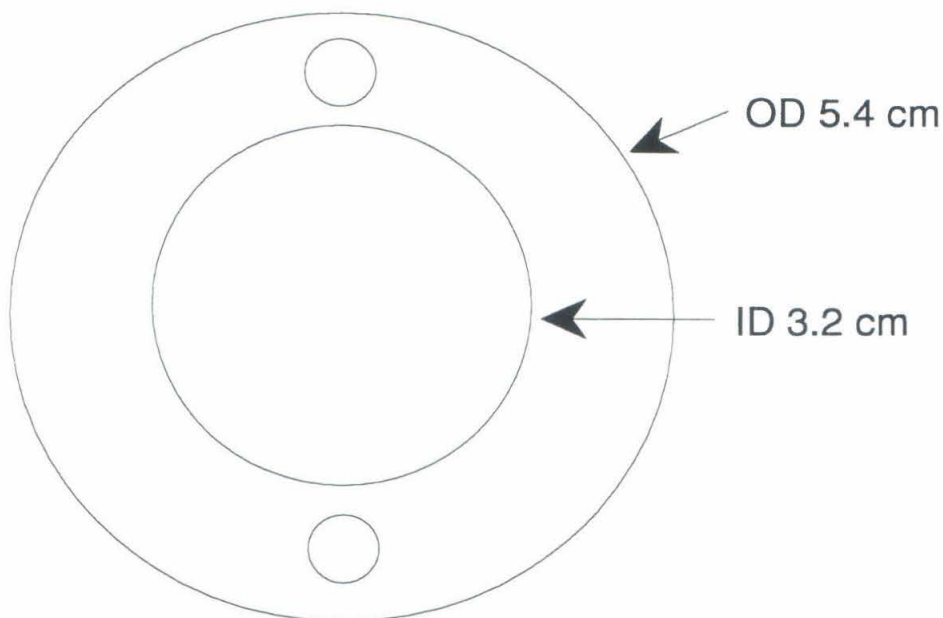


Figure 3.5: Aluminum rings for mounting the source foils.

the rings, 0.9  $\mu\text{m}$  thick Mylar foil was stretched across the circular opening and glued to the aluminum. This foil/ring surface was then coated with a very small amount of gold. The source backing material must be metalized to prevent the accumulation of charge on the source foil, which could potentially alter the energy spectrum of the emitted electrons. The gold metalization was accomplished by vacuum evaporation.

For the  $^{57}\text{Co}$  calibration source, vacuum evaporation of  $^{57}\text{CoCl}_2$  was used to deposit 100  $\mu\text{Ci}$  activity on the foil. A mask was aligned and mounted in front of the source foil during the vacuum deposition to expose a slot area of dimensions 2 mm  $\times$  20 mm, containing the activity. When mounted in the spectrometer, the long dimension of the source area lies along the vertical z-axis of the spectrometer.

For the  $^{35}\text{S}$  sources, a hybrid technique of vacuum deposition and chem-

ical adsorption [36] was employed. The chemical adsorption technique to prepare ultra-thin sources was also employed by Hime in his Oxford experiment [41]. In our technique, we first deposited barium onto the gold-coated Mylar foil through a mask of the same dimensions as the calibration source, 2 mm  $\times$  20 mm. Instead of  $\text{CoCl}_2$ , we placed  $\text{BaCl}_2$  in the molybdenum boat for evaporation. After depositing a controllable amount of barium on the foil, we brought an aqueous solution of  $(\text{NH}_4)_2^{35}\text{SO}_4$  into contact with the barium-coated region. A crude but effective apparatus was constructed to hold the drop of ammonium sulfate solution and is shown in Fig. 3.6. This glass cover slip assembly could be aligned over the barium-coated area of the source foil and lowered slowly onto it. The drop, injected in the space between the cover slips, stayed between the glass, clinging by surface tension, until lowered onto the foil. When the drop made contact with the foil, it wetted the exposed foil surface uniformly, without spilling out of or under the liquid deposition contraption. The source foil and drop were covered with an inverted beaker and left to sit for about an hour after being brought together.

In the chemical adsorption technique, insoluble compounds are found to precipitate out of solution and adsorb onto the gold-plated Mylar foils. In our source preparation, we placed sulfate solution above the barium-coated region of the foils;  $\text{BaSO}_4$  precipitated and presumably adsorbed onto the surface of the foil. This hybrid technique allowed us to deposit controlled amounts of barium sulfate activity with the important advantage (over the drop technique used by Hime) that we were able to define the geometry of the deposition. This is vitally important for preparing sources for a magnetic spectrometer while it was not a concern for Hime's experiment.

After sitting for about an hour, the solution between the glass cover slips

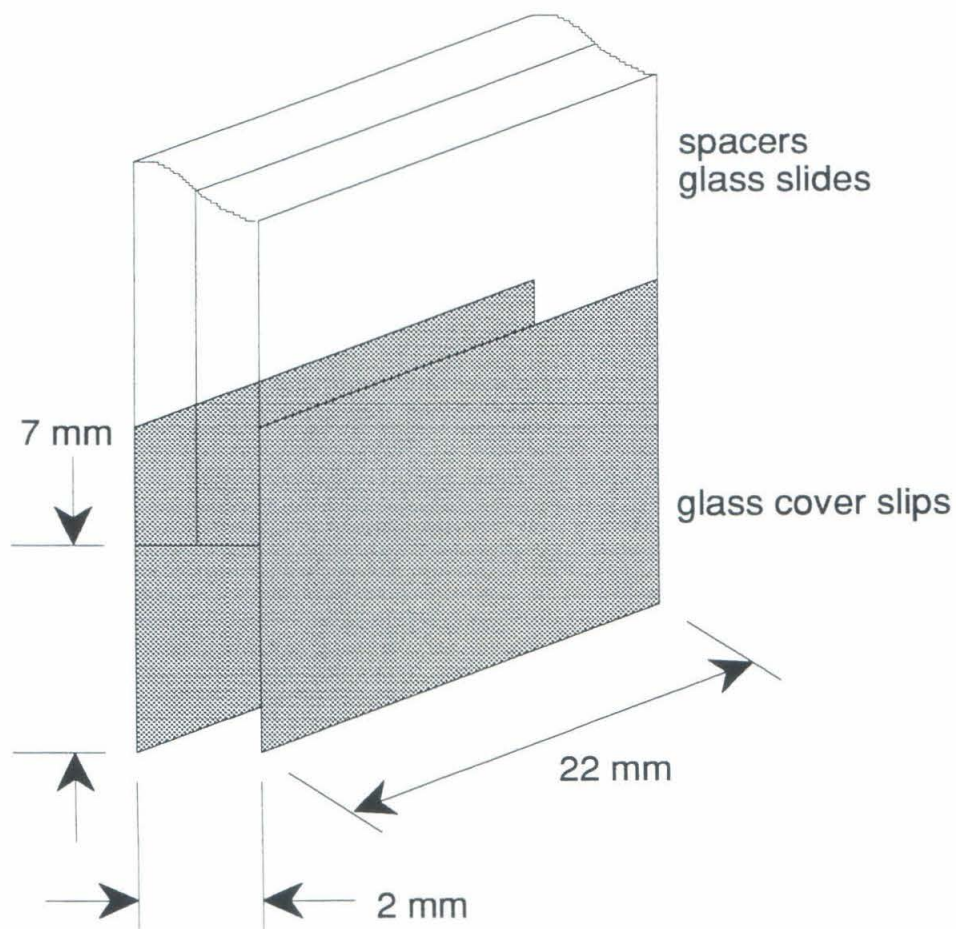


Figure 3.6: Crude sulfate solution deposition apparatus.

was drawn out with a micro-pipette. We would extract roughly half of the solution and would replace it with ultra-pure water. This was repeated a number of times to accomplish a gradual “washing” of the foils. Finally, the water and solution were drawn out completely, and the glass cover slips were lifted and removed. Typically a few small drops of solution remained on the foil and these were extracted with ultra-pure water in a micro-pipette. From tests, we found that the washing procedure did remove some of the activity from the surface as the ultra-pure water probably carried some of the barium sulfate off of the surface of the gold-coated foil. However, we felt better about using the washing procedure, believing it would be safer to do so just to eliminate the possibility of any residual ammonium sulfate crystals remaining on the foil. Ultimately, we estimate that our yield for this process was about 40%, enabling us to efficiently and effectively produce thin sources of high activity. We used this hybrid technique to produce a 3 mCi and a 7 mCi source and both were used in this new series of measurements.

### 3.3 Detector and Data Acquisition

A silicon surface barrier detector, Ortec BE-013, was mounted at the spectrometer focus. It has an active area of  $25 \text{ mm} \times 3 \text{ mm}$  and has a sensitive thickness  $> 300 \mu\text{m}$ . Gold forms the thin metal layer ( $40 \mu\text{g}/\text{cm}^2$ ) deposited over the silicon. Just in front of the detector, the openings of the resolving slits were set at  $23 \text{ mm} \times 2.5 \text{ mm}$ , smaller than the active area of the detector. The detector was Peltier cooled to approximately  $5 \text{ }^\circ\text{C}$ , to reduce electronic noise. There was no problem with material condensing onto the detector surface at these temperatures. The detector was operated at a bias of  $+110 \text{ V}$ .

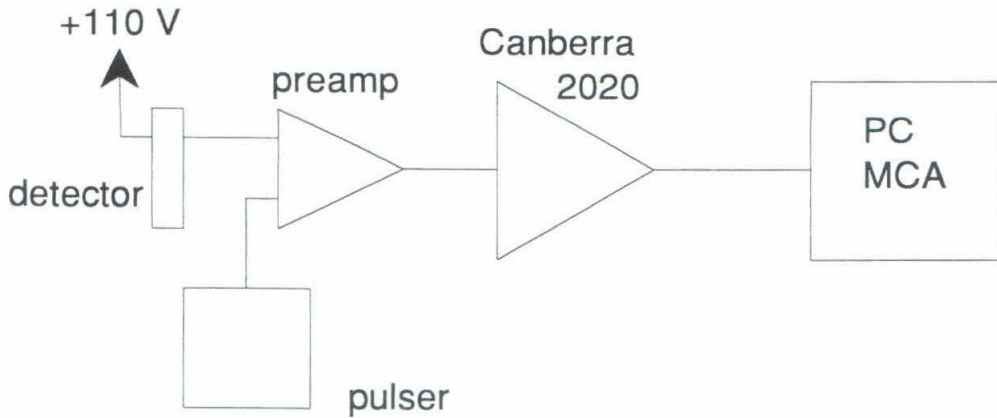


Figure 3.7: Diagram of the spectroscopy portion of the data acquisition system.

The signal from the detector was fed through an Ortec 142A preamplifier into a Canberra 2020 spectroscopy amplifier. The shaping time constant of the amplifier was set at  $1 \mu\text{s}$ . A precision pulser, BNC BH-1, was also fed through the same preamplifier. It operated at 11.1 Hz and was used to monitor the stability of the electronics and to gauge the dead time of the data acquisition system. The output from the spectroscopy amplifier went directly to an Ortec 916A, a PC mounted multichannel analyzer card. A diagram of the data acquisition system is shown in Fig. 3.7.

With this system, one is able to record, via computer control, a spectrum from the surface barrier detector at any magnetic field setting. A sample spectrum is shown in Fig. 3.8. This spectrum was taken using the  $^{35}\text{S}$   $\beta$  source, with the spectrometer set to transmit electrons of momentum  $420 \text{ keV}/c$ , corresponding to an energy of 150.5 keV. A full-energy peak and backscattered tail are visible. The energy resolution of the surface barrier detector for energies around 150 keV is 4.0% at FWHM, as seen from the full-energy peak of the sample spectrum. The backscattered tail contains

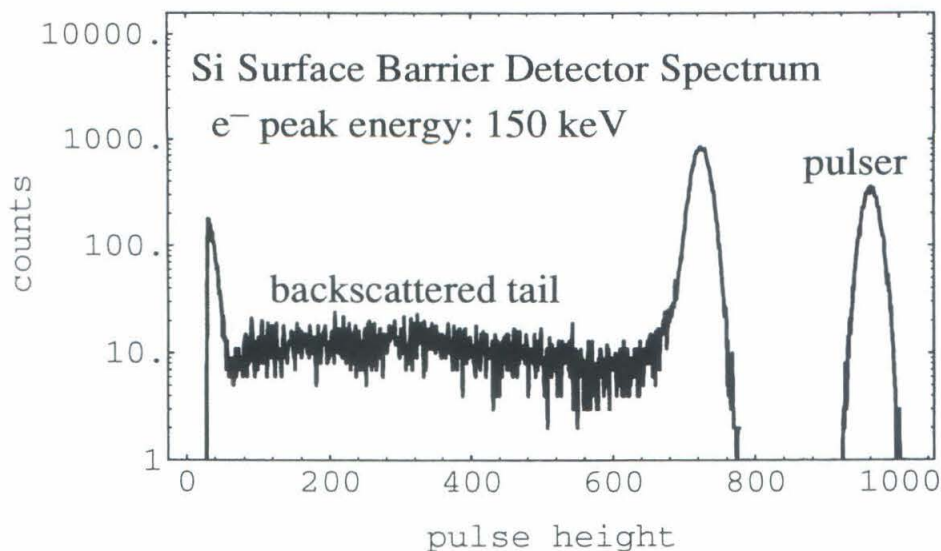


Figure 3.8: Sample detector spectrum with the spectrometer field set to transmit 150 keV electrons.

17% of the total spectral intensity. For this sample spectrum, in which data were accumulated for 15 minutes, the counting rate of the data acquisition system (including the pulser) was 50 Hz.

### 3.4 Current Supply and Magnetic Field Instrumentation

In lieu of calibrating the spectrometer with measurements of the current supplied to the field coils, we chose to calibrate the spectrometer based on direct measurements of the magnetic field in the spectrometer. In this way, the experiment would not be affected by uniform, global shifts in the ambient magnetic field caused, for example, by the natural variations of the Earth's field.

A Kepco ATE 55-5M power supply was hooked up directly to the spec-

trometer coils, without any intervening resistors or dividers. It supplied current to the magnetic field coils and was itself plugged into a three-phase voltage regulator, which maintained stable power conditions from the mains.

The output current of the Kepco supply is adjustable by applying a 0–1 V control signal to an external programming connector. This feature was employed in this experiment to automate the stepping of the current supply in the process of sweeping out a momentum spectrum. This control input could have been used as a feedback system; however, it was felt that a more stable magnetic field could be established without feedback (wherein the magnetic field fluctuations, if they occurred, would just be recorded for later evaluation). Plugged into the data acquisition 386 computer was an Analogic DAS board, a multiple purpose data acquisition card providing DAC and ADC functions. The DAC output, issued from the computer, was connected as the control signal to the Kepco current supply. The DAC had only 12-bit precision; nevertheless, this proved sufficient. An external, DC voltage reference standard was supplied as input to the DAC dividing circuitry. A sketch of the power supply implementation in the experiment is presented in Fig. 3.9.

To measure the magnetic field in the spectrometer, a Bartington Instruments MAG-01, single-axis fluxgate magnetometer was used, equipped with a MAG-D model, high field probe. These probes can be placed in fields as high as 2 mT and still achieve 10 nT resolution. The magnetic field measured by the magnetometer was read out from an analog voltage output by a Fluke 8505A digital multimeter (5 ppm accuracy). A GPIB (IEEE-488) interface connecting the Fluke with the data acquisition computer provided for computer-controlled sampling of the magnetic field.

The magnetometer probe must be accurately positioned so as to sample

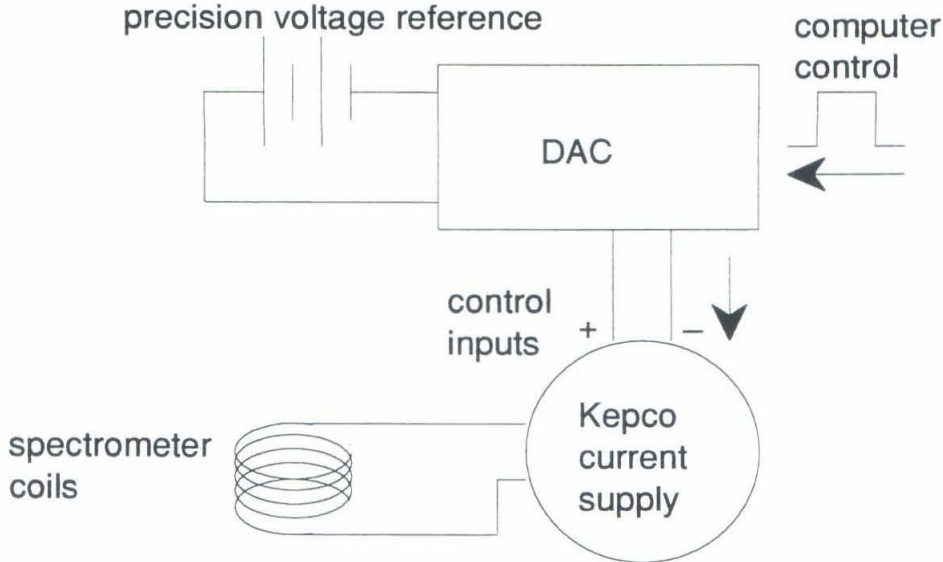


Figure 3.9: Power supply and control for the spectrometer coils.

the field at one location in the double-focusing spectrometer, and its orientation must be precisely fixed. This was accomplished by mounting the probe in a semi-cylindrical aluminum block, of diameter 4.5 inches, into which a vertical hole was bored. The probe fit snugly into this hole and was potted into place. This block was clamped to one of the structural posts of the spectrometer which support the upper windings of the largest coil (coil 1 in Fig. 3.1). The block was machined to fit squarely onto the post, providing an accurate vertical orientation for the fluxgate probe. The location of the probe was at a radius of 79 cm and at an azimuth of roughly half the angle between the source and the anti-scattering baffles. The  $z$ -position of the probe was aligned such that the sensing element of the fluxgate probe was positioned right in the orbital symmetry plane (at  $z = 0$ ).

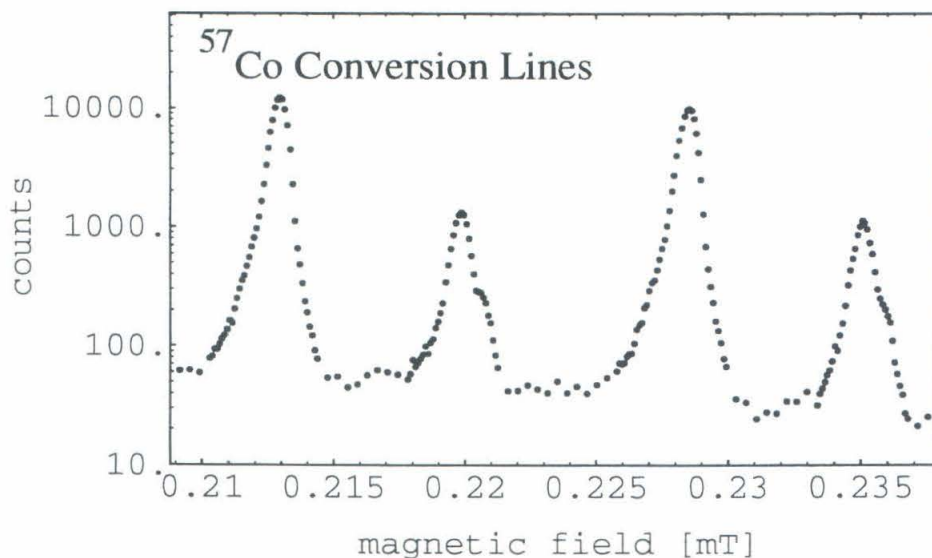


Figure 3.10:  $^{57}\text{Co}$  calibration spectrum.

With this system, a momentum spectrum could be swept and accumulated, all under computer control. One could program the computer with a sequence of values to output, through the DAC, to the Kepco current supply. Once the current supply ramped up to the desired value given by this control voltage, the computer would be instructed to record a pulse-height distribution from the silicon surface barrier detector. This provided a measure of the counting rate at the detector with the spectrometer magnetic field set to transmit electrons of the desired momentum. While the spectrum was accumulating, the computer could be programmed to sample the magnetic field being measured by the high field fluxgate probe. A counting rate would then be known at each magnetic field setting and this could be translated into a momentum spectrum,  $dN/dp$ .

The  $^{57}\text{Co}$  source was used to calibrate the spectrometer. Internal conver-

sion electron lines (K-conversion) are available with energies of 114.95 keV and 129.36 keV. L-conversion lines can also be used (energies 121.21 keV and 135.63 keV). Fig. 3.10 is a calibration spectrum, without background subtraction, showing the  $^{57}\text{Co}$  K and L IC lines, recorded as the count rate versus the measured magnetic field.

### 3.5 Environmental Monitoring

Throughout the course of the experiment, various environmental conditions could be monitored. Most of this data served only as a check to identify any extreme condition which might have appeared unexpectedly and to correlate this with any effect in the data. Fortunately, no such thing was observed, with the notable exception of environmental magnetic field fluctuations, to be discussed later.

The vacuum in the spectrometer chamber was kept at  $3\text{--}4 \times 10^{-6}$  torr. A turbo-molecular pump backed by a rotary vane vacuum pump were employed. When exchanging between  $\beta$  and calibration sources, the butterfly valves in the source positioning assembly (seen in Fig. 3.4) could be closed, allowing the high vacuum in the main spectrometer envelope to be maintained. The rotary pump could subsequently be used to evacuate the small source chamber right after such a foil exchange, and prior to the re-opening of the shutters. The vacuum pressure was measured with a Varian ionization gauge.

Mounted in the same aluminum block as the high field magnetometer probe was a platinum resistance thermometer. Its resistance could be used as an accurate indicator of the temperature of the magnetometer probe. The placement in the aluminum block provided for greater thermal inertia. The resistance of the Pt RTD was measured with a Keithley digital multimeter

and a GPIB interface provided the means of communicating the resistance to the data acquisition computer. The temperature dependence of the magnetometer probe is specified by the manufacturer as 30 ppm/°C.

Two thermistors were used to monitor the air temperature in the room. They were driven by a simple circuit providing a constant current supply and the voltage drops across the thermistors were recorded through the analog-to-digital converters on the Analogic DAS card, plugged into the 386 computer. Due to the high sensitivity of these devices, the wildly fluctuating measurements provided by the thermistors were not valuable at all. The average air temperature in the room was observed to vary less than 1 °C, between day and night; this should not be significant enough to have any effect on anything.

A second fluxgate magnetometer was employed to monitor the ambient magnetic field. Unlike the high field probe, this Walker Scientific magnetometer was placed horizontally, instead of vertically, and was positioned outside of the spectrometer coils. Its purpose was to identify external magnetic field fluctuations — it was thought that placement orthogonal to the main probe would allow greater directional coverage of any possible stray field. The horizontal probe was not located all that far from the spectrometer (it was roughly 4 m away from the large spectrometer coils), consequently it also sampled some of the return field generated by the spectrometer itself. Accompanied by measurements with the vertical high field probe, the horizontal magnetometer did observe irregular magnetic field fluctuations, during the experimental runs. Details regarding these fluctuations and the rejection of data on account of observed field disturbances will follow.

## Chapter 4

# Data and Analysis

### 4.1 Calibration

There are four internal conversion electron lines available from  $^{57}\text{Co}$  (see Fig. 3.10). The two K-conversion lines were fit to Gaussian distributions,

$$f(x) = Ae^{-(x-\mu)^2/2\sigma^2}, \quad (4.1)$$

and are shown in Fig. 4.1. Table 4.1 below lists the fitted parameters for each of the four IC lines. The M-conversion lines are visible as shoulders on the L-conversion peaks and were not cleanly separated; the L peaks themselves are actually composed of three lines, ( $L_I$ ,  $L_{II}$ ,  $L_{III}$ ) with orbital binding energies of 0.848 keV, 0.7207 keV and 0.7076 keV respectively [46]. Thus, the fitted widths,  $\sigma$ , for the L peaks appear somewhat broader.

In fitting the IC line data, the points on the upper half of the peaks and points extending part of the way down the lower half were used. A low-energy

Energy [keV]	Momentum [keV/c]	A	$\mu$ [mT]	$\sigma$ [mT]
114.95	361.513	12303	0.21296	$2.5685 \times 10^{-4}$
121.21	372.253	1282	0.21984	$3.2972 \times 10^{-4}$
129.36	385.932	9943	0.22851	$2.7263 \times 10^{-4}$
135.63	396.238	1071	0.23510	$3.1480 \times 10^{-4}$

Table 4.1: Gaussian fitted parameters for the  $^{57}\text{Co}$  calibration lines.

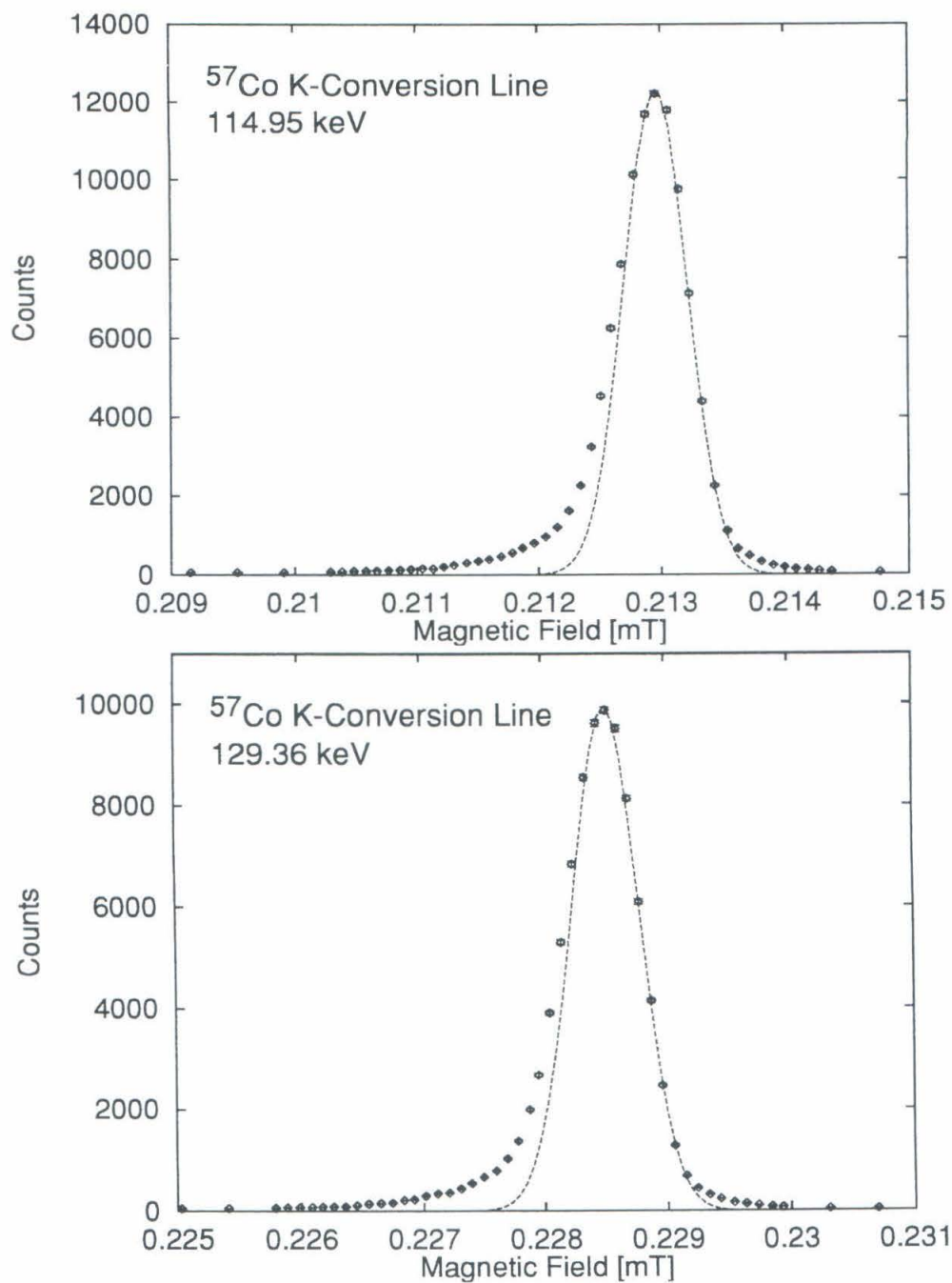


Figure 4.1: Fitted Gaussian peaks to the  $^{57}\text{Co}$  K-conversion lines.

exponential tail is visible in the data, on top of the Gaussian response. This tail was observed in the Becker and Imel work [39] and a low-energy tail was also reported in the Chalk River measurement [33]. Certainly a large part of the low-energy tail is attributable to shake-up and shake-off effects on the internal conversion, following the electron capture decay of  $^{57}\text{Co}$ ; however, the exact contribution of the tail from shake-up/off is not precisely known. Consequently, for this work, as was done in the Hetherington analysis, a symmetric Gaussian distribution was used as the response function of the spectrometer for analysis of  $\beta$  electrons. Notes from the analysis of Becker and Imel, which included an exponential tail in the spectrometer response, indicate that the inclusion or omission of this tail has a negligible effect on the shape factor of the fitted  $\beta$  spectrum and has no impact on the suppression or enhancement of a heavy neutrino spectral kink. Indeed, this is to be expected as the momentum bin size, in the data analysis, was wider than the peak resolution of the spectrometer — thus, the exact shape of the peak is not critically important.

From the fitted widths of the K-conversion lines, we find the momentum resolution of the spectrometer: 0.28% FWHM. The four fitted peak centroids were used to calibrate the measured magnetic field in terms of momentum. Fig. 4.2 plots these four calibration points with a linear fit. The calibration function is:

$$p = 1569.66 B + 27.218, \quad (4.2)$$

where  $p$  is the momentum in units  $\text{keV}/c$  and  $B$  is the magnetic field in  $\text{mT}$ . The uncertainty in the slope is  $\pm 0.52$  and  $\pm 0.126$  in the intercept.

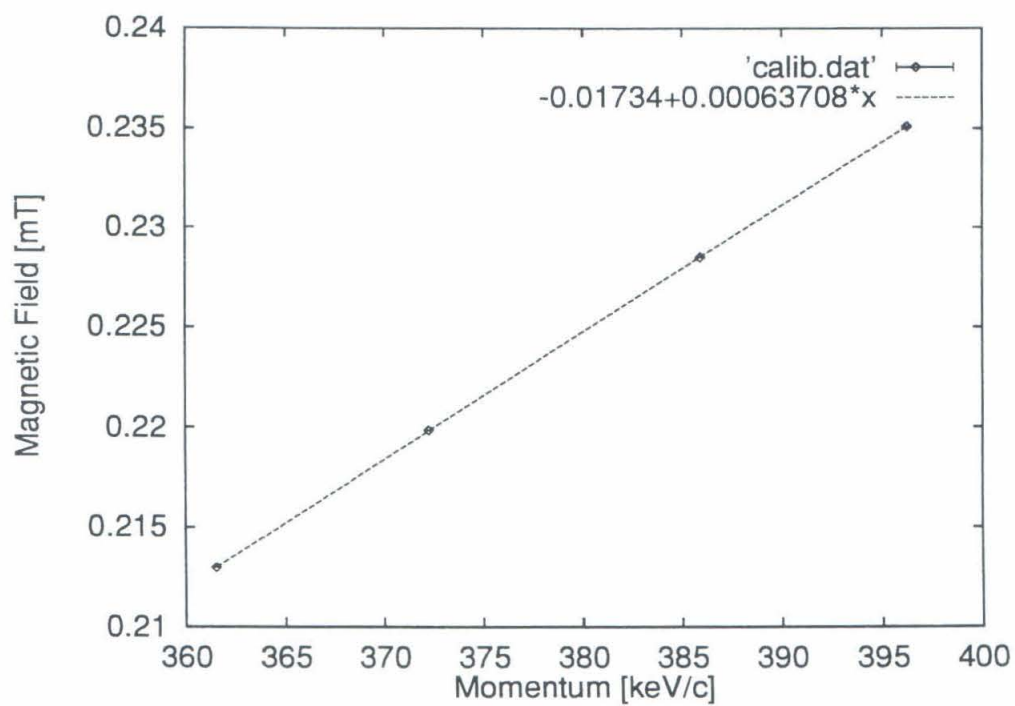


Figure 4.2: Momentum calibration of the spectrometer. The calibration is linear and the error bars on the measured peak centroids are  $\pm 0.00001$ .

## 4.2 Analysis of the Silicon Detector Spectra

At each momentum setting of the spectrometer, one must determine, from the measured pulse-height distribution from the silicon surface barrier detector, the total count rate or intensity of the transmitted electrons. All counts, including those in the backscattered tail (in which the electrons deposited less than their full energy) should be included. One must determine how many counts were inaccessible because their recorded pulse heights fell below the noise level of the detector.

It is possible to model the detector response down to zero energy using a Monte Carlo, and to utilize the model to determine how many counts in a measured spectrum lie below the noise. It is also possible to employ a parameterization, based upon actual measurements of the response of a surface barrier detector, to determine the count rate below the noise. A study [38] by Damkjaer of the response of a silicon surface barrier detector to monoenergetic electrons of various energies included a parameterization of the detector response. This was initially employed in the analysis of our  $^{35}\text{S}$  data to extract the counts below the noise.

Damkjaer parameterizes the shape of the low-energy tail as [38]:

$$T(\epsilon) = A \frac{\sin[p(1-\epsilon)\pi]}{1 + Ce^{-\epsilon^2/\alpha}} + B \frac{\epsilon}{1 - \epsilon + e^{(\epsilon-1)/\beta}}, \quad (4.3)$$

in which  $\epsilon = E/E_0$  is the ratio of the deposited energy,  $E$ , over the incident electron energy,  $E_0$ .  $A$ ,  $p$ ,  $C$ ,  $\alpha$ ,  $B$ ,  $\beta$  are all parameters which were fit to measurements of the low-energy tail response, for incident electron energies of 100, 200,  $\dots$ , 600 keV. Damkjaer found the parameter  $\alpha$  to be constant with energy, whereas  $p$ ,  $B$ , and  $\beta$  were linear functions of the incident elec-

tron energy,  $E_0$ , and parameters A and C were found to be slowly varying quadratics. The first term in the sum arises from backscattering and the second term represents energy loss by bremsstrahlung.

Before delving too deeply into the details of this parameterization, which ultimately was not used in our analysis, we should consider the consequences of employing such a parameterization in the uncertainty of our detector response. How well could we be assured that Damkjaer's parameterization is completely applicable to our detector properties, focus and geometry? How certain could we be that this parameterization agreed with our data (our measured backscattered tail)? Could we even be certain that this parameterization was correct, down to zero energy? After all, Damkjaer had to deal with this very same problem. How were the counts and shape of the backscattered tail below Damkjaer's *own* detector noise determined?

Instead of relying on any modeling or parameterization and being forced to accept an unknown uncertainty, it was felt that a simpler approach would be more justified. In order to avoid the problem of counts below the noise, we chose to sum the contents in the surface barrier detector spectrum from the full-energy peak all the way down to a fixed fraction, 20%, of the incident electron energy. Thus, for an electron of energy 125–170 keV, this corresponded to a lower summation threshold of 25–34 keV, which was above the noise level in our detector. We can estimate the fraction of counts excluded by this method (counts in which the electron deposited less than 20% of its incident energy) from our own data (see sample detector spectrum in Fig. 3.8). Taking the counting rate just above the detector noise and performing a simple extrapolation to down to zero, we estimate that about 2% of the spectral intensity lies in this excluded region (compare this to 17% total backscattered intensity). The energy dependence of this fraction of excluded counts was

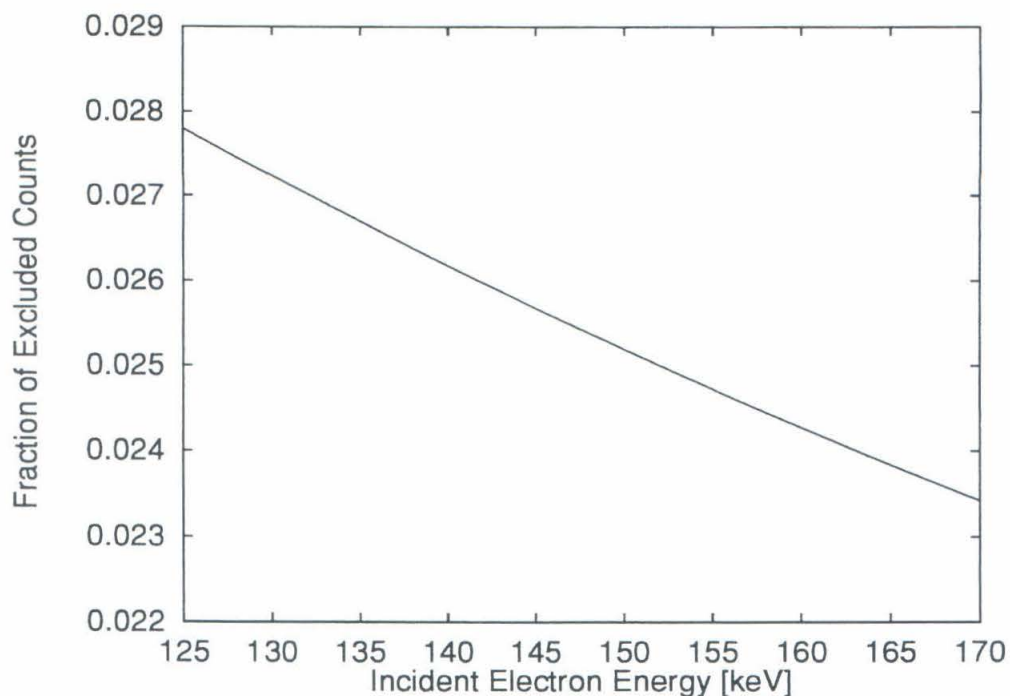


Figure 4.3: Energy dependence of the fraction of excluded counts below 20% of the peak energy. These calculations were based on the detector response parameterization of Damkjaer.

estimated, using the Damkjaer parameterization, to vary less than 0.4%, for incident electron energies across our range of interest (from 125–170 keV); this is shown in Fig. 4.3.

In measuring the  $\beta$  spectrum of  $^{35}\text{S}$ , a data “run” consisted of a sweep of the magnetic field of the spectrometer from low momentum to above the endpoint of the decay. Silicon detector spectra were recorded at each magnetic field setting and typically within a run, 50–100 spectra would be measured. We used the information from the full-energy peaks in these spectra to calibrate the silicon detector energies. This energy calibration was performed for each and every run.

The energy calibration procedure was executed as follows. For each de-

tector spectrum, the transmitted electron momentum would be known from the measured magnetic field setting of the spectrometer. Thus, the incident electron energy would be known. In each detector energy spectrum, the analysis code would attempt to fit a Gaussian to the full-energy peak, using the pulse-height data in a window approximately 60 channels wide, centered on the peak (peak position at channel:  $\approx 700$ , peak FWHM:  $\approx 30$ ). For spectra taken very close to the  $\beta$  endpoint, a peak usually could not be found, due to the insufficient counting rate. A fitted, full-energy peak was identified as being valid, for calibration purposes, if the fit routine converged, had a fitted width less than 50 channels (near the endpoint, the pulse-height spectra sometimes would exhibit a scattering of counts close to where the peak would typically be and this sparse grouping of counts would usually result in the fitting routine converging on a large width), and had a  $\chi^2/\nu < 1.5$ . A set of valid peak centroids, collected in each run, would be fit to a straight line using the known incident electron energy, to calibrate the detector channel number into energy. Thus, in each run, a fresh detector energy calibration could be extracted. The slope and offset of the energy calibration, as well as the  $\chi^2$  of the linear fit could be compared from run-to-run to monitor the stability of the electronics; data from the pulser peak was similarly used as a stability check.

It should be noted that with this run-to-run energy calibration and with our fixed fraction counting method (which embodies 98% of the total spectral intensity), our measurement of the count rate becomes rather insensitive to details of the detector energy calibration and response. This is as it should be, to take full advantage of the dispersion/detection dichotomy of a magnetic spectrometer.

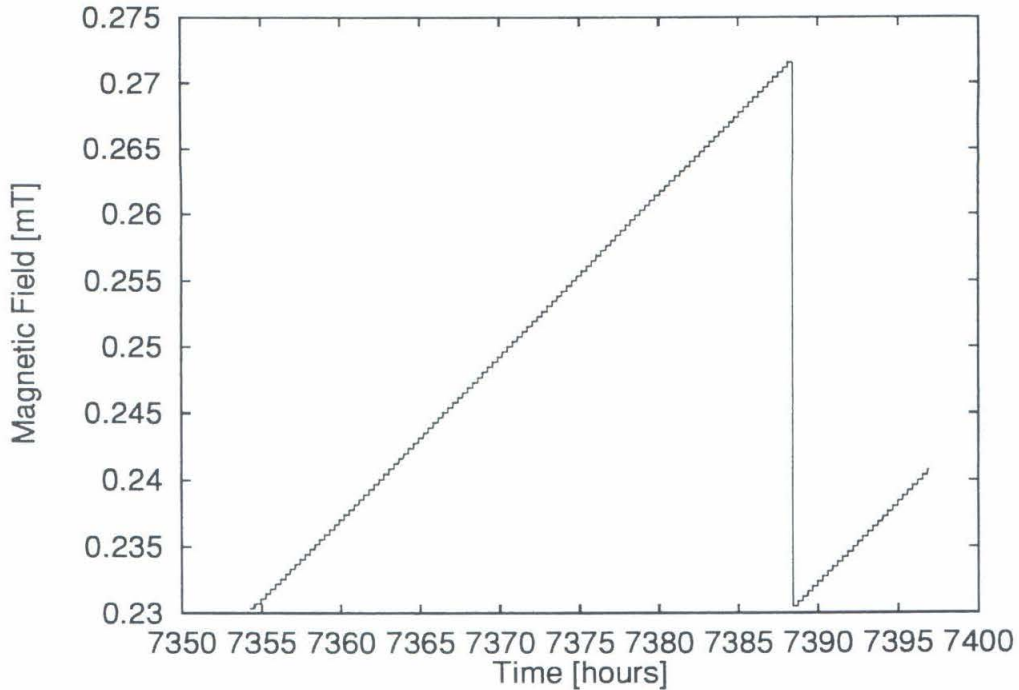


Figure 4.4: Magnetic field measurements swept during a wide scan data run.

### 4.3 Magnetic Field Stability

The quality of the magnetic field surrounding the spectrometer could be describe as inconsistent. During quiet periods, in which no fluctuations were observed, the stability of the field would be excellent. When fluctuations would appear, they would typically be random and unpredictable, with deviations large enough to either distort the measured count rate or simply to just displace the measurement of the magnetic field in an unrepresentative manner.

In the sweeping of a  $\beta$  spectrum, the magnetic spectrometer would be ramped from low field to high field, sampling many momentum points. A depiction of the magnetic field measurements made during the course of a

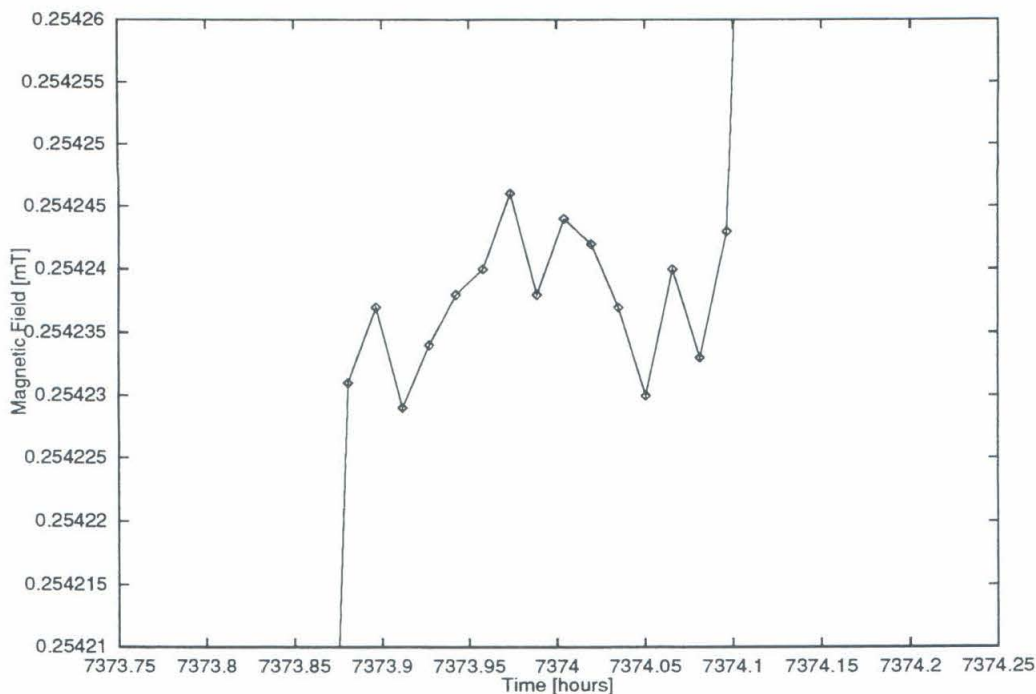


Figure 4.5: Magnetic field stability during a 15 minute spectrum measurement.

run is contained in Fig. 4.4. In this figure, which plots 2062 individual magnetic field measurements, the many little steps on the overall sawtooth ramp illustrate the general magnetic field sweeping strategy. Each measurement of a detector spectrum would correspond to a flat field period of each step. The vertical step “risers” correspond to the moments when the computer-controlled power supply stepped up to a new magnetic field setting, beginning the measurement of the next momentum point.

A closer look at a few, select field measurements is necessary to reveal the underlying field stability of the spectrometer, over the course of accumulation of a detector spectrum. Fig. 4.5 displays a highly expanded view of the previous plot, showing 15 field measurements that were taken while a silicon detector spectrum was being collected at this momentum setting. The first

field measurement occurred three minutes after the computer had instructed the current supply to step to this new field setting, in order to allow the spectrometer time to stabilize at the new field. One can see that the first 14 samples, taken at intervals approximately one minute apart, were completed before the spectrum had finished accumulating. The last point was measured after the data taking had finished, before the current supply was ramped to the next setting. During this measurement period, the average value of the magnetic field was 0.254237 mT and the RMS fluctuation was  $\pm 0.000005$  mT (i.e. 5 nT). The RMS error, used as an indicator of the field stability during a 15 minute counting period, was 20 ppm for this particular sample. The peak-to-peak field excursion was about 15 nT.

The previous discussion of a specific set of magnetic field data was to serve as an example, in order to explain the general features and concepts of our magnetic field measurements, which we used to determine the momentum setting of the spectrometer (using the average value of the 15 field samples to compute the momentum). When the ambient field was quiet, as it was in the period highlighted above, the current supply and control would be able to maintain excellent field stability. Typically, our observations showed that the field would be stable to better than 30 ppm over a 15 minute period, as measured by the RMS fluctuations within a set of 15 measurements. This level of fluctuation corresponds to a count rate stability of better than  $\pm 0.1\%$ , considering the steep slope of the  $^{35}\text{S}$   $\beta$  spectrum near the endpoint.

A cut was used to reject momentum points that were measured during periods of field instability and to flag the occurrence of large ambient field disturbances. If the measured RMS deviation of the magnetic field, during any 15 minute counting period, was greater than 15 nT (roughly 60 ppm fluctuation), the analysis code would automatically throw out that individual

point of the momentum spectrum. The selection of 60 ppm for this cut was based on the desire to maintain count rate stability at the few tenths of a percent level. When the field was stable, the measured RMS fluctuations would be less than 7–8 nT. When fluctuations were observed, small shifts were typically around 50 nT in magnitude and large disturbances would be easily identified with field variations of some 200 nT. Rarely would a set of field measurements report RMS deviations between 10–20 nT — that is to say that when the field was disrupted during a measurement, the effect would be clearly distinguishable. Recall that the measured magnetic field at the fluxgate probe was around 0.25 mT, for settings near the  $^{35}\text{S}$  endpoint, and the vertical component of the Earth's magnetic field is 0.0205 mT, at these latitudes. The magnetic field step corresponding to a 1 keV/c momentum increment in the spectrometer was 637 nT.

The nature of the field disturbances should be considered. If a global, short-timescale shift in the field were to occur, say due to some variation of the Earth's field, then the counting period during which this shift took place should not give an accurate measure of the rate. Thus, the validity of throwing out singular momentum points is justified, to accommodate such field fluctuations. Any long-timescale magnetic disruption that was uniform over the entire spectrometer should not have any effect, nor should the count rate be affected for momentum points measured after a short fluctuation had passed, because our spectrometer was calibrated on the measured magnetic field. Thus, if the ambient field were shifted between one counting period to another, the fluxgate probe should be measuring this shift and the spectrometer should be transmitting electrons with the properly shifted momentum.

On the other hand, if the field disturbance were local in nature, there is the possibility that the degree of magnetic field shift, as measured by

the fluxgate probe, would not be representative of the overall magnetic field disturbance felt by the electron trajectories. The disturbance of the count rate could then be out of relation with the measured fluctuation at the probe. In this case, the cutting of just a single momentum point (the one in which the field disturbance was manifest) would not be sufficient. The field conditions would likely be different before and after such a short, local fluctuation. The flagging of a momentum point possessing an RMS field deviation greater than 15 nT would then serve to identify when such a shift had potentially occurred. Inspection of the horizontal magnetometer readings and examining the effects on the measured count rate would then reveal whether such a disruption was the onset of a local magnetic field disturbance or not. For measurements taken with the 3 mCi  $^{35}\text{S}$  source, data runs in which a local field disturbance was observed were rejected entirely.

#### 4.4 Other Analytical Issues

To arrive at a final value for the transmitted electron intensity (count rate) at any given momentum setting, the following additional corrections were made to the raw data.

Background was subtracted from each spectrum. The background counting rate was determined by examining the silicon detector spectra taken with the spectrometer set above the  $^{35}\text{S}$  endpoint. A background spectrum is shown in Fig. 4.6. This spectrum was accumulated for 15 minutes (the typical duration at each magnetic field setting in the data runs). The shape of the background cannot be determined from this spectrum; however, this is not important as it is the total count rate, over the summing range, that is relevant. From this spectrum we see that the background counts num-

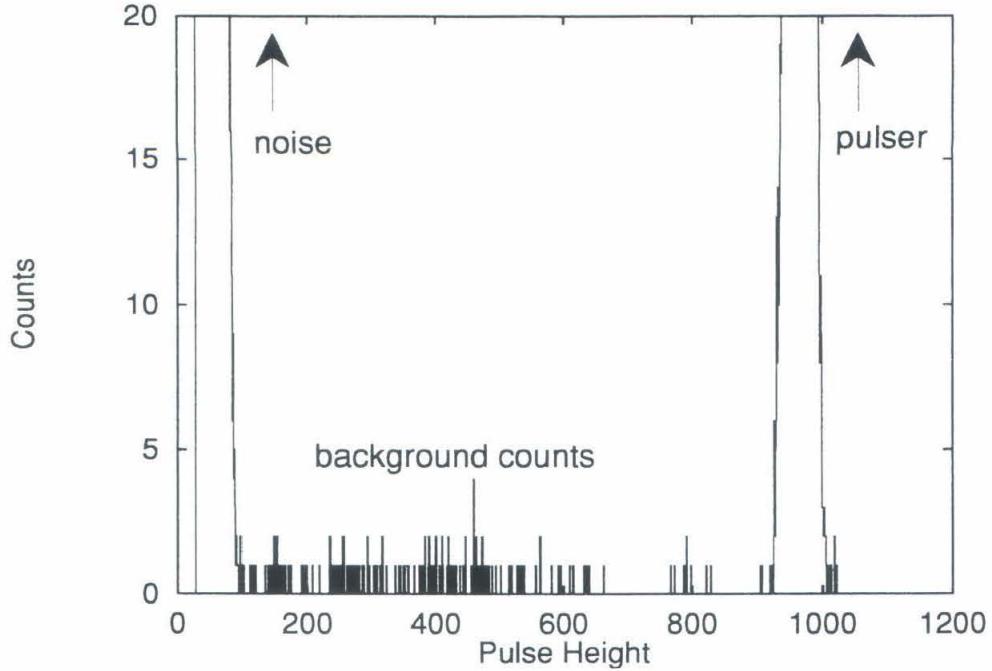


Figure 4.6: Background spectrum measured above the  $^{35}\text{S}$  endpoint.

ber about 200 in a 15 minute interval and this should be compared to the roughly 45,000 counts accumulated with the spectrometer set at a momentum of 420 keV/c. Of course, the background subtraction has a much larger relative impact on the counting rate for momentum points taken very close to the endpoint.

The time and date when each momentum point was being measured was recorded and the observed count rate at each point was corrected for the decay of the  $^{35}\text{S}$  source.  $^{35}\text{S}$  has a tabulated half-life of 87.4 days [46] and our observation of the decay of the count rate over time agreed with this value. Fig. 4.7 shows a plot of the count rate, measured at the same specific momentum setting (around 420 keV/c), recorded over the course of the data taking period. It agrees well with an exponential having  $t_{1/2} = 87.4$  days.

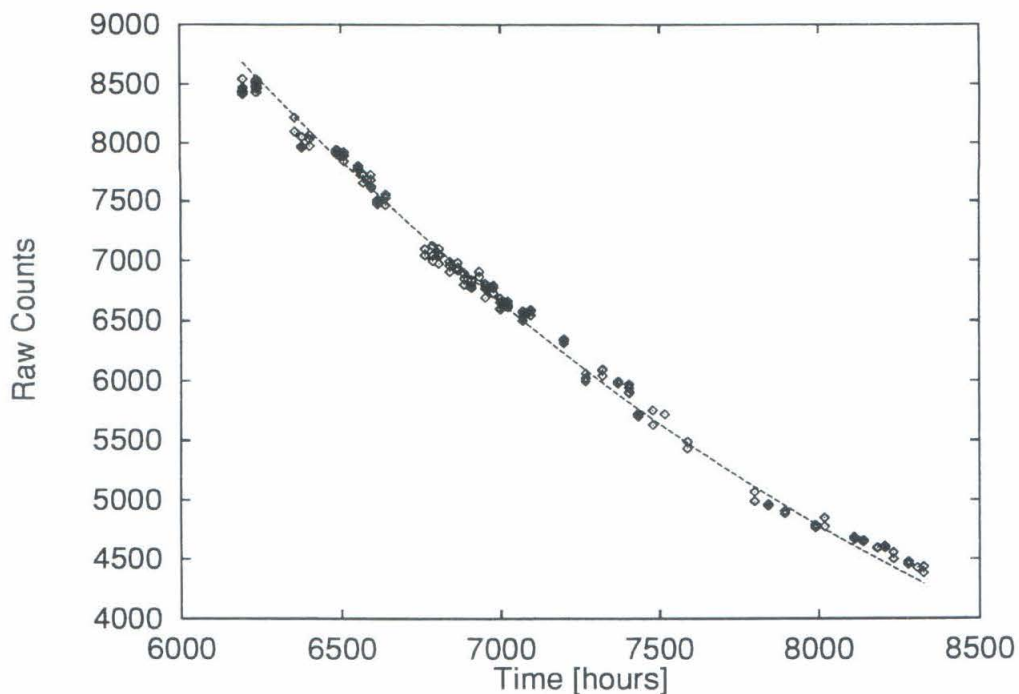


Figure 4.7: Decaying intensity of the  $^{35}\text{S}$  source. Raw uncorrected counts have been plotted versus time. The overlying exponential, drawn for comparison, is of  $t_{1/2} = 87.4$  days, and was not fit.

One final correction that is applied to the count rate is for dead time. The ADC on the Ortec 916A card kept track of the elapsed live and real time during data taking. These values were used to maintain the same live time in each spectrum accumulated. Throughout the course of the experiment, the actual, reported dead time fraction was  $< 0.2\%$ .

## 4.5 Wide Scan Data

Our first look at the  $^{35}\text{S}$   $\beta$  spectrum comes from a set of data taken with the 3 mCi source. Data was collected over a wide momentum range; we designate this data set as run A. In sweeping over this momentum range, from about

388 keV/c (energy of 131 keV) to beyond the  $\beta$  endpoint, the spectrometer field was ramped consistently from low momentum to high momentum, as illustrated by Fig. 4.4. Data points were accepted only from the upgoing-ports of a momentum sweep, in order to avoid any possible hysteresis effect that might persist in the room (steel reinforcing bars in the concrete walls) or in any of the ferromagnetic materials that, by necessity, had to lie close to the spectrometer (vacuum pumps, bellows, etc.). Of course, the spectrometer was constructed iron-free and any residual hysteresis effect should be small.

The momentum step size selected for the wide scan data runs was approximately 0.5 keV/c. As mentioned earlier, spectra that were collected from settings above the  $\beta$  endpoint were studied in order to extract the background counting rate in this run. The processed count rates from run A, analyzed at each measured momentum point, are displayed in Fig. 4.8, with both a momentum spectrum and a Kurie plot shown. The endpoint for  $^{35}\text{S}$  decay is readily seen at about 167 keV; thus, one would expect the kink from a 17 keV neutrino to appear at 150 keV (momentum 420 keV/c), though such a small kink would not be visible on a plot of this scale.

This processed data was subsequently binned and fit with the allowed  $\beta$  spectrum for  $^{35}\text{S}$  decay, including Fermi function and radiative corrections from [47]. The Gaussian response function of the spectrometer, invoked as a constant dependence:  $\Delta p/p = 0.28\%$  FWHM, was convolved with the theoretical  $\beta$  spectra, with and without heavy neutrino, as a part of this fitting procedure. A few words concerning the binning and fitting of the data are in order.

Each data point in a momentum spectrum consists of three values: the momentum obtained from the fluxgate probe reading, the analyzed count rate seen at the detector, and the identically analyzed statistical error on

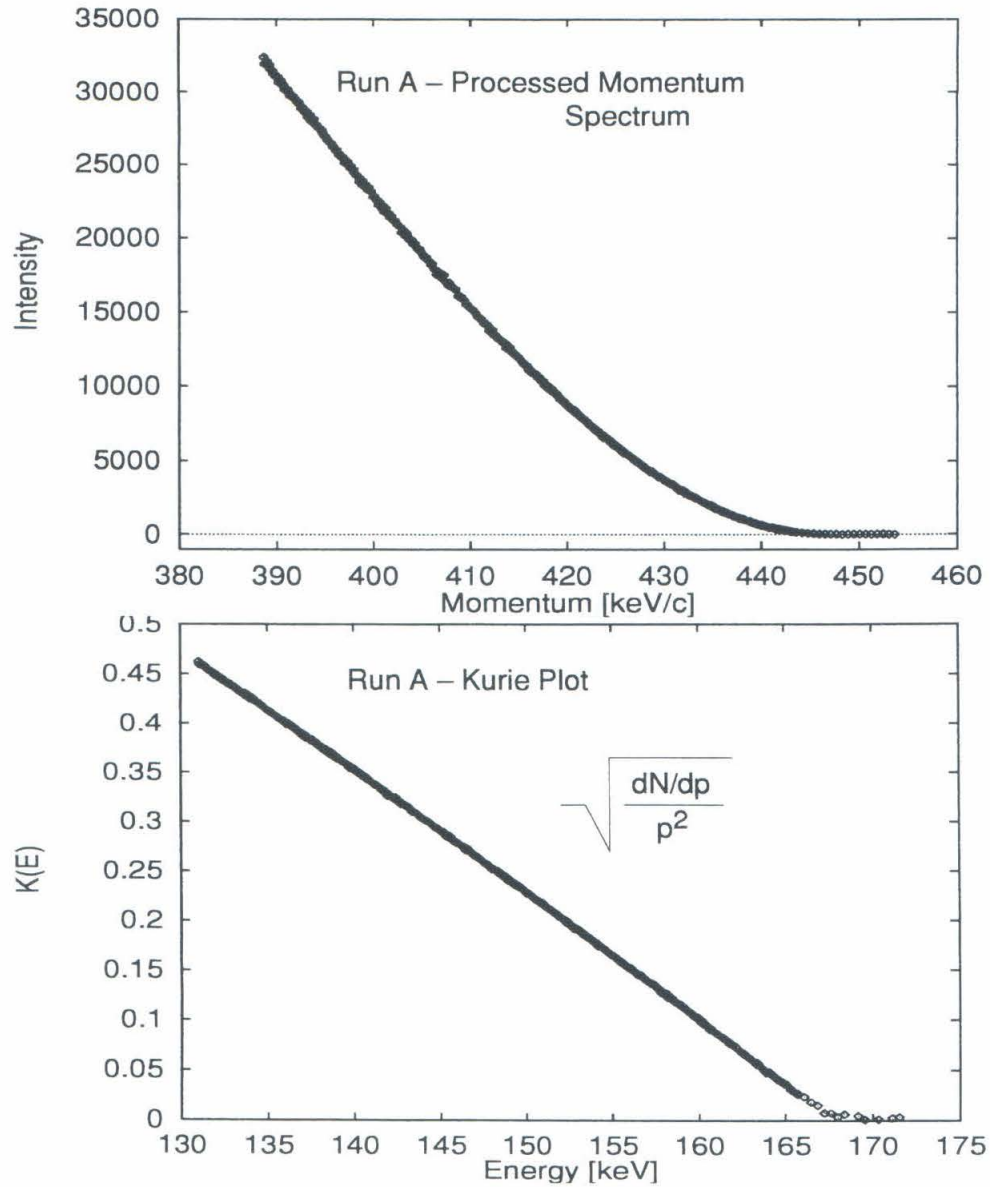


Figure 4.8: Wide scan data. A momentum spectrum, extracted from the data, is displayed above. Error bars are smaller than the size of the points. Below, the spectrum is shown as a Kurie plot, before application of the Fermi correction.

the counts. Within a given momentum bin, say of width 1.0 keV/c, the spectrometer might have sampled something like ten or more data points (with momentum falling into this bin), in all the sweeps that constitute the wide scan data run A. The task at hand is then to average each of the three values from the 10 data points. The average momentum is given simply by,

$$\bar{p} = \frac{1}{n} \sum_{i=1}^n p_i. \quad (4.4)$$

This is such that if all the momentum values tend to cluster around some value within the bin, as they should if the magnetic field in each of the samples were accurately reproduced from sweep-to-sweep, the simple average would represent a better value to use than say the central value of the momentum bin. The average counts are given by,

$$\bar{y} = \bar{p} \frac{1}{n} \sum_{i=1}^n \frac{y_i}{p_i}, \quad (4.5)$$

and the average error by,

$$\bar{\sigma} = \bar{p}^2 \frac{1}{n} \sum_{i=1}^n \frac{\sigma_i^2}{p_i^2}, \quad (4.6)$$

where the weighting by the momentum is necessitated by the known linear increase of the spectrometer acceptance,  $\Delta p$ , with momentum.

While it is not at all necessary to bin the data prior to fitting them with  $\beta$  spectra, this procedure was applied so that the binned data, with smaller error bars at each point, were much easier to interpret visually. A check was made to confirm that data, which had and had not been binned, yielded the same analytical results when fit. This was the case. Thus, subsequent presentation of data in this document will be of binned counts.

In fitting the data, the parameters that one could choose to vary freely

were: the overall normalization,  $A$ ; the  $\beta$  endpoint energy,  $Q$ ; the heavy neutrino admixture,  $\sin^2 \theta$ ; and the heavy neutrino mass,  $m_H$ . The two-component  $\beta$  spectrum, containing the fitting parameters listed above,

$$\frac{dN}{dp} = A F(Z, E) p^2 [\cos^2 \theta (Q - E)^2 + \sin^2 \theta (Q - E) [(Q - E)^2 - m_H^2]^{1/2}], \quad (4.7)$$

with  $p$  being the electron momentum,  $E$  the kinetic energy of the electron, and  $F(Z, E)$  representing the Fermi and radiative corrections, would be convolved with the Gaussian response function,

$$R(p, p') = \frac{1}{\sigma \sqrt{2\pi}} e^{-(p-p')^2/2\sigma^2}, \quad (4.8)$$

where  $\sigma = 0.00118905 \times p$ . After the convolution, we arrive at the theoretical intensity of the  $\beta$  spectrum, to be used for least-squares fitting,

$$I(p) = [1 + k_1(p_0 - p) + k_2(p_0 - p)^2] \int R(p, p') \frac{dN}{dp'} dp', \quad (4.9)$$

in which two additional free parameters, in the form of linear and quadratic terms in a smooth polynomial shape correction, could also be included in the fit. The parameter,  $p_0$ , is the momentum endpoint of the decay.

Data from run A was fit, with the heavy neutrino admixture fixed to zero, allowing only the normalization and endpoint to vary. The resulting  $\chi^2/\nu = 66/51$  was not a good fit and the data are shown in Fig. 4.9. If we include a freely varying linear shape factor, the fit improves,  $\chi^2/\nu = 51/50$ . By any standards, this is a reasonably good fit. If we were to continue, however, and include the quadratic term (thus allowing four free parameters in the fit), the resultant  $\chi^2/\nu = 37/49$  is a further improvement.

What does this imply? Is the quadratic shape term required, or not? The

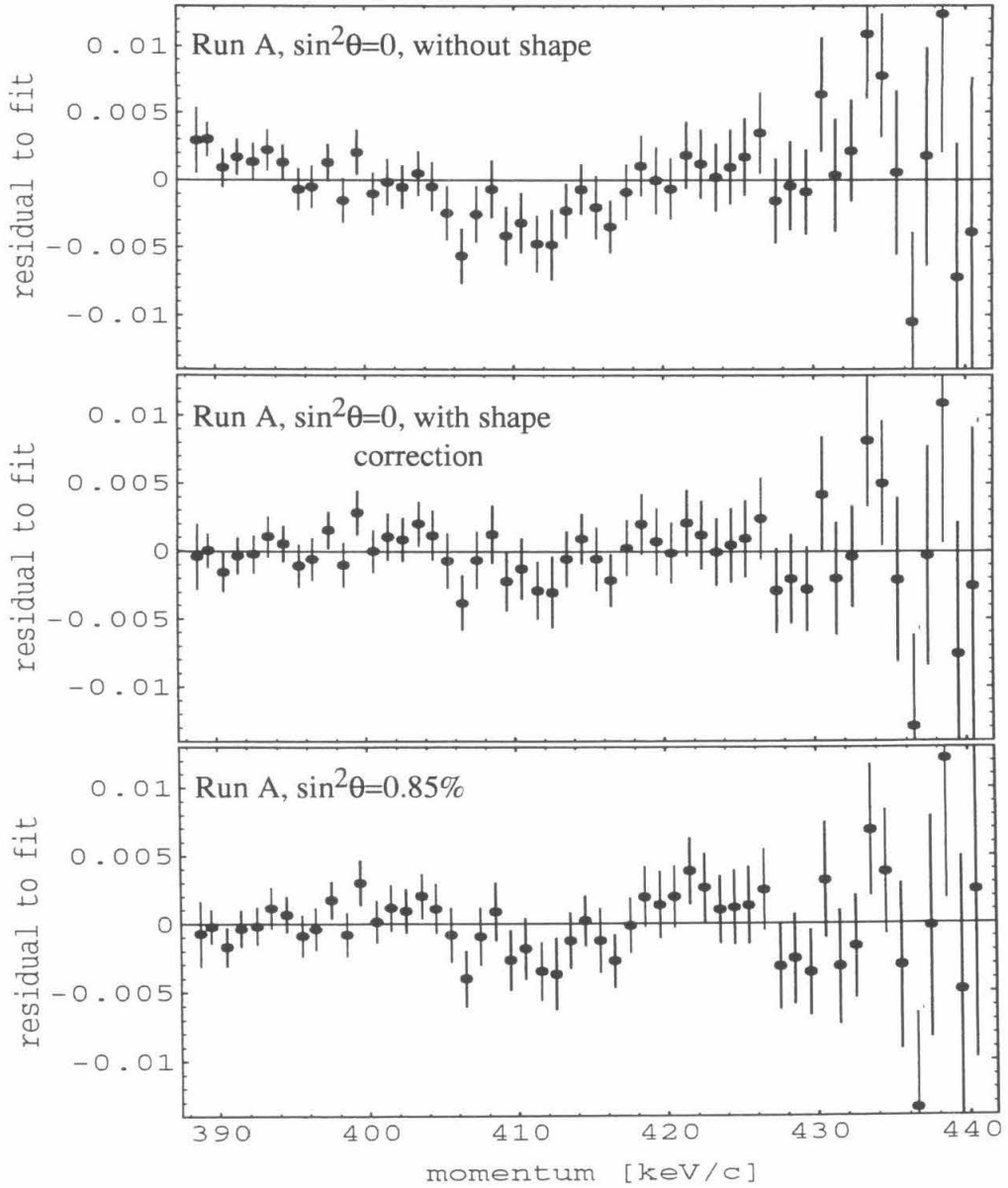


Figure 4.9: Fitted wide scan data. The data points are plotted as residual to the fits (i.e. data/theory - 1), with and without a 17 keV neutrino.

$k_1$ (keV/c) $^{-1}$	$k_2$ (keV/c) $^{-2}$	Q [keV]	$\sin^2 \theta$ (%)	$\chi^2/\nu$
0	0	167.61(1)	0	66.1/51
$2.0(5) \times 10^{-4}$	0	167.66(2)	0	51.0/50
$-1.2(3) \times 10^{-3}$	$1.4(3) \times 10^{-5}$	167.56(3)	0	36.5/49
0	0	167.67(1)	0.85	88.4/51
$0.5(5) \times 10^{-4}$	0	167.68(2)	0.85	87.4/50
$-2.2(3) \times 10^{-3}$	$2.4(3) \times 10^{-5}$	167.51(3)	0.85	45.2/49
$-0.4(7) \times 10^{-3}$	$0.8(6) \times 10^{-5}$	167.60(4)	-0.58(44)	34.8/48

Table 4.2: Results from fits to the wide scan data. The heavy neutrino mass was fixed at 17 keV.

change in  $\chi^2$  is significant and this seems to indicate that the quadratic shape term has statistical merit for inclusion. Is it sufficient for an experiment to declare everything satisfactory, just when  $\chi^2/\nu \approx 1$ ? Perhaps it is, though no other experiment on the 17 keV neutrino, up to this point, has ever reported results when their fits were taken one extra degree of freedom beyond what they had declared satisfactory. We proceed with the analysis of the data from run A, with the quadratic shape factor included.

When the heavy neutrino admixture was fixed at 0.85% (the level at which it was observed by Hime and Jelley), and the mass fixed at 17 keV, the same fits to the data from run A gave:  $\chi^2/\nu = 88/51$  without shape terms,  $\chi^2/\nu = 87/50$  with a linear term and  $\chi^2/\nu = 45/49$  including the quadratic shape factor as a free parameter. Table 4.2 lists the results of these various fits to data from run A, with and without the 17 keV neutrino.

If one includes the admixture as a free parameter in the fit, along with the other four freely varying parameters, the best fit admixture (for mass 17 keV) deduced is  $\sin^2 \theta = (-0.58 \pm 0.44)\%$ . The estimated errors in the fitted parameters come from taking the square root of the diagonal elements of the covariance matrix, in the method of least squares, minimum  $\chi^2$  fit.

Our data set was the statistical outcome of a measurement, wherein the

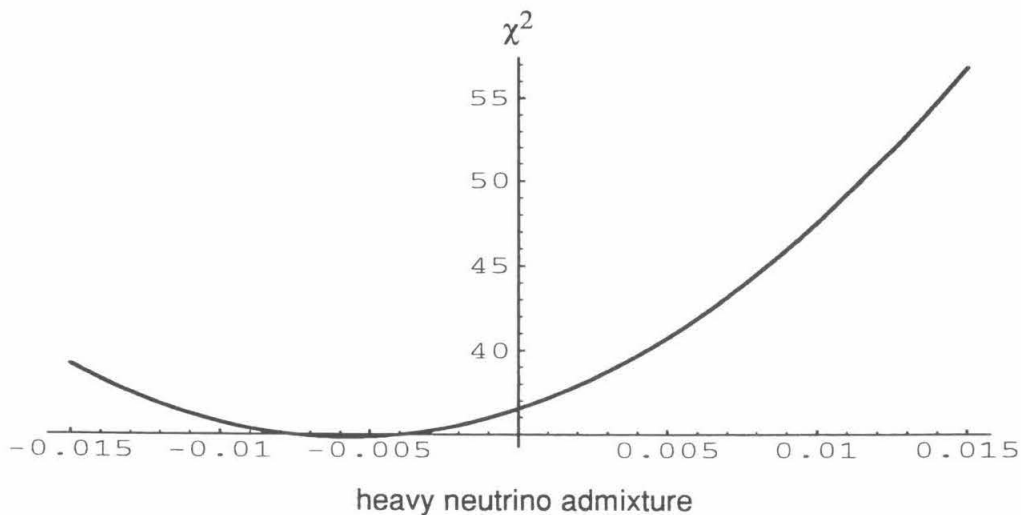


Figure 4.10: Minimum  $\chi^2$  parabola, from the wide scan results.

true value of the physical parameters are unknown. In fitting our data, a model which contains these parameters was the basis, and the Levenberg-Marquardt method was employed [48]. The likelihood to arrive at a specific value for a single parameter (as estimated by our data set), in a measurement with the rest of the relevant parameters free to vary in the fit, yields a  $\Delta\chi^2 \equiv \chi^2 - \chi_{min}^2$ , distributed as the square of a normally distributed quantity. From our data set, which has a minimum  $\chi^2$  for an admixture of  $-0.58\%$ , which we believe is not too far from the true value of the parameter, a plot of  $\chi^2$  versus the admixture indicates the likelihood of other values for this parameter. Such a plot, displayed in Fig. 4.10, is a parabola. The difference at  $0.85\%$  mixing,  $\Delta\chi^2 = \chi^2(0.85\%) - \chi_{min}^2$ , is  $45.2 - 34.8 = 10.4$ . Thus, the likelihood that a subsequent measurement, similar to this one, would by chance arrive at a fitted admixture  $\geq 0.85\%$  is  $\sqrt{10.4} \rightarrow 3.2\sigma$  on a normal distribution, or  $0.0687\%$ .

While the previous statistical considerations seem to rule out a 17 keV

neutrino with an admixture of 0.85%, nevertheless, the issue is not entirely satisfying as the actual data could be fit to the spectrum with the heavy neutrino branch, giving a good  $\chi^2/\nu = 0.92$ . It would be more visually convincing if the data could be shown well fit to the spectrum without heavy neutrino and poorly fit to the spectrum with the 17 keV kink. If we go back and look at the wide scan data, fit with only a linear shape correction, the results are more striking. Fig. 4.11 shows again the wide scan data, this time fit with just the linear shape factor. The poor fit of the data to the spectrum which includes the 17 keV neutrino is seen. If, in place of the earlier analysis, we take the fitted  $\chi^2$  values when only a linear shape term was included, the difference in  $\chi^2$  between zero and 0.85% admixture is  $36.4 \rightarrow$  a  $6\sigma$  exclusion.

The slight quadratic curve of the data points is visible in this plot. It can be seen and understood now that the effect of including the quadratic shape term was that the statistical error in the fitted admixture was increased, due to the interdependence of this parameter,  $\sin^2\theta$ , with the additional quadratic free parameter in the fitting procedure. By choosing to include a quadratic shape term, a choice which is justified to account for any smooth uncertainty remaining in the spectrometer response, the statistical strength of our data set was voluntarily diminished. Nevertheless, the sharp threshold effect of heavy neutrino emission could be distinguished from such a smooth deviation; data with the linear and quadratic correction both strongly reject the 17 keV neutrino hypothesis.

## 4.6 Narrow Scan Data

The narrow scan data runs were a successful attempt to acquire very a high statistics spectrum, in a narrow momentum region about the hypothetical

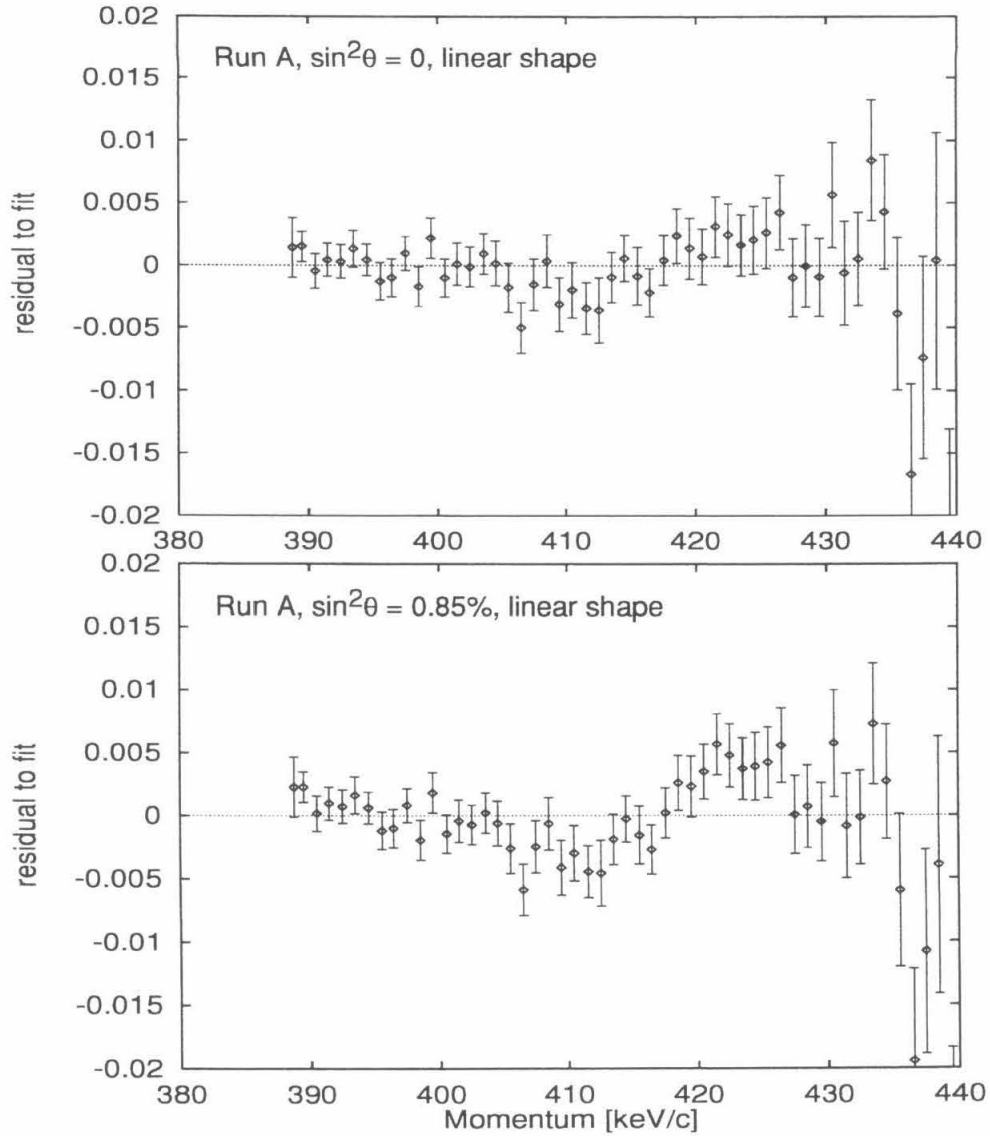


Figure 4.11: Wide scan data with linear shape correction. The data points are plotted against spectra with and without a 0.85% admixed, 17 keV neutrino.

17 keV neutrino kink. The data in the narrow scan, hereafter designated as run B, were acquired over a 15-day period that overlapped with Christmas break. This is a significant point as the observed magnetic field behavior during this time was unusually quiet. It is surmised, though it could not be verified, that this period was one in which LIGO laser equipment, near the spectrometer, was probably not in operation due to the holidays; one particular laser was later found to be responsible for the generation of magnetic field disturbances, local to the building, that affected the experiment.

During the narrow scan sweeps, the spectrometer field was repeatedly stepped from 410 keV/c to 430 keV/c, in increments of 0.2 keV/c. Originally, it was desired that this data set span a 20 keV/c momentum region, centered upon 420 keV/c; however, the first few momentum points from each sweep, between 410–413 keV/c, had to be discarded because the stepping algorithm programmed in the computer did not properly implement the three minute waiting period following a field change at these settings. At these momentum points, the data acquisition did not allow the spectrometer field to properly stabilize before counts began to accumulate. Thus, valid momentum points began only from 413.5 keV/c.

The data set for run B was acquired with the 3 mCi  $^{35}\text{S}$  source. The analytical procedure to extract the count rate at each momentum point was identical to that described for the wide scan data. Data from run B were collected into 0.5 keV/c bins and fit to  $\beta$  spectra.

With the heavy neutrino admixture fixed at zero, the data points could be fit very well without any shape correction. Varying only the endpoint and overall normalization, the resultant fit to the narrow scan data yielded a  $\chi^2/\nu = 28/30$ . This should be compared to the fit when a 17 keV neutrino with an admixture fixed at 0.85% was included. In that case, the fit was poor,

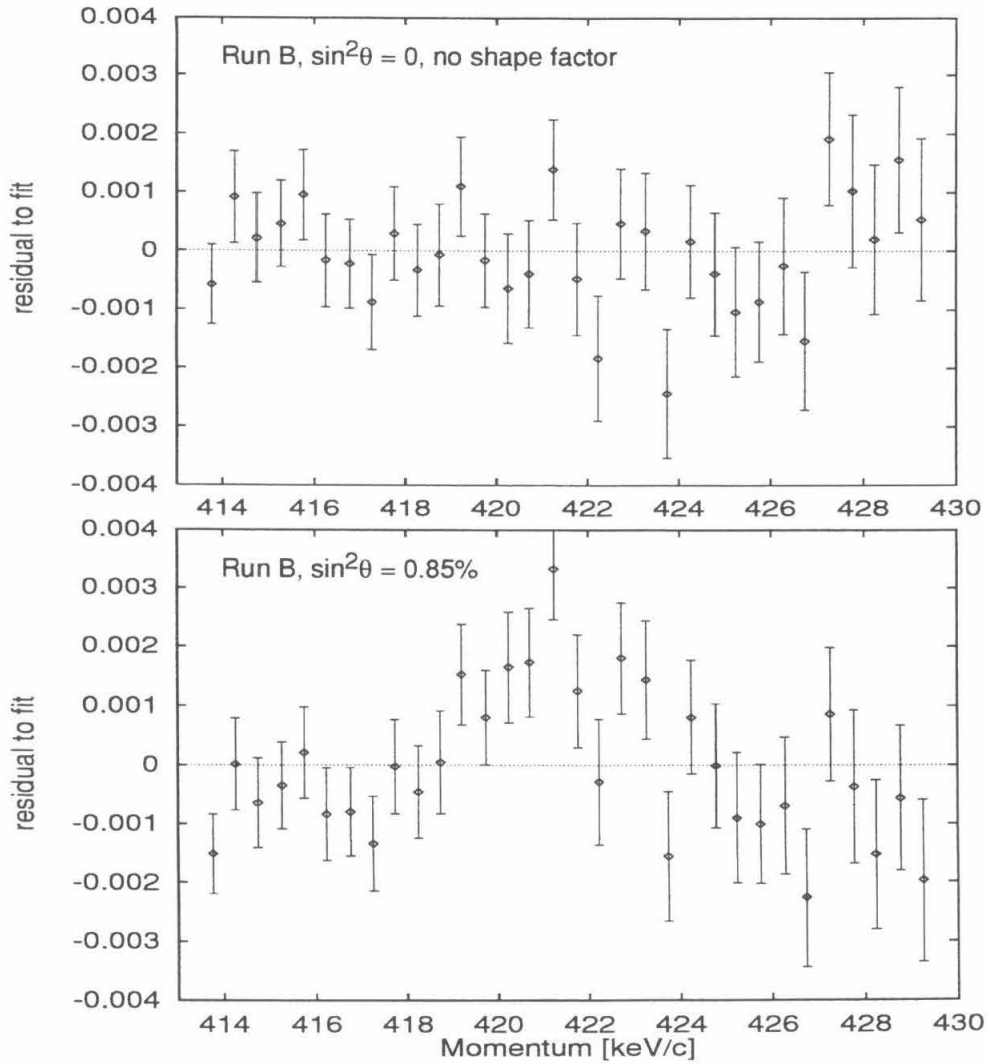


Figure 4.12: Narrow scan data without any shape correction. The data points are plotted as residuals to fits with and without a 0.85% admixed, 17 keV neutrino.

producing a  $\chi^2/\nu = 58/30$ . The fitted data are displayed in Fig. 4.12. One comment to make is to note the scale of the residuals plotted in Fig. 4.12. It is a five times larger scale, with error bars on the data points at the  $\pm 0.001$  level. The exclusion of a mixing probability of  $\sin^2 \theta = 0.0085$ , interpreted from these fits without shape correction, is at the  $5.5\sigma$  level.

Since the narrow scan data spans a small momentum range, it is easily understood and even expected that the data from run B could be fit without invoking any shape corrections. Proceeding beyond this stage, we continue by including a linear shape term as a free parameter in the fit. When this is done, the fitted results are  $\chi^2/\nu = 26/29$ , for no heavy neutrino, and  $\chi^2/\nu = 36/29$ , with a 0.85% mixing probability, 17 keV neutrino. Going even further, we can include a quadratic shape factor also in the fits. The resultant  $\chi^2/\nu = 26/28$ , for zero mixing and  $\chi^2/\nu = 36/28$ , with a 0.85% admixture, show no improvement in goodness-of-fit over the previous case. We state that, because the fit was not improved with the addition of a quadratic free parameter, it is statistically warranted to exclude the quadratic term in the analysis of the narrow scan data. Thus, for our final results, we quote the mixing fraction deduced from the statistical analysis which included only a linear shape correction. Table 4.3 summarizes the results from various fits to the narrow scan data.

From Table 4.3, we find that the best fit admixture, for  $m_H = 17$  keV, is  $(-0.03 \pm 0.27)\%$ , based on the results which invoked the linear shape correction. This measurement provides a statistical exclusion of the 0.85% admixed, 17 keV neutrino at  $3.26\sigma$ , or the 99.94% confidence level. There are a few things to note from this table and from Table 4.2, results of the wide scan analysis. If we compare the wide and narrow scan fits, with linear shape correction only, we find the fitted linear shape terms are consistent, within

$k_1$ (keV/c) $^{-1}$	$k_2$ (keV/c) $^{-2}$	Q [keV]	$\sin^2 \theta$ (%)	$\chi^2/\nu$
0	0	167.48(1)	0	27.9/30
$3.3(22) \times 10^{-4}$	0	167.55(4)	0	25.7/29
$-0.5(394) \times 10^{-4}$	$4.6(523) \times 10^{-6}$	167.52(25)	0	25.8/28
0	0	167.56(1)	0.85	57.5/30
$-9.6(20) \times 10^{-4}$	0	167.37(4)	0.85	36.4/29
$5.4(189) \times 10^{-4}$	$-2.1(26) \times 10^{-5}$	167.46(12)	0.85	35.6/28
0	0	167.50(1)	0.16(12)	26.4/29
$3.8(49) \times 10^{-4}$	0	167.55(7)	-0.03(27)	25.7/28

Table 4.3: Results from fits to the narrow scan data. The heavy neutrino mass was fixed at 17 keV. The errors, in the last digit, are given in parentheses.

the estimated error (without heavy neutrino of course). Since the wide scan results “required” the quadratic shape, a comparison of the fitted endpoints from the quadratic-fit wide scan with the linear-fit narrow scan show endpoint estimates of  $167.56 \pm 0.03$  keV and  $167.55 \pm 0.04$  keV, respectively. The statistical errors on the fitted endpoints of the  $\beta$  decay are larger in the narrow scan results than the fits from the wide scan, despite the higher statistics, since the short lever arm provided by the narrow momentum region extrapolates with greater uncertainty.

To conclude the discussion of the narrow scan data and analysis, a plot is presented of this data, normalized above the threshold for emission of a 17 keV neutrino. This form of plot has become rather popular in the “17 keV community”; however, one should be cautioned about extracting any statistical information from the accompanying analysis, as not all the data points are incorporated in the least-squares fit. The rationale behind displaying the data in this form is the visual impact. What is done is to take a subset of the data above 420 keV/c momentum, which is 17 keV below the endpoint energy of  $^{35}\text{S}$ . Using this set of data, it does not matter whether one fits it with or without a heavy neutrino; the spectral shape is identical

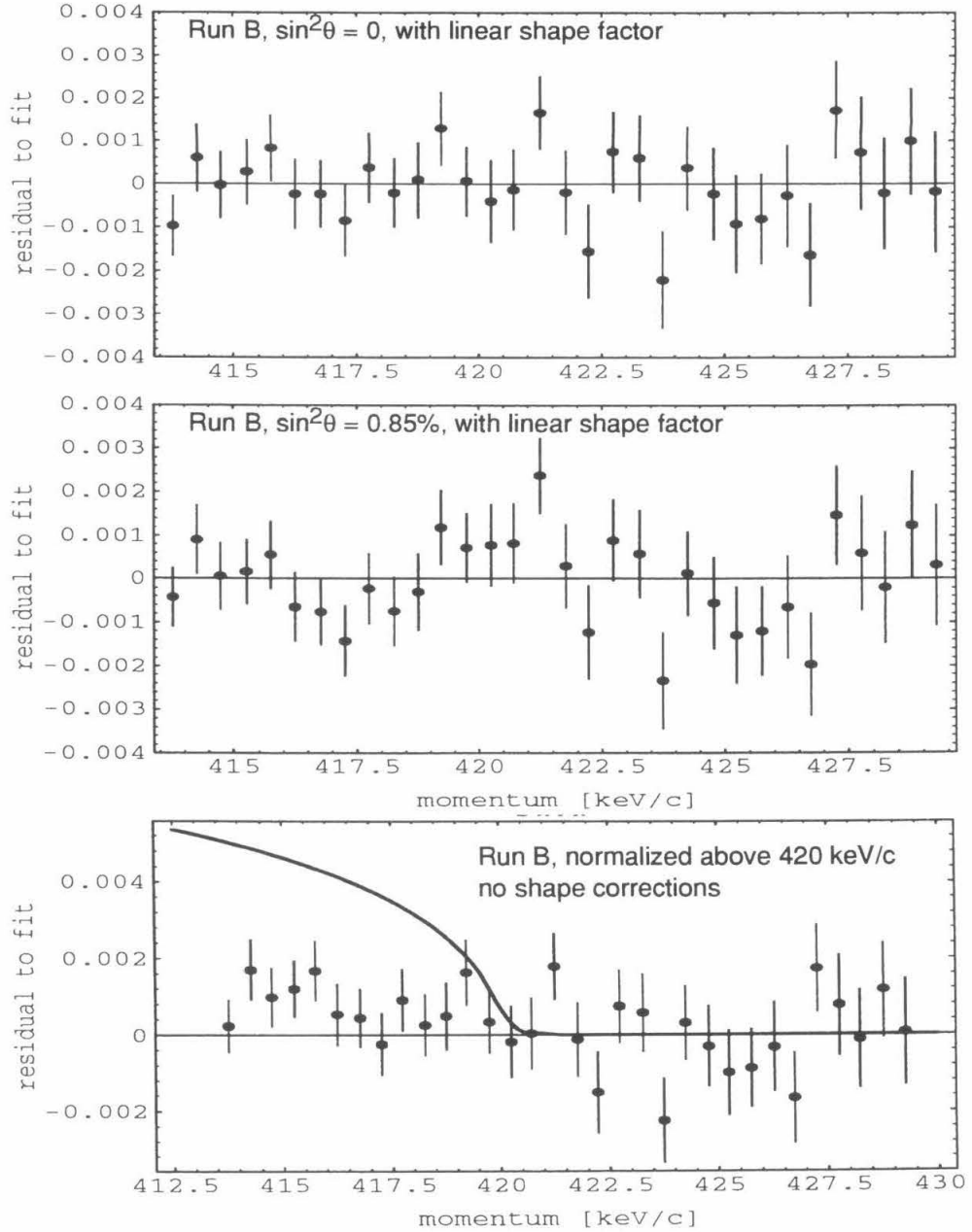


Figure 4.13: Fitted narrow scan data. Above, data points with linear shape are plotted as residuals. Below, points above 420 keV/c served to normalize the data. The solid curve shows the expected shape for 17 keV neutrino emission.

in either case, if one is above the emission threshold. After the subset of data is fit, the rest of the data points below the threshold are plotted using those fitted parameters. No shape corrections are invoked. Such a plot is shown in Fig. 4.13, accompanied by a regular plot of fit residuals, from the analysis wherein the linear shape correction was included. One can see from this figure that the data points, below the threshold, fall slightly above the line of zero residual — a smooth, linear polynomial deviation nicely describes the shape of the data. However, the points clearly do not show any sharp departure from a straight line extrapolation backwards, as exhibited by the curve showing the expected spectral shape that would result from a 17 keV neutrino, emitted with 0.85% probability. Would anybody believe that the magnetic spectrometer has exactly this abrupt shape, inverted, as a defect in its response function in order to produce this data, given that the 17 keV neutrino really existed?

## 4.7 Strong Source Data

Unlike the data taking period which corresponded to the narrow scan, the data accumulated with the 7 mCi, “strong” source occurred during a period in which the magnetic field, measured by the vertical and horizontal fluxgate probes, experienced frequent disruptions. Since our calibration is based on field measurements at one fixed position in the spectrometer, we know that a global deviation in the magnetic field, if it were uniform over the entire spectrometer, would be harmless. However, a local field disturbance can result in a non-uniform deviation in the magnetic field across the orbital plane of the spectrometer. Thus, a measurement of the magnetic field deviation at one position may not be representative of its true effect on the electron

paths and correspondingly on the spectrometer acceptance.

Many data sweeps in the post-Christmas runs, taken with both of the  $^{35}\text{S}$  sources, were discarded on the grounds that local field fluctuations were observed during the measurements. It should be mentioned that after removing the 3 mCi source and prior to the insertion of the strong  $^{35}\text{S}$  source, the spectrometer momentum calibration was checked with the  $^{57}\text{Co}$  source. Repeats of the momentum calibration runs verified the long-term applicability of the magnetic field calibration values that were determined prior to the collection of the wide and narrow scan data. In these calibration runs, due to the sharpness of the IC lines, the observation of a count rate shift is much less likely since the total time duration at field settings which have an appreciable count rate is such a small fraction of the overall data sweeping time. Looked at another way though, this is advantageous in that the momentum calibration of the spectrometer, deduced during such a run, could only be affected by magnetic field shifts in a very limited way.

Conversely, in order to explore issues related to count rate stability, the steep edges of the IC lines were ideal. During the time that the  $^{57}\text{Co}$  source was in place, a few studies were performed with the spectrometer field setting fixed at the half-maximum point of the upper edge of the first K-conversion line. Any fluctuations in the magnetic field would then have a strong effect on the count rate, due to the steep slope of this line. During these studies, numerous effects such as temperature, hysteresis, current stability and other factors were explored to pin down any potential source of fluctuations in the count rate. None of these were significant. It was concluded from these studies that local magnetic field disturbances were clearly identified as the cause of the observed count rate shifts. The task remained to identify the origin of these field fluctuations.

The confirmation of a field fluctuation requires that one look at more than just a single probe reading. We had instrumented the data acquisition to record field readings from a second, so-called horizontal magnetometer. It was thus a simple task to correlate fluctuations in the main Bartington probe with fluctuating measurements from the horizontal probe, and to positively identify the occurrence of any magnetic field deviation. However, we were initially not capable of performing an exact comparison of the relative extent of any such deviation in one probe to the relative deviation in the other, at least not very well. This was because the horizontal field probe originally had its analog output sampled by the DAS analog-to-digital converter. The stability and precision of this ADC on the plug-in PC card was not sufficient and the readings from the horizontal fluxgate, while usable to pinpoint short-timescale excursions in the field, could not be relied upon to yield precisely repeatable readings from run-to-run.

During the stability studies at the  $^{57}\text{Co}$  conversion line, a second precision digital multimeter, a Fluke 8842A, was acquired and instrumented to read the analog voltage output from the Walker magnetometer, replacing the poor ADC for all future measurements. This new multimeter was connected via GPIB interface to the data acquisition computer. In addition to the readout change, the Walker probe was re-mounted. It was re-oriented vertically and was positioned at the diametrically opposite end of the spectrometer from the Bartington calibration probe. The probe was attached to the field-cancelling Helmholtz coils. This setup provided a better platform to further probe the subtleties of the magnetic field deviations.

It is perhaps useful to display the observed effects of a field fluctuation on the count rate in the spectrometer. Fig. 4.14 displays first a plot of magnetic field from one probe versus magnetic field reading from the other.

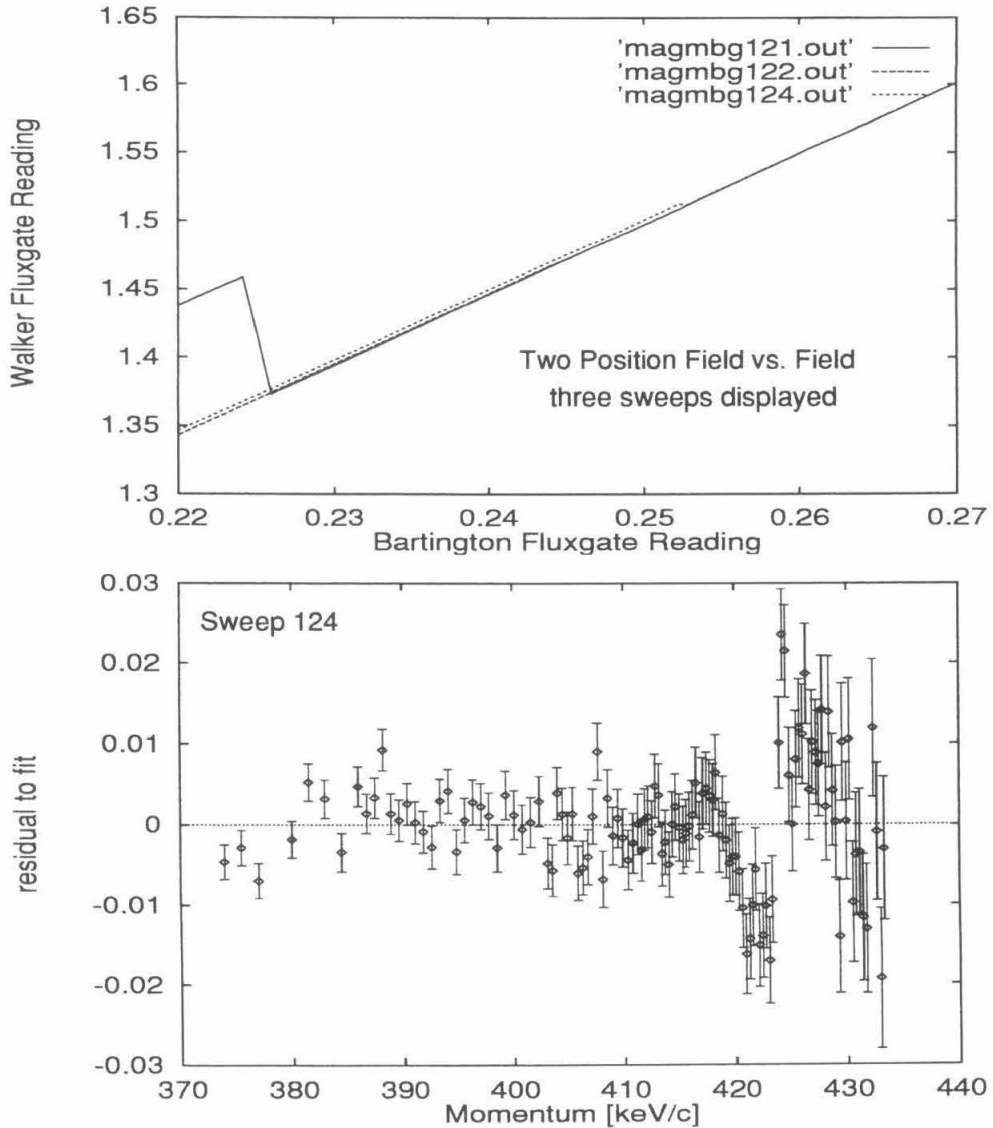


Figure 4.14: Effects of field fluctuations on the count rate. Above, probe versus probe values are plotted for three data sweeps. Below, the count rate for sweep 124 is displayed.

Three data taking sweeps are shown. The individual measured points are not plotted as they would be obscuring and error bars are not shown as they are small; instead, a line connects the points to adjacent ones in time and the smoothness of the line indicates the level of fluctuation of the field readings.

From this plot, we can notice three features. First, a large step is seen in “sweep 121,” at the first few data points. Interestingly, during “sweep 122,” which repeated those field measurements 3 days later, the plotted probe versus probe values fall into the line one would have expected for those points from sweep 121. Finally, it is seen that “sweep 124” begins slightly displaced from the proper probe-probe line; however, at a larger field setting, much later in the data taking sweep, the magnetic field has shifted and subsequent points once again lie on the proper probe-probe relative line.

Below in Fig. 4.14, the count rate spectrum extracted from sweep 124 is shown and has been fit to a  $\beta$  spectrum, including a linear shape factor, so that small deviations could be seen on top of the  $\beta$  spectral shape. At the field values where the small shift in the probe-probe ratio took place, the count rate exhibits a sharp discontinuity, at the corresponding momentum value. It can be understood now, that without the benefit of a relative field versus field study, one would not know whether to accept the data points that were measured above or below this observed discontinuity. This explains the rationale for discarding entire sweeps when local fluctuations were identified, as was done for the runs before the second magnetometer probe was re-instrumented. When the relative probe-probe readings are compared, it becomes clear that one should accept the data points from sweep 124, above 425 keV/c.

In this manner, data were acquired using the strong 7 mCi  $^{35}\text{S}$  source. Observations of the relative deviations recorded in both probes would be

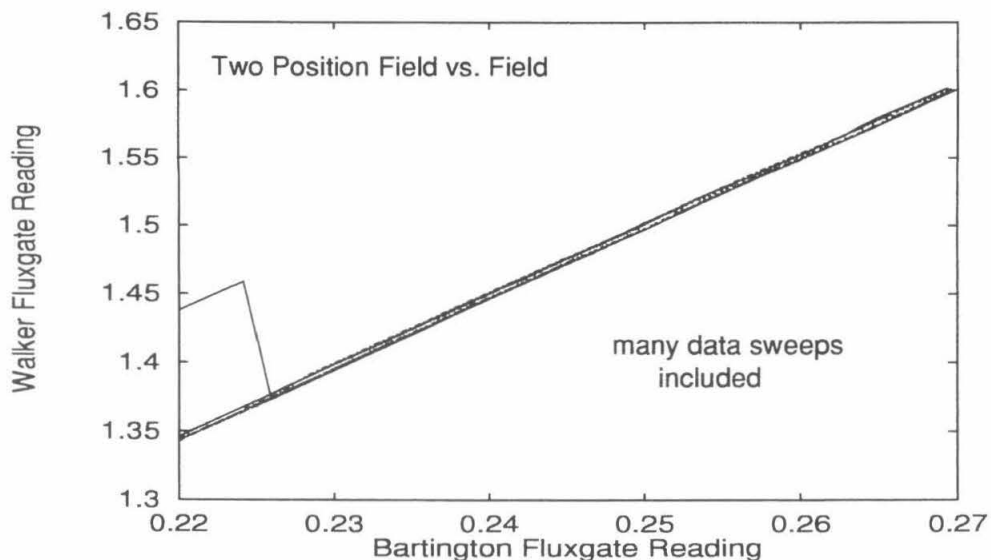


Figure 4.15: Field versus field scatter plot for many sweeps.

used to set standards for the field consistency. After many data runs were accumulated, a plot of the field versus field values showed two distinct lines that were clearly separated from each other! These should be more accurately described as two scatter bands, about which the measured probe readings clustered. Fig. 4.15 shows the accumulated field-field scatter plot for many data sweeps, including those discussed before. Occasionally, a transition from one band to another would occur within one sweep, as was highlighted in the sweep 124 data. Thus, we could determine that these transitions were abrupt and took place over a short period of time.

Identification of this feature in the probe-probe readings led us to search for the origin of this obviously local field disturbance (only a local deviation could affect the two probes at different positions, by different relative amounts). The source of the disturbance, powerful LIGO lasers directly underneath the spectrometer, was discovered. These gas discharge lasers

employ a solenoidal magnetic field to condition the discharge! Talk about something we should have known about prior to proceeding with the experiment — and right underneath the spectrometer no less! The operation cycle of the lasers was compared to the recorded times at which these fluctuations were observed and tests which switched the LIGO lasers on and off were performed to correlate with our readings [49]. One probe-probe band corresponded to the laser being off and the other occurred with the laser on.

Data from the strong source runs were thus extracted into two independent runs, C and D, corresponding to laser on and off periods. The slope and offset, relating the two probe readings into distinct bands, were determined and used as a field consistency cut. Each data point was screened and it was required that the measured readings between the Bartington and Walker magnetometers, at each momentum point, fall onto either of the two selected straight line relations, to within 1 part in  $10^4$ . Two data sets were extracted, point-by-point, collected over many sweeps.

The data sweeps, binning, background subtraction (determined above the endpoint in these runs) and fitting were performed in an identical fashion as described earlier for the wide scan data. Fig. 4.16 displays the data from runs C and D, plotted as residuals to the fit without heavy neutrino emission, including a free linear shape factor. When a quadratic term is included, the fitted  $\chi^2$  does not improve; thus, we quote results from the strong source data with only the linear shape correction invoked. Table 4.4 summarizes the fitted results for both runs C and D of the strong source data.

The first question one might ask is what those gaps in the momentum spectrum are, occurring at 380–390 keV/c and again at 395–400 keV/c. It is strange that none of the measured points were accepted by the field cut for either of the two bands. The first thing to point out is that the field

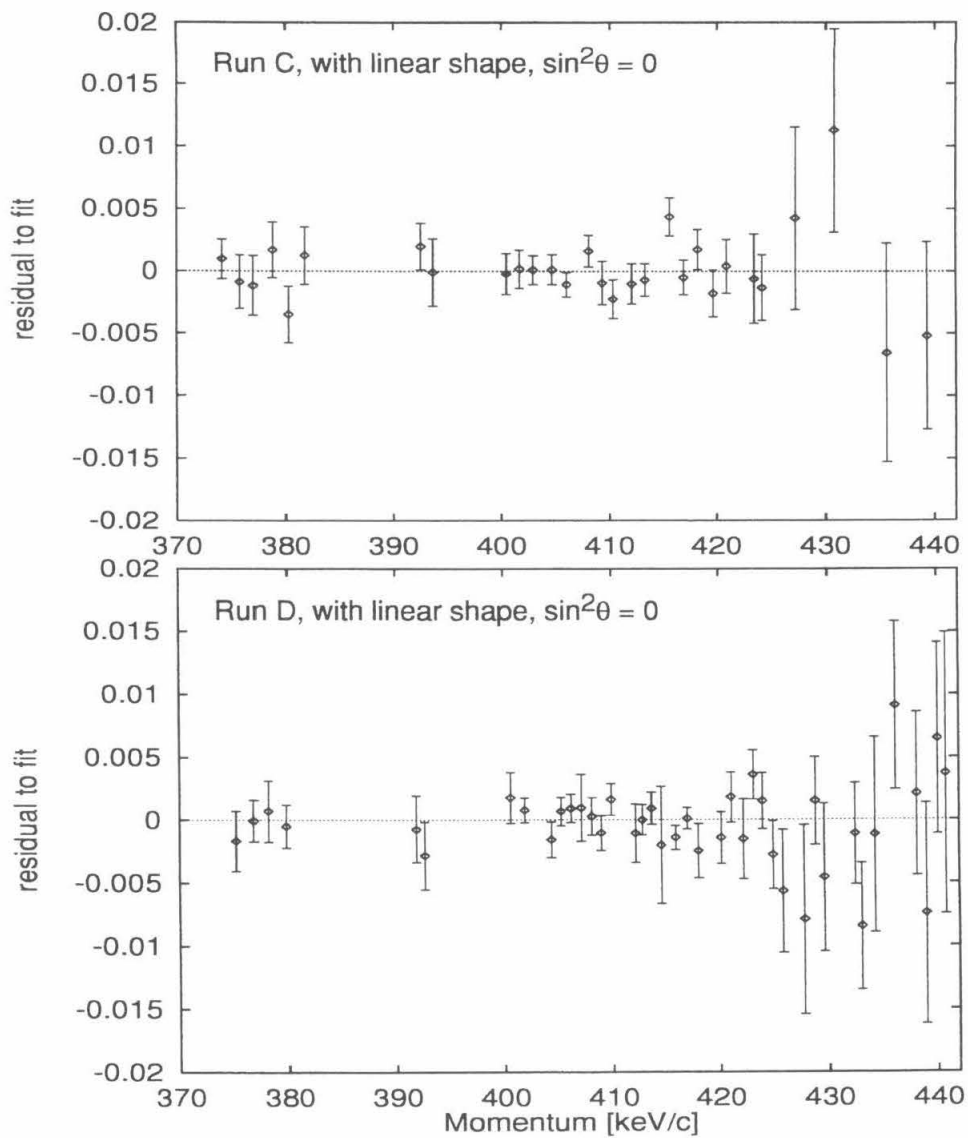


Figure 4.16: Fitted strong source data.

Run C

$k_1$ (keV/c) $^{-1}$	$k_2$ (keV/c) $^{-2}$	Q [keV]	$\sin^2 \theta$ (%)	$\chi^2/\nu$
0	0	167.87(1)	0	84.8/27
$3.3(4) \times 10^{-4}$	0	168.00(2)	0	25.3/26
$2.5(30) \times 10^{-4}$	$0.8(32) \times 10^{-6}$	167.99(3)	0	25.2/25
0	0	167.93(1)	0.85	79.3/27
$2.9(4) \times 10^{-4}$	0	168.04(2)	0.85	34.6/26
$-4.8(29) \times 10^{-4}$	$6.6(32) \times 10^{-6}$	167.97(3)	0.85	27.9/25
$3.3(5) \times 10^{-4}$	0	168.00(3)	-0.04(28)	25.3/25

Run D

$k_1$ (keV/c) $^{-1}$	$k_2$ (keV/c) $^{-2}$	Q [keV]	$\sin^2 \theta$ (%)	$\chi^2/\nu$
0	0	167.73(1)	0	61.9/38
$2.1(4) \times 10^{-4}$	0	167.78(1)	0	28.4/37
$4.8(23) \times 10^{-4}$	$-2.5(32) \times 10^{-6}$	167.80(2)	0	28.0/36
0	0	167.77(1)	0.85	52.8/38
$1.2(4) \times 10^{-4}$	0	167.80(1)	0.85	42.5/37
$-3.7(22) \times 10^{-4}$	$4.5(32) \times 10^{-6}$	167.77(2)	0.85	37.7/36
$2.1(4) \times 10^{-4}$	0	167.78(1)	0.06(21)	28.3/36

Table 4.4: Results from fits to the strong source data. The heavy neutrino mass was fixed at 17 keV. The errors, in the last digit, are given in parentheses.

step size in the sweeps tends to be a little larger at these lower momentum settings, away from the anticipated 17 keV neutrino kink. Similarly, in the data collection, not all sweeps began at the same low momentum settings; the sweeping strategy was altered a number of times during the data taking with the strong source, in an attempt to ferret out the problems with the field fluctuations. So, indeed, the number of points sampled here is lower. Perhaps the consistency cut, 1 part in  $10^4$ , is harder to achieve at lower field values, as the absolute error is smaller here? Perhaps the lines corresponding to the two field-field bands were incorrectly parameterized? It is not known why these gaps exist. We must accept the few data points below the momentum gaps, as they were shown to satisfy the magnetic field consistency cut. There

is no concern about incorporating these “separated” points into the fitting procedure as they should not introduce any bias and were properly selected, in an identical manner as the other points.

The best fit admixtures for  $m_H = 17$  keV, deduced from runs C and D, allowing a freely varying linear shape term, were  $-(0.04 \pm 0.28)\%$  and  $(0.06 \pm 0.21)\%$ , respectively. The strong source data are inconsistent with the hypothesis that a 17 keV neutrino is emitted with probability 0.85%.

## 4.8 Unified Discussion

The fitted strong source data give the  $^{35}\text{S}$  endpoint as:  $168.00 \pm 0.02$  keV and  $167.78 \pm 0.01$  keV, from two separate data sets. These values are far from the ones obtained from the data runs with the 3 mCi source, which gave an endpoint more like 167.55 keV. These fitted statistical errors are meaningless; clearly, the systematic errors involved in the procedure of extracting a  $\beta$  endpoint from the data must be considerable. It was not the intent of this experiment to minimize the uncertainty in the measured endpoint; this should have very little impact on the sensitivity of the experiment to the spectral features of heavy neutrino emission. The reason the endpoints differ between the two strong source runs is largely due to the different magnetic field configurations surrounding the spectrometer, for the cases of laser on and off. A potential difference between the weak and strong  $^{35}\text{S}$  sources is the precise location of the deposited material on the foil; this could account for the difference in the fitted endpoints between their respective data sets. Any radial displacement of the source strips, compared to the  $^{57}\text{Co}$ , could introduce a momentum offset, thus affecting our knowledge of the absolute value of the transmitted momentum in the spectrometer, introducing a systematic

uncertainty.

Aside from the endpoint, we see that the best fit linear shape term, from all the data sets, comes out to around  $2\text{--}3 \times 10^{-4} \text{ (keV/c)}^{-1}$ . It is interesting that these values are roughly consistent, considering the differences in the data acquisition styles for the wide scan, for the narrow scan, and with the two different cuts in the strong source data. In all the data sets, the data were well fit, with  $\chi^2/\nu \approx 1$ , when just a linear shape correction was included. Only the wide scan data was selected as “requiring” a quadratic free parameter. What could be the reason that the quadratic term was able to improve the fitted  $\chi^2$  value in the wide scan? Perhaps, this was a background subtraction effect. The wide scan data was acquired with the weaker  $^{35}\text{S}$  source and the data points extended close to the endpoint, unlike the narrow scan. It is possible that the uncertainties in the background subtraction and in the background dependence with momentum present themselves as a large effect only near the endpoint, and only for data acquired with the weaker source. The strong source may have a sufficiently enhanced counting rate that the background is relatively unimportant. Thus, it could be that the quadratic parameter, that was included in the wide scan analysis, served to accommodate the uncertainties in the background.

If we consider the four data sets to be independent, as they were each acquired under quite different conditions, we can proceed to average their results. Taking the best fit admixtures deduced from the four data sets, weighting them by their own errors, we arrive at a mean value for the admixture of a 17 keV neutrino of:  $\sin^2 \theta = -0.0005 \pm 0.0014$ , consistent with the absence of a neutrino of this mass. With this result, we can state a 90%

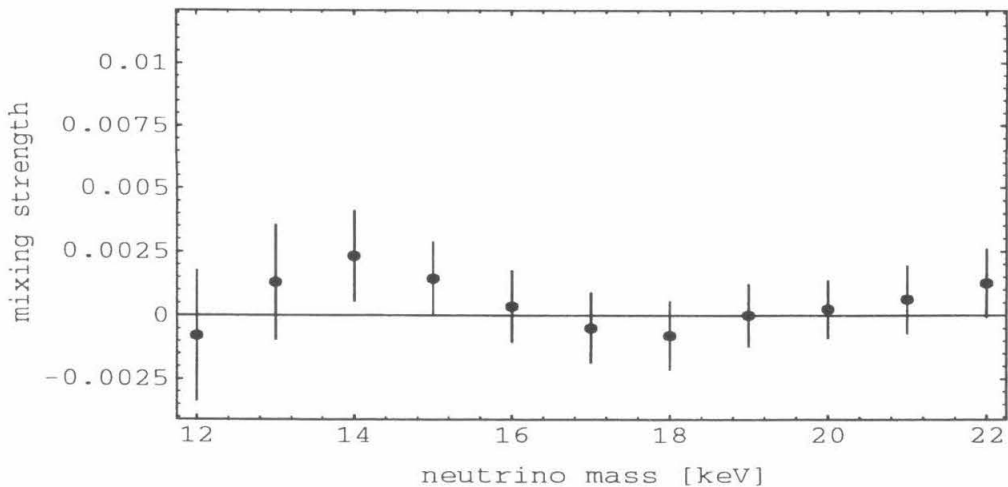


Figure 4.17: Mixing probability versus heavy neutrino mass, as obtained by averaging the fitted results from all four data sets.

confidence level upper limit for the admixture of a 17 keV neutrino of:

$$\sin^2 \theta < 0.0020, \text{ at } 90\% \text{ CL.}$$

The prescription of the Particle Data Group [50], for estimating parameters constrained to lie within a bounded physical region (in this case, we know that  $\sin^2 \theta \geq 0$ ), was employed.

The same analysis in all the four data sets was performed, with the mass of the heavy neutrino fixed at various other values between 12–22 keV. Fig. 4.17 plots the best fit mixing strength deduced by averaging the fitted admixtures, obtained at each mass, from all of the four data sets. Our data is consistent with zero mixing probability across this mass range. In particular, we rule out at the  $6\sigma$  level or greater, a heavy neutrino emitted with a mixing probability of 0.85%, with mass between 16–20 keV.

## Chapter 5

### Demonstration of Sensitivity

In order to demonstrate that magnetic spectrometer experiments are sensitive to the features of heavy neutrino emission, namely the kink produced by the emission of a 17 keV neutrino, an auxiliary measurement was performed. We were able to artificially introduce a kink into the  $^{35}\text{S}$   $\beta$  spectrum, of known size and displacement from the endpoint, by placing an energy loss foil or “mask” in front of the  $^{35}\text{S}$  source in the spectrometer. The mask covered only a part of the source area such that some fraction of the emitted electrons suffered a discrete energy loss upon emerging through the foil.

An aluminum foil strip of thickness 17  $\mu\text{m}$ , and of width 2 mm, was stretched across the center of a second ring (the ones normally spanned by Mylar, for use as source backings). This ring could be placed directly in front of the one holding the  $\beta$  source, with both fastened to the same source positioning assembly. When mounted, the aluminum strip would run perpendicular to the vertical line of the source, across the center; thus, approximately 10% of the 20 mm source length and area would be masked by the aluminum foil. The reason that such a large fraction was selected is that the spectral distortion created by energy loss is somewhat smoother than the kink expected at the threshold for heavy neutrino emission. In addition, some fraction of the electrons incident on the foil are scattered away from the transmission aperture of the spectrometer — some electrons are even

backscattered off the aluminum foil back towards the source. This serves to reduce the overall magnitude of the spectral distortion produced by the foil.

Aside from the magnitude of the artificially induced kink, the amount of the resultant energy loss is important. We find that for a 150 keV electron passing through 17  $\mu\text{m}$  of aluminum foil, the expected minimum energy loss is estimated at 14 keV. Thus, with such an energy loss foil in front of the  $^{35}\text{S}$  source, masking some of its area, we hoped to be able to replicate the distorted shape of a  $\beta$  spectrum possessing a 14 keV heavy neutrino component with roughly 1% mixing strength.

## 5.1 Calibration Lines with the Foil

The first thing to look at would be the shape of the distorted spectrum when the energy loss foil is mounted in front of the  $^{57}\text{Co}$  IC electron source. For a monoenergetic electron, one would expect the effect of the foil to be the creation of a displaced “energy loss peak,” below the monoenergetic full-energy peak, with a characteristic shape given by the *complement* of the energy loss profile for a charged particle passing through a thin absorber (for a discussion of energy loss, see [51], for example). However, with many electron IC lines emitted by the  $^{57}\text{Co}$  source, each having shake-up/off tails, the foil-distorted spectrum turns out to be slightly less ideal to model. Furthermore, from the  $^{57}\text{Co}$  source, gamma emission, rather than internal conversion, is more probable. Thus, there is also a contribution arising from Compton scattered electrons emerging from the aluminum foil, that will also tend to degrade the sharpness of the energy loss response.

Nevertheless, the foil was placed in front of the  $^{57}\text{Co}$  source to view the result. Fig. 5.1 shows the resultant measured electron intensities, with the

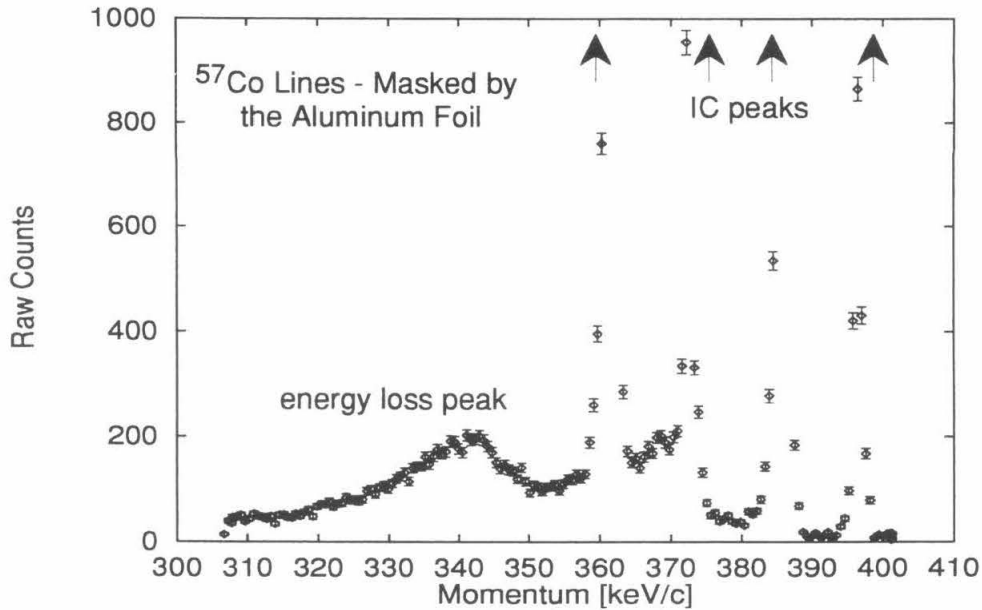


Figure 5.1: Internal conversion lines from  $^{57}\text{Co}$ , with the energy loss foil.

foil in place, over a range of magnetic field values swept by the spectrometer. A displaced energy loss peak does appear in the spectrum. It is shifted by about 13 keV energy below the lowest K-conversion line; its shape is broadened by contributions from the other IC lines. Additional energy loss “edges” appear at higher momenta, corresponding to the displaced energy loss edges from the higher energy lines. The height of the energy loss peak at 342 keV/c is approximately two orders of magnitude down from that of the first K-conversion line — this would be about right to induce the desired amplitude of the artificial kink. To properly determine the complete extent of the energy loss response, integrations over the shapes of all the IC lines would be required. No further analysis of this archetypal spectrum was performed.

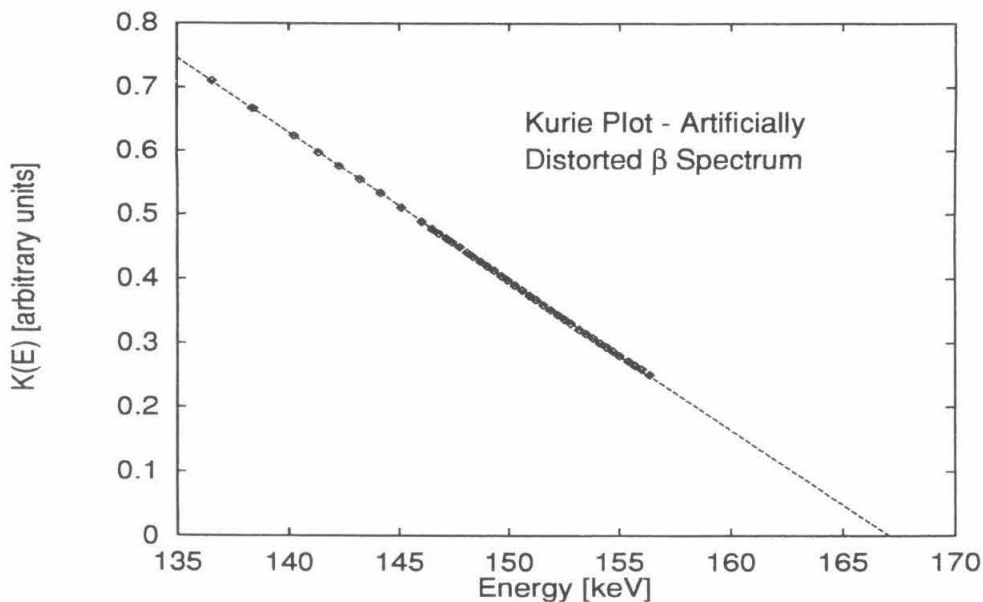


Figure 5.2: Kurie plot of the artificial kink data. Error bars are smaller than the point size. The Fermi correction has not been included.

## 5.2 Observing an Artificial Spectral Kink

The aluminum foil strip was mounted in front of the 7 mCi  $^{35}\text{S}$  source and the magnetic spectrometer acquired data, with this masked configuration, over a short 48 hour run. Momentum points were swept in an identical manner as the wide scan runs. Background subtraction was performed, with the intensity measured above the  $\beta$  endpoint. The processed count rate at each momentum point was extracted using the same analysis code as for the real  $^{35}\text{S}$  data. A Kurie plot of the artificially distorted data is displayed in Fig. 5.2.

The Kurie plot of the binned, artificial kink data shows no gross distortion, proving that it would at least be reasonable to consider further analysis of the data to test the sensitivity of the spectrometer to this small spec-

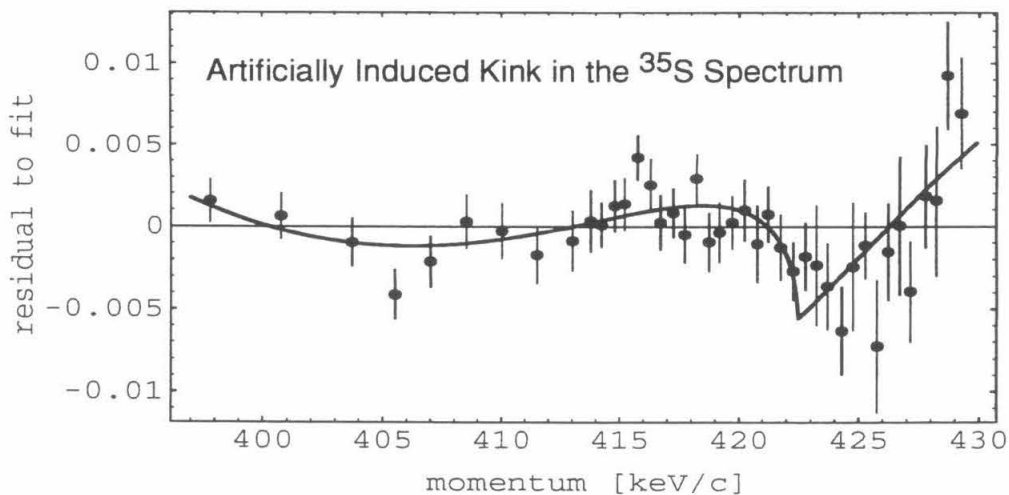


Figure 5.3: Artificial kink induced in the  $^{35}\text{S}$   $\beta$  spectrum. Residuals were determined against the fitted  $\beta$  spectrum without heavy neutrino emission. The solid curve outlines the fitted shape of a spectrum which includes the hypothetical 15.6 keV heavy neutrino identified by the fit, for comparison purposes only.

tral deviation. The extrapolated endpoint from this plot even comes out to roughly the correct value, about 167 keV (the straight line drawn on the Kurie plot was not a fitted result).

We proceeded to fit this data to a  $\beta$  spectrum without heavy neutrino emission. We allowed the linear and quadratic terms of the shape correction to vary freely, with the overall normalization and endpoint, all as free parameters in the minimum  $\chi^2$  fit. Fig. 5.3 plots the residual of our data to the fit (i.e. data/theory  $- 1$ ). A kink-like distortion is visible in the spectrum and was not rendered undetectable, even though linear and quadratic shape factors were included. The fitted  $\chi^2/\nu = 61.9/37$  was poor. It is interesting to re-run the fitting routine, allowing the heavy neutrino admixture and heavy neutrino mass to vary also. There is nothing to be learned from this exercise, other than perhaps to test whether the fitting routine is capable

of converging on its own to reasonable values, when a kink-like structure is actually present in the data. The foil-distorted data is supposed to be similar to, though it is not intended or expected that the data be well fit by, a spectrum including admixed heavy neutrino emission. The fitting routine found a fitted  $\chi^2/\nu = 34.3/35$ , if a heavy neutrino mass of  $15.6 \pm 0.2$  keV with an admixture of  $(2.3 \pm 0.4)\%$  were included in the  $\beta$  spectrum. This exercise demonstrates that the magnetic spectrometer would indeed be sensitive to a spectral distortion similar to that of heavy neutrino emission, regardless of the shape factor.

It is important to point out that the chronological order in which the data sets were acquired do not necessarily correspond to the order in which they have been discussed. In particular, these runs with the artificial kink took place prior to the collection of the strong source data, which made use of a re-instrumented horizontal fluxgate probe and of the field consistency cuts to deal with the laser field disturbances. Here, the collection of the artificial kink data was carried out with the original placement of the horizontal magnetometer and incorporated only the ordinary single-probe magnetic field RMS fluctuation cut, as used in the real data analysis. The artificially-induced kink data were acquired *prior* to the Christmas period during which the narrow scan data were swept.

### 5.3 Analysis of the Spectral Distortion

For the sake of completeness, we attempt to understand the magnitude of the spectral distortion caused by the aluminum foil. In this way, we can know that we simulated a spectral distortion equivalent to a heavy neutrino kink with a mixing probability of about 1%, and that such a spectral structure

would have been detectable by the magnetic spectrometer.

The EGS4 Monte Carlo code [52], ported to FORTRAN-77, was employed to model the transport of electrons through the aluminum foil strip. From the outset, it is worthwhile to mention that the simulation of this energy loss strip is far from trivial. Transmission and scattering effects in the foil must be folded in with aperture and acceptance factors for the spectrometer. Edge effects for the foil strip could give untold trouble. As this is a side calculation, wherein precision is not required, the task at hand is thus to attempt a crude but credible simulation of the energy loss foil.

The two most important effects caused by the aluminum foil mask are: the straightforward energy loss experienced by  $\beta$  electrons emerging through the foil; and the radial-broadening of the source strip due to scattering of electrons, through and out of the aluminum foil, displaced from the vertical line of the true source, due to the perpendicular radial extent of the aluminum strip. Numerous Monte Carlo calculations were run to simulate the energy loss profile and the scattered radial distribution of the emerging electrons, for incident electrons of various relevant energies. Fig. 5.4 displays a sample of the Monte Carlo results.

These Monte Carlo distributions were parameterized for their small energy dependence and were included in the  $\beta$  spectrum fitting routines. A calculated fraction of the  $\beta$  spectrum, corresponding to the Monte Carlo deduced probability for a  $\beta$  electron to strike the foil strip, is triply-convolved: including the spectrometer Gaussian response, the energy loss profile, and the momentum-broadening response due to the radial displacement of the aluminum strip. The remainder of the spectral intensity undergoes the ordinary analysis. The combined spectrum could be used for fitting the data acquired with the foil.

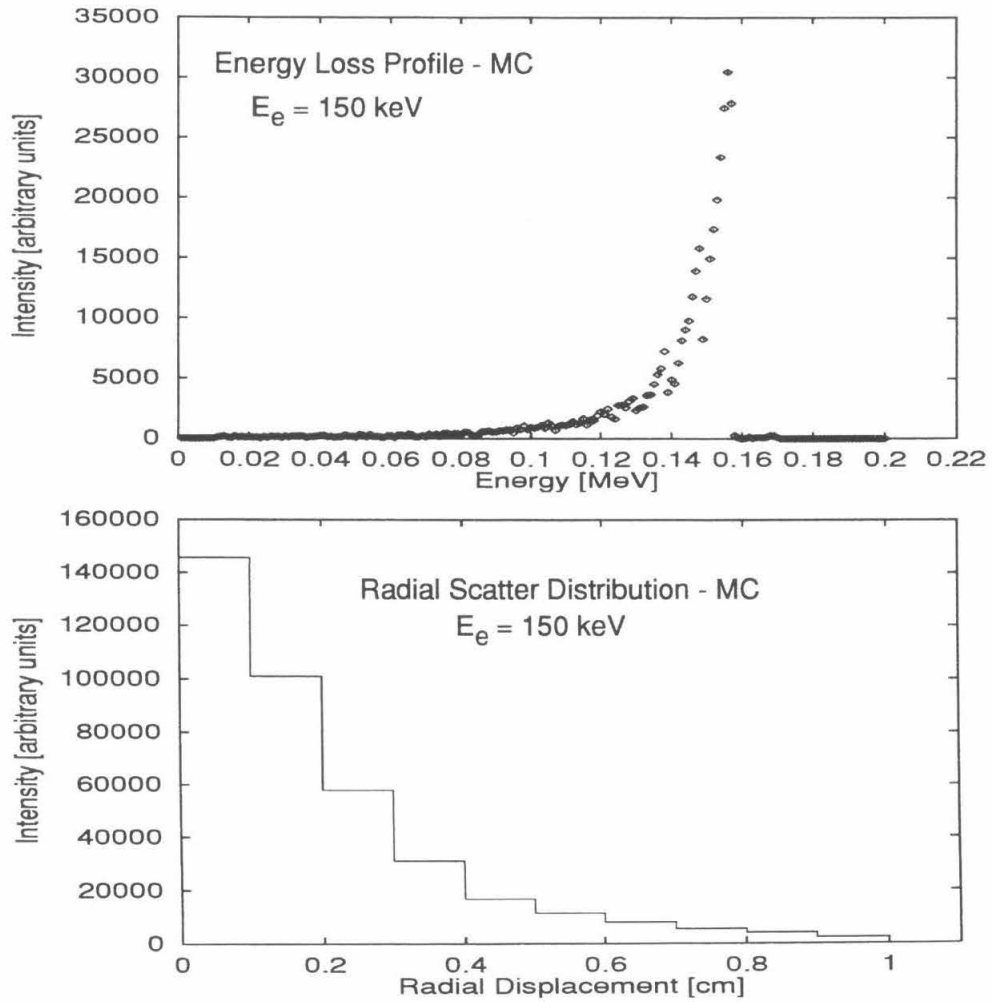


Figure 5.4: Sample Monte Carlo calculations of the aluminum foil strip. The energy loss experience by an electron traversing the foil and its scattered, radial displacement distribution have been calculated.

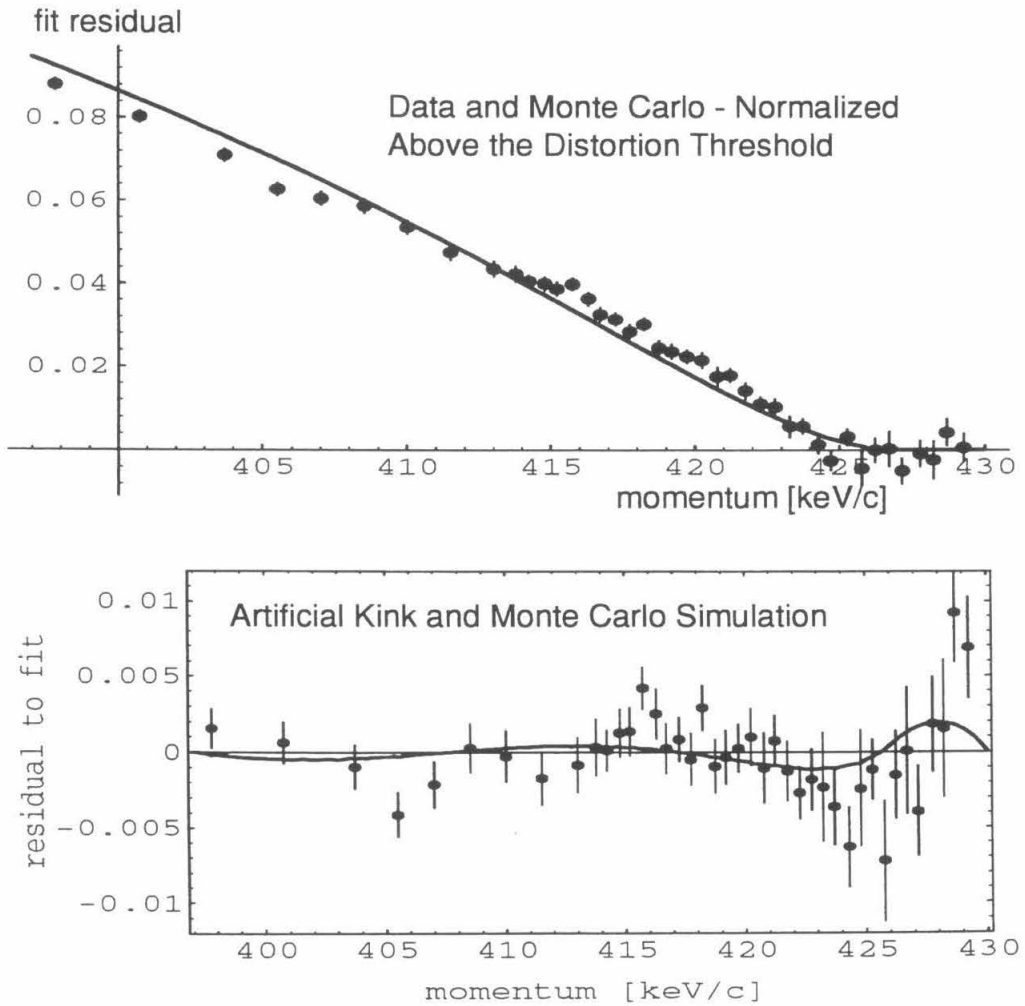


Figure 5.5: Artificial kink with Monte Carlo simulation of the distortion.

Fig. 5.5 shows two plots. The top is a plot wherein the data points above the distortion threshold served to normalize the theoretical spectrum. The remaining data points fall where they may, when the theoretical shape is extrapolated backwards. The solid curve represents the simulated effects of the energy loss foil. This agreement we deem reasonable, as the general behavior of the foil-distorted spectrum seems to be understood. Note that no additional free parameters have been included in the fit, on account of the aluminum foil. In fact, no shape terms were included in this plot. There is no concern that the low momentum data points extend to large residuals as the few points that were used for normalization are not expected to provide an accurate slope or shape, for extending to lower values uncorrected. Below this, the same data versus theoretical spectrum without heavy neutrino, as in Fig. 5.3, is plotted. Here though, the solid curve represents the attempt of the Monte Carlo convolved spectrum to fit the measured data, with linear and quadratic shape parameters included. The overlaid curve exemplifies the marginal agreement that could be achieved. The peculiar extra wiggle in the curve at high momentum is due to the interplay of the shape factors in the fit, at these larger momentum data points, with larger errors.

Based on the Monte Carlo calculated effects of the foil, we estimate that the aluminum strip mask induces a spectral distortion equivalent in magnitude, in a  $\pm 3$  keV region about the distortion threshold, to a 1.5% admixture of a heavy neutrino of mass 14 keV. The fact that our artificially-induced kink data exhibit a distortion that is not removed by the inclusion of free shape factors in the fit is conclusive. The magnetic spectrometer would have seen the spectral distortion, if a heavy neutrino were present in the real data.

## Chapter 6

# The End of the 17 keV Neutrino

### 6.1 Magnetic Spectrometers Retaliate

As the results of this and other experiments were reported, in this the third (now seen as the final) round of experimental activity involving the 17 keV neutrino, it should be noted that magnetic spectrometer experiments answered the call. It was mentioned earlier that magnetic spectrometer experiments could settle the question about the existence of this heavy admixed neutrino, resolving the outstanding issues, if they could either:

- a) provide indisputable statistical precision in data that would be unassailable by critics of the shape factor,
- b) demonstrate their sensitivity to a spectral distortion similar to that of heavy neutrino emission, in spite of the shape factor, or,
- c) explain the origin of the shape correction, showing a good understanding of the instrumental response and applying it to their data.

All three of these requirements were satisfied; it took three new experiments to address each item of this list.

The demonstration of sensitivity to a kink in the  $\beta$  spectrum, provided by this experiment [53], should in fact apply “retroactively” to all previous and concurrent magnetic spectrometer results, assuming comparable or better statistics and proper analysis. It affirms that the inclusion of a shape

correction is acceptable, as it does not eliminate the kink of a heavy neutrino threshold. As a side note, this result was the first, amongst the negative experiments, to confirm sensitivity to the 17 keV neutrino by creation of an artificial kink; there was no effort amongst proponents of the 17 keV neutrino to demonstrate the “smoothness” of their instruments, over their relevant energy regions.

An impressive measurement of the  $\beta$  spectrum of  $^{63}\text{Ni}$  was undertaken at the Institute for Nuclear Study of the University of Tokyo, first reported in [54], with a follow-up, detailed discussion [55]. Their goal was to acquire extremely high statistics data, in a narrow energy region around the expected threshold for emission of a 17 keV neutrino. They employed a 75 cm radius,  $\pi\sqrt{2}$ , iron-free, double-focusing magnetic spectrometer. This beautiful instrument, presumably located far from any local field disturbances, possesses three sets of Helmholtz coils (east-west, north-south, and up-down) that were employed to cancel the external magnetic field and its fluctuations down to the 1 nT level! Their momentum resolution was set at 0.2% for this measurement.

A thin, but high intensity  $^{63}\text{Ni}$  source was prepared, with activity of 580  $\mu\text{Ci}$  and dimensions of  $4\times 20\text{ mm}^2$ . They used a 30-cell, multi-window, proportional wire chamber to detect the focused  $\beta$  electrons. The entrances to the independent proportional chambers were covered by a thin 1.5  $\mu\text{m}$  polyester film.

They performed a careful measurement of the detector response function with a  $^{109}\text{Cd}$  IC electron source. Attention was paid to the window transmission and discrimination in their detector chambers (comparable, in our case, to the Si detector noise threshold).

An interesting approach was taken in the scanning of the spectrum, targeting the threshold and the endpoint regions separately. This allowed the interplay of the shape terms (there were 30 parameters, one for each detector chamber, all with values of a few  $10^{-4}$  (keV) $^{-1}$ ) and admixture values with the endpoint and background to be reduced somewhat in their analysis.

The discussion of the quality of their data, presented in [55], showed excellent consistency. The data exhibited only statistical fluctuations in the count rate. Their measurement was very convincing and their statistics were unmatched, benefiting from the lower Q-value of  $^{63}\text{Ni}$  decay, compared to  $^{35}\text{S}$ . Their data are illustrated in Fig. 6.1. They quote a best fit admixture for a 17 keV neutrino of  $\sin^2 \theta = (-0.011 \pm 0.033 \pm 0.030)\%$ , consistent with zero, and decisively ruling out an admixture at the 0.85% level. They quote an upper limit of  $\sin^2 \theta < 0.073\%$ , at the 95% confidence level.

It is interesting, from the sociological point of view, that even after this seemingly overwhelmingly negative result was first reported, the 17 keV neutrino question in the physics community still remained unresolved. Many disregarded this experiment, simply because the data were acquired with a magnetic spectrometer, as though that alone were sufficient to invalidate the result. How tragic it was that after concerns of the shape factor had been countlessly overstated, many took it to heart by dismissing magnetic spectrometers without care for the subtle experimental difficulties also present in semiconductor measurements, being unable, ultimately, to judge each experiment for its own merit!

A nice study was performed by the Princeton group, to address the third item on the list. Their original 1985 experiment [30], possessed linear and quadratic terms in the shape correction. It was demanded by critics of the shape factor that the origin of this imperfect response be understood and

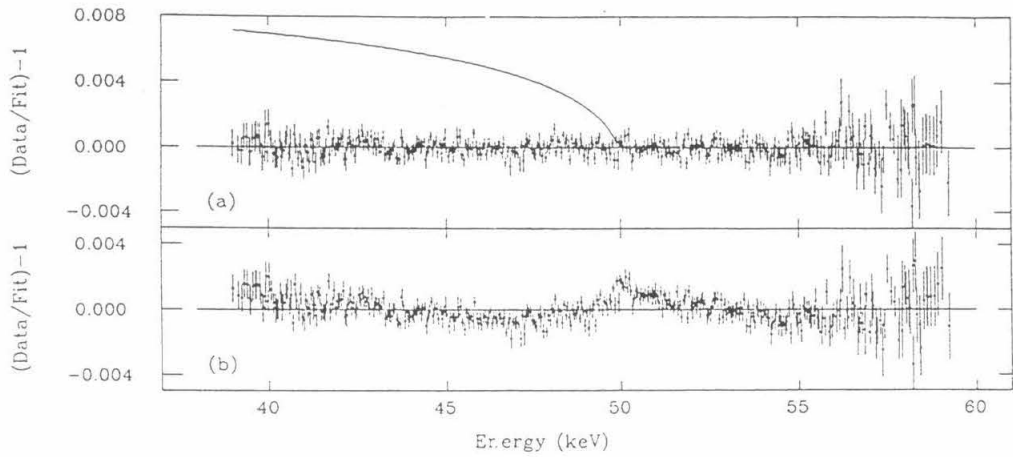


Figure 6.1: Data from the Tokyo INS  $^{63}\text{Ni}$  experiment. Above, the data are plotted for the best global fit, with an admixture consistent with zero. The solid curve illustrates the size of a 1% admixture, normalized above 50 keV. The plot below is an attempted fit to the data, with the admixture fixed at 1%.

explained. A re-analysis of this data [56], was performed in which two additional issues, important to the instrumental response, were addressed. First, detailed modeling of the focal point detector was carried out. A realistic EGS4 Monte Carlo study improved upon the earlier simplistic treatment of the backscattered component in the detector, lost below the noise threshold. This Monte Carlo was successful in reproducing the shape and energy dependence of the detector backscattered tail and could be used to account for the detected electrons, lost below the noise. A second correction was invoked for the energy-dependent steering of  $\beta$  electrons, caused by imprecisely-cancelled transverse magnetic fields in the spectrometer (components of the Earth's field). These are examples of two sources of instrumental response, that were discussed earlier in this thesis as being the origin of the shape factor.

Their 1985 data set was re-analyzed and the resultant data set could be fit to an ordinary  $\beta$  spectrum, without requiring any shape correction. The shape factor had been understood and could be eliminated. From the re-analyzed data, they could exclude the 17 keV neutrino, with a mixing strength of 0.85%, at the  $7\sigma$  level; when they chose to allow a linear shape term, of magnitude  $(-0.6 \pm 2.2) \times 10^{-5} (\text{keV})^{-1}$ , and even a quadratic term in their fits in order to be conservative, a statistical exclusion of  $5\sigma$  was the result, confirming the old conclusions. The re-analyzed data are plotted in Fig. 6.2 and the flatness of the new shape factor is readily apparent, compared to Fig. 2.2.

A new  $^{35}\text{S}$  measurement was completed by the Princeton group [57], employing the same improved analytical techniques from [56]. The new data finds a best fit 17 keV neutrino admixture of  $(0.01 \pm 0.15)\%$ ; this result also excludes the 0.85% admixture, claimed by Hime and Jelley, at a greater than  $5\sigma$  statistical level.

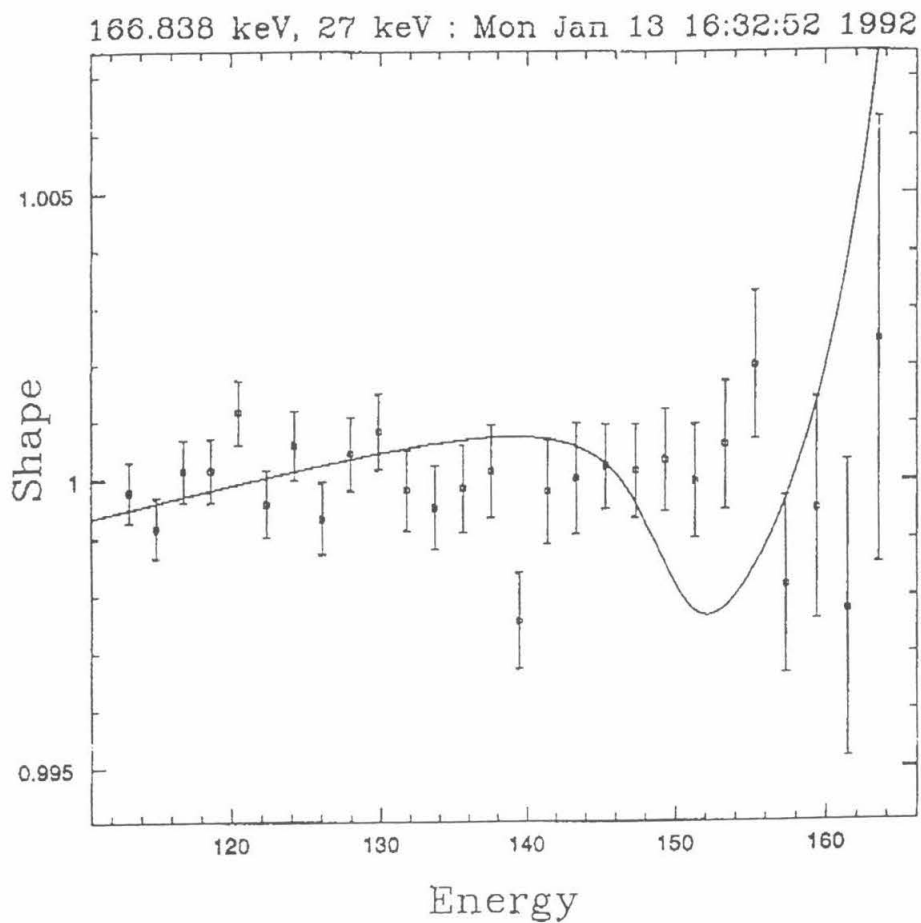


Figure 6.2: Re-analyzed data from the Princeton 1985  $^{35}\text{S}$  measurement. The flatness of the new shape is commendable. The solid line is the fit for a 17 keV neutrino with 0.85% admixture.

## 6.2 Results from Other New Experiments

A number of new results were reported during this heightened period of experimental interest. A sample of these experiments will be discussed below. Each of these experiments featured instruments that belonged neither to the magnetic spectrometer, nor the conventional semiconductor detector mold.

Mortara et al. undertook a search for the 17 keV neutrino [58], using an apparatus which employed a Si(Li) detector placed within a superconducting solenoid. The profile of the axial magnetic field in this device was such that the source sat at the peak of the magnetic field strength, and the detector resided at a position in the solenoid with a much lower field. As such, electrons emitted from the source at large angles, travelling along helical trajectories to the detector, find the angle between their velocity and the solenoid axis decreases as they propagate into the decreasing magnetic field region. Thus, this configuration provides for a solid angle acceptance of roughly  $2\pi$ , with the strong advantage that no collimators or apertures are required, even though a large fraction of the electrons strike the detector at near normal angles of incidence.

In addition to this effect of the magnetic field guiding the incident angles of the electrons toward the normal, a magnetic mirror effect was also exploited. Some electrons which manage to backscatter from the detector at certain angles, in propagating back towards the high field strength region, are reflected again, back to the detector, at a magnetic mirror point reached before making it all the way back to the source. This gives these reflected electrons another chance at depositing their energy into the detector, further enhancing the full-energy peak in the response of the Si(Li) detector, and minimizing the backscattered tail component. The apparatus employed in

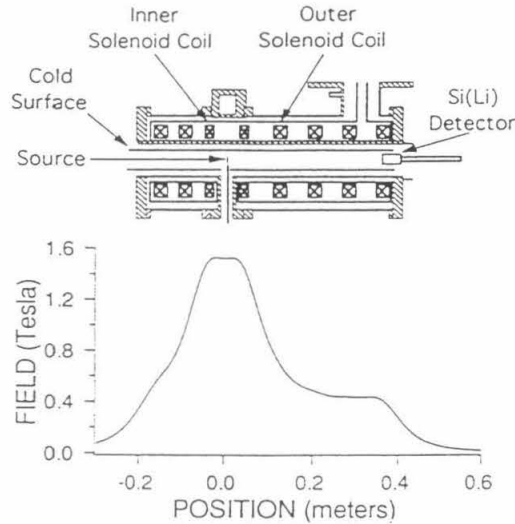


Figure 6.3: Apparatus of Mortara et al.

this experiment is shown in Fig. 6.3.

With this clever device, they measured the  $\beta$  spectrum of  $^{35}\text{S}$  with the Si(Li) detector. The measured backscattered tail in their detector response was less than 7% of the total incident intensity (measured with a  $^{139}\text{Ce}$  conversion line). Their data could be fit to an ordinary  $\beta$  spectrum, without any shape corrections. They report a best fit mixing probability of  $\sin^2 \theta = -0.0004 \pm 0.0008 \pm 0.0008$ , consistent with zero. Their data are presented in Fig. 6.4.

This experiment performed a convincing demonstration of its sensitivity to an artificially created distortion in the  $\beta$  spectrum, similar to that expected from heavy neutrino emission. In a secondary measurement, they prepared a mixed source of  $^{35}\text{S}$  and  $^{14}\text{C}$ , wherein the activity of the  $^{14}\text{C}$  was 1.34% of the total.  $^{14}\text{C}$  has a  $\beta$  endpoint at about 156 keV, compared to that from  $^{35}\text{S}$  of 167 keV. Thus, the presence of a small, second  $\beta$  spectral shape, displaced by 11 keV, should resemble the situation in which a massive neutrino is emitted

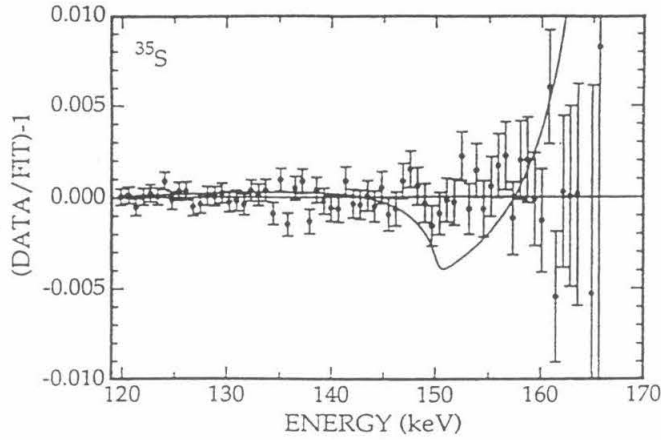


Figure 6.4: Data from Mortara et al. The solid curve represents the expected shape for a 17 keV neutrino with  $\sin^2 \theta = 0.85\%$ .

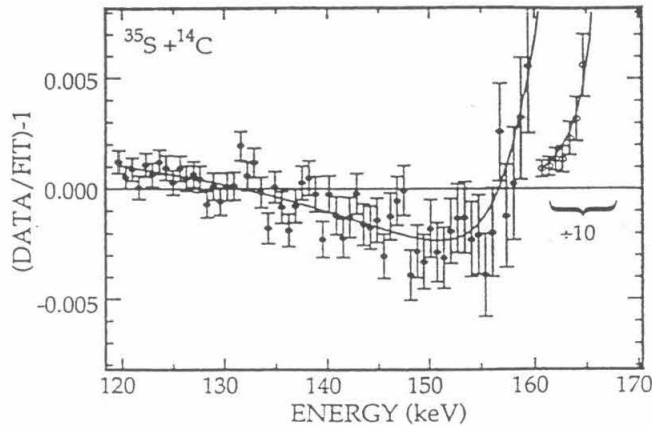


Figure 6.5: Artificial kink from  $^{35}\text{S}$  and  $^{14}\text{C}$ , fit with just the  $^{35}\text{S}$  shape. The solid curve represents the expected shape when both components are included in a fit, in agreement with the expected fraction prepared.

with about 1% probability. The measurement of this mixed  $\beta$  spectrum, displayed in Fig. 6.5, demonstrates that this experiment had the sensitivity to see a kink from heavy neutrino emission.

In retrospect, this mixed source appears to be a superior method of inducing a kink in an otherwise smooth  $\beta$  spectrum, than the use of an energy loss foil. The complexities of electron transport through our foil geometry limited our understanding of the artificial distortion. With a known mixture, prepared into the source, our demonstration of sensitivity would have been more straightforward.

With regards to the situation in  $^3\text{H}$ , the original  $\beta$  emitter in which an excess of counts at low energy was reported by Simpson, new measurements of its  $\beta$  spectrum were performed by Bahran and Kalbfleisch, using a proportional chamber (first reported in [59], with an extension discussed in [60]). In the case of  $^3\text{H}$ , where 17 keV is relatively far below the endpoint, the experimental challenge was never statistical accuracy, but rather one of a careful understanding of all possible effects, atomic and instrumental, that occur in this low energy range.

At such low energies, it is quite a feat to perform these proportional chamber measurements well. In this study, the backgrounds from tritium adsorbed to the chamber walls were handled carefully. This measurement did in fact collect greater statistics than Simpson's original data or the later experiment of Hime and Simpson, for what it's worth. They quote an upper limit for the admixture of a 17 keV neutrino of:  $\sin^2 \theta < 0.28\%$ , at the 99% confidence level, taken from their more recent analysis. Their data are displayed in Fig. 6.6.

Up until this point, I have carefully avoided discussing the searches for the 17 keV neutrino which looked at the internal bremsstrahlung spectra

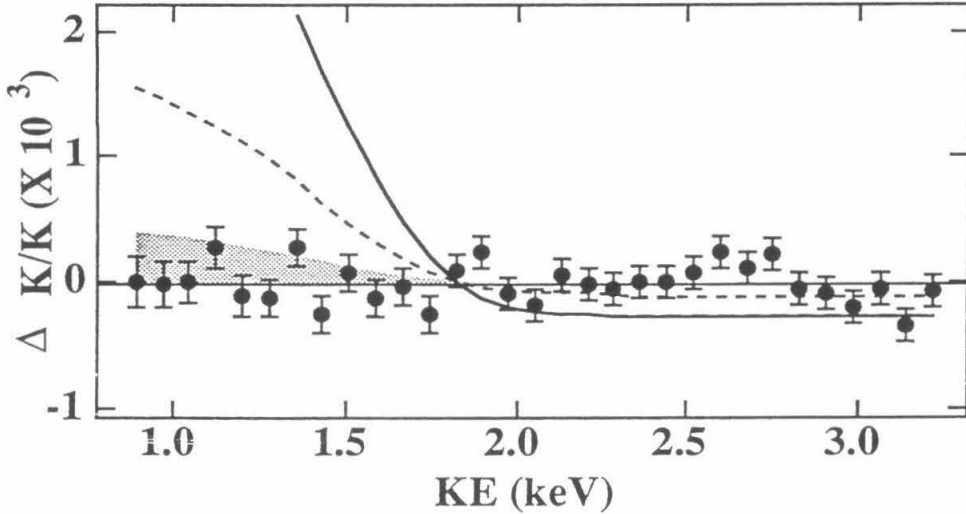


Figure 6.6: Proportional counter  ${}^3\text{H}$  data. The solid curve outlines Simpson's original shape, the dashed line is from Hime and Simpson's result and the shaded region is at the excluded limit of 0.28% mixing strength.

from the electron-capture decay of several nuclei, in lieu of a  $\beta$  spectrum. Venturing into this style of experiment was a journey fraught with peril, wherein results which confirmed the 17 keV neutrino [43], accompanied other results, from the same individuals, that excluded it [61]. Recent searches in IBEC, motivated by the 17 keV neutrino fervor, turned up a  $21 \pm 2$  keV neutrino in the decay of  ${}^{55}\text{Fe}$  [62] and also a  $13.8 \pm 1.8$  keV neutrino, from the IBEC of  ${}^{71}\text{Ge}$  [63]. The situation with IBEC was certainly confusing, to say the least!

Improved IBEC experiments with higher statistics were completed and these should be listed along with the other new results that came during this period, from  $\beta$  decay. In particular, a detailed, high statistics study of  ${}^{55}\text{Fe}$  [64], by the same group that had earlier seen some effect, ruled out a 17 keV neutrino admixture of 0.8%, at the  $7\sigma$  level. This IBEC measurement analyzed second derivatives of their spectrum, which was a nice tool to use,

Experiment	Source	Technique	$\sin^2 \theta$ , $m_H = 17$ keV
Kawakami et al.	$^{63}\text{Ni}$	magnetic	$< 0.00095$ 95% CL
Bahran and Kalbfleisch	$^3\text{H}$	prop. chamber	$< 0.004$ 99% CL
Chen et al.	$^{35}\text{S}$	magnetic	$< 0.002$ 90% CL
Mortara et al.	$^{35}\text{S}$	Si(Li) solenoid	$< 0.002$ 95% CL
Berman et al.	$^{35}\text{S}$	magnetic	$< 0.002$ 90% CL
Ohshima et al.	$^{63}\text{Ni}$	magnetic	$< 0.00073$ 95% CL
Kalbfleisch and Bahran	$^3\text{H}$	prop. chamber	$< 0.0028$ 99% CL
Wietfeldt et al.	$^{55}\text{Fe}$	IBEC	0.8% excl. at $7\sigma$
DiGregorio et al.	$^{71}\text{Ge}$	IBEC	1.6% excl. 99% CL

Table 6.1: Results from new experiments that reject the 17 keV neutrino hypothesis. The  $^{63}\text{Ni}$  and  $^3\text{H}$  results have each been reported twice, with improved limits published in the later report.

being sensitive to spectral discontinuities. Separately, the previously reported  $^{71}\text{Ge}$  result, which saw an effect at 13.8 keV, was revised [65] by including contributions from the 3s subshell that corrected for this discrepancy. Their new result excludes Zlmen's observation of a 17 keV neutrino in  $^{71}\text{Ge}$ , at the 99% confidence level.

Table 6.1 provides a summary of the reported findings of all of these new experiments. Taken together, it was clear that the 17 keV neutrino claim was decisively and indisputably rejected.

### 6.3 Retraction of Positive Claims

It was identified by Piilonen and Abashian, from their Monte Carlo studies of source and slit scattering in the Oxford experiment, that distortions might be present in the Oxford data, at significant levels [66]. Though the statistical significance of the kink is strong in the Hime and Jelley  $^{35}\text{S}$  data, this is owing, in part, to the assumption that the electron response function was perfectly understood in the experiment and that no unknown distortions were

present. In light of the Monte Carlo studies, it appears that this assumption might not be valid — allowance could be made for residual response effects, which remain uncorrected, by the inclusion of free shape parameters. The price one pays for the inclusion of a shape correction is statistical precision; conversely, the lack of shape parameters, able to accommodate for unknown smooth distortions, results in exaggerated statistical significance.

Faced with this array of new evidence against the 17 keV neutrino, Hime proceeded to re-analyze [67] the Oxford  $^{35}\text{S}$  and  $^{63}\text{Ni}$  data. He took the hint from Piilonen and also from the Mortara experiment, which employed no collimators or slits, and examined small scattering effects that previously had not been considered. He discovered, through Monte Carlo studies of his own, that an aluminum baffle present in his apparatus provides a possible path into his detector (see Fig. 2.7). Roughly 1% of the electrons that strike the detector originate from electrons that scattered from the baffle. The energy lost by electrons, going from source-baffle-detector, making this glancing incident scatter, creates a low-energy peak in the electron response function. Such a secondary-peaked response could create a distortion similar to heavy neutrino emission, if uncorrected.

When Hime looked for this in his measured internal conversion lines, he was able to confirm that such a low-energy peak was indeed present in the measured response function, buried beneath larger contributions from energy loss and backscattering tails. How these were missed previously is not an issue for speculation; rather, it is a fact that the other components in the response were sizable and this small contribution could have been lost therein. Thus, it becomes apparent that free shape correction parameters really should have been included in the analysis, to accommodate for just these sorts of small uncertainties remaining in the response.

When the scattering from the baffle was properly treated and the data corrected, the  $^{35}\text{S}$  and  $^{63}\text{Ni}$  measurements taken at Oxford no longer showed any sign of heavy neutrino emission. Hime even quotes limits on the heavy neutrino admixture, from the re-analyzed data.

In this same discussion [67], Hime comments on the  $^{35}\text{S}$  measurements performed at Guelph [35]. This apparatus did not possess any baffles or apertures, but it did possess a significantly larger backscattered tail. This lack of baffles does not mean that the amount of scattering is reduced; in fact, the opposite is true. Electrons could scatter from the “effective aluminum baffle housing the detector” and the absence of collimation allows for many scattering sites (i.e. one is not limited to analysis and correction for just one set of baffles). It becomes easily conceivable that hidden, uncorrected components in the low-energy response lie buried under the enormous low-energy tail that is a consequence of a diffuse geometry instrument.

The interesting  $^{14}\text{C}$  experiment, in which the source was implanted in the Ge detector, was immune to scattering effects presumably, and they cited a different explanation of why they had mistakenly reported a heavy neutrino kink [68]. Systematic effects, such as cross-talk and other factors, between the main detecting body of the Ge crystal, and a surrounding active guard ring, manifested themselves as a heavy neutrino-like distortion! The concern with this detector is for electrons that deposit energy too close to the edges of the active volume; their full energy might not be contained and the feature of total calorimetry would be lost. Thus, surrounding the active central volume, a guard ring could be used to veto events which deposited energy there. Problems existed with operations of the guard ring as a veto. It was found that energy could be deposited there without the ring firing the veto. Thus, events were recorded in the original data set, in which electrons had not

deposited their full energy. These electronic effects conspired, astonishingly, to create a false 17 keV neutrino! Further details explaining the solution to these difficulties and the presentation of new data collected that were not prone to these problems, are awaited from this group.

As such, the significant positive claims of a 17 keV neutrino were retracted. Only the  $^3\text{H}$  results, with their inherent atomic and instrumental difficulties, remain unexplained. It was noted by Bahran that in 1959, Conway and Johnson [69] observed a spectral excess of magnitude 1%, at about 1 keV energy in the  $^3\text{H}$   $\beta$  spectrum. They attributed the excess to a possible non-linearity in the response of their proportional chamber at low electron energies.

The large dependence of the fitted mixing strength on the screening potential, cited in [26], allows for quite a broad range of acceptable values. Additionally, the exact extent of the damage suffered by a crystal during the ion implantation process is unknown. Thus, even an ordinary explanation for the spectral excess, such as non-linearities in the detector response, could be applied to the Simpson and Hime results also, and it wouldn't be completely unreasonable. Regardless, the 17 keV neutrino issue had reached its end.

## 6.4 Conclusions

The 17 keV neutrino saga closes with a historical note, just as it had opened with one. It has been known for 60 years (since 1934) [70], that the Kurie plots of measured  $\beta$  spectra were not as straight as expected by theory. In particular, excesses were seen at lower energies in the spectrum — see, for example, Fig. 9.4 in Krane's introductory nuclear physics textbook [7], which displays a Kurie plot containing in the caption “The deviation from

the straight line at low energy arises from the scattering of low-energy electrons within the radioactive source.” At the time though, this excess was interpreted as potentially indicating that Fermi’s theory of  $\beta$  decay [8] was incomplete. There was even a proposed revision of the theory by Konopinski and Uhlenbeck [71], to account for the observations. A great deal of careful experimental work ultimately deduced that these excess counts at low-energy resulted from energy loss and scattering, in the source and the detector.

In the modern history of  $\beta$  decay, these low-energy excess counts surfaced as an issue again. This time, however, they were attributed to the emission of a 17 keV neutrino. Scattering turned out again to be the culprit. It had been maintained all along by some [72], that scattering was the explanation for the spectral distortions measured by Hime; it took this new round of experiments to convince the physics community that the massive neutrino hypothesis was incorrect and that a more mundane origin for these distortions be considered.

It is perhaps a little too simplistic to attribute the entire situation to scattering alone. The nature of the instruments that measured the  $\beta$  spectra is important to bear in mind. In a semiconductor detector, when scattering (or other response distortions) occurs, intensity at one value of energy is mistakenly transferred into intensity at another locus. In contrast, a magnetic spectrometer features, as pointed out earlier, dispersion and detection processes unrelated to each other. Thus, if uncorrected scattering were to occur (aside from inside the source substrate) say at the detector, intensity would be lost at that value of energy, but it would not be coupled to another point in the spectrum. Magnetic spectrometer experiments are, in this aspect, inherently less susceptible to these difficulties than a semiconductor detector.

Compounding this problem, a semiconductor detector accumulates counts

over the entire spectrum simultaneously. This can certainly be viewed as an advantage; it should be mentioned, though, that the resultant data will, as a consequence, always possess much greater statistical accuracy at low energy than at high. Thus, the statistical analysis will always be strongly biased to the low-energy data points and it is precisely this portion of the data which is most susceptible to scattering and other low-energy, response function uncertainties which must be integrated from these lower values all the way up to the endpoint.

Some new things were learned and some things re-learned, during this period of heightened interest in  $\beta$  decay. The 17 keV neutrino was convincingly refuted by this and other measurements and new limits were set on the emission of a heavy neutrino in nuclear  $\beta$  decay, in a mass range of 10-25 keV. The search for neutrino mass and mixing must wait for new evidence to be presented, with the eager anticipation that a finite neutrino mass will again surface.

## **Part II**

# **Fast Neutron Backgrounds for the San Onofre Neutrino Detector**

## Chapter 7

# A Detector for Neutrino Oscillations

### 7.1 Physics of Neutrino Oscillations

The phenomenon of neutrino oscillations is an interesting consequence of the physics of neutrino mass and mixing. Once again, parallels can be drawn to the observations of this behavior in the quark sector of the Standard Model, for comparison. In 1955, Gell-Mann and Pais [73] proposed the idea that, due to the Cabibbo mixing observed amongst the mesons, the neutral kaon, while propagating freely through space, could change into its anti-particle. Such an effect, purely quantum mechanical in nature and possible only for neutral particles, leads to “oscillations,” and was applied by Pontecorvo [74] to the leptons, where he was first to propose, in 1957, that neutrinos and antineutrinos could undergo similar oscillations. Later, when the presence of different neutrinos flavors was confirmed, Pontecorvo [75] and others [76] extended these ideas to oscillations amongst the different flavors of neutrinos, including lepton family number non-conservation.

If we recall equation (1.3), which expresses the mixing between neutrino flavors,

$$\nu_l = \sum_{i=1}^3 U_{li} \nu_i, \quad (7.1)$$

where  $\nu_i$  are the mass eigenstates and  $\nu_l$  are the flavor weak eigenstates, and if we consider again a two-component simplification, we can express two of

the weak neutrino eigenstates in terms of mass eigenstates:

$$\nu_e = \cos \theta \nu_1 + \sin \theta \nu_2 \quad (7.2)$$

$$\nu_\mu = -\sin \theta \nu_1 + \cos \theta \nu_2. \quad (7.3)$$

The mass eigenstates,  $\nu_1$  and  $\nu_2$  propagate in time as:

$$|\nu_1(t)\rangle = e^{-iE_1 t} |\nu_1(0)\rangle \quad (7.4)$$

$$|\nu_2(t)\rangle = e^{-iE_2 t} |\nu_2(0)\rangle. \quad (7.5)$$

As a result, a pure eigenstate of an electron neutrino (for example), created at time  $t = 0$ , will evolve at time  $t$ , into

$$|\nu_e(t)\rangle = \cos \theta e^{-iE_1 t} |\nu_1(0)\rangle + \sin \theta e^{-iE_2 t} |\nu_2(0)\rangle \quad (7.6)$$

$$\begin{aligned} &= (e^{-iE_1 t} \cos^2 \theta + e^{-iE_2 t} \sin^2 \theta) |\nu_e(0)\rangle + \\ &\quad \cos \theta \sin \theta (e^{-iE_2 t} - e^{-iE_1 t}) |\nu_\mu(0)\rangle. \end{aligned} \quad (7.7)$$

At this time  $t$ , the probability of detecting this mixed neutrino state as a muon neutrino,  $\nu_\mu$ , is the square of the amplitude in (7.7), i.e.,

$$|\langle \nu_\mu | \nu_e(t) \rangle|^2 = \frac{1}{2} \sin^2 2\theta \left[ 1 - \cos \frac{m_2^2 - m_1^2}{2p_\nu} t \right], \quad (7.8)$$

where  $m_1$  and  $m_2$  are the masses of the two neutrino eigenstates, and where

$$E_i = \sqrt{p_\nu^2 + m_i^2} \approx p_\nu + \frac{m_i^2}{2p_\nu}$$

has been substituted, assuming the common neutrino momentum,  $p_\nu$ , is much larger than the neutrino masses. From (7.8) we see how the nomenclature

of this phenomenon originated. The probability for such a mixed neutrino state to appear as a specific flavor eigenstate oscillates as the neutrino propagates freely, without interaction. This behavior is typical of any quantum mechanical interference effect.

Expression (7.8) is frequently re-written in terms of the distance travelled by the neutrino, as opposed to the time. Inserting common units into this expression, we can write the oscillation probability as

$$P(\nu_l \rightarrow \nu_{l'}) = \sin^2 2\theta \sin^2 \frac{1.27 \times \Delta m^2 [eV^2] \times L [m]}{E_\nu [MeV]}, \quad (7.9)$$

where the parameter,  $\Delta m^2 = |m_2^2 - m_1^2|$ , is in units of  $eV^2$ , and the distance travelled,  $L$ , is in meters. The description of neutrino oscillations is often characterized by these two parameters, the mixing angle,  $\sin^2 2\theta$ , and the mass difference,  $\Delta m^2$ .

Various experiments have searched for evidence of neutrino oscillations, using neutrinos and antineutrinos from accelerators and reactors; an overview of these experiments and their results is contained in [16]. So far, no evidence for neutrino oscillations has been found and regions of oscillation “parameter space” have been excluded (see [16]) by these experiments.

## 7.2 Experimental Motivation

Enticing results have been presented from deep underground experiments which hint at the possibility of neutrino oscillations. Two exciting experimental observations, which developed from the detection of neutrinos of completely different origins, suggest that neutrino mass and mixing may indeed be present.

The detection of solar neutrinos, since 1970 in the Homestake Mine chlo-

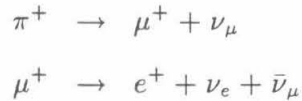
rine experiment [77], first identified a potential discrepancy between the measured solar neutrino capture rate and the rate predicted by the so-called Standard Solar Model (SSM) [78]. The deficit of neutrinos was large; only 30% of the predicted neutrino rate was observed in this experiment, which continues to take data. This observation was corroborated by the Kamiokande experiment [79], which observes the interaction of solar  $\nu_e$  scattering off electrons in a water Čerenkov detector, with unmistakable solar origin. This experiment reports observing 46% of its anticipated flux.

Recently, results from two gallium radiochemical experiments have been reported. The flux deficit measured by the SAGE [80] and GALLEX [81] experiments is also large; the gallium neutrino reaction probes a low-energy region of the solar neutrino spectrum that is insensitive to allowable variations in the SSM. Taken all together, it is difficult to reconcile these results with the model calculations, unless new physics is postulated. Whether this is due to some effect of astrophysical origin or due to some previously unknown and interesting properties of the emitted solar neutrinos is the central question.

Many have suggested (among them [82]), that the deficit of solar neutrinos, referred to as “the Solar Neutrino Problem” might arise from oscillations of neutrinos, from the electron-type, into some other flavor which existing experiments do not detect. Included in these considerations is an effect arising from neutrinos propagating through matter, known as the MSW effect after its originators [83, 84], which could be potentially very important for neutrinos of solar origin. The presence of electrons in ordinary matter affects the propagation of neutrinos of mixed flavor eigenstates, as the electron-flavor components possess additional charged-current weak interactions with electrons in matter, as opposed to the other flavors which can only interact via

the neutral current. The MSW effect finds that this modification for passage through dense matter allows for the resonant conversion of solar neutrinos, produced as electron-type, into another flavor, effectively depleting the flux of detectable electron neutrinos emerging from the Sun.

A second hint of neutrino oscillations comes from the detection of neutrinos which originate from cosmic ray interactions in the atmosphere. High energy cosmic rays produce pions in the atmosphere. Greatly simplified, the pions decay in the following sequence:



where the  $\pi^+$  was used as an example and charge conjugation provides the decay sequence for  $\pi^-$ . The flux ratio of muon neutrinos (and antineutrinos) versus electron neutrinos is thus approximately 2:1. If neutrino oscillations were present and significant, the flux ratio of the atmospheric neutrinos, arriving at an underground detector, could be different than this predicted value.

Two experiments have published results which report a substantial anomaly in the atmospheric neutrino ratio [85, 86]. The measured flux ratio between  $\nu_\mu/\nu_e$ , compared to the theoretical ratio calculated by [87] (as an example), was observed to be about 60% of the expected value, in both experiments. Many have suggested that neutrino oscillations could account for this deficit of muon neutrinos. The oscillations could be between muon and tau neutrinos, resulting in the depletion of some of the muon neutrino flux, or, the oscillations could be mixing muon and electron neutrinos, again changing the flux ratio between the two.

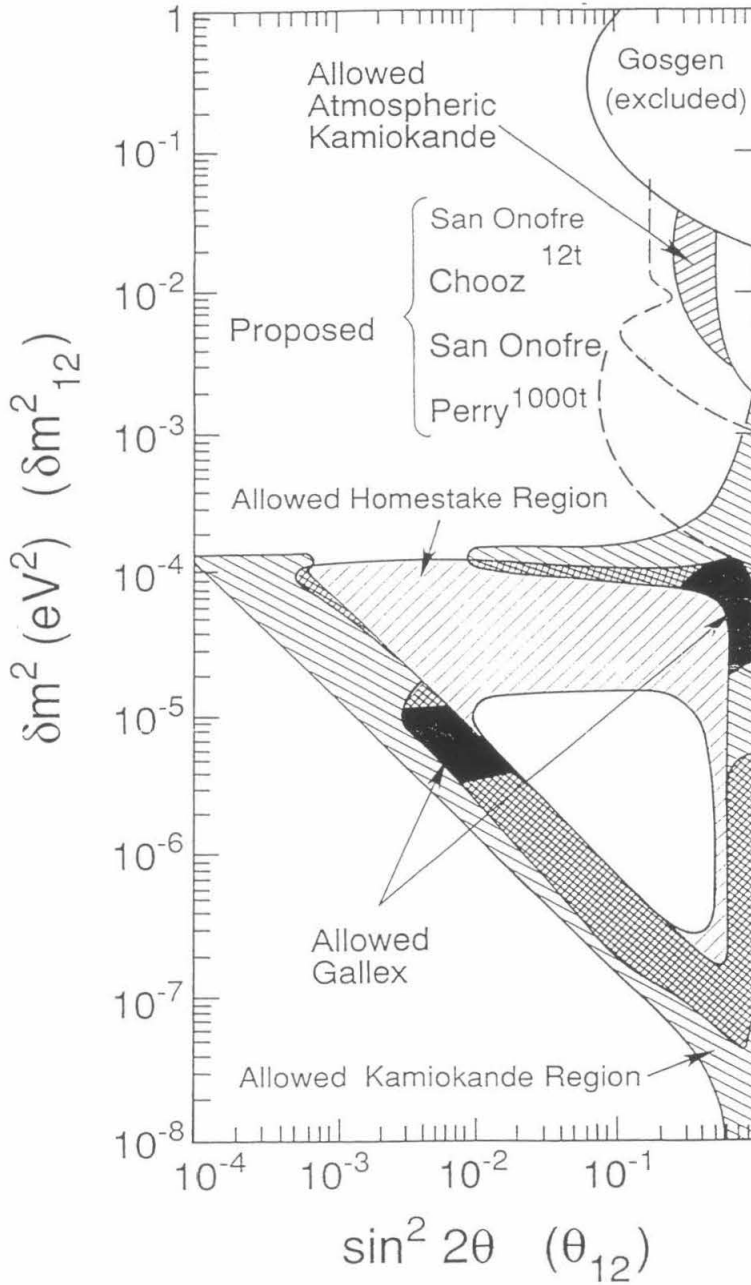


Figure 7.1: Oscillation parameter space for  $\nu_e$ , allowed and excluded, from [16]. The regions suggested by the atmospheric and solar neutrinos are shown hatched.

The regions in oscillation parameter space suggested by the Solar Neutrino Problem and the atmospheric neutrino anomaly are illustrated in Fig. 7.1. Also shown in this plot is the region of parameters excluded by the Gösgen reactor neutrino oscillation experiment [88].

When one performs a reactor-based neutrino oscillation experiment, one is conducting what is known as a “disappearance” experiment. That is to say that since one can know the expected flux of electron antineutrinos emanating from a reactor, by attempting to measure it, one can search for any deficit in this flux, caused by neutrino oscillations. Reactor-based experiments are sensitive to oscillations between electron antineutrinos and everything else, including oscillations to the muon-type. Thus, a reactor-based experiment could explore the region of oscillation parameters suggested by the atmospheric neutrino anomaly, assuming that the anomalous flux ratio arises from oscillations between  $\nu_\mu$  and  $\nu_e$  and assuming that CPT is invariant ( $\bar{\nu}_e$  compared to  $\nu_e$ ).

We see from the expression (7.9) that the oscillation probability contains both the length and the parameter  $\Delta m^2$  in the oscillating term. We observe, from Fig. 7.1, that in order to extend the regions explored by reactor-based experiments to the lower values of  $\Delta m^2$  hinted at by the atmospheric neutrinos, the distance that the neutrinos propagate, from the reactor to the detector, must be extended. Longer “baselines” are able to probe regions of smaller  $\Delta m^2$ . This forms the experimental motivation for several proposed long-baseline reactor neutrino experiments; the regions of parameter space that these proposed experiments could explore are also shown in Fig. 7.1. One of the experiments being considered, the San Onofre neutrino oscillation experiment, will be discussed below.

### 7.3 Detector Description

In order to probe the region of oscillation parameter space suggested by the anomaly in the atmospheric neutrino flux ratio between  $\nu_\mu/\nu_e$ , a reactor-based oscillation experiment is proposed [89]. The San Onofre neutrino oscillation experiment is to be located 0.65 km from the reactors of the San Onofre Nuclear Generating Station in Southern California. At this distance, the experiment is capable of exploring oscillations with a projected sensitivity for  $\Delta m^2$  of  $10^{-3}$  eV<sup>2</sup> and a mixing angle sensitivity down to  $\sin^2 2\theta = 0.1$ .

The detector we are proposing employs a segmented fiducial volume, filled with 12 tons of Gd-loaded liquid scintillator, and is shown in Fig. 7.2. The detector reaction most suitable for low energy antineutrinos,

$$\bar{\nu}_e + p \rightarrow e^+ + n,$$

calls for a proton-rich target, such as a mineral oil-based liquid scintillator.

The detector will be installed in an underground vault, 25 meters water equivalent (mwe) below the surface, at a distance of 0.65 km from the Units 2 and 3 reactors at San Onofre. These reactors have a combined thermal power of 6.5 GW, which corresponds to a neutrino flux, at 0.65 km, of about  $3 \times 10^{10}$  cm<sup>-2</sup> s<sup>-1</sup>. Permission has been obtained to install an underground vault on a site that has been selected. Drilling and sampling at the site have been completed.

A neutrino event is defined by a time-correlated signal between a positron and a neutron capture signal in the target scintillator. In this design, a positron is identified by requiring a fast coincidence between its energy loss ( $E_{e^+} \geq 0.8$  MeV), in one cell, and two 511 keV annihilation gammas, deposit-

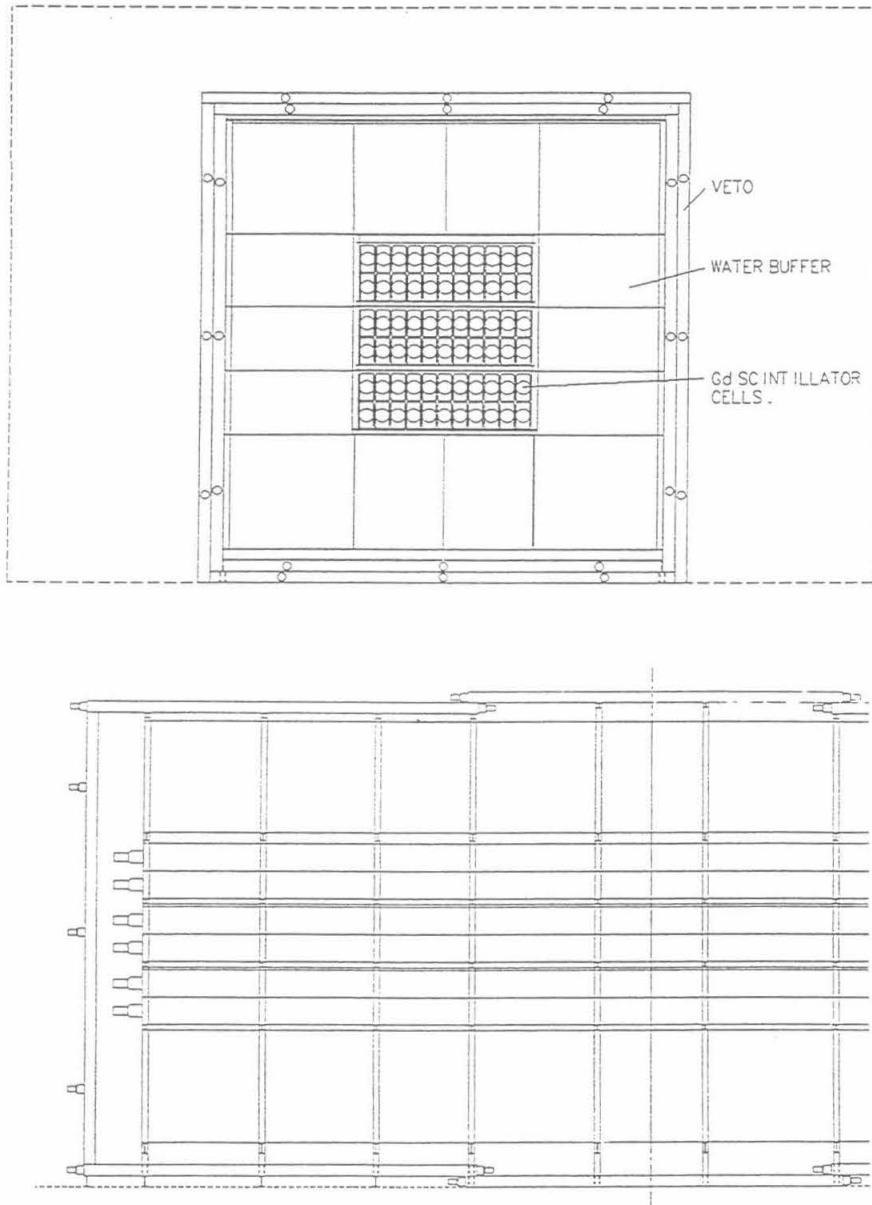


Figure 7.2: The San Onofre detector.

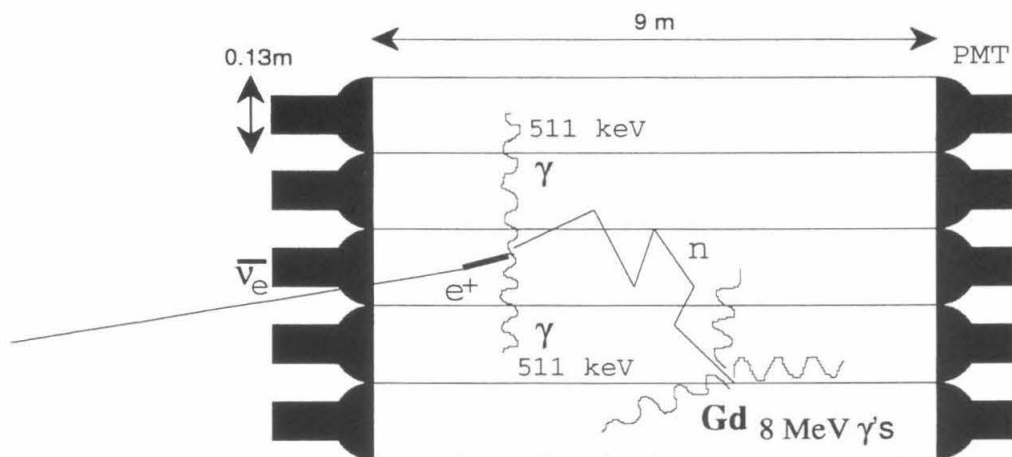


Figure 7.3: Neutrino detection scheme in the segmented detector.

ing energy between 50–600 keV, detected in two or more adjacent cells surrounding the cell containing the neutrino interaction. This detection scheme is illustrated in Fig. 7.3. Following a fast triple coincidence, the neutron produced in the reaction is detected via its capture on Gd, from which gamma rays are emitted in a burst with a total energy of 8 MeV (strong lines at 5.9 and 6.8 MeV). The neutron capture time in a scintillator containing 0.1% Gd-loading, by weight, is  $27 \mu\text{s}$ .

The detector is surrounded by passive neutron shielding, consisting of 1 m of purified water held in steel tanks surrounding the scintillator cells. Outside of the water tanks is an active muon veto. All scintillator cells are made of acrylic and have dimensions:  $9 \text{ m} \times 0.25 \text{ m} \times 0.13 \text{ m}$ , including an end chamber of 0.8 m at each end in front of the photomultipliers, filled with mineral oil, serving to attenuate the gammas from radioactivity in the glass of the PMT's and also serving to moderate external fast neutrons.

## 7.4 Signal and Background in the Detector

Neutrino experiments typically have, as a unifying characteristic, very low signal rates. The San Onofre experiment will be in the same situation. Studies were made of the efficiency of the proposed segmented detector design and they found a value of 20%, for the complete neutrino signal detection efficiency. Using this figure, the estimated, detected neutrino counting rate in the experiment is  $34 \text{ d}^{-1}$ . The challenge in this experiment is thus to ensure that background rates in the detector are comparably low.

The sensitivity of the San Onofre experiment to neutrino oscillations can be estimated for various signal-to-background values. In this calculation, I assumed that oscillations are not present and that the experiment has accumulated a hypothetical data set over say a 400 day period at full reactor power. During this time, the detector has recorded both signal and background counts. During a second hypothetical period of data taking, of typical duration 70 days, I assumed that one reactor was shutdown for refuelling. Data during this period contains the full background rate but only half the signal rate; thus, this data set can be used for background subtraction. With various background rates added to the anticipated signal of 34 neutrino events per day, the estimated statistical quality of the final data set and excluded regions of oscillation parameter space were calculated. Fig. 7.4 plots the regions of parameter space, expected to be excluded at the 90% confidence level, for various amounts of background. Systematic uncertainty in the absolute neutrino flux was included as an additional error of 6%, added in quadrature to the statistical error deduced after hypothetical background subtraction. We see from this figure that it is important to maintain backgrounds in the detector as low as achievable, in order to preserve maximum

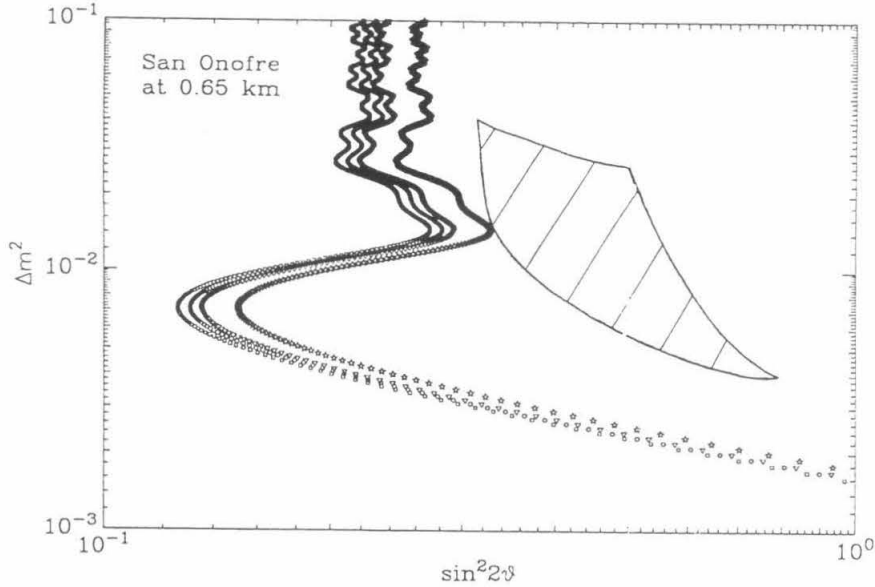


Figure 7.4: Excluded regions of parameter space anticipated for this experiment. From outermost going inwards, the curves correspond to 0, 6, 12, and 34 background counts per day.

sensitivity to oscillations within this region of parameter space indicated by the atmospheric neutrino flux anomaly.

Backgrounds in this detector can be divided into two categories. The signature of a neutrino event is a coincidence between a positron-like signal and a neutron-like signal, within a limited time window. Thus, there exists backgrounds that are “accidental,” in which two uncorrelated signals, one similar to the positron and the other resembling the neutron, happen to occur near each other spatially and temporally. An advantage of Gd-loading in the scintillator is the reduction of the accidental background components, due to the shortened mean neutron capture time and to the higher energy capture gammas, placing the neutron-like signal above the energies of natural radioactivity.

The second class of backgrounds that exist are the correlated ones, in which a source of background can produce correlated interactions in the de-

detector, similar to both the positron and neutron signal. These correlated backgrounds, indistinguishable from the neutrino signal, are far more dangerous; they can only be subtracted from the true signal by performing a measurement during reactor shutdown. Perhaps the most significant of the correlated background components arises from fast neutrons. In the Gösigen experiment, fast neutrons, penetrating to the target cells, were seen to interact in the scintillator, giving rise to recoil protons. The energy deposited by the protons in the scintillator faked the positron signal. Subsequently, the same neutron thermalized in the detector and was captured, creating a neutrino-like correlated signal in the detector. That experiment employed pulse-shape discrimination to separate proton events from the positron signal, using the difference in the characteristic time profile of their scintillation light output to distinguish the two.

In the San Onofre detector, the requirement of a triple coincidence, searching for 511 keV annihilation gammas, imposes a strict requirement on the positron-like signals and seeks to strongly reject the background from fast neutrons. Nevertheless, there exists some finite probability for a fast neutron to mimic a positron in the detector. This can happen due to multiple scattering events in adjacent target cells, in which exactly the correct amount of energy is left, by recoiling protons in each cell, to look exactly like a positron and its annihilation gammas. Alternatively, the fast neutron could scatter inelastically from carbon in the scintillator, leaving the  $^{12}\text{C}$  nucleus in an excited state. It decays via emission of a 4.4 MeV gamma and this gamma can mimic the triple coincidence through multiple Compton scattering — even pair production is possible, in which case a true positron appears inside the scintillator cells. All the while, the fast neutron that initiated these signals could have thermalized and captured within the detector, a short time

later, completing the imitation of the neutrino signature. Monte Carlo studies of fast neutron interactions in the San Onofre detector estimate that the probability for a fast neutron to completely fake the neutrino signal in this manner is about  $3 \times 10^{-3}$ . The rejection of the fast neutron background is seen to be quite good for a segmented detector design.

The constraint that reactor-based experiments must be placed close to their neutrino source makes things more difficult. Usually, only a shallow depth site can be considered for installation of a neutrino detector, close to a reactor. Consequently, backgrounds from cosmic rays could be significant. At a depth of 25 mwe, the San Onofre detector has enough overhead shielding that the hadronic component of the cosmic rays has been completely attenuated. However, the muon flux is down by only a factor of 4–5 from the flux at the surface. Consequently, muon-induced fast neutrons become the dominant background at this depth. Muons are capable of producing neutrons of fairly high energy, which are difficult to attenuate, whereas neutrons from  $(\alpha, n)$  reactions in the rock surrounding the underground lab are typically lower in energy — these neutrons are easily absorbed by the 1 m water buffer surrounding the target cells. It is clear that the fast neutron background, produced by muons, is an important consideration for the San Onofre neutrino oscillation experiment and a study of the production of fast neutrons by muons is warranted.

## Chapter 8

# Fast Neutron Production by Muons

Muons can produce neutrons through two processes, spallation and capture. The former is less well understood than the latter. The emission of neutrons following the capture of  $\mu^-$  by various nuclear targets is discussed by Charalambus [90], in which all aspects of this process are described, including the stopping of muons, the nuclear capture probability and the neutron multiplicity distribution. A discussion of measurements of the energy spectrum of neutrons emitted after negative-muon capture on various nuclei appears in [91]. Rather than reiterate these findings, the discussion below will focus on the production of neutrons from spallation.

### 8.1 Muon Spallation

Unlike its cousin process, the production of neutrons from spallation has not been as thoroughly studied. By spallation, we are referring to the electromagnetic interaction, whereby a muon exchanges a virtual photon with a nucleus, causing the emission of hadrons or the disintegration of the nucleus itself; this process has also been discussed in the literature as muon-induced nuclear disintegrations, muon-generated hadronic cascades, and muon-nuclear inelastic scattering. All of these terms deal with the same basic interaction.

As far back as 1950, George and Evans [92] reported observing nuclear disintegrations induced by muons, in photographic plates. The following

year, Cocconi and Tongiorgi [93] confirmed the muon origin of these interactions by directly detecting the neutrons that are produced, using a battery of  $\text{BF}_3$  proportional counters immersed at various depths in Cayuga Lake, showing that the measured neutron rate dropped with depth proportional to the muon flux. Hayakawa described the physics of muon-induced nuclear disintegrations in 1951 [94], based on these two original measurements.

The Cocconi measurement is to this day, still one of the more revealing experiments in that it examined the multiplicity of neutrons arising from these interactions. However, it was precisely what he observed, namely that as the thickness of “absorber” used increased, the observed mean neutron multiplicity also increased, which prompts the question: are the multiple neutrons emitted directly in the muon interaction or are the secondary cascades within the absorber material responsible for producing the majority of these additional neutrons?

Aside from the multiplicity, one would like to know the energy spectrum of the neutrons that emerge, following a muon-nuclear interaction. The difficulty in measuring these fast neutrons explains why the knowledge of the spallation neutron spectrum is as poor and uncertain as it is. Measuring neutron energies is typically accomplished by time-of-flight or by observing the recoiling protons they collide with, in a scintillating detector. For fast neutrons (10's of MeV), a time-of-flight detector becomes large and cumbersome. As for a scintillating detector, the response function of neutrons in a scintillator is rather broad, unless the detector is again very large such that total calorimetric containment becomes significant. The broadness of the response makes it difficult to precisely extract the neutron spectral shape. Some attempts at measurements of the underground neutron spectrum have been performed, with [97, 98] being the more recent experiments. Since there

have not been many measurements of the steep energy spectrum of the underground spallation neutrons that have been performed, we can't be surprised that the spectral behavior in different materials hasn't been explored.

Finally, the neutron yield from these muon-nuclear interactions is another area where our interest lies. This was really only looked at for the first time in 1973 [104]. In such a measurement, one basically counts muons which pass through a target and observes what fraction of the muons were followed later by neutron capture, obtaining a neutron yield per muon. Such a measurement has become interesting recently, in light of the development of new underground laboratories and experiments which might be sensitive to neutron backgrounds.

## 8.2 Neutron production processes

It is useful to consider the various processes that contribute to neutron production from muon spallation. The basic interaction between the muon and the nucleus is electromagnetic. Thus, in addition to virtual photon excitations, our discussion also includes the production of real photons by muons (from bremsstrahlung of delta electrons, for example), and the resulting  $(\gamma, n)$  processes. We can categorize the various sources of neutrons based on the amount of momentum transfer by the photon.

At low energies, the giant dipole resonance plays a role in the production of neutrons. A passing muon could excite the resonance and the energized nucleus, above the nucleon emission threshold, could eject a neutron (proton or other clump of nucleons possible also). This is the most straightforward method of neutron production and probably also the easiest to calculate. It has been noted [96] that in their calculation of the virtual photon spectrum,

folded with the resonance cross-section, they were unable to produce enough neutrons by the giant dipole resonance method alone, to agree with the existing measurements of the neutron yield. Thus, other processes must contribute substantially to the neutron yield from spallation.

At virtual photon energies higher than about 30 MeV, above the giant dipole resonance, excitation and emission of nucleons still takes place. These processes are sometimes modeled with “pseudo-deuterons” [99]. Conceivably, the neutrons emitted are harder than those following the giant dipole excitation.

As the photon energy increases above the pion production threshold, there are new sources of neutrons that arise. In the production of a free charged pion, the nucleus must absorb the opposite charge in an exchange-like process. This most likely leaves the nucleus in an excited state that could decay by particle emission. As a second mode of neutron production, we also have the secondary interactions produced by the pions. For example, nuclear  $\pi^-$  capture typically results in the emission of neutrons (similar in some ways to negative muon capture). Some of the neutrons following muon spallation might trace their origin to these pion secondary reactions.

As more pions are produced in higher energy spallation interactions, we have the possibility that hadronic cascades could occur. Here, the energetic mesons and nucleons make secondary interactions within the nucleus and with other nuclei, producing even more nucleons. If these cascades contribute at a significant level, they could explain the Cocconi result, which seemed to indicate that neutron multiplication took place in the material, apart from direct production.

Finally, as the virtual photon becomes even harder, the interaction becomes a very deep-inelastic scattering. The recoiling quark in the interaction

fragments and hadrons are produced. The large momentum transfer and high density of hadronic material makes it very unlikely that the nucleus stays together under such circumstances. Thus, we can imagine that the emission of many neutrons would be the result. This represents the contribution by nuclear disintegrations to the total neutron production by muons.

This chapter has perhaps created more uncertainty and given rise to more questions about the underground fast neutrons than it has provided answers. That is, unfortunately, the situation with muon spallation. There hasn't been very strong motivation, until perhaps recently, to tackle the problems involved in further probing the details of muon-induced neutron production.

## Chapter 9

# Measuring Neutrons from Muon Spallation

In order to further our understanding of the potential backgrounds that the San Onofre neutrino oscillation experiment might face, a new measurement of the production of neutrons, following muon spallation, was initiated. This would be a measurement based on materials which are relevant to the neutrino detector, namely a Gd-loaded liquid scintillator used simultaneously as the target material for neutron production and as a neutron detector. The underground measurement was performed in the Stanford Underground Facility, a shallow depth underground lab shielded by approximately 20 mwe overburden. This site is at a depth similar to that planned for the oscillation experiment.

The general concept of this neutron production yield and multiplicity measurement is as follows. The detector triggers on muons which have passed through it, in coincidence with scintillating paddles placed below and also above the detector. Following a through-going muon trigger, we search for the gammas from neutron capture on Gd, in order to identify neutrons that might have been produced by muon spallation. In this experiment, up to two delayed neutron capture signals could be recorded, following a trigger. Thus, some indication of the neutron multiplicity can also be inferred from this measurement.

The purpose of such a measurement, similar to the experiment of Bezrukov et al. [104], is to verify the results they obtained. One question that should be raised about that experiment was the large mass of paraffin that was employed to shield their detector. It is not clear from their discussion whether or not production of neutrons outside of their detector, in the surrounding paraffin, was included. In addition, the value they estimate for their neutron capture efficiency seems surprisingly high. In any case, a new measurement of the muon-induced neutron production in liquid scintillator is appropriate to assist in understanding the neutron background in the San Onofre detector and in other underground experiments.

## 9.1 Experimental Apparatus

As the neutron yield from the muon spallation process is anticipated to be rather small, a large quantity of sensitive material is required in this experiment to achieve a sufficient counting rate. The detector we employed was a large cubical vessel, of dimensions: 60 cm  $\times$  60 cm  $\times$  60 cm. The walls of this container were made from 3/8-inch thick acrylic panels that were glued together to form a cube. This vessel was filled with approximately 200 liters of scintillator, roughly its maximum capacity. This detector and experiment will hereafter be referred to as the CUBE (Cosmic-ray Underground Background Experiment).

Four 8-inch diameter, Hamamatsu R1408 photomultipliers were mounted outside of the cube, viewing the scintillation light. These hemispherical bulbs were coupled to the flat acrylic vessel wall, using an acrylic wedge-shaped adapter. The adapter pieces were solid rectangular blocks of acrylic, 2 inches thick. A bowl was machined into the upper surface of the adapters, to fit the

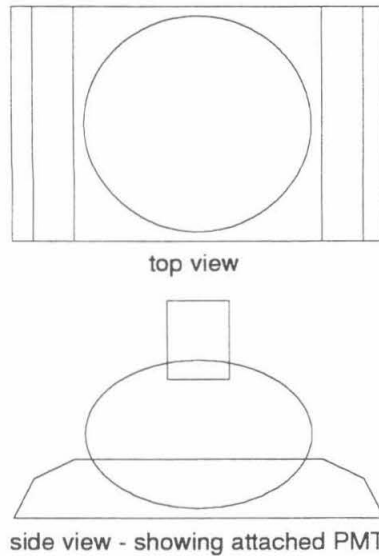


Figure 9.1: Adapters for the 8-inch PMT's.

curvature of the photomultiplier tubes. In one of the remaining dimensions of the block, the rectangular corners were cut at  $25^\circ$  angles, to approximate a crude light-gathering wedge. Fig. 9.1 is a sketch of one of these adapters. After machining, the outer surfaces of the adapters were polished and the photomultipliers were bonded in the adapter bowls using Sylgard. These solid adapter wedges were then optically coupled to the walls of the scintillator box using a thin layer of mineral oil; acrylic molding strips were glued at the edges where the adapters couple to the walls, leaving a gap between them in the middle, into which mineral oil could be injected. Two PMT's were placed on each opposing end of the detector.

Surrounding the CUBE on the four sides that do not have photomultipliers attached to them are muon veto counters. The purpose of the veto counters is to reject the accidental background arising from muons. As an example of the veto function, following an original muon which initiated

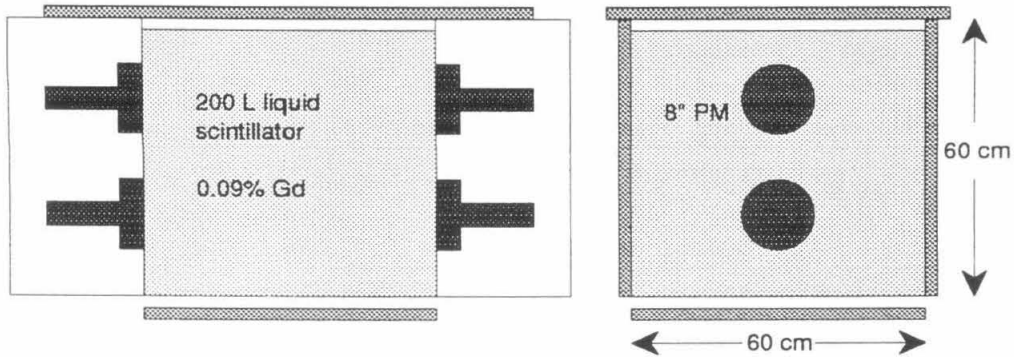


Figure 9.2: Experiment for measuring neutron production by muons. Surrounding the CUBE are muon veto counters, which were in reality, not as tightly arranged as illustrated.

a trigger in the experiment, a second muon could pass through the CUBE slightly afterwards, depositing energy that might be mistaken for the neutron capture signal. The veto paddles assist in rejecting this accidental component. Fig. 9.2 shows the arrangement of these counters, around the main detector. The entire apparatus was placed on an 30-inch high, square aluminum table,  $2' \times 2'$ , so that the CUBE could sit off of the floor. This is to reduce the probability for any neutron, produced by muons in the floor, below the experiment, to reach the detector. In this way, we attempt to measure neutron production strictly in the liquid scintillator itself.

The top veto counter was large and covered the entire box. The bottom counter, used as the main triggering paddle as well as serving as a veto, was exactly  $60 \text{ cm} \times 60 \text{ cm}$  in dimension and fit perfectly under the CUBE. A sheet of styrofoam,  $7/8$ -inch thick, was placed above the bottom muon paddle; the acrylic vessel could rest on this, cushioned from the bottom muon counter. On one side of the CUBE, not as tightly assembled as illustrated, another large paddle was positioned. It was longer than 60 cm and it covered

its side quite well. These three counters performed very well as muon vetos and were each made from large, 1-inch thick plastic scintillator sheets. In contrast, the other side veto performed poorly. It was an overlapping assembly made of four, 1/4-inch thick, smaller muon paddles that were scrounged up in the Stanford Underground Facility. Practically all of the optical couplings of the tubes to these thin scintillators were damaged and the muon signals in these paddles were not convincing. Ultimately, as our veto system was not completely tight to begin with (largely due to the lack of coverage on the PMT ends), we chose not to include this side counter in our analysis.

## 9.2 The Liquid Scintillator

The Gd-loaded liquid scintillator used to fill this detector was specially developed [95] to suit the requirements for the San Onofre detector. It is based on mineral oil of high optical clarity into which is mixed 15% pseudocumene as the primary scintillator and 4 g/L PPO and 40 mg/L bis-MSB wavelength shifters. In order to dissolve Gd into the cocktail, a solvent, TBP (tributyl phosphate), was used. Gadolinium nitrate is soluble in the TBP solvent, under a process including vacuum distillation and filtration, which produces a clear concentrate that can be added to the scintillator. A Gd-loading of 0.09% (verified by neutron activation and by ICP-MS measurements) was achieved in the preparation of 200 L of scintillator for this experiment.

The light yield of the scintillator was measured to be about 55% anthracene — this was a comparative measurement made relative to the light yield from another scintillator cocktail that we used as a standard, which was itself previously compared to a commercial scintillator, NE235C, whose light yield, as a fraction of anthracene, is given by Nuclear Enterprises. The light

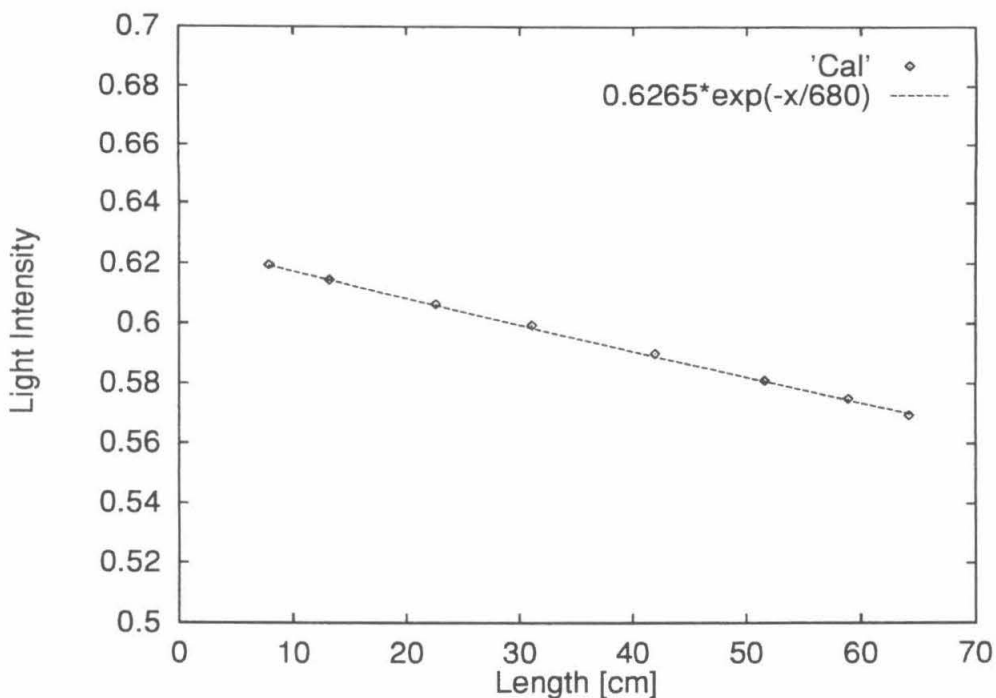


Figure 9.3: Light attenuation length measurements for the Gd-loaded scintillator.

attenuation length in this scintillator was measured in our vertical liquid column spectrophotometer to be 6.8 m, at a wavelength of 440 nm. Fig. 9.3 plots the light absorption measurements for this scintillator.

### 9.3 Electronics and Data Acquisition

A schematic of the data acquisition and trigger electronics for this experiment is presented in Fig. 9.4. To fill in some details missing from that diagram, the linear fan-in used to sum the matched PMT outputs was a LeCroy 428F. The four 8-inch PMT's were operated with negative high voltage. We used an Ortec 934 quad constant-fraction discriminator (CFD) to set thresholds for the muon and neutron signals. This constitutes the front-end electronics for our experiment.

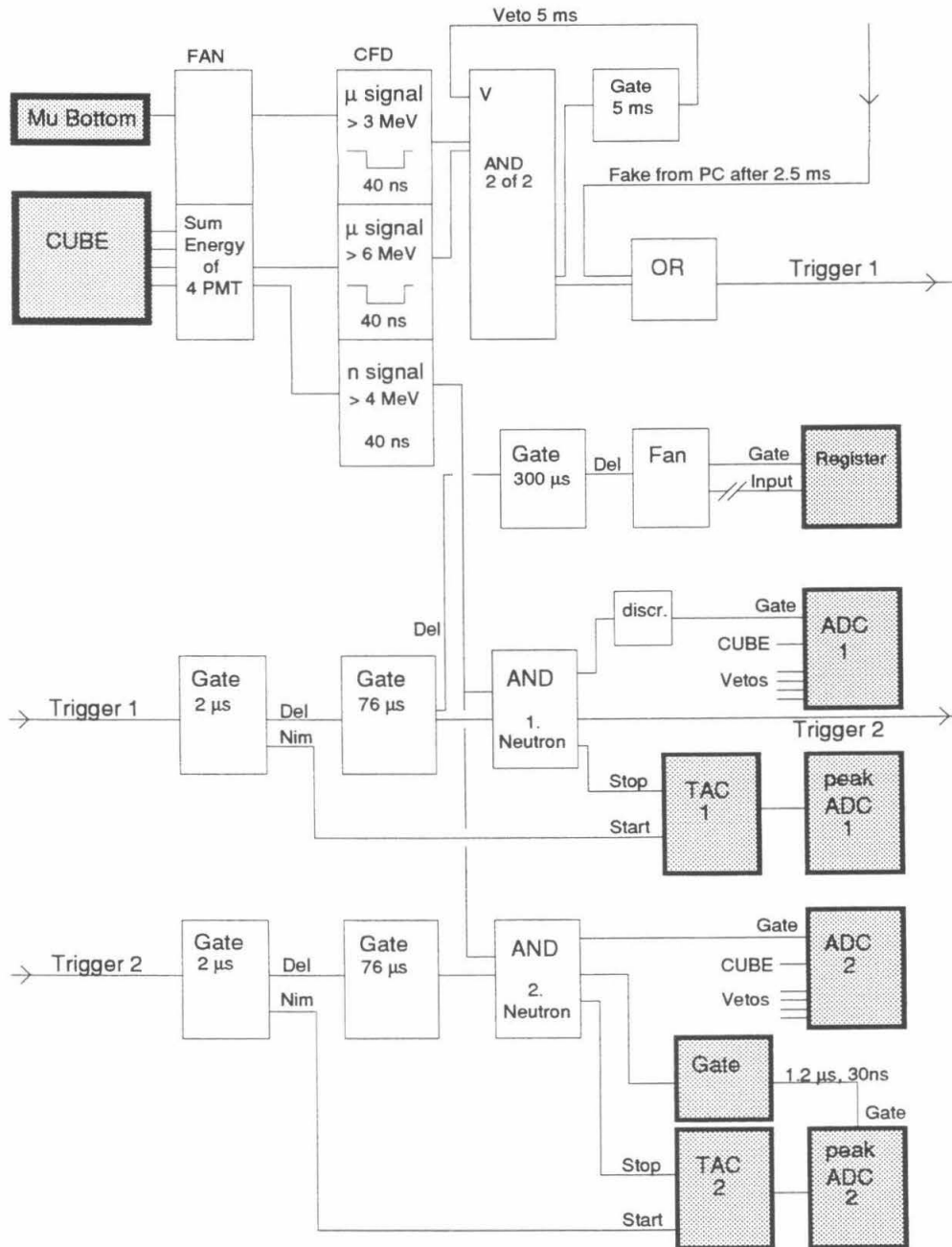


Figure 9.4: Schematic of the CUBE electronics. Thick items are detector components; shaded items were CAMAC modules; unshaded modules were implemented in NIM.

As for the trigger logic, the coincidence AND modules that were used were LeCroy 365AL four-fold logic units (one of the modules was an older model 364AL). LeCroy 222 gate generators were employed in NIM; one of the gate modules that was used was a 4222, the CAMAC variant. It is seen from the electronics diagram that following a through-going muon trigger, a  $76 \mu\text{s}$  gate is opened and serves as the time window in which we look for a delayed signal from neutron capture on Gd. This window would be initiated after a  $2 \mu\text{s}$  delay, to allow the scintillator and electronics time to settle after a muon had passed through the detector. We set the discriminator threshold roughly at 3.5 MeV to select candidate neutron capture signals. This is well enough above the 2.6 MeV  $^{208}\text{Tl}$  line, coming from the thorium decay-chain, that we were able to operate our detector unshielded, without suffering from too large an accidental background due to natural radioactivity.

The energy and time of the neutron capture events were recorded. As a means of investigating the neutron multiplicity, the data acquisition system was setup to repeat an identical time window, if a neutron capture occurred within the first one. In this way, the measurement seeks to observe what fraction of the muons, whose total trigger rate is counted by the register, are followed by single and double neutron capture events. The ADC's used to measure the neutron capture energies were standard LeCroy 2249A, charge-integrating converters. Into the ADC's were also fed signals from the surrounding muon veto counters, such that whenever the CUBE was readout, the signals of the veto counters could also be examined. The Ortec time-to-amplitude converters (TAC) were only able to extend to a maximum usable range of  $80 \mu\text{s}$ , explaining the choice of our gate length ( $76 \mu\text{s}$ , perfectly adequate for a neutron capture time constant of  $28 \mu\text{s}$ ). The two TAC's were readout via two peak-sensing ADC's.

One final point to discuss concerns the implementation of the “fake” trigger in the data acquisition and electronics. Following a valid muon trigger, and after any subsequent delayed neutron capture-like signals, the data acquisition computer, a 386 PC, initiates a false re-triggering of the electronics, 2 ms after the true trigger. This occurred each time a real muon trigger took place. A single-bit digital output was taken from the computer and fed into a single channel analyzer (SCA) NIM module. The signal of the digital bit going high and back down to zero would fire the SCA, whose fast NIM output was used to re-trigger the electronics.

The purpose of the fake trigger is to provide a continuous and contemporaneous measurement of the accidental background in this experiment. In searching for correlated, delayed neutron captures following a muon trigger, it is necessary to subtract the contribution from unrelated events that occurred by chance within the correct time window. The fake trigger provides a reliable data set of equivalent statistics, with which one can subtract this accidental component, measured 2 ms later, after almost all the possible correlated happenings following a through-going muon have taken place. With this setup, there is no need to worry whether the experiment had drifted between the time of the real data set and the time the accidental data were collected — this is the big advantage of such a fake trigger.

Seen in Fig. 9.4 is a 5 ms self-veto loop which follows any true muon trigger. This 5 ms ensures that following a valid trigger, the upcoming fake one, 2 ms later, is not contaminated by any additional muons latching up the gate and logic elements. There is no bias introduced by this veto as this period is simply equivalent to a dead time. Nor is there a perpetual self-veto of this setup, as the 5 ms gate is fixed and is not extended by any additional trigger. Lastly, the self-veto affects only the real muon trigger and it does

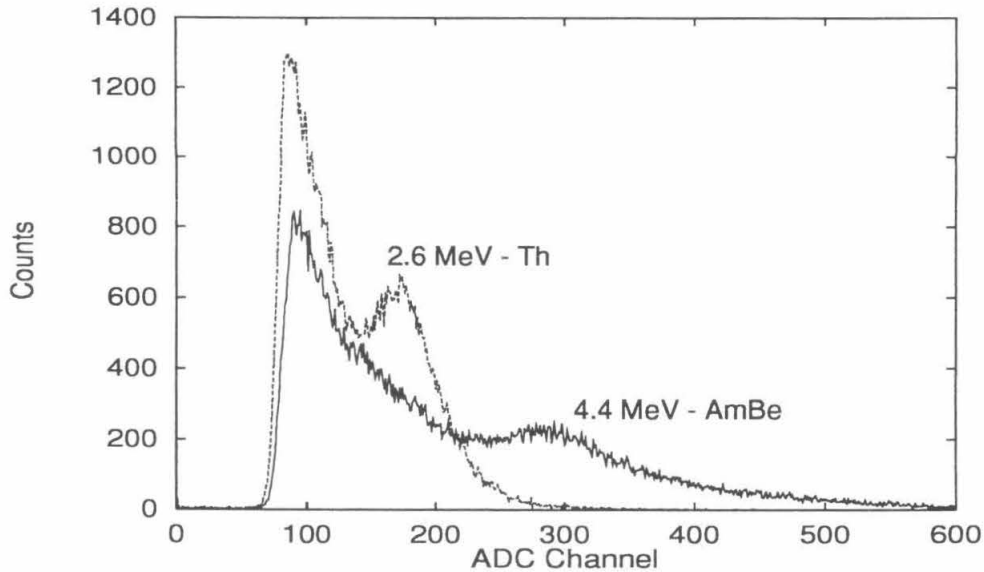


Figure 9.5: Th and AmBe calibration spectra in the CUBE.

not impact, at all, the rate or chance at which muons, passing through the detector, might resemble a delayed neutron capture signal.

## 9.4 Energy and Time Calibrations

For this experiment, it is not crucial that the energy calibration of the detector be extremely precise. The energy deposited by a neutron capture on Gd should not exceed 8 MeV, the total energy of the gammas released. Other than that, the energy of the neutron signal provides us with little else. Consequently, it was deemed sufficient to calibrate the CUBE detector with just two sources. Fig. 9.5 shows the calibration spectra taken with a Th source, providing a gamma at 2.6 MeV, and an AmBe neutron source, which provides neutrons and also emits 4.4 MeV gammas, following the de-excitation of  $^{12}\text{C}$  (the reaction is  $\alpha + {}^9\text{Be} \rightarrow \text{n} + {}^{12}\text{C}^*$ ).

From these spectra, we observe that the energy calibration appears to be approximately linear over this range. Channel 670 would then roughly correspond to 8 MeV energy. The capture signal threshold that we selected for this experiment was at about channel 300, placing the energy cut at 3.5 MeV. One interesting observation to make in the spectrum taken with the neutron source is the lack of a peak at 2.2 MeV (from neutron capture on protons in the hydrocarbon scintillator). Anyone familiar with neutron counting in conventional liquid scintillators will find this missing peak odd. In our case, we can interpret the lack of 2.2 MeV counts as confirmation that our scintillator contains a sizable loading of Gd. In examining the neutron source spectrum, we also find that it ends somewhere near channel 650–700; we again interpret this as confirmation of Gd loading, where counts from the capture gamma rays, extending up to the expected value, have been observed.

The time of capture data, consisting of TAC outputs recorded as peak-sensing ADC values, required separate calibration for the first and second neutron. In the first neutron readout, the peak-sensing ADC was a LeCroy 3511 spectroscopy module. For the time readout of the second neutron, an Ortec AD811, peak-measuring ADC was employed. In calibrating the TAC readouts, fixed start and stop intervals were sent to the TAC subsystems; the durations of these intervals were observed on an oscilloscope. Fig. 9.6 displays the time calibration deduced for each neutron readout mode. Both appear linear over their respective ranges.

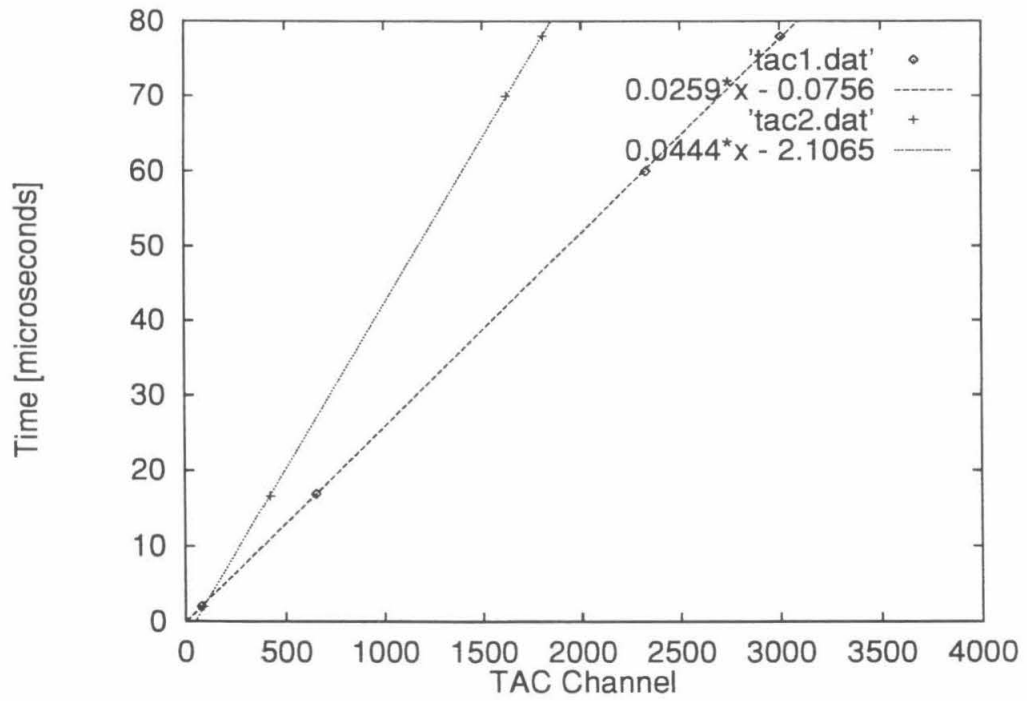


Figure 9.6: Neutron capture time calibration for TAC1 and TAC2.

## Chapter 10

# Stanford Data and Analysis

### 10.1 Phase I - Preliminary Run

The CUBE was installed in the Stanford Underground Facility and began taking data January 12, 1994. The period referred to as Phase I includes measurements taken up until January 29, 1994. A number of minor bugs were discovered during this data taking period. Among the problems, the second TAC module failed near the end of the period and a peculiarity in the second ADC module was detected. Initially, this unit was a LeCroy 2249W module, different than the 2249A model used in the first neutron channel. A problem intrinsic to the 2249W module was discovered, related to large amplitude signals locking up the converter, producing intermittent strange values upon readout. Replacing the 2249W with a 2249A module in the subsequent data taking periods corrected this problem (this is better, also, in the sense of compatibility of results, that identical ADC's could be employed in both neutron channels). Though a correction could be applied to extract a portion of the second neutron data, plagued by these problems, I chose instead to ignore the second neutron in the analysis of this preliminary data set.

Additionally, the 5 ms self-veto loop was not initially implemented, during the preliminary runs. The lack of this feature and its effect are not known, though it is certainly not expected to be very significant.

A total of  $1.4 \times 10^7$  real muon triggers (and an equal number of computer generated fake triggers) were collected over 14 days of data taking. Following a trigger, any delayed signal within  $76 \mu\text{s}$ , above 3.5 MeV, would be recorded. Fig. 10.1 represents the rawest form of the data, before analysis cuts were applied, showing histogrammed ADC (energy) and TAC (capture time) values. The trigger rate in this underground site (not corrected for dead time), for coincident muon signals through the detector and the bottom muon counter, was 11.5 Hz.

From this figure, we see that correlated counts do exist following a valid muon trigger, as evidenced by the visible excess, in both ADC and TAC plots, of the real trigger data versus the fake. Features to note on the ADC plot include: the overflow bin which also shows an excess of real over fake; the dashed fake histogram which is equivalent to the “singles” spectrum in the CUBE; the threshold for writing delayed events at channel 300; and the peculiar counts below the threshold which were due to ADC value “wraparound,” for very large pulses. From the time data, we can see that the fake histogram is perfectly flat, indicating that the fake trigger implementation truly was a good measure of the accidental counting rate. We also see immediately, from the time histogram, that there may exist two exponential time constants in the correlated data, one with a long decay time and another branch with a short time constant.

The longer time correlated counts are theorized to be delayed neutron capture signals. The short time constant exponential, however, seems roughly consistent with  $2 \mu\text{s}$ , approximately the muon lifetime. What could be the possible origin of correlated counts that are related to the muon lifetime, for supposedly through-going muon triggers? Three sources are postulated.

One could be from horizontally incident muons, scattered upward through

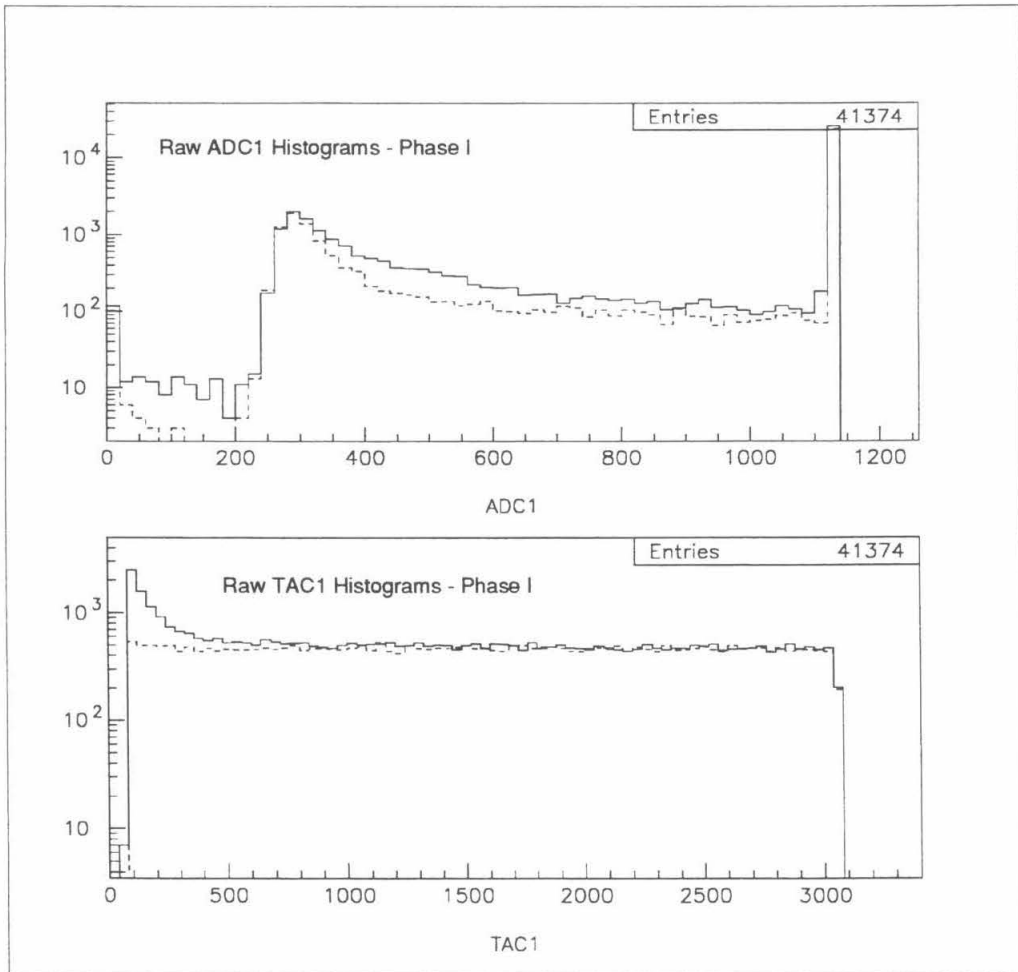


Figure 10.1: ADC1 and TAC1 data, before analysis cuts. The solid histograms are data of the real triggers, the dashed plots are the fakes. The data were accumulated during the Phase I - preliminary run.

the bottom muon counter and then into the CUBE, stopping and decaying. This should be a consideration as we are still at a shallow underground depth; consequently, the muon spectrum is not extremely hard yet and the angular distribution is not as vertically-peaked as it is at a deeper site. A second source of these counts are from ordinary downgoing muons, which had stopped in the bottom muon paddle. If doing so, they still could have triggered a coincidence. Following the muon decay, the energetic electron has a sizable range in plastic (several cm), and some fraction of these electrons could have “punched-through” the thin material between the bottom paddle and the acrylic detector box, depositing delayed, correlated energy in the main detector. Finally, we postulate that some of the  $2.2 \mu\text{s}$  time component counts arise from the production of free pions in the muon-nuclear interaction. A  $\pi^+$  that was produced, could have stopped in the detector, decaying to  $\mu^+$  and then into a positron. In such an event, the correlated time signature would have the characteristic lifetime of the muon. These are all interesting considerations, especially the pion production, as it is relevant to the production of neutrons (hadrons, in general) via the muon-induced hadronic cascades.

With this hypothesis, we decided to place a time cut on the data. For TAC1 values greater than channel 428, equivalent to  $11 \mu\text{s}$  from the time calibration, we attempt to select the neutron component of the correlated counts. For values less than this, we are selecting the  $2.2 \mu\text{s}$  component (the cut was placed at  $5\tau$ ). Fig. 10.2 shows the ADC1 histograms, after the time cut was implemented.

These histograms are very informative. We see in the neutron selected ADC histograms that the visible real over fake excess extends only up to channel 700 or so — this is roughly the 8 MeV limit one would expect from

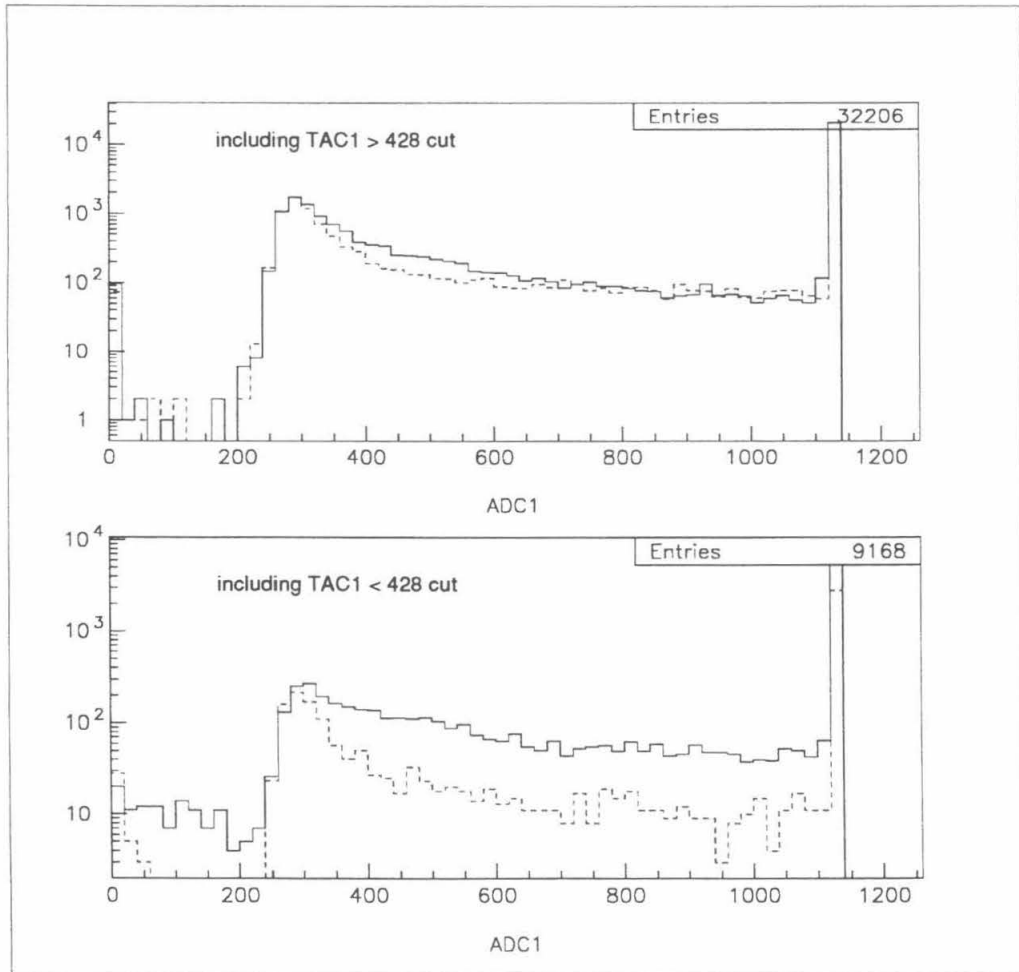


Figure 10.2: ADC1 data, with an  $11 \mu\text{s}$  time cut. The upper histograms are data with time values greater than the cut; below, the histograms are for time less than  $11 \mu\text{s}$ . From Phase I - preliminary run.

the neutron capture on Gd signals. There is no longer any statistically significant excess above these energies, including in the overflow bin (containing, presumably, muons which are purely accidental). In contrast, the short time component data display excess correlated counts across a broad energy range, including the overflow peak and the wraparound peculiar counts (these will be ignored later). We would expect such a continuum, extending to large energies, for the Michel electrons that follow muon decay, that we believe are responsible. In these two plots, the real over fake excess values, over the full ADC range, are 1,821 counts for the neutron selected subset and 4,974 counts for the muon selected subset.

We pause now to consider the muon veto counter data. It was implemented that each time a candidate delayed neutron was recorded, the veto counters would be read at the same time, to examine whether an accidental muon, passing through the experiment, was the cause. In Fig. 10.3, the histogrammed values of the three active muon counters are plotted. The symbology, VEB1, VET1, and VEK1, refer to the bottom, top and the working side muon counters, respectively. In selecting where to place the muon veto cut, it was felt that maintaining full signal efficiency would be our primary concern, by relaxing the muon rejection requirements. We chose the following muon veto cuts, requiring:  $VEB1 < 175$ ,  $VET1 < 100$  and  $VEK1 < 30$ , for an acceptable event.

Applying the veto cut to our two data subsets produces the histograms plotted in Fig. 10.4. We see that a large quantity of accidental data were rejected; previously we had 32,206 and 9,168 total counts in the real histograms of the two subsets and after the veto cut, we are left with 9,743 and 3,395 counts. This rejection of the muon accidentals, the most significant source of counts at these high energies, greatly improves the signal-to-background

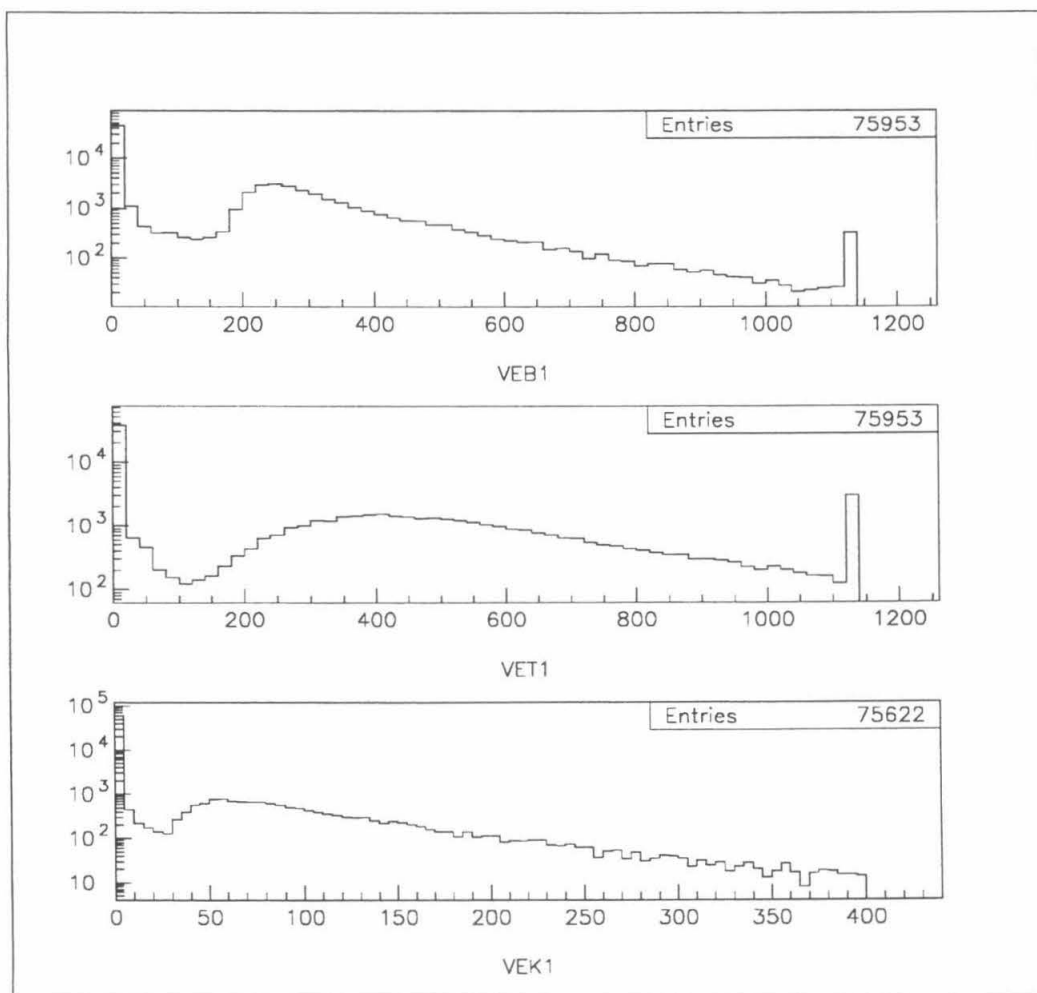


Figure 10.3: Spectra from the muon veto counters. The fourth side counter was not included in the analysis. The VEK1 spectrum is displayed on an expanded range, to better view the region of the cut. From Phase I - preliminary run.

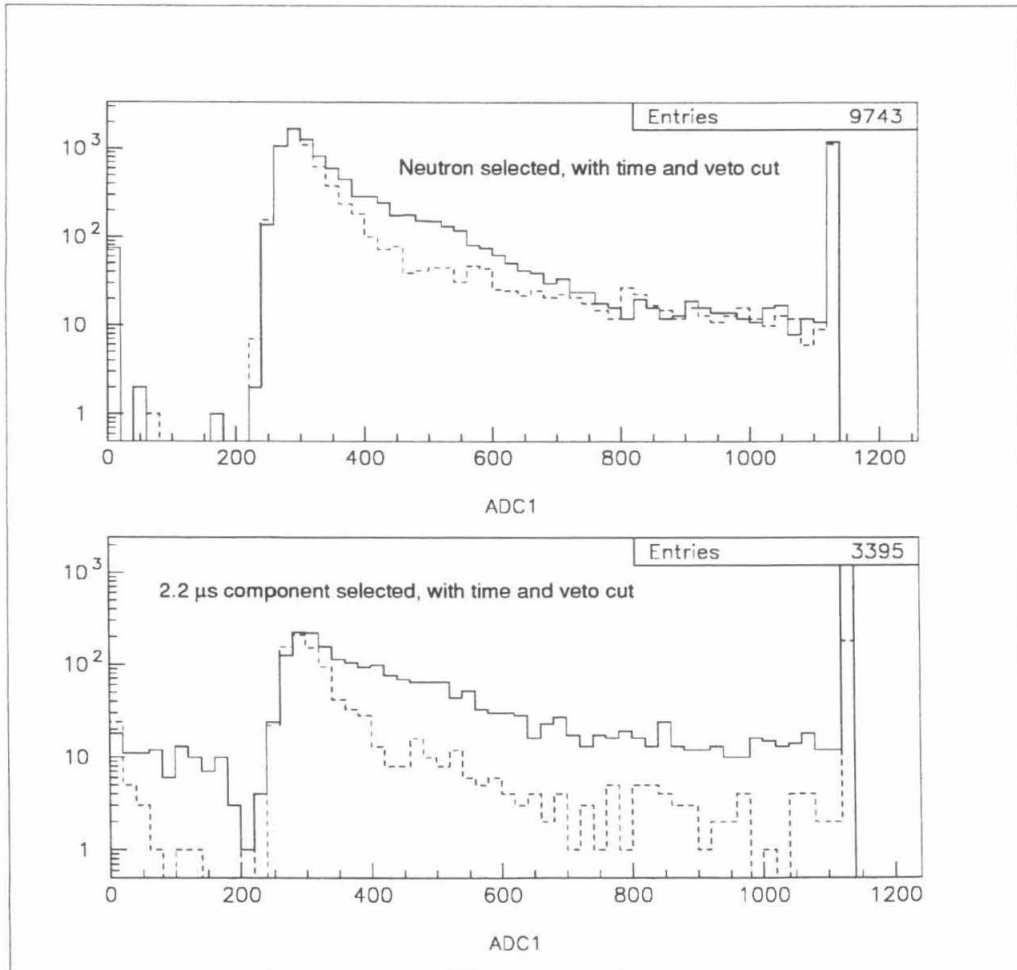


Figure 10.4: ADC1 data, including time and veto cuts. Above, the neutron selected data show excess counts of unmistakable neutron capture origin. Below, the muon lifetime component data are plotted. From Phase I - preliminary run.

ratio. In the neutron selected data set, the excess of correlated counts, real versus fake, is visually striking. The shape of the spectrum of the real counts appears to agree nicely with our expectations for the Gd neutron capture signal. We find the real minus fake excess to be 2,164 counts, not substantially different than before the veto cut was applied.

In contrast, the muon lifetime data subset, also strongly suppressed by the veto cut, now shows a real over fake excess of only 2274. This is much smaller than before the veto cut was applied, indicating that correlated counts, in addition to accidental ones, were rejected preferentially. This we can understand for the case that these counts come from stopped muons in the bottom paddle. In this style of correlated event, when the muon decay occurred in the paddle, the electron, which had to have entered the CUBE, must also have traversed some scintillating material in the paddle itself, providing a veto signal in the bottom paddle. Consequently, a veto cut rejects not only accidental muons but also correlated events of this nature. We conclude that, prior to the cut, a sizable portion of the correlated counts, with the  $2.2 \mu\text{s}$  time constant, had their origin from muons stopping in the bottom counter.

Turning now to the analysis of the capture time data, we examine the effect of placing the veto cut on the capture time histograms. Fig. 10.5 plots the real and fake TAC1 histograms after the same veto cut discussed earlier was applied. This suppression of the accidental background is useful as it brings the correlated neutron capture data, real versus fake, into prominence. The long time constant exponential is now clearly observed as well as the shorter one.

Instead of placing time cuts on the energy information, we can place energy cuts on the time information. We noted, in our analysis of the neutron selected data subset, how the real correlated counts were in excess only within

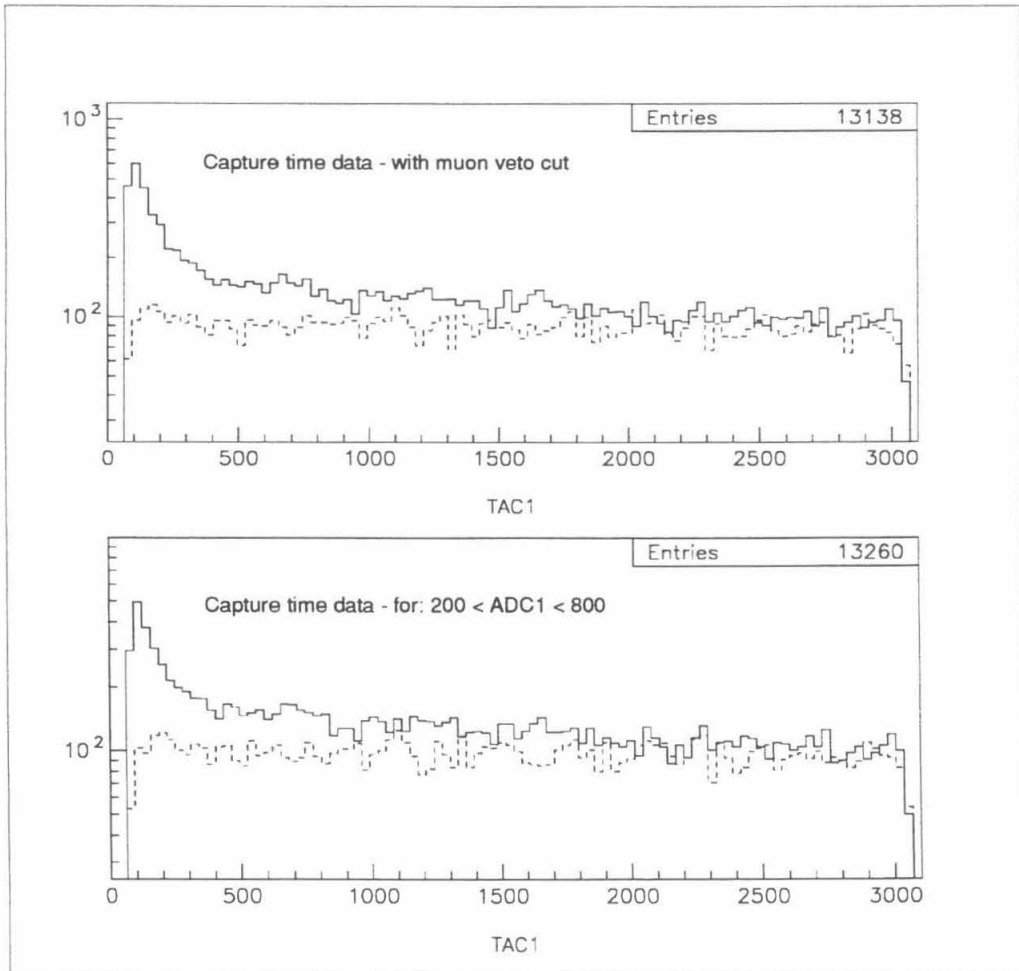


Figure 10.5: TAC1 data, with veto or energy cut. Above, the veto cut was applied. Below, an energy cut selecting Gd neutron capture-like signals was imposed. From Phase I - preliminary run.

the range associated with the energy released by Gd neutron capture. We can thus place a selection cut, requiring that:  $200 < \text{ADC1} < 800$ ; this is a very loose cut on the energy of the Gd neutron capture as we are again favoring full signal efficiency (though some optimization of the cuts could be statistically rewarding). Plotted also in Fig. 10.5, are the resultant real and fake time histograms, when this energy cut was imposed. The short time component excess seems weaker when we focus within this energy range — by employing the energy cut, we are excluding the very large energy Michel electrons that might otherwise contribute here.

Finally, we look at the data when both veto and energy cuts were placed. The resultant real and fake trigger histograms are shown in Fig. 10.6. The fake histogram was fit with a flat line, giving a value of 72.4 counts. Allowing two exponential components to be fit in the real trigger data, and including this constant background term fixed at 72.4, produced the fitted results overlaid in the figure. The fitted  $\chi^2/\nu \approx 1$  was good and the two exponential time constants, from parameters P2 and P4 in the fit, were extracted using the TAC1 calibration. We find one component with  $\tau = 29.3 \pm 3.5 \mu\text{s}$  and the other with a lifetime of  $1.15 \pm 0.67 \mu\text{s}$ . The first value is what we would expect for the neutron capture time in 0.09% Gd-loaded liquid scintillator. Our cuts did not focus on the selection of the muon lifetime component; nevertheless, we find a not entirely inconsistent value with  $2.2 \mu\text{s}$ , for the short time constant from the fit.

If we determine the real minus fake excess, with energy and veto cuts, for capture times greater than  $11 \mu\text{s}$ , we arrive at an excess of 2,067 counts. We attribute these correlated counts to neutron production from muon spallation. This excess, identical throughout all stages of the analysis, reinforces our belief that our selection criteria were properly chosen. With full cuts,

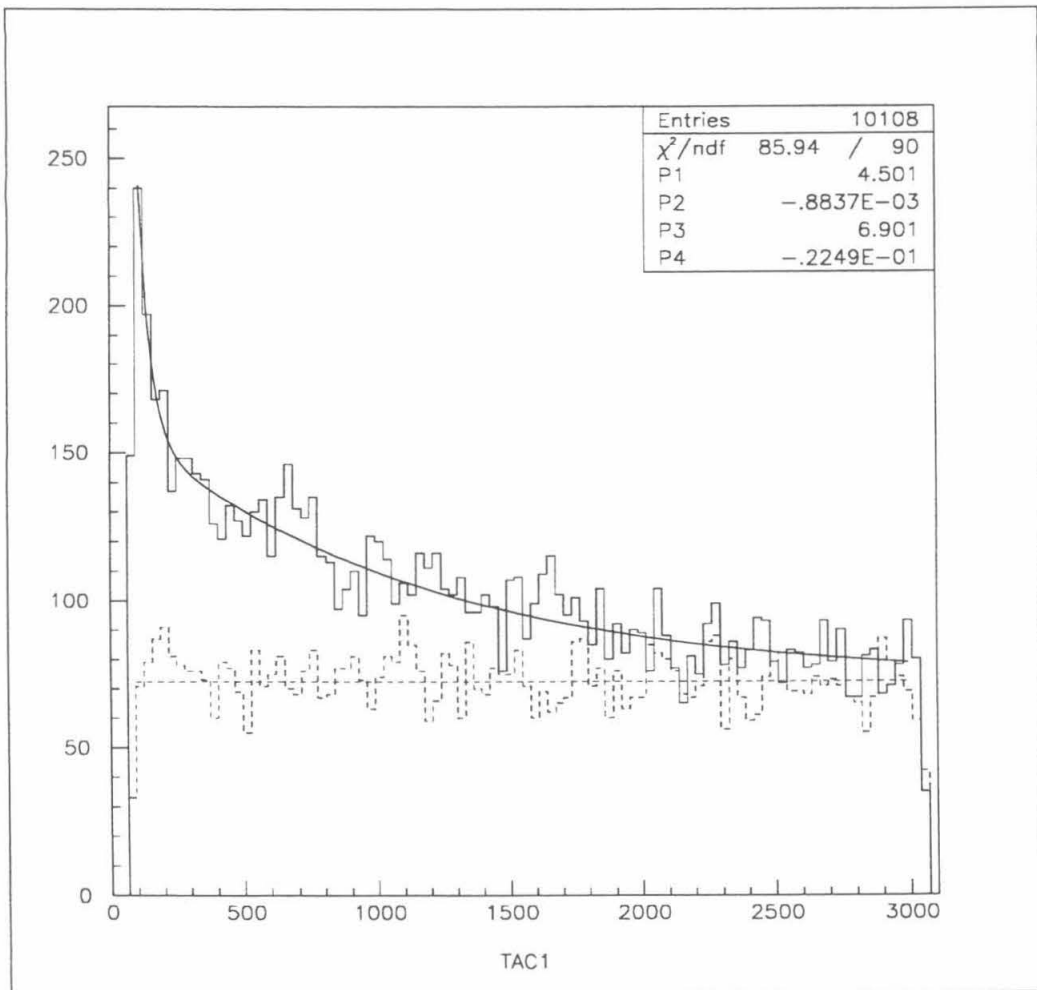


Figure 10.6: Fitted capture time data, with all neutron selection cuts. The solid histogram, for the real triggers, was fit with the sum of two exponentials (solid curve). The dashed histogram is for the fakes. It was fit to a constant background of 72.4 counts (dashed line), and this was fixed in the analysis of the real data. From Phase I - preliminary run.

we have reduced the accidental background to just 6,171 counts. Thus, our signal-to-background ratio was 1:3, not so bad considering 14 million muon triggers were accumulated and out of that 2,067 neutrons were selected and identified.

## 10.2 Phase II - Single and Double Neutrons

All of the bugs that were uncovered during the preliminary runs were fixed and the CUBE took data in Phase II, with the same trigger mode as before, requiring coincidences between the detector and the muon paddle below it. The setup of the electronics was exactly as described in Section 9.3. The data taking period began February 10, 1994, and continued through until March 1, 1994. The goal of the Phase II data runs was the extraction of a good sample of double neutron capture events, following muon spallation.

All together, a total of  $1.675 \times 10^7$  real muon triggers were accumulated, over a period of about 17 days. In the analysis of the Phase II data, we also searched for correlated, excess counts in the first neutron channel, following a through-going muon trigger, as we did in the analysis of the preliminary data set. Fig. 10.7 shows the ADC1 and TAC1 histograms, for the real and computer-initiated fake data. The correlated neutron counts, extending up to about 8 MeV energy (channel 700) are clearly visible. We find an excess of 2,934 counts, for real delayed events subtracting accidentals, in the energy window corresponding to channel 200–800. The accidental background in this range was 6,608 counts, after all neutron selection cuts (veto, energy and time) were applied.

It is worth pointing out that the peculiar counts that appeared below the threshold in the preliminary data set now seem eliminated in the Phase II

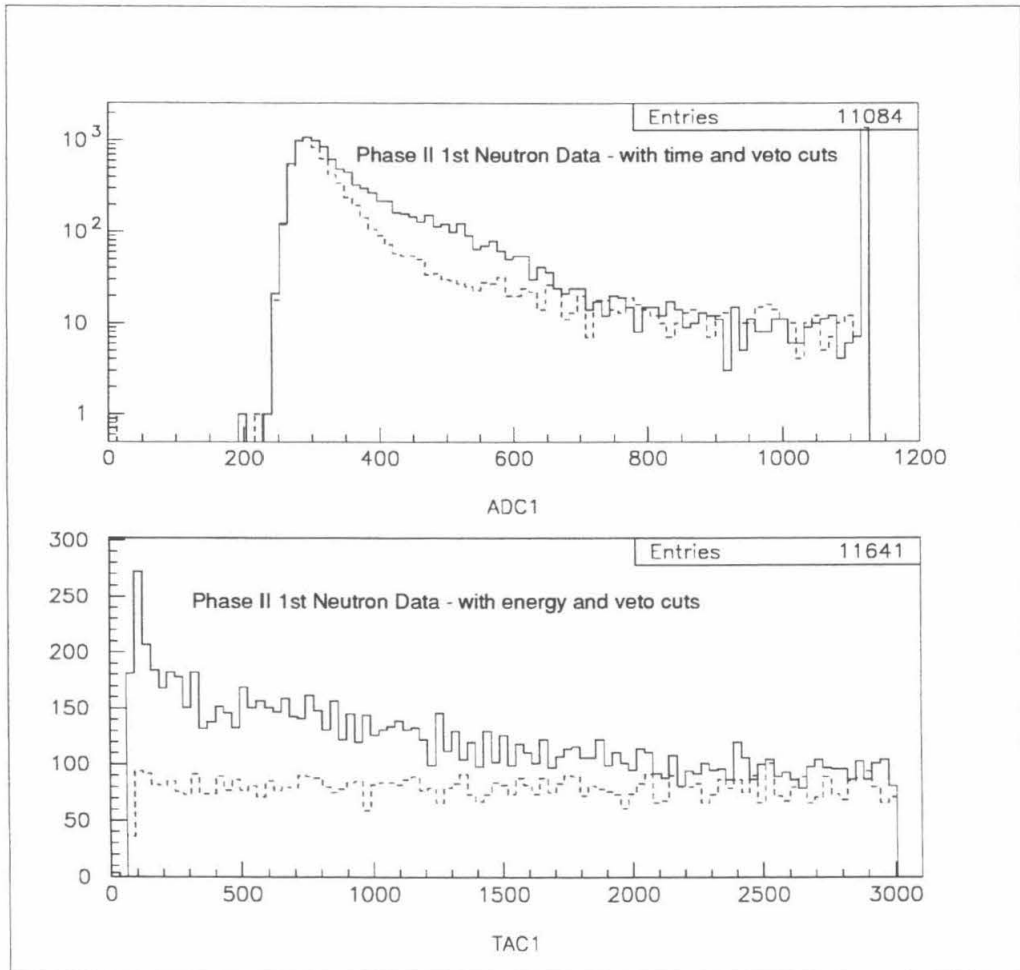


Figure 10.7: ADC1 and TAC1 histograms from the Phase II data. Real trigger data are in the solid lines; the fake data are plotted with dashed lines.

data. With the implementation of the self-veto loop and other modifications in the trigger logic, we have perhaps avoided the occurrence of signals falling between the “cracks” in the triggering sequences, inappropriately latching up the gates and ADC’s. In any case, those spuriously counts do not affect the extraction of the correlated neutron sample, either way.

We now examine the data for events in which two neutron capture candidates were recorded, following a muon trigger. Fig. 10.8 shows the raw ADC2 data, for the real and fake triggers, without any selection cuts.

The meaning of the terms real and fake must be re-evaluated when considering the events that contain two delayed counts. For the one neutron data, real and fake refer unambiguously to data which might be time correlated with the initial muon trigger and data which are purely accidental. This same relationship also carries over to the second neutron counts; the real data are possibly time correlated with the initial trigger, and the fake data are not. However, in events with two delayed counts, it could be that the second count is correlated with the first one, or it could be that the second count occurred accidentally, and this is without regard to whether the overall event was or was not correlated to the initial trigger.

For example, it could be that the event observed was a “real” neutron spallation event, in which one neutron capture was observed following the trigger. A second delayed count might occur accidentally, in this so-called real data sample. A contrary example would be the case where following the initial muon trigger, at any time, a second muon happened to follow. This second muon could be recorded as the first delayed count. It might be that this muon stopped ordinarily in the CUBE; its decay electron would then be registered as the second delayed event. The second count is time correlated with the first one, and neither have any relation to the initial muon trigger.

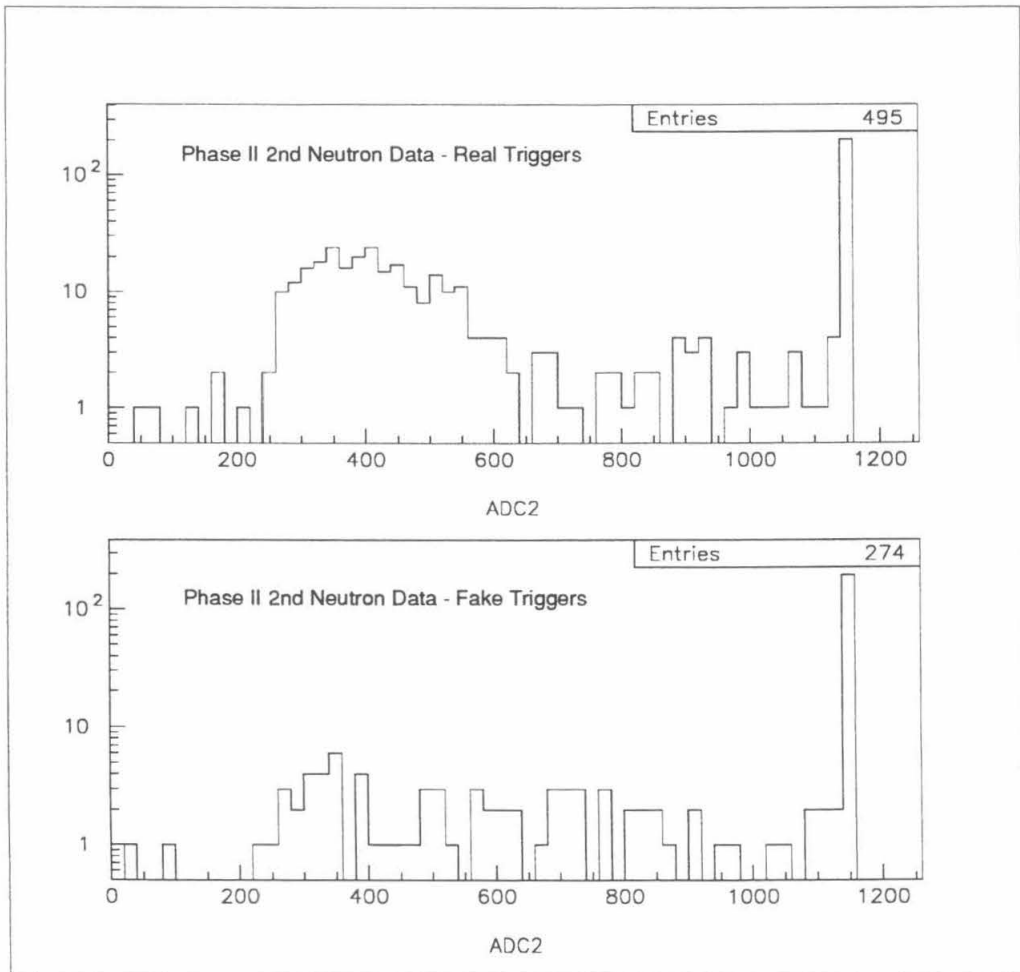


Figure 10.8: Raw ADC2 data from the Phase II runs. The upper plot is the real trigger data; the lower plot is for the fakes.

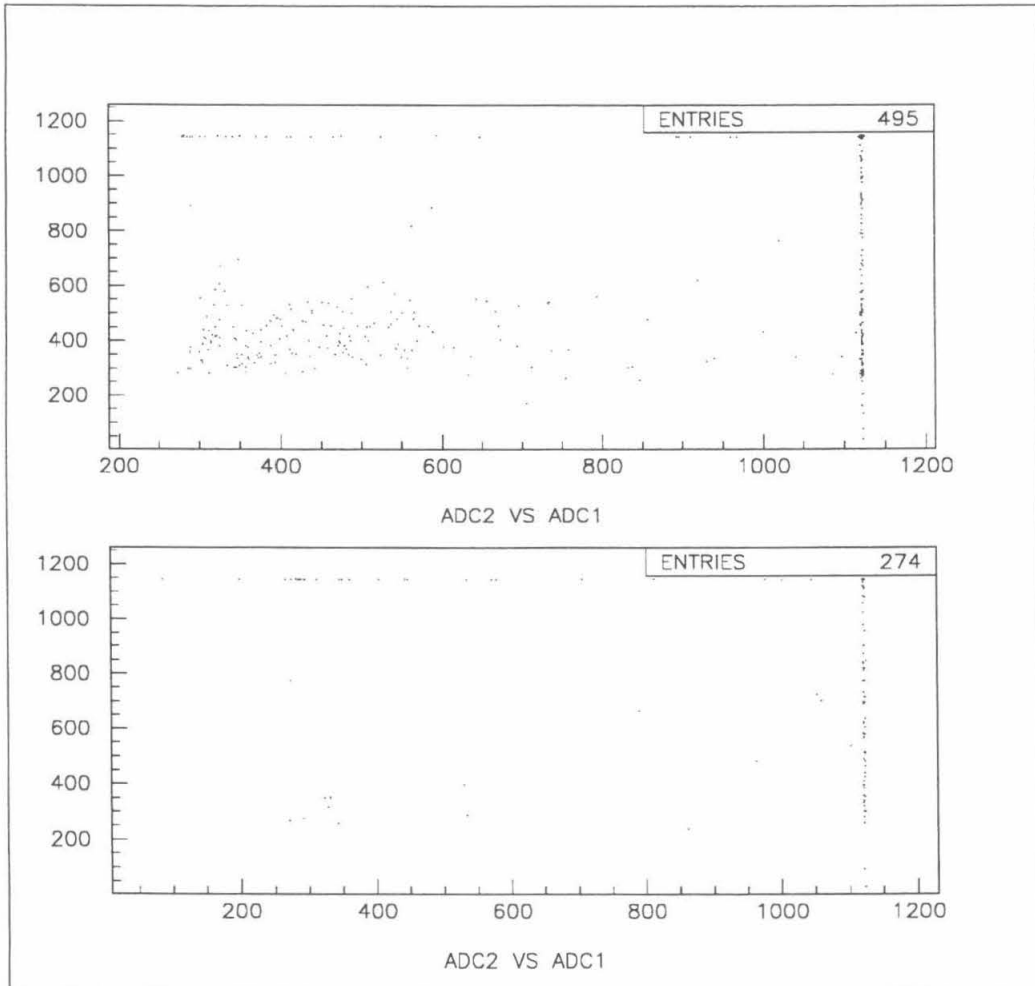


Figure 10.9: Scatter-plot of ADC2 versus ADC1, before cuts. The upper plot is for the real data; the lower plot is of the fakes.

Thus, the subtraction of the accidental *and* correlated backgrounds from the true double neutron capture events must be handled slightly differently than just the straightforward, one-for-one subtraction. In order to illustrate the analysis sequence, we display a scatter-plot of the events with two delayed counts, showing ADC2 versus ADC1 values. Fig. 10.9 shows the data before cuts were applied.

The high density of points, in this plot, along the vertical line at the overflow bin for ADC1, indicates a large quantity of  $\mu \rightarrow e$  events (stopped muon decay in the detector) in the two-neutron data set. The decay electron in ADC2 is time correlated with the muon in ADC1; these events could appear in either the real or fake data sample. Taking the fake data for illustration, we attempt to eliminate these events. Supposing that the first count was a muon, we imposed the muon veto cuts on this data sample. Fig. 10.10 shows the result, on the upper plot. A large amount of these events were rejected. Presuming that these are muon decay events, we can further remove this component by requiring that the second capture time data, recorded as TAC2, be greater than  $11 \mu s$ . After this cut, we find that even more of these correlated background counts were eliminated; the results are shown in the lower plot of Fig. 10.10.

With just those two cuts, designed to remove the muon decay background and preserve any neutron related delayed events, we went from 274 counts in the fake data set to 29 counts. The rejection of this correlated background component in the two-neutron data sample was quite effective.

In order to extract the number of two-neutron correlated events from the data, we proceed with identical cuts as described for the first neutron, and include similar constraints on the second delayed count. The procedure of progressively including the various cuts, designed to select the true two-

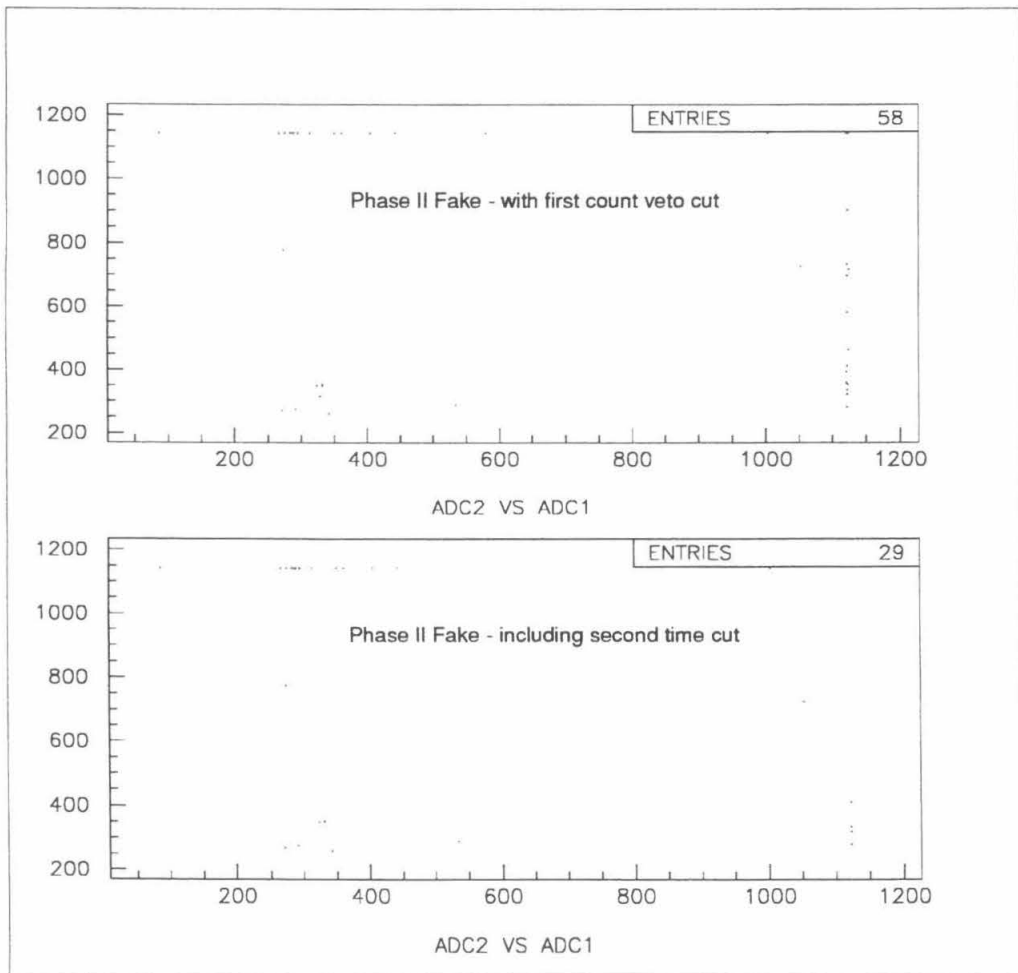


Figure 10.10: Scatter-plot of the fake data, with cuts to remove  $\mu$  decay. The upper plot has utilized the veto cut on the first delayed data. The lower plot has selected the time of capture of the second count, requiring it to be greater than  $11 \mu\text{s}$ . From the Phase II data set.

cut description	real counts	fake counts
before cuts	495	274
VEB1 < 175, VET1 < 100, VEK1 < 30	236	58
TAC1 > 428	121	48
VEB2 < 175, VET2 < 100, VEK2 < 30	99	32
TAC2 > 295	75	9
ADC1 < 800	73	5
ADC2 < 800	72	5

Table 10.1: Effect of analysis cuts on the Phase II second neutron data. The counts remaining show the cumulative effect of applying the successive cuts.

neutron capture events, is highlighted in Table 10.1. Here, a list of the analysis cuts is presented. The number of counts remaining in the real and fake data sets, at each stage of the analysis, is given. The muon veto cuts were as described in the analysis of the preliminary data. The TAC cuts selected capture times greater than  $11 \mu\text{s}$ ; the calibrations of the two TAC's were different. The conservative upper limit on the ADC values, channel 800, corresponds to an energy somewhat greater than 8 MeV.

When the TAC2 > 295 cut was applied, it was at the last stage where the muon decay correlated background could contribute. We see that this cut removed 24 counts from the real data set and 23 counts in the fake. This is as we would expect as this source of correlated first-second counts contributes with equal probability in the real and fake. After that cut, we have 75 counts left in the real and 9 in the fake. Fig. 10.11 shows the scatter-plot of these few counts, for both of the data sets.

A crude division of these events is made with respect to the values of ADC1 and ADC2. Two categories are created for both ADC's, low and high, corresponding to counts below channel 800 and those above. The purpose of this division is to identify and attribute the origin of the counts, that fall into each class, to their various sources: accidentals, correlated backgrounds,

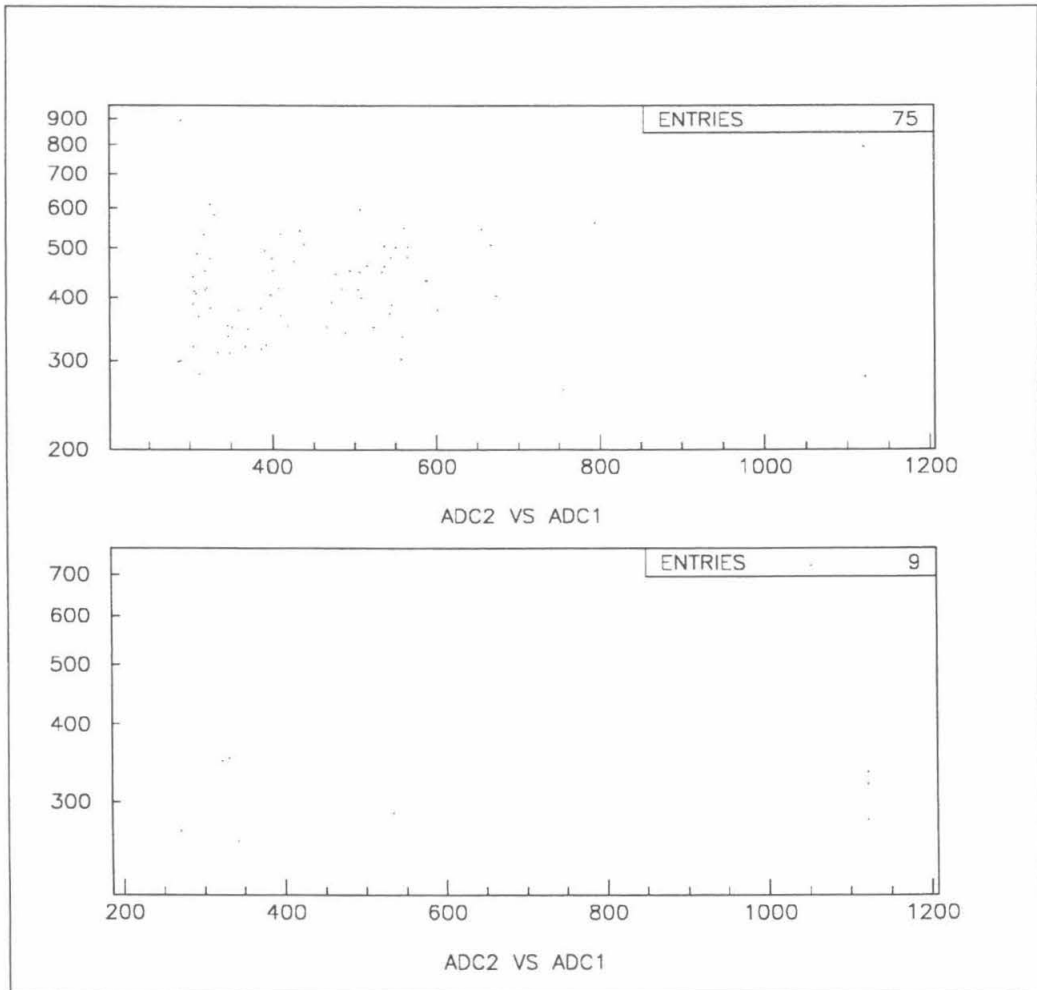


Figure 10.11: Double neutron scatter-plot, after veto and time cuts. The upper plot is the real data set; the lower plot contains the fake counts.

ADC1	ADC2	<i>measured</i>		<i>calculated accidental</i>	
		real	fake	real	fake
L	L	72	5	3.8	2.6
L	H	1	0	0.95	0.66
H	L	2	4	0.61	0.66
H	H	0	0	0.15	0.17

Table 10.2: Accidental contributions to various classes of double neutron counting events. The measured counts, after veto and time cuts were applied to the first and second delayed data, are also given.

and true double neutron events. This additional breakdown of the 75 real trigger counts and the 9 fake counts is presented in Table 10.2.

In this table, the calculated accidental backgrounds that should appear in each data class are given. These were determined from the fake first neutron counting probability versus the total number of muon triggers, with muon veto and time cuts imposed. We observed, in the first neutron fake data sample, that 6,608 counts with  $\text{ADC1} < 800$  were recorded and that 1,672 counts, with  $\text{ADC1} > 800$ , were observed. These counts, divided by the total number of muon triggers, 16.75 million, give the accidental probability for a delayed count to occur within the time window, passing all cuts. These ratios are then multiplied by the observed number of first delayed counts in the real and fake data samples, to obtain the expected accidental second counting rate. In such a calculation, events of the nature where a true first neutron was observed, and an accidental second count was recorded, are correctly included.

Within these classes, there exist correlated first-second counts, unrelated to the initial muon, that are backgrounds of the following nature. There might exist events where a muon made the first count, and neutrons produced by this muon made the second count. Thus, correlated single neutron

production could occur incidentally to the original muon trigger, simulating a double neutron event. We would expect such events to fall in the H-L category, and possibly in the L-L one as well. A second such correlated event might be one where a fast neutron entered the CUBE, giving rise to recoil protons that are recorded as the first count. This neutron captures and makes the second count. This type of correlated background would likely fall into the L-L category. There are no correlated backgrounds in the L-H or the H-H classes that we can think of.

From Table 10.2, we observe that no H-H counts were measured, agreeing with our hypothesis of the small accidental rate and no correlated sources. We find that the one measured L-H count is consistent with the predicted accidental rate for events of that class. For events of the H-L nature, we find that more of these events were observed than one would expect just from accidentals. These counts, 2 in the real and 4 fakes, are probably of the correlated single neutron production by muons type, described above, and are not violently in disagreement with each other. Finally, in the L-L category, we find that the measured fake rate was 5 counts and the predicted value was 2.6. This is also not unreasonable — let us treat these statistics as though they were more significant than actually warranted. Thus, out of these 5 counts, only 2.6 were accidental and 2.4 must come from correlated backgrounds, presumably of the fast neutron type. We must subtract 2.4 counts from the real data sample to remove this correlated background and we must subtract 3.8 counts from the real data, to account for the accidental background, properly scaled. Thus, we arrive at the conclusion that, in the real data sample, 65.8 counts could not be attributable to accidentals or to correlated backgrounds, unrelated to the initial trigger, and thus must be true events where two delayed counts were observed, correlated with the

initial muon trigger.

Thus, we find evidence for double neutron production following muon spallation, in the Phase II data set, wherein the signal is indisputably greater than the virtually negligible background, after selection cuts. Examining where the points fall on the scatter-plot show that the real data extend to values up to channel 700 in both ADC's, which is the proper energy limit for Gd neutron capture. The counts do not extend all the way up to the artificially placed cut at 800, confirming that no biasing effect was introduced by the cut. Looking at the fake data plot, the five counts are seen clustered at lower ADC values, where the singles counting rate is higher. This tends to confirm our conclusion that they are largely due just to accidental backgrounds; however, it is not incorrect to interpret the measured five counts as either accidental or correlated background that must be subtracted.

### 10.3 Phase III - Pion Production by Muons

Our attention shifts focus from the long time constant neutron counts in the data to the shorter lifetime exponential. In particular, it is the production of pions that is of interest to us, as it is closely related to the muon-induced neutron background. It is possible, through observation of the decay sequence,  $\pi^+ \rightarrow \mu^+ \rightarrow e^+$ , with the characteristic lifetime of the muon, to get some indication of its significance.

As was discussed earlier, there are two other sources, in addition to the  $\pi^+$ , that contribute to the correlated counts with the short exponential. A large fraction of these events are from muons that stopped in the bottom paddle, followed by their decay electrons which punched-through into the main detector. The other origin of these counts comes from muons scat-

tered upwards, that stop and decay in the CUBE. Our approach to isolate the pion signal was as follows. To reject the stopped muon events in the bottom paddle, the energy information in the paddle itself could be used to identify any decay electron which might have originated there. To eliminate the upward muon component, a top and bottom coincidence trigger for the data acquisition was implemented. This would ensure that any muon, which had passed through the detector, must have traversed it completely as the coincidence would have required muon paddles above and below the detector to have been hit. It would still be possible for upgoing muons to stop in the top paddle, similar to those that had been seen to stop in the bottom, but it would no longer be possible for them to stop in the large volume of the CUBE.

For the Phase III data runs, the top veto paddle was run through a discriminator and the master trigger for the experiment was converted to a triple coincidence between the top paddle, the CUBE, and the bottom muon counter. In doing so, the overall muon trigger rate of the experiment dropped to 6.4 Hz (not corrected for dead time). However, this is not expected to have such a detrimental effect on the production of neutrons or pions as the average path length of target material (scintillator) through which the muons pass is lengthened in this triggering geometry. It should be interesting to compare the results with this trigger mode to the previous ones.

Data were collected from March 2, 1994 through until March 16, 1994. In total,  $7.2 \times 10^6$  muon triggers were collected over this 13 day period. We first present single and double neutron results, extracted in an identical manner as described previously.

Fig. 10.12 presents the first neutron excess counts in the ADC1 and TAC1 histograms. Between channels 200–800, the correlated neutron excess was

ADC1	ADC2	<i>measured</i>		<i>calculated accidental</i>	
		real	fake	real	fake
L	L	36	6	1.6	1.1
L	H	0	0	0.35	0.24
H	L	2	0	0.27	0.24
H	H	0	0	0.06	0.05

Table 10.3: Double neutron analysis for the Phase III data. The accidental background rates expected in each category are listed.

1,327 counts over an accidental background of 2,784 counts. In the time histogram, both the 2.2  $\mu$ s and the neutron capture time components are visible.

In Fig. 10.13, two scatter-plots are presented, real and fake triggers, of the double neutron data sample. Veto and time cuts were imposed on the first and second delayed data. Table 10.3 shows the breakdown of the counts into the various low-high classes, with an estimate of the expected contribution just from accidental events.

Once again, in analyzing the sparse double neutron counts, we make statements based on our expectations of the correlated backgrounds. For example, the two counts of the H-L variety, observed in the reals, are probably of the single neutron correlated event type. None happened to be observed in the fake trigger data. In the L-L data sample, the observed 6 counts in the fake again seem higher than the predicted rate from accidentals alone. We attribute these L-L events to correlated backgrounds, possibly of the fast neutron type. Thus, it is correct to subtract the 6 counts fake, from the real data set. We are left with 29.5 counts (accounting for the difference in the expected accidental counts, 1.6 versus 1.1), that must be double neutron capture events, associated with the initial through-going muon trigger.

Turning to the  $\pi^+$  data, we now examine the first delayed counts, follow-

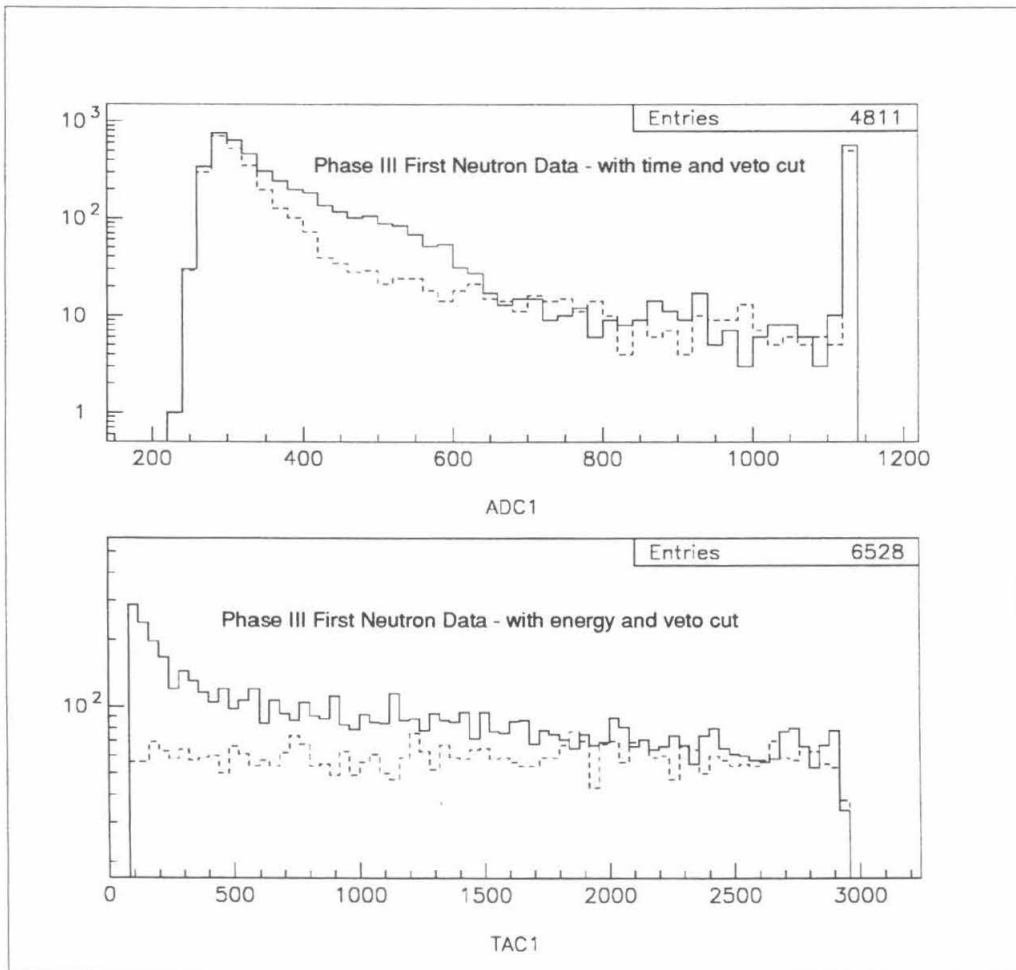


Figure 10.12: Single neutron excess in the Phase III data.

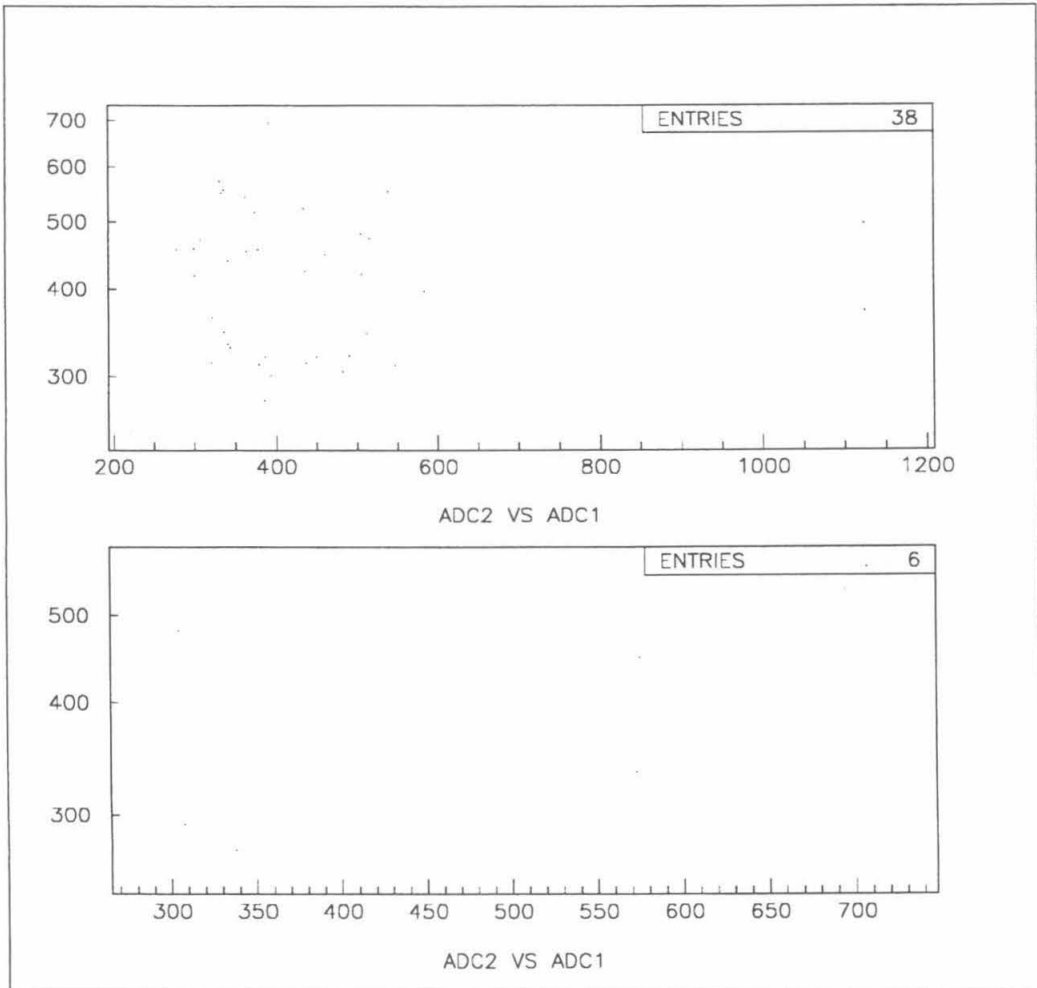


Figure 10.13: Double neutron scatter-plots, for the Phase III data.

ing the muon triggers. We can place a time cut on the events, requiring that  $TAC1 < 428$ , in order to look for delayed counts less than  $11 \mu s$  from the initial trigger. Within this short interval, there is still the possibility that a correlated neutron capture might occur. These events can be eliminated by a subsequent energy cut, if desired. In the analysis, we can also include the traditional veto cuts, rejecting accidental muons that registered in the veto counters, to further reduce the background. For the time being, we will postpone our examination of the energy in the bottom muon counter, that might be associated with the stopped muons that are expected to contribute to the short, time correlated counts.

In Fig. 10.14, the real versus fake histograms, with time and veto cuts, are presented. We see in the upper plot that the real count excess extends throughout the energy spectrum, for these short capture times, as opposed to the neutron capture excess, previously analyzed, which extended only up to channel 700. Above this energy, we can think about cleaning up the muon lifetime data sample, getting rid of any neutron captures remaining, by placing a cut requiring  $ADC1 > 700$ . After such a cut, we should have eliminated any neutron capture events from the data sample, but we will have rejected some of the valid  $\pi^+$  events. This is not a significant concern as the difference between a 3.5 MeV and an 8 MeV threshold on the electrons from muon decay is a small one. Placing this energy cut gives the resultant time histogram displayed in the lower plot of Fig. 10.14. The real data were fit to a single exponential plus a constant background. The quality of the fit was very good and the flatness of the fake histogram also agreed in magnitude, with the real histogram, at large time values. Extracting the fitted time constant, with our calibration, reveals that the rapidly decaying exponential has  $\tau = 2.0 \pm 0.15 \mu s$ , in agreement with the muon lifetime.

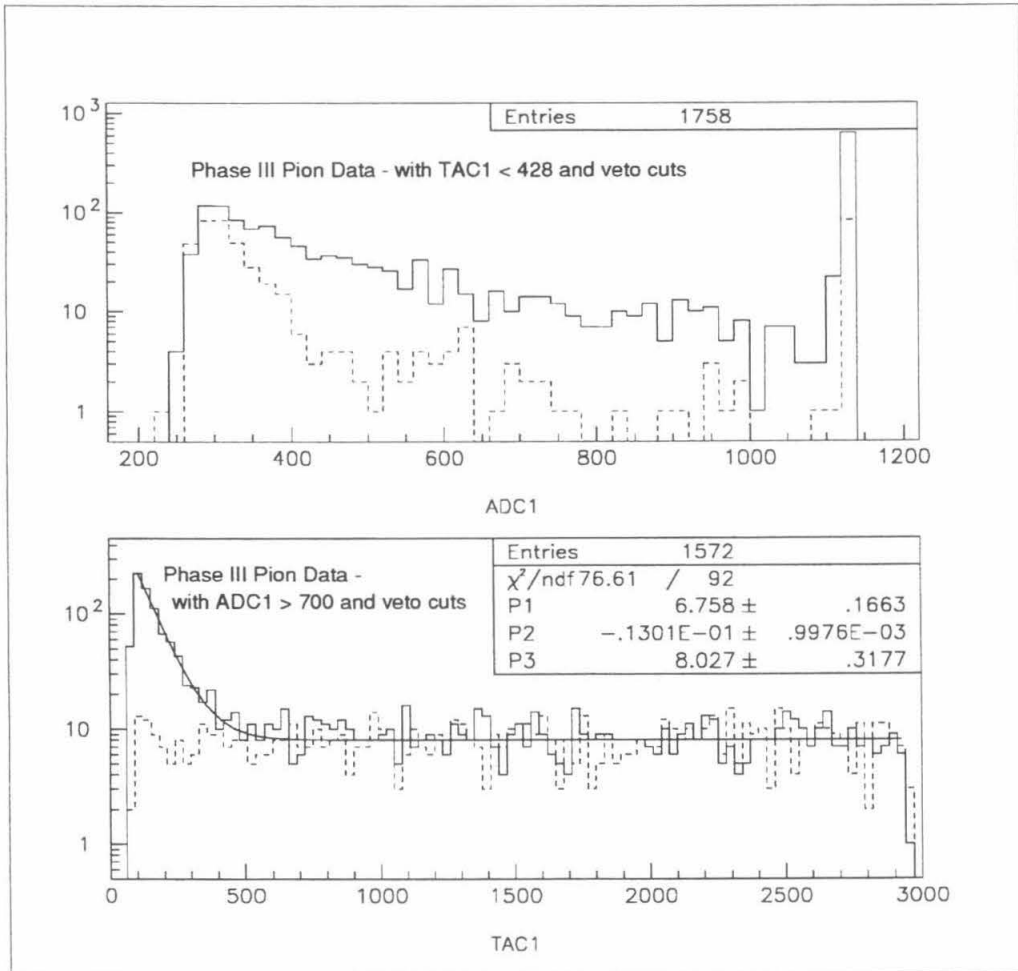


Figure 10.14: Short time constant histograms, for the Phase III data. Above, the energy histogram shows excess across the entire spectrum. Below, only the muon lifetime component remains in the time spectrum after cuts.

When all the cuts are included, time, energy and veto, we are left with 820 counts in the real data set and 100 counts recorded after the fake triggers. These pion candidates are high energy events that were recorded in the CUBE, within a time interval consistent with muon decay. The 100 counts seen in the fake data indicate the level of accidental background in the real data sample. Of the remaining correlated counts though, the question to ask is how many of these were  $\pi^+ \rightarrow \mu^+ \rightarrow e^+$  events, produced by muon-nuclear interactions, and how many of these were just stopped muons, in the bottom paddle, that fired their decay electron into the main detector?

By examining the recorded ADC values of the muon counters, in these events, we are able to get some insight into this problem. Plots of the muon veto values, readout at the same time as the CUBE, are displayed in Fig. 10.15. In comparing the 820 real events with the 100 fake ones, we would expect that if the muon veto counter were completely unrelated to the nature of the correlated event, that the shape of the real and fake data would be identical and that the amplitude of the fake histograms would be about a factor 8 lower, uniformly across their ranges, compared to the real histograms.

We see quite clearly in the plot of VEB1 that this is not the case. Counts appear in the real histogram with a good portion of the spectral intensity extending away from the ADC pedestal (where we expect to find most of the ADC counts of the muon paddles). There certainly appears to be correlated energy deposited in the bottom paddle in these events. These are the events in which a muon stopped in the bottom paddle, triggering the experiment. Its decay electron made it into the detector, giving rise to a large signal there. As this electron had to travel out of the bottom counter where it was produced, it leaves energy here also. Note that the energy scale of this

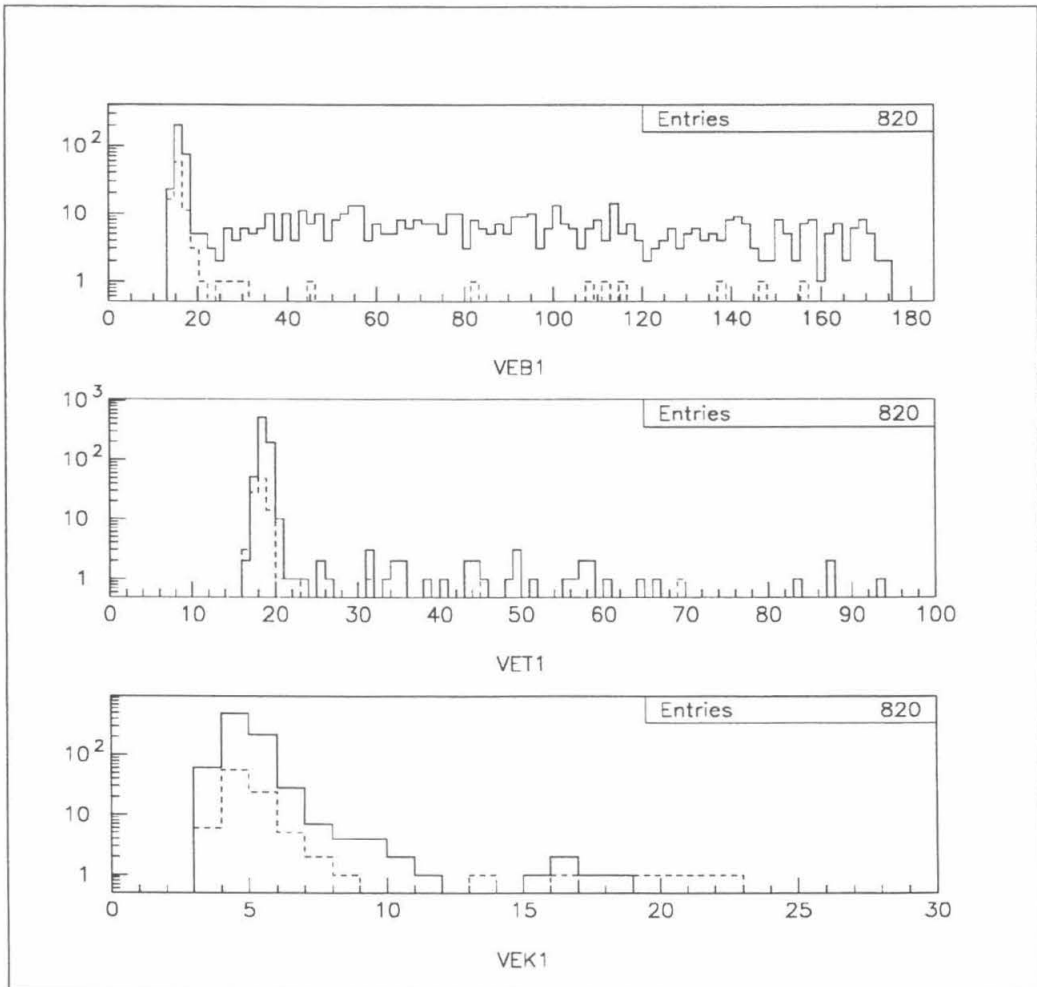


Figure 10.15: ADC readout of the muon vetoes, for the  $\pi^+$  candidate events. The real trigger data are in the solid histograms; the fakes are plotted in the dashed histograms.

VEB1				VET1			
cut	real	fake	real/fake	cut	real	fake	real/fake
< 175	820	100	8.20	< 100	820	100	8.20
< 100	602	94	6.40	< 50	806	99	8.14
< 40	362	92	3.93	< 30	787	97	8.11
< 35	342	92	3.72	< 20	771	94	8.20
< 30	328	91	3.60				
< 21	308	87	3.54				
< 20	306	85	3.60				
< 18	288	82	3.51				

Table 10.4: Real over fake ratios in the veto counters.

histogram already excludes muons (the ordinary veto cut at channel 175), at the lower edge of their distribution (see Fig. 10.3). Thus, the upper range of this histogram corresponds to something like 5 MeV.

In contrast, the histograms for VEK1 appear to show that the real data are indeed just scaled up from the fakes; this confirms that our side muon counter is unrelated to the nature of the correlated counts. It is a little harder to see the ratio of the VET1 histograms, from the way they happened to be plotted. Table 10.4 gives some indication of their comparative shapes. We see there that the integrated counts, up to various values in the spectra, all possess the same ratio of real counts over fakes, quite unlike the data from VEB1. Thus, we also conclude that the top muon counter is unrelated to the circumstances of the correlated events.

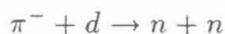
From Table 10.4 we also see where we should place the additional cut in VEB1 to eliminate the stopped muon contribution. Looking down the list, we see that as we continue lowering the allowable value for VEB1, the ratio of real versus fake counts drops until it reaches a value of about 3.6. At this point, we know that our cut affects the real and fake data equally; i.e., we would be cutting only accidental counts from both samples if we continued

lower. This is confirmed by examining the excess of counts, real minus fake, for cut values near 20. We find that the difference does fluctuate, but by only  $\pm 1\sigma$ . Thus, we can place our cut anywhere here, say at  $\text{VEB1} < 20$ , safely below the value where the stopped muons begin to contribute. Finally, we conclude that the correlated excess from  $\pi^+$  production, that we find in our pure data sample, is 221 counts.

## 10.4 Associated Pion-Neutron Production

When considering neutron production, pions are interesting to examine in parallel (hence our motivation for extracting the  $\pi^+$  signal from our data). For neutrons that are released in violent muon-induced nuclear disintegrations, it is possible that free pions are produced in the resultant high energy hadronic showers or cascades. Thus, we might expect that neutrons could be accompanied by pions, following muon spallation. Alternatively, we might consider lower energy interactions leading to neutron production, initiated by muon spallation, that actually proceed via pion intermediaries. That is, it might be that the secondary pion-nuclear interactions contribute significantly to the production of fast neutrons, that we are interested in.

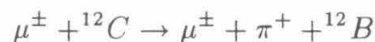
As an example of the latter, it has been postulated by some [96], that nuclear  $\pi^-$  capture might be a significant source of muon-induced fast neutrons. The  $\pi^-$  is produced in the spallation process by a passing muon. The  $\pi^-$  captures on a “pseudo-deuteron” in a nucleus:



giving rise to double neutron emission.

As an example of the former case for pion-neutron associated production,

at somewhat lower energies, consider the case where a muon-induced interaction, via virtual photon exchange, creates a free  $\pi^+$ , from the nucleus of  $^{12}\text{C}$ . The interaction:



requires that a proton in the nucleus be converted to a neutron to conserve charge. The  $^{12}\text{B}$  nucleus, left in an excited state, could give up some of its energy by nucleon emission. For this nucleus, possessing too many neutrons, there would be the tendency to evaporate a neutron, bringing the nucleus to stable  $^{11}\text{B}$ . In such a process then, we would expect that  $\pi^+$  production would be accompanied by neutron evaporation.

As we were able to extract the pion production signal from our data taken in Phase III, we can also consider proceeding to examine what fraction of the detected pions were accompanied by delayed second counts. Starting with candidate pions, where we have required that the first delayed capture time be less than  $11 \mu\text{s}$  and we have included the ordinary veto cuts in both the first and second delayed data, we find that 59 events have a second delayed count, in the real trigger data sample, and only 4 events in the fake are double counting events. Fig. 10.16 shows the scatter-plot of these events.

Here, unlike the earlier plots discussing the extraction of the double neutron events, the high density of points on the vertical line at the overflow bin of ADC1 appear only in the real data sample and quite clearly not in the fake. These are not the H-L correlated single neutrons we discussed previously; that was a source of background, unrelated to the initial muon, that appeared equally in the real and fake. These real points indicate events correlated to the initial muon. They could be the correlated pion-neutron

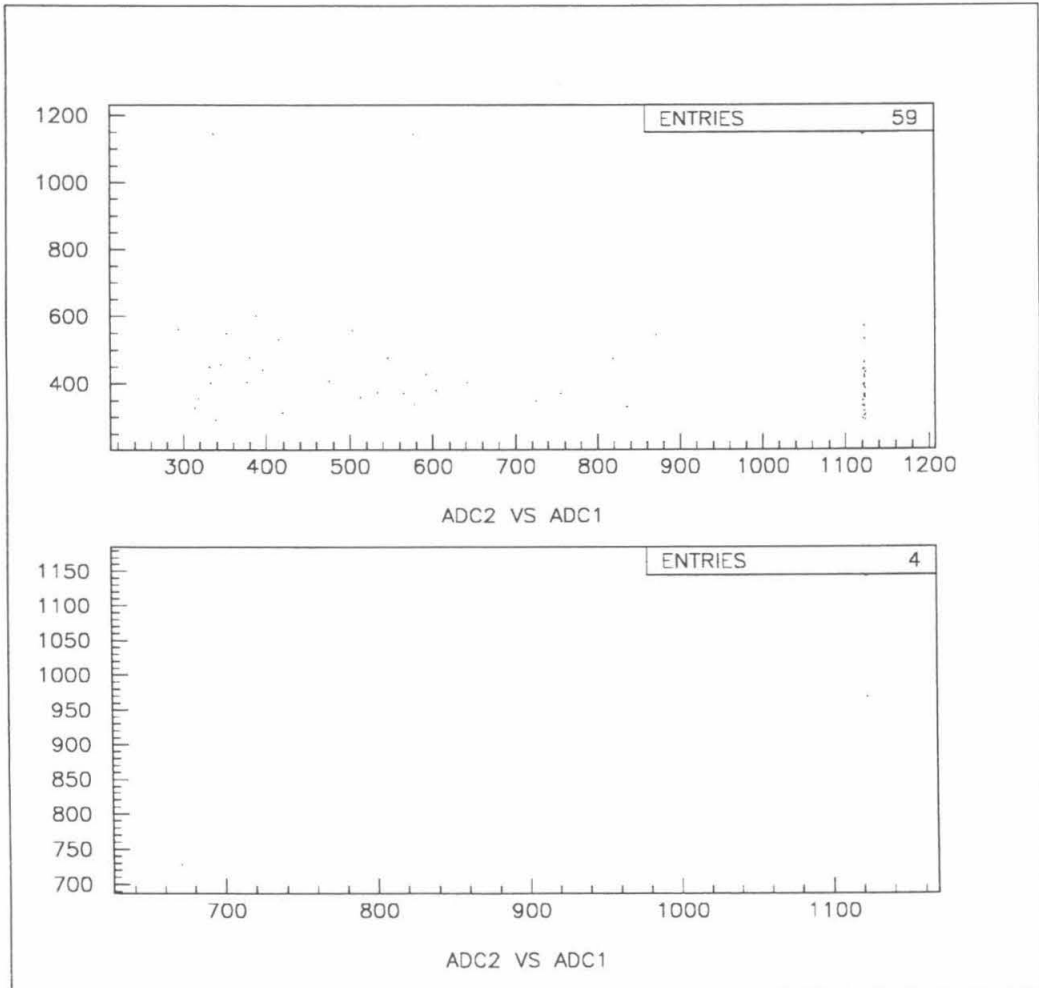


Figure 10.16: Associated pion-neutron scatter-plots, from Phase III data. The upper plot is for the real trigger data set and the lower one is for the fakes.

ADC1	ADC2	<i>measured</i>		<i>calculated accidental</i>	
		real	fake	real	fake
L	L	26	1	0.44	0.17
L	H	2	0	0.10	0.04
H	L	29	0	0.34	0.04
H	H	2	3	0.08	0.01

Table 10.5: Pion-neutron double count analysis for the Phase III data. The accidental background rates expected in each category are listed.

associated production events, that we are searching for.

We proceed with the same low-high categorization of these counts as was done previously. The results are listed in Table 10.5. We see that the predicted accidental background rates are negligible. What is the nature, then, of the observed counts, correlated background or events of interest?

We find about the same number of counts in the H-H category, in the real and fake. This leads us to believe that these counts, correlated first-second events, unrelated to the initial muon trigger, were ordinary muons which stopped in the CUBE and decayed. No time cut was placed on the TAC2 values; thus, we expect to find these events at short capture times. The L-H counts in the reals could also be of the same origin. The low energy in the first delayed count indicates that the muon stopped very soon in the CUBE, depositing a smaller amount of energy than typical. The decaying electron could make the second high energy count. Indeed, upon examining the TAC2 values for the two H-H reals and the two L-H reals, we find that all four occurred at shorter times than  $4.3 \mu\text{s}$ . Of the three H-H fakes, and the 1 L-L fake, which was just barely low in both the first and second ADC, the latest capture time was  $9 \mu\text{s}$ ; another was  $5.2 \mu\text{s}$  and the others were shorter.

Fig. 10.17 plots a histogram of the TAC2 values for the 59 real double

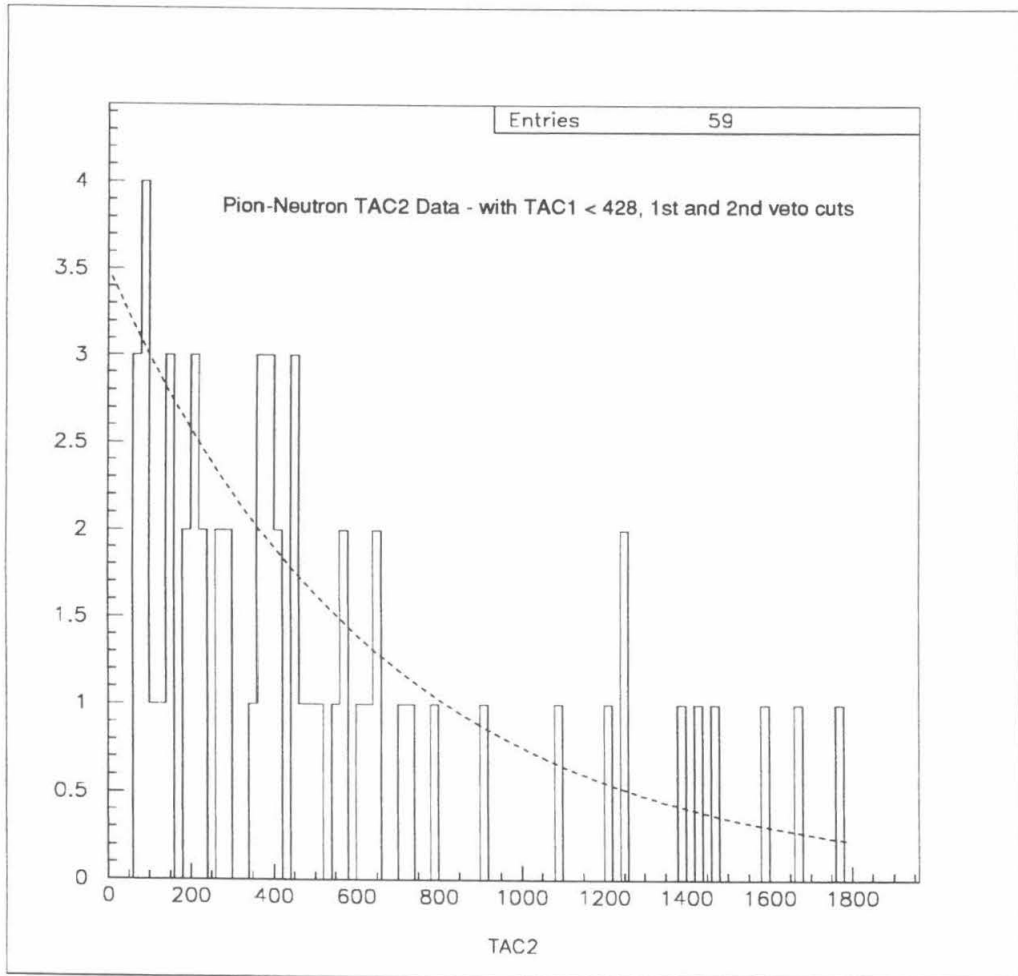


Figure 10.17: TAC2 histogram of the real pion-neutron events. The exponential constant of  $29 \mu\text{s}$  was not fit to the data. From the Phase III runs.

counting events. We observe, in this plot, that the TAC2 values appear consistent with a long time constant correlation. The exponential plotted in this figure has the neutron capture time constant of  $29 \mu\text{s}$ , and was placed there just to deceive the eye — it was not a fit to these sparse counts.

In Fig. 10.18, the ADC2 values of the 59 real double counting events are displayed (projection of the scatter-plot). This plot shows quite clearly that, aside from the four L-H and H-H events, the rest of the second counts fall within the proper energy range for neutron capture on Gd.

Just to make sure that the first counts, in this real data sample, are the  $\pi^+$  signals, Fig. 10.19 plots the ADC readout of the VEB1 veto counter, for the first delayed signals. Unlike the earlier analysis, now none of these events appear with substantial energy in the bottom paddle. We are reassured that these are indeed pions that were produced in the CUBE by the passing muon trigger, and are not the background stopped muon signal.

From these results, we conclude that the 55 counts of the L-L and H-L categories are undeniably correlated to the initial muon trigger. The nature of these events is consistent with them being from  $\pi^+ \rightarrow \mu^+ \rightarrow e^+$  decay in the first delayed window (short time, any energy) and possessing a neutron capture in the second delayed window (correct energy range, long time constant). The trigger, first and second events are all correlated. We conclude that these events are observations of associated pion-neutron production, following through-going muon spallation.

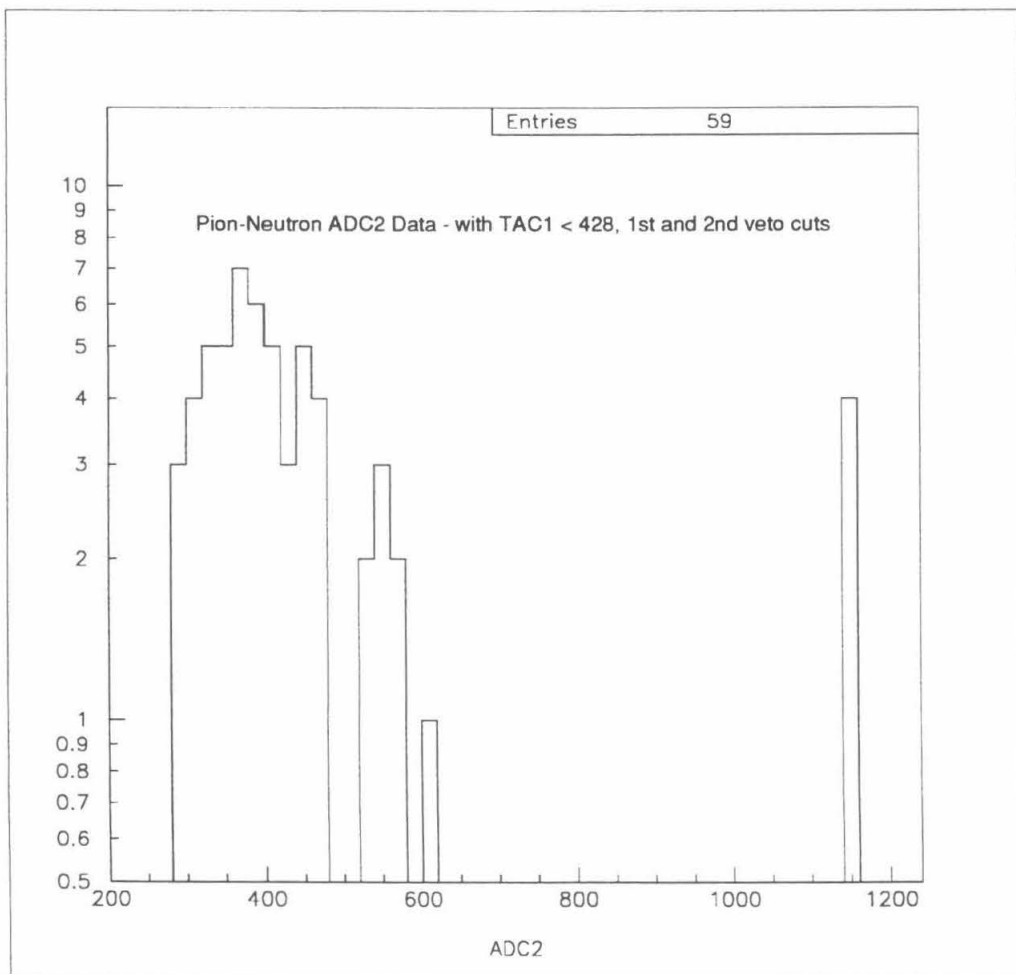


Figure 10.18: ADC2 histogram of the real pion-neutron events.

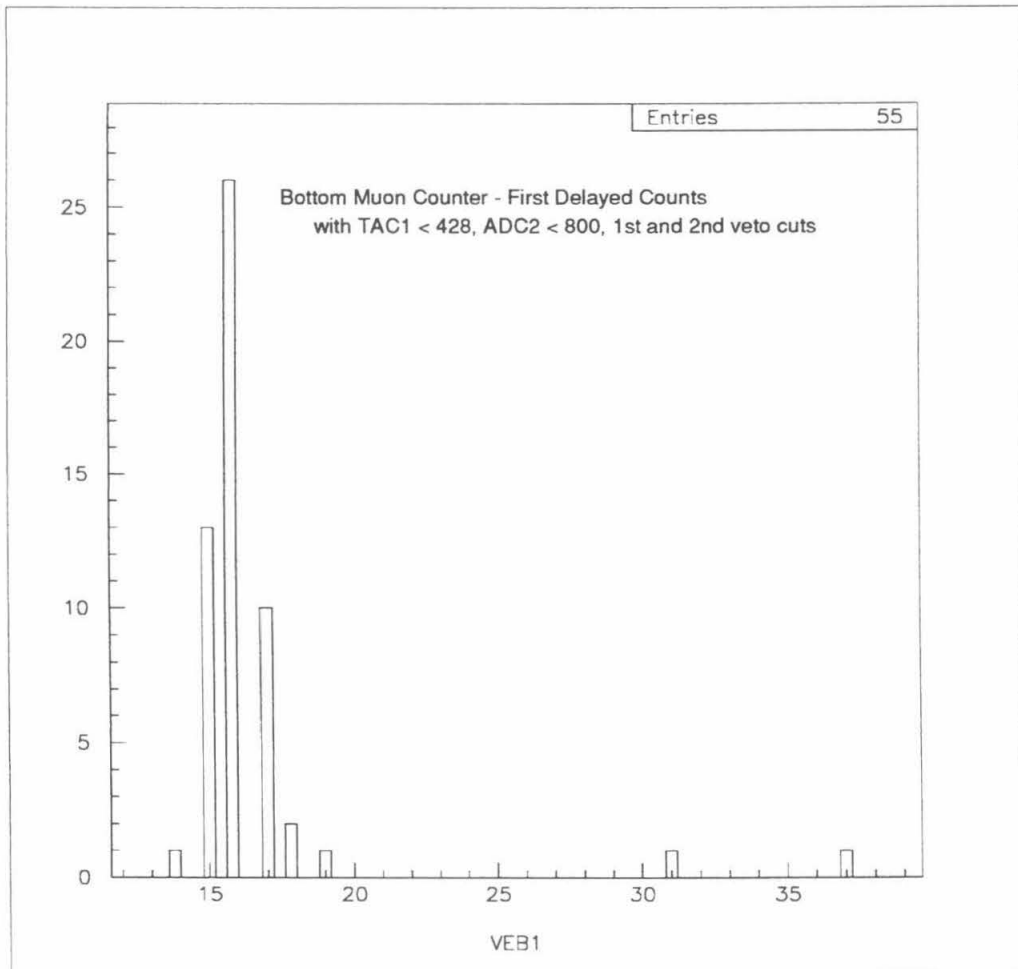


Figure 10.19: VEB1 values for the real pion-neutron events. No substantial energy is seen in the bottom muon counter, ruling out that stopped muons somehow contributed in this data sample.

## Chapter 11

# Discussion of Neutrons and Pions

### 11.1 Modeling Neutrons in the Detector

For the purpose of generalizing and comparing our measurements to other experimental geometries, it is necessary to perform some modeling of our detector, in order to extract the spallation neutron yield from our measurements of the correlated, excess neutron counts. The relationship between yield and detected neutrons is given by,

$$N_n = N_\mu Y \bar{X} \epsilon, \quad (11.1)$$

where  $N_n$  is the total observed neutron excess,  $N_\mu$  is the number of muon triggers that passed through the detector,  $\bar{X}$  is the average path length of the triggered muons through our CUBE, in units  $\text{g}/\text{cm}^2$ ,  $\epsilon$  is the effective neutron detection efficiency of our experiment, and  $Y$  expresses the spallation probability or yield in terms of neutrons produced per muon per  $\text{g}/\text{cm}^2$  of material traversed.

The average path length of the triggering muons in our detector was determined with a simple ray-tracing Monte Carlo calculation. Muons with a  $\cos^2 \theta$  angular distribution were randomly generated, striking the bottom muon paddle. It was straightforward to calculate the path length of scintillator that these muons would have traversed, in our detector geometry. In

the calculations, the 7/8-inch thick styrofoam piece separating the bottom counter from the CUBE was taken into account, as was the maximum liquid level in the detector (it was only filled up to about 2 cm from the very top).

There are two trigger modes to consider. In the simulation of the detector-bottom coincidence trigger, it was required in the calculation that the muon traverse more than 3 cm of liquid scintillator, in order to have triggered the 6 MeV discriminator that was a part of this implementation. The result of this calculation was that, for muons which served as the trigger in the Phase I and II data runs, the average path length was 43.1 cm. For a liquid scintillator density of  $\rho = 0.86 \text{ g/cm}^3$ , this path length comes to  $37 \text{ g/cm}^2$  of material.

For the other trigger which required top counter, bottom counter and main detector in coincidence, the Monte Carlo calculation finds the average path length to be 58.1 cm. Note that these were not necessarily straight up-down paths through the CUBE as the top muon counter extended slightly beyond the dimensions of the box. Thus, in the Phase III data runs, the triggered muons pass through, on average,  $50 \text{ g/cm}^2$  of scintillator.

The total neutron detection efficiency of the experiment can be broken down into three components. First, there is the efficiency for the muon-produced fast neutrons to thermalize and capture in the CUBE. Second, there is the requirement that the 8 MeV total energy, Gd capture gammas are detected above the 3.5 MeV threshold. Finally, there is the efficiency term that is introduced by the analysis cuts, considered separately from the previous, hardware-imposed efficiency component.

As our certainty of the shape of the energy spectrum of the neutrons from muon spallation is somewhat murky, our greatest uncertainty, in this experiment, lies in our inability to precisely estimate the neutron capture

efficiency. In a study by Barton [97], it is given that the spectrum of neutrons from hadronic cascades falls off in energy as  $\sim E_n^{-1/2}$ , between 10 to 50 MeV. It is also mentioned that the process of  $\pi^-$  capture by pseudo-deuterons produces neutrons with a flat spectrum up to about 100 MeV. However, no one has ever directly measured these very high energy neutrons to determine how much they contribute. In general, the intensities of each of these neutron branches, including the excitation of the giant dipole resonance, by a passing muon, followed by neutron evaporation at low energies, are not well specified in any reference. Thus, without a definitive choice as to how the energy spectrum should be parameterized, in our calculation, a combined shape, including an exponential component and the  $-1/2$  power term, was used to approximate the spectral shape indicated by Barton's measurements — this spectrum, suggested by [100], was also used in [101].

A second source of uncertainty lies in the neutron transport calculations. The code that was used [102], an unpublished neutron Monte Carlo, has been proven to give reasonable agreement in some measurements [101]; nevertheless, uncertainties are inherent in any Monte Carlo. This neutron transport code includes elastic scattering on H and C, in the scintillator; it includes the inelastic scattering cross-sections on C and also the neutron capture cross-sections on H and Gd. As a sample of the Monte Carlo's general capabilities, Fig. 11.1 presents the calculated neutron capture time in a 0.11% Gd-loaded liquid scintillator. The Monte Carlo finds a time constant of 23  $\mu\text{s}$ , not in bad agreement with the expected value of 24  $\mu\text{s}$ . From the figure, we also note that the neutron thermalization time is about 6  $\mu\text{s}$ , and before that time, the capture probability is not appreciable.

The neutron Monte Carlo was employed to model the capture probability for fast neutrons produced by muon spallation. The probability that

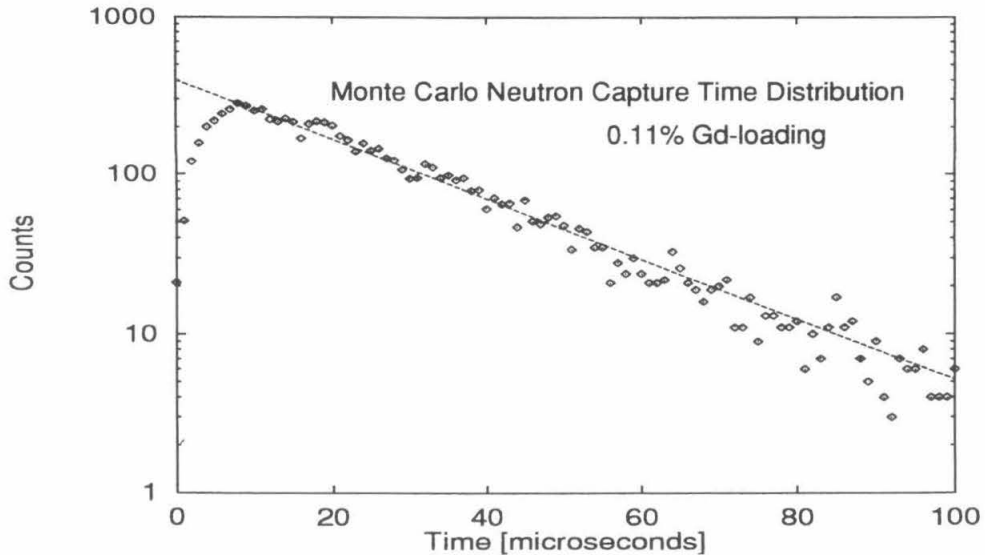


Figure 11.1: Monte Carlo calculated neutron capture time, in Gd-loaded liquid scintillator. The exponential dashed line has a time constant of  $23 \mu\text{s}$ .

a neutron, produced at various energies, would be captured on Gd within the volume of the CUBE detector was simulated. Neutrons were distributed homogeneously throughout the detector volume. In Fig. 11.2, these probabilities are plotted. When this efficiency curve was folded with the neutron energy spectrum, we arrive at an estimate for the effective, weighted, neutron capture probability of 37%. The relative uncertainty in this calculation could be as high as 20%, implying that our efficiency estimate could be off by  $\pm 7\%$ , due to our inability to pin down the exact shape of the neutron energy spectrum.

For the gamma portion of the efficiency, the EGS4 Monte Carlo was run to track the capture gammas. From the results of these simulations, we found a gamma detection probability of 40%, above the 3.5 MeV threshold. Combining both the neutron and gamma terms leads us to a total neutron

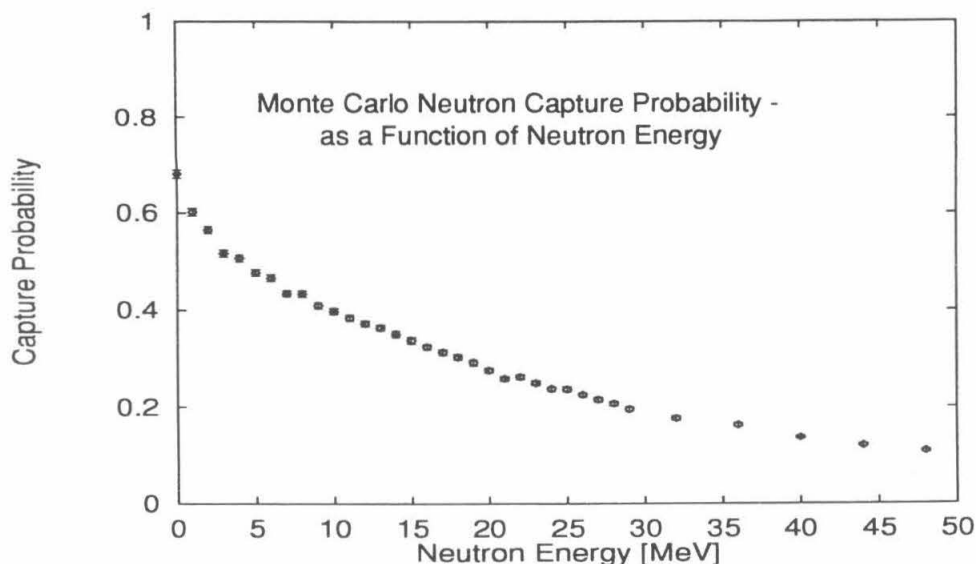


Figure 11.2: Monte Carlo calculation of the neutron capture probability in the CUBE detector. Neutrons were produced homogeneously in the volume and it was required that the neutron be captured on Gd, within the detector.

detection efficiency of 15%, in the Gd-loaded scintillator, aside from the analysis cuts.

In our analysis, we reject events based on energy, veto and time information. The energy window which was selected was not restrictive enough to reject any neutron signal. That cut maintains 100% signal efficiency. It is conceivable that in using our veto cuts, we might have thrown out a true neutron signal if a portion of the Gd capture gamma rays interacted in one of the paddles, leaving enough energy to look like a muon (about 5 MeV). This would actually be rather unlikely as we did require 3.5 MeV to be deposited in the CUBE itself for the event to be counted. Thus, almost all of the remaining energy of the other gammas in the cascade would have to deposit their full energy in one relatively thin paddle, to total up to 4.5 MeV, close to where the muon veto cut was placed. Therefore, let's also assume

Data Run	$N_n$	$N_\mu$	$\bar{X}$ [g/cm <sup>2</sup> ]	$Y$ [n/ $\mu$ /(g/cm <sup>2</sup> )]
Phase I	2067	$1.4 \times 10^7$	37	$3.3 \times 10^{-5}$
Phase II	2934	$1.675 \times 10^7$	37	$3.9 \times 10^{-5}$
Phase III	1327	$7.2 \times 10^6$	50	$3.1 \times 10^{-5}$

Table 11.1: Single neutron production yield.

that our veto introduces no inefficiency. Only the time window of 11–78  $\mu\text{s}$  is significant in the analysis efficiency. Within this interval, we would expect to detect only 82% of the Gd neutron captures, for a 29  $\mu\text{s}$  mean capture time. In this estimate, the neutron thermalization time of 6  $\mu\text{s}$  was also factored into the calculation.

Thus, we arrive at a total neutron detection probability, for events which recorded a single neutron, of  $0.37 \times 0.40 \times 0.82 = 12\%$ .

Inserting the measured or calculated values of the various terms in expression (11.1) for each data set, we can compare the calculated neutron yields. Table 11.1 presents the single neutron production yield results, computed from the measured single neutron excess in each of the three data runs.

The excess neutron counts were determined by a subtraction of fake histograms from the real ones. To determine the proper statistical error in the value of  $N_n$ , it is necessary to take the square root of the *sum* of the real and fake counts. Thus, the errors in  $N_n$  for the three data sets are  $\pm 120$ ,  $\pm 127$ , and  $\pm 83$  counts, for Phase I–III respectively, and this comes to  $\pm 0.2 \times 10^{-5}$  in the neutron yield. Results from Phase I and II can be compared directly without introducing any systematic terms, as they both collected data with the same trigger configuration. The spallation yields measured in the two runs differ by  $3\sigma$ , not so terrible. Perhaps some of this discrepancy is due to the minor modifications made to the electronics — ultimately, this difference will not be important when the systematic errors are factored in.

When comparing to the Phase III data, we must also include an error estimate in the calculated muon path lengths. The ray-tracing code couldn't be off by more than  $\pm 2$  cm in its calculation of the average amount of material traversed by the muon; this translates to a systematic error of  $\pm 0.2 \times 10^{-5}$  in the yield. Combining this with the statistical error, we can average the three results. Finally, by adding to this the systematic uncertainty of 20% arising from the imperfect knowledge of the neutron capture efficiency, we arrive at our final conclusion for the production of neutrons by muon spallation:

$$Y = (3.4 \pm 0.2 \pm 0.7) \times 10^{-5} [\text{n}/\mu (\text{g}/\text{cm}^2)],$$

where the first error term is statistical plus the systematic error of the path length, and the second error term encompasses the uncertainty in our knowledge of the neutron capture probability.

## 11.2 Neutron Multiplicity

The same efficiency terms that were considered for extraction of the single neutron production yield also carry over to the analysis of the double neutron events. There are, however, some unique issues to think about for the double neutrons.

For one, the energy spectrum of the muon-induced doubly emitted neutrons is even more poorly known than for the ordinary spallation neutrons. It seems reasonable that since two neutrons share the excitation energy, that per neutron, the energy would be lower than in single neutron events. However, the postulated double neutron mechanism of  $\pi^-$  capture on a pseudo-deuteron would instead suggest a broader and flatter spectrum (system approximates two-body kinematics, in a moving center-of-mass frame), and

some neutron spectrum measurements by Madey et al. [103] seem to concur. Until further studies can resolve which is more important in the muon spallation process, we apply the same 37% effective neutron capture probability on both neutrons, assuming that each neutron had the same capture probability as if they were emitted individually.

The other issue is the capture time. Assuming that both neutrons thermalized and captured on Gd in the CUBE ( $37\% \times 37\%$ ), and that both cascades of gammas fired the 3.5 MeV threshold (40% probability, squared), finally, we need to determine what fraction of these captures would have occurred within acceptable time windows. In a system with two possible captures and two actual captures, the first and the second are unambiguous; it is not necessary to worry about any “double-counting” problem. However, the capture time distribution of the first neutron is affected by the presence of the second neutron. As the first capture could have been from either neutron, the probability to observe one interaction is doubled — the capture time constant, in the first window, should be half of its normal value, for double neutron events. Thus, we expect the first window time histogram to fall off with a  $14.5 \mu\text{s}$  lifetime. Fig. 11.3 plots the TAC1 values for the 72 count double neutron data sample from the Phase II runs. The fitted exponential decay time of  $19.4 \pm 7.9 \mu\text{s}$  is shorter than the nominal value for single neutrons of  $29 \mu\text{s}$ . We shouldn’t read too much into this fitted result as the error bar is large. It was just interesting to look at this distribution.

Thus, in our first time window, 11–78  $\mu\text{s}$ , taking the thermalization into account, we find 80.5% acceptance for the first count. In the second window, the normal  $29 \mu\text{s}$  capture time applies again. Here, we do not account for the thermalization time again as the second neutron presumably did so at the same time as the first. In this time window, we calculate a 61.6% efficiency.

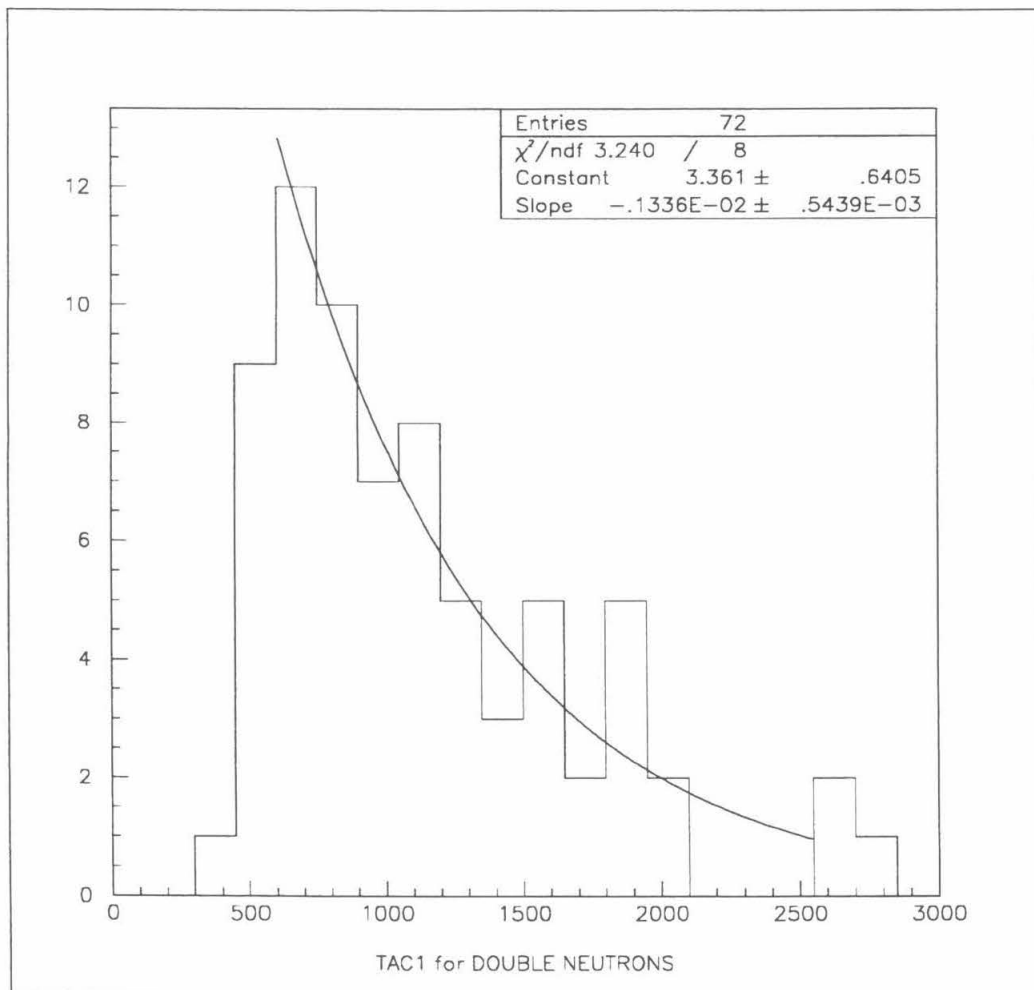


Figure 11.3: TAC1 histogram for double neutron events. The fitted exponential decay is shorter than the nominal value of  $29 \mu\text{s}$  for a single neutron.

Data Run	measured $N_n$	measured $N_{2n}$	neutrons produced single : double ratio
Phase II	2934	65.8	$(4.0 \pm 0.7) : 1$
Phase III	1327	29.5	$(4.0 \pm 1.0) : 1$

Table 11.2: Double neutron production and multiplicity.

Table 11.2 lists the measured, excess single and double neutron counts, from the Phase II and III data runs. It relates the results and expresses them as a multiplicity ratio, after correcting for the additional efficiency terms in the second neutron capture. The comparison is thus between the production of single and double neutrons as opposed to their detection ratio.

### 11.3 Relating Neutrons and Pions

We are poorly equipped to study the necessary terms that play a role in the pion detection efficiency. As our goal in this measurement was to examine the neutron production by muon spallation, the pion production excesses that we observed were bonuses. However, some effort to understand, qualitatively at least, the role pions play in fast neutron production would be useful. A number of issues will be discussed below.

When considering the produced pion spectrum and a calculation of the efficiency for  $\pi^+$  to stop within the CUBE, we are even more in the dark than for the neutrons. For those  $\pi^+$  that do stop and decay, at least the outgoing  $\mu^+$  momentum is known. However, no calculation was performed to factor in this muon range with a distribution of these events within the detector. Finally, for those  $\mu^+$  which stop and decay in the detector, we can state that we have close to full efficiency for observing the positron, aside from any energy threshold considerations for the moment. Let us make a simple guess at the efficiency, with a little help from re-wording the problem. We will

guess that for those positive-pions, produced by muons, of the appropriate energy range that they could stop in the detector, about 90% of them will actually do so and decay through a muon which also stops in the CUBE, that then decays into a positron, detected in the scintillator.

In our selection of the  $\pi^+$  signal, the time window of 2–11  $\mu\text{s}$  is only 39.6% efficient. The energy cut, requiring greater than 8 MeV in the detector for the Michel electron, removes some of the potential signal. Lastly, the general muon veto cut plus the VEB1 cut on the bottom paddle might also reject some of the true  $\pi^+$  signal. This could happen in a manner converse to the stopped muon in the bottom paddle background. In the case of our signal, the  $\pi^+ \rightarrow \mu^+ \rightarrow e^+$  might fire the energetic decay electron out of the detector, into one of the adjacent veto counters. The electron would then deposit coincident energy in the veto, looking either like a muon or like the punch-through electron of the stopped muon background, vetoing the event. This inefficiency should be a small quantity also as it is only possible for those muon decays which originate less than a few centimeters from the edges of the CUBE box (so that the electron can make it out to the veto). Taken all together, we make a second guess that an 80% efficiency term should be included to account for the selection cuts, (mostly the energy threshold).

Thus, from the 221 pion excess counts, out of 7.2 million triggers, we estimate the pion yield as

$$Y_{\pi^+} = 2.2 \times 10^{-6} [\pi^+/\mu (\text{g}/\text{cm}^2)],$$

where the amount of material traversed was 50  $\text{g}/\text{cm}^2$  and the overall efficiency was 28.5%.

With this value for the pion yield, probably correct only in order of mag-

nitude, we can make the statement that pion production appears not to be solely responsible for all of the fast neutron production by muons. We conclude that there must be other processes, in addition to the pion-nuclear secondary interactions, which contribute most of the neutrons produced in muon spallation.

A second observation relates to the production of double neutrons. In our attempt to quantify the  $\pi^+$  production, we can also make the claim that about as many  $\pi^-$  were made by the muon interaction. We believe that  $\pi^-$  capture is a mechanism for double neutron emission (the measured mean neutron multiplicity for nuclear  $\pi^-$  capture, on many targets including carbon, is  $1.74 \pm 0.28$  [103]). We see from our analysis, however, that the  $\pi^-$  production/capture mechanism, by itself, would not be sufficient to yield all of the double neutron events that we observed following muon triggers in our detector — it comes short by a factor of four. Thus, there must exist additional, direct processes whereby multiple neutrons are emitted following a muon-nuclear interaction.

From our observation of associated  $\pi^+$ -n events, we can determine the fraction of  $\pi^+$  events which also contained a second neutron. In our  $\pi^+$  selection, we required time, energy and veto cuts. If we maintain the same selection criteria on the first  $\pi^+$ , and require that a second neutron-like count appear with  $\text{ADC2} < 800$ , we find 31 events satisfying the criteria for  $\pi^+$ -n associated production, out of the 221 pions. There were zero background counts in the fake trigger data, passing all of these cuts. Thus, the ratio of detected neutrons versus number of  $\pi^+$  is just 31/221.

To get the actual ratio produced, we need to include the efficiency terms. There was 37% for the neutron capture. The applicability of this value, determined for the direct spallation neutrons, should be questioned as the

energy spectrum of the associated neutrons might tend to be softer and more similar to the evaporation spectrum. Secondly, there was the 40% gamma detection efficiency term. Finally, for the capture time window, we used the full 2–78  $\mu\text{s}$  interval since the background was so low, giving us an efficiency for the analysis cuts of 86.5%. All combined, the neutron detection efficiency is estimated at 12.8%. Therefore, we conclude that the fraction of  $\pi^+$  events which were accompanied by a produced neutron is

$$\frac{N_{\pi^+-n}}{\epsilon N_{\pi^+}} = 1.1 \pm 0.2,$$

with the statistical error given.

There are many ways to interpret the above value. It could be, quite simply, that this measurement indicates that neutrons typically accompany every free  $\pi^+$  that is produced on  $^{12}\text{C}$ . Perhaps the  $^{12}\text{B}$  neutron evaporation process, discussed previously, occurs with near 100% branching probability, following muon spallation production of  $\pi^+$ . If, on the other hand, one wishes to doubt the 37% capture probability, on account of the possibly lower energies of these associated neutrons (as opposed to direct spallation neutrons), then from Fig. 11.2, one might suggest that perhaps the effective probability is more like 50%. With this value, we still find that 80% of the measured positive pions would have been produced with a second neutron. Thus, our uncertainty in the neutron capture efficiency can be included as a systematic error of another  $\pm 0.2$  in the neutron fraction.

Alternatively, it could be that a much smaller fraction of the free pions are accompanied by neutrons; but, when they are, there are typically multiple neutrons emitted with the pions (complete nuclear disintegration process). In such a case, the probability to detect one of these many neutrons would

be significantly higher, allowing the neutron/pion ratio to actually be much smaller. Though the nuclear disintegrations could contribute at some level to the total neutron and/or pion production by muons, it seems more likely that the lower energy process of free pion creation, and the associated evaporation of neutrons, are still a good explanation for these  $\pi^+$ -n events.

## 11.4 Comparison to Other Experiments

The one experiment we are most interested in comparing our result to was the measurement by Bezrukov et al. [104], performed at a depth of 25 mwe. Their measurement was very similar to the one that we performed and will be described briefly below.

The Russian experiment employed a roughly cubical detector which could hold a volume of 314 liters of Gd-loaded liquid scintillator, larger than our CUBE which holds roughly 200 liters. The quantity of Gd that they selected to load in their scintillator resulted in a neutron capture time of 50  $\mu$ s. Counters were placed above and below their middle chamber; unlike our muon paddles, these counters were boxes of liquid scintillator 32 cm thick. They triggered their detector in a mode requiring only coincidences between the central detector and the bottom layer.

Surrounding their middle detector, they packed paraffin blocks which presumably served as shielding. Their signals were readout on a 5-beam oscilloscope and photographed. They claim a neutron registration threshold of 2.6 MeV (for the Gd capture gammas), but it was not described how this threshold was implemented. Furthermore, details regarding the subtraction of accidental backgrounds during the 50  $\mu$ s were not supplied. They make a statement that 50% of the events were true and 50% random at the 25 mwe

site. How well this was determined is unknown.

They measured 1,520 neutron counts over a period of 25 hours! This was quite a good rate, despite their Gd-loaded detector being not that much larger than ours. They give the average path of the muons in their counter as 43 g/cm<sup>2</sup>. They do not include the material outside of the middle counter, through which the triggered muons also pass, possibly producing neutrons all along the path. Just as a point to note, the total height of their detector, muon layers and paraffin stack was 154 cm. They give their neutron detection probability as being 60%. When divided by their total number of muons, they quote a neutron spallation yield of  $(4.7 \pm 0.5) \times 10^{-5}$  neutrons per muon-g/cm<sup>2</sup>. The error estimate they gave was due to the uncertainty in their neutron registration efficiency (they chose  $\pm 10\%$ ).

Before we begin comparing their results with ours, we should consider the neutron efficiency they estimated. The 60% value is hard to reconcile with our 12% efficiency. Certainly their detector is bigger; the presence of paraffin surrounding the detector has an impact on the efficiency by acting as a moderator. Fast neutrons, created in the middle detector, which would otherwise exit the experiment (as in our case) might be thermalized in their surrounding paraffin. The thermalized neutrons can walk some distance in unloaded paraffin, maybe even walking back into the Gd-loaded detector, which acts as a neutron sponge, and captures them. It is understandable that their neutron capture probabilities might be substantially larger than our 37% value; but, it is not understood how, with a not so substantially different Gd-loaded sensitive volume and with only a slightly lower gamma detection threshold, they seem not impacted by the 40% gamma efficiency that we calculated. It could be that they summed the gamma energies over their large upper and lower muon counters as well as the middle counter, in which

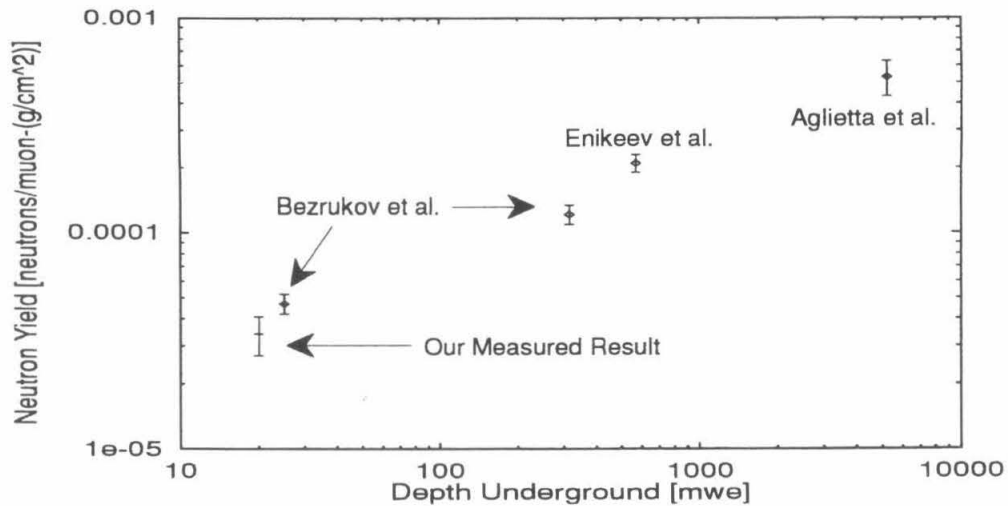


Figure 11.4: World plot of underground neutron yield measurements.

case they might actually have a somewhat improved gamma containment. Unfortunately, they do not describe their procedure.

Assuming for the moment that their efficiency and muon path length were correctly identified, we can compare their yield of  $4.7 \times 10^{-5}$  at 25 mwe with our value of  $3.4 \times 10^{-5}$ , at 20 mwe.

In Aglietta et al. [105], the neutron yield as a function of underground depth is plotted. Four experimental results are shown on this “world plot.” We duplicate this figure and add our data point at 20 mwe.

As the average muon energy increases with depth, so does the neutron spallation yield. When our data point is plotted with the other results [104, 106, 105], we see reasonable agreement with the general trend of the neutron yield versus underground depth.

In the measurement of Bezrukov, they observed 72 counts which were attributed to double neutron events. This is compared to the 1,261 events in which only a single neutron was observed. In order to compare this with our

estimated neutron multiplicity ratio of 4:1, single-to-double, we must employ their dubious 60% neutron detection efficiency again. One would then infer from their data, though they never extracted such a value, that they see a single-to-double ratio more like 11:1. This is in strong disagreement with our measurement. As this was not a claim of theirs, it may not be worthwhile to struggle too much with this difference. We did, however, learn very recently [100], that due to the necessarily large contribution of neutron production outside of their main detector, a different correction other than just the standard neutron efficiency must be included. If indeed most of their single neutrons came from the large amount of paraffin surrounding their middle detector, it is not necessarily true that their double neutron events also came from the outside. This is because the geometry/random walk probability for both outside neutrons to be detected inside the Gd-loaded volume is strongly reduced by the squaring of the probabilities. Thus, since the efficiency for double neutron detection is much greater for those events produced inside, it may be that they have measured the double neutrons produced inside the detector and the single neutrons produced both inside and out. This additional factor, considered recently by Ryazhskaya, would correct their 11:1 ratio and bring it more in line with our measured 4:1 single-to-double multiplicity.

## 11.5 Conclusions

The motivation for this experiment, which measured the neutron yield and multiplicity following muon spallation, was to further our understanding of the fast neutron backgrounds that will be present in the San Onofre detector. Despite the fact that the general features of the muon spallation process have

been known since the early 1950's, a complete understanding of the exact nature of all aspects of the production of fast neutrons is lacking.

In this experiment, we measured the neutron spallation yield on a liquid scintillator target (carbon), at an underground depth of 20 mwe. Our result of  $(3.4 \pm 0.2 \pm 0.7) \times 10^{-5}$  neutrons per muon-g/cm<sup>2</sup>, agrees reasonably with other experimental results.

We've also discovered that one out of every four such muon interactions produce two (or more) neutrons. The determination of these multiplicity ratios is complicated somewhat by the efficiency estimates and the increased probability to detect a single neutron, when many are present. Nevertheless, so long as the mean multiplicity is close to one, we are in a regime where our simply calculated probabilities and ratios are acceptable and valid.

Our observation of  $\pi^+ \rightarrow \mu^+ \rightarrow e^+$  events gives us some idea as to the level of contribution of pions to the total neutron production. Additionally, the observation of associated pion-neutron production confirms, undoubtedly, that a large fraction of the spallation pions are accompanied by neutrons, either produced simultaneously in the direct hadronic cascade or through secondary processes.

Without regard to how this measurement compares with others, we know at least that this measurement is applicable to the San Onofre experiment. It was performed at a similar underground depth and studied production of neutrons from muon spallation with the liquid scintillator target only. The results of these measurements establish a solid base upon which further estimates of the fast neutron background and its ramifications in the San Onofre detector can be made.

## Bibliography

- [1] W. Pauli, *Letter to the Physical Society of Tübingen*, unpublished (1931); reproduced in L.M. Brown, *Physics Today* **31**, 23 (1978); see also W. Pauli, in *Noyaux Atomiques*, proceedings of the Solvay Congress, Brussels, 324 (1933).
- [2] C.S. Wu et al., *Phys. Rev.* **107**, 641 (1957).
- [3] S. Weinberg, *Phys. Rev. Lett.* **19**, 1264 (1967).
- [4] S.L. Glashow, *Nucl. Phys.* **22**, 579 (1961).
- [5] A. Salam, in *Nobel Symposium, No. 8*, ed. N. Swartholm, (Almqvist & Wiksell, Stockholm, 1968).
- [6] J.J. Simpson, *Phys. Rev. Lett.* **54**, 1891 (1985).
- [7] K.S. Krane, *Introductory Nuclear Physics* (Wiley, New York, 1988).
- [8] E. Fermi, *Z. Physik* **88**, 161 (1934).
- [9] V.A. Lubimov et al., *Phys. Lett. B* **94**, 266 (1980).
- [10] V.A. Lubimov et al., *Sov. Phys. JETP* **54**, 616 (1981).
- [11] S. Boris et al., *Phys. Rev. Lett.* **58**, 2019 (1987).
- [12] R.G.H. Robertson et al., *Phys. Rev. Lett.* **67**, 957 (1991).
- [13] E. Holzschuh et al., *Phys. Lett. B* **287**, 381 (1992).

- [14] H. Kawakami et al., Phys. Lett. B **256**, 105 (1991).
- [15] Ch. Weinheimer et al., Phys. Lett. B **300**, 210 (1993).
- [16] F. Boehm and P. Vogel, *Physics of Massive Neutrinos, 2nd Edition* (Cambridge University Press, Cambridge, 1992).
- [17] M. Kobayashi and T. Maskawa, Prog. Theor. Phys. **49**, 652 (1973).
- [18] N. Cabibbo, Phys. Rev. Lett. **10**, 531 (1963).
- [19] M. Nakagawa et al., Prog. Theor. Phys. **30**, 258 (1963).
- [20] W.R. Dixon et al., Nucl. Instrum. Methods B **12**, 304 (1985).
- [21] W. Haxton, Phys. Rev. Lett. **55**, 807 (1985).
- [22] B. Eman and D. Tadić, Phys. Rev. C **33**, 2128 (1986).
- [23] E.G. Drukarev and M.I. Strikman, Sov. Phys. JETP **64**, 686 (1986).
- [24] J. Lindhard and P.G. Hansen, Phys. Rev. Lett. **57**, 965 (1986).
- [25] J.J. Simpson, Phys. Lett. B **174**, 113 (1986).
- [26] A. Hime and J.J. Simpson, Phys. Rev. D **39**, 1837 (1989).
- [27] A. Hime, Ph.D. thesis, Oxford (1991).
- [28] V. Datar et al., Nature **318**, 547 (1985).
- [29] T. Ohi et al., Phys. Lett. B **160**, 322 (1985).
- [30] T. Altzitzoglou et al., Phys. Rev. Lett. **55**, 799 (1985).
- [31] A.M. Apalikov et al., JETP Lett. **42**, 289 (1985).

- [32] J. Markey and F. Boehm, *Phys. Rev. C* **32**, 2215 (1985).
- [33] D. Hetherington et al., *Phys. Rev. C* **36**, 1504 (1987).
- [34] D. Wark and F. Boehm, in *Nuclear Beta Decays and Neutrinos*, proceedings of the International Symposium, Osaka, Japan, eds. T Kotani et al., (World Scientific, Singapore, 1986).
- [35] J.J. Simpson and A. Hime, *Phys. Rev. D* **39**, 1825 (1989).
- [36] H.A. Wyllie and G.C. Lowenthal, *Int. J. Appl. Radiat. Isot.* **35**, 257 (1984).
- [37] B. Planskoy, *Nucl. Instrum. Methods* **61**, 285 (1968).
- [38] A. Damkjaer, *Nucl. Instrum. Methods* **200**, 377 (1982).
- [39] H.-W. Becker et al., in *Proceedings of the Tenth Moriond Workshop*, Les Arcs, France, eds. O. Fackler and J. Tran Thanh Van, (Frontières, Gif-sur-Yvette, 1991).
- [40] D.A. Imel, Ph.D. thesis, Caltech (1990).
- [41] A. Hime and N. Jelley, *Phys. Lett. B* **257**, 441 (1991).
- [42] B. Sur et al., *Phys. Rev. Lett.* **66**, 2444 (1991).
- [43] I. Žlimen et al., *Phys. Rev. Lett.* **67**, 560 (1991).
- [44] C. De Vries, in *Construction of and Measurements with an Ironfree double Focusing Beta ray Spectrometer*, Academisch Proefschrift, Amsterdam (1960).

- [45] S. Wolfram, *Mathematica: A System for Doing Mathematics by Computer, 2nd Edition* (Addison-Wesley, Redwood City, 1991).
- [46] C.M. Lederer and V.S. Shirley, *Table of Isotopes, 7th Edition* (Wiley, New York, 1978).
- [47] P. Vogel, private communication.
- [48] W.H. Press, B.P. Flannery, S.A. Teukolsky, W.T. Vetterling, *Numerical Recipes: the Art of Scientific Computing* (Cambridge University Press, Cambridge, 1986).
- [49] F. Raab, A. Gillespie, T. Lyons, M. Regehr, private communications. I appreciate their cooperation and assistance in identifying the LIGO laser as the source of the local field disturbances.
- [50] Particle Data Group, *Review of Particle Properties*, Phys. Rev. D **45**, III.39 (1992).
- [51] W.R. Leo, *Techniques for Nuclear and Particle Physics Experiments*, 47 (Springer-Verlag, Berlin, 1987).
- [52] W.R. Nelson, H. Hirayama, D.W.O. Rogers, *The EGS<sub>4</sub> Code System*, SLAC-Report 265 (1985).
- [53] M. Chen et al., Phys. Rev. Lett. **69**, 3151 (1992).
- [54] H. Kawakami et al., Phys. Lett. B **287**, 45 (1992).
- [55] T. Ohshima et al., Phys. Rev. D **47**, 4840 (1993).
- [56] M.M. Lowry et al., Bull. Am. Phys. Soc. **37**, 887 (1992).
- [57] G.E. Berman et al., Phys. Rev. C **48**, R1 (1993).

- [58] J.L. Mortara et al., Phys. Rev. Lett. **70**, 394 (1993).
- [59] M. Bahran and G.R. Kalbfleisch, Phys. Lett. B **291**, 336 (1992).
- [60] G.R. Kalbfleisch and M. Bahran, Phys. Lett. B **303**, 355 (1993).
- [61] I. Žliment et al., Phys. Scr. **38**, 539 (1988).
- [62] E.B. Norman et al., in *Proceedings of the Fourteenth Europhysics Conference on Nuclear Physics, Rare Nuclear Decays and Fundamental Processes*, Bratislava, Czechoslovakia, J. Phys. G. Nucl. Part. Phys. **17**, S291 (1991).
- [63] D.E. DiGregorio et al., TANDAR preprint LNY584 L-1 SB (1991).
- [64] F.E. Wietfeldt et al., Phys. Rev. Lett. **70**, 1759 (1993).
- [65] D.E. DiGregorio et al., Phys. Rev. C **47**, 2916 (1993).
- [66] L. Piilonen and A. Abashian, in *Proceedings of the Twelfth Moriond Workshop*, Les Arcs, France, eds. O. Fackler and J. Tran Thanh Van, (Frontières, Gif-sur-Yvette, 1992).
- [67] A. Hime, Phys. Lett. B **299**, 165 (1993).
- [68] F.E. Wietfeldt et al., Bull. Am. Phys. Soc. **38**, 1855 (1993).
- [69] D.C. Conway and W.H. Johnson, Phys. Rev. **116**, 1544 (1959).
- [70] C.D. Ellis and W.J. Henderson, Proc. R. Soc. London **A146**, 206 (1934).
- [71] E.J. Konopinski and G.E. Uhlenbeck, Phys. Rev. **48**, 7 (1935).
- [72] F. Boehm, private communication.

- [73] M. Gell-Mann and A. Pais, *Phys. Rev.* **97**, 1387 (1955).
- [74] B. Pontecorvo, *Sov. Phys. JETP* **6**, 429 (1958).
- [75] B. Pontecorvo, *Zh. Eksp. Theor. Fiz.* **53**, 1717 (1967); S. Bilensky and B. Pontecorvo, *Phys. Lett.* **61B**, 248 (1976); S. Bilensky and B. Pontecorvo, *Phys. Reports* **41**, 225 (1978).
- [76] Z. Maki et al., *Prog. Theor. Phys.* **28**, 870 (1962).
- [77] R. Davis, in *Frontiers of Neutrino Astrophysics*, proceedings of the International Symposium on Neutrino Astrophysics, Takayama, Japan, eds. Y. Suzuki and N. Nakamura, (Universal Academic Press, Tokyo, 1993).
- [78] J.N. Bahcall and R. Ulrich, *Rev. Mod. Phys.* **60**, 297 (1988); J.N. Bahcall, *Neutrino Astrophysics* (Cambridge University Press, Cambridge, 1989).
- [79] K.S. Hirata et al., *Phys. Rev. D* **44**, 2241 (1991); K.S. Hirata et al., *Phys. Rev. Lett.* **65**, 1297 (1990).
- [80] A.I. Abazov et al., *Phys. Rev. Lett.* **67**, 3332 (1991).
- [81] P. Anselmann et al., *Phys. Lett. B* **285**, 390 (1992).
- [82] J.N. Bahcall and H.A. Bethe, *Phys. Rev. Lett.* **65**, 2233 (1990); J.N. Bahcall et al., *Rev. Mod. Phys.* **54**, 767 (1982).
- [83] S.P. Mikheyev and A.Yu. Smirnov, *Sov. J. Nucl. Phys.* **42**, 1441 (1985).
- [84] L. Wolfenstein, *Phys. Rev. D* **17**, 2369 (1978).
- [85] D. Casper et al., *Phys. Rev. Lett.* **66**, 2561 (1991).

- [86] K.S. Hirata et al., Phys. Lett. B **280**, 146 (1992).
- [87] T.K. Gaisser, T. Stanev, et al., Phys. Rev. Lett. **51**, 223 (1983).
- [88] G. Zacek et al., Phys. Rev. D **34**, 2621 (1986).
- [89] F. Boehm et al., in *Proposal for the San Onofre Neutrino Oscillation Experiment*, Caltech preprint, CALT-63-657A (1994); M. Chen et al., to appear in *Proceedings of the Third International Workshop TAUP '93*, Assergi, Italy, ed. A. Bottino, (1993).
- [90] S. Charalambus, Nucl. Phys. A **166**, 145 (1971).
- [91] T. Kozlowski et al., Nucl. Phys. A **436**, 717 (1985).
- [92] E.P. George and J. Evans, Proc. Phys. Soc. London **A63**, 1248 (1950).
- [93] G. Cocconi and V. Cocconi Tongiorgi, Phys. Rev. **84**, 29 (1951).
- [94] S. Hayakawa, Phys. Rev. **84**, 37 (1951).
- [95] R. Hertenberger, private communication.
- [96] M. Ericson, T.E.O. Ericson and P. Vogel, private communication.
- [97] J.C. Barton, Proc. of 19th Int. Cosmic Ray Conf., La Jolla, USA **8**, 98 (1985).
- [98] F.F. Khalchukov et al., Nuovo Cimento **6C**, 320 (1983); also, later results from their Artemovsk station (570 mwe), presented at conferences.
- [99] S. Homma et al., Phys. Rev. C **27**, 31 (1982).
- [100] O.G. Ryazhskaya, private communication.

- [101] M. Chen, V.M. Novikov, and B.L. Dougherty, Nucl. Instrum. Methods A **336**, 232 (1993).
- [102] R. Heaton originally developed the neutron code for simulations of the SNO detector; the code was brought to us and adapted by T.J. Radcliffe, and further modified by M. Chen.
- [103] R. Madey et al., Phys. Rev. C **25**, 3050 (1982).
- [104] L.B. Bezrukov et al., Sov. J. Nucl. Phys. **17**, 51 (1973).
- [105] M. Aglietta et al., Nuovo Cimento **12C**, 467 (1989).
- [106] R.I. Enikeev et al., Sov. J. Nucl. Phys. **46**, 1492 (1987).